Ollscoil na hÉireann, Corcaigh

National University of Ireland, Cork

Nanowire and Microband Arrays for Enhanced Electrochemical Sensing

Thesis presented by

Ian Seymour

for the degree of

Doctor of Philosophy

University College Cork

Tyndall National Institute

Head of School/Department: Dr Fatima Gunning

Supervisors: Dr James Rohan and Dr Alan O'Riordan

2020

Table of Contents

Declaration

I hereby certify that the work I am submitting is my own and has not been submitted for another degree, either at University College Cork or elsewhere. All external references and sources are clearly acknowledged and identified within the contents. I have read and understood the regulations of University College Cork concerning plagiarism. Any contribution made to the research by others, with whom I have worked directly at Tyndall National Institute - University College Cork or elsewhere, is explicitly acknowledged in the thesis. I also declare that the intellectual content of this thesis is the product of my own work, except to the extent that assistance from others in the project's design and conception or in style, presentation and linguistic expression is acknowledged.

_____

Ian Seymour

June 2020

Abstract

Water quality monitoring is crucial to ensure that (i) water is safe to be consumed by humans, and (ii) that it is of adequate quality for aquatic life. The European Union has dedicated two of its seventeen sustainable development goals for 2030 to water quality. While many methods are available to monitor water quality, these typically involve the use of additional reagents, or require specialist equipment or personnel to carry out the required analysis. In this thesis, electrochemical methods are explored and developed such that they allow for reagent-free, point-of-care testing without the need for specialist training. The main goal of this thesis was to develop interference free measurements that could be applied to remote analysis. To do this, interdigitated micro-electrode arrays were designed and fabricated wherein each comb of electrodes could be biased at different potentials allowing for unique analysis opportunities.

The first section deals with the detection of residual free chlorine, the most common disinfectant in water. To do this a pH control method using the interdigitated electrodes was developed that forced the free chlorine in solution to convert to hypochlorous acid, which can be easily detected. This approach prevents loss of signal due to presence of hypochlorite, which is less active in the potential window investigated. Concentrations as low as 0.35 ppm were measured and this method was applied to both buffered water samples and tap water samples.

Following from this, the pH control method was applied to the detection of monochloramine. This is the second most common disinfectant for water, typically used in North America. It is also a by-product of water chlorination, so it also needs to be monitored in systems where it is not used as the primary disinfectant. The pH control method was refined in this section and resulted in a sensor that could detect monochloramine by converting it to dichloramine. Monochloramine detection is hindered by the presence of dissolved oxygen, while dichloramine is free from oxygen interference. A detection limit of 0.03 ppm was calculated

and this method was applied to water distribution networks even those with high conductivity and alkalinity.

Finally, a reagent free method of dissolved oxygen quantification was developed. Dissolved oxygen is a measure of water quality typically used to determine how well the water supports aquatic life. Low dissolved oxygen concentrations can also indicate the presence of bacteria or contaminants like nitrates and nitrites. The detection method developed herein involves reduction of dissolved oxygen to produce hydrogen peroxide, which is subsequently detected at the other comb of electrodes free from interference. Gold and platinum mixed arrays were used to take advantage of both materials properties for oxygen reduction and peroxide oxidation. Oxygen concentrations between 0 and 10 ppm were detected using this method (benchmarked against commercial gold standards), and this approach was applied to real water samples taken from farm run off. This water typically contains high concentrations of fertilizer, yet accurate oxygen measurements were obtained.

Abbreviations and Acronyms

ADC	Analog to Digital Converter
ads	Adsorbed
ADW	Artificial Drinking Water
Ag	Silver
AgCl	Silver Chloride
Au	Gold
CA	Chronoamperometry
CE	Counter Electrode
Cl_2	Chlorine
Cl_2:N	Chlorine to Nitrogen Ratio
CV	Cyclic Voltammetry
DAC	Digital to Analog Converter
DCA	Dichloramine
DNA	Deoxyribonucleic acid
DNS	Dinitrosulphatoplatinum
DO	Dissolved Oxygen
DPD	diethyl-p-phenylene diamine
DPI	Dots Per Inch
e^-	Electron
EDX	Energy Dispersive X-ray
EIS	Electrochemical Impedance Spectroscopy
FCA	Ferrocene Carboxylic Acid
Fe	Iron
$Fe(CN)_6$	Ferri/Ferro Cyanide
FEA	Finite Element Analysis
FeCpOH	Iron Cyclopentanol
GC	Generator-Collector
H^+	Hydrogen Ion
H_2O	Water
H_2O_2	Hydrogen Peroxide
H_2SO_4	Sulphuric Acid
HCl	Hydrochloric Acid
HDMI	High Definition Multimedia Interface
HOCl	Hypochlorous Acid
HOMO	Highest Occupied Molecular Orbital
IDE	Inter Digitated Electrode
IHP	Inner Helmholtz Plane
INEA	Interdigitated Nano Electrode Array
IPE	Ideal Polarizable Electrode
LOD	Limit of Detection
LSV	Linear Sweep Voltammetry
LUMO	Lowest Unoccupied Molecular Orbital

MCA	Monochloramine
NaOCl	Sodium Hypochlorite
NaOH	Sodium Hydroxide
NH_3	Ammonia
NH_4Cl	Ammonium Chloride
NHE	Normal Hydrogen Electrode
NO_2	Nitrogen Dioxide
O_2	Oxygen
OCl^-	Hypochlorite Anion
OH^-	Hydroxyl Anion
OHP	Outer Helmholtz Plane
ORR	Oxugen Reduction Reaction
pAP	para Aminophenol
pAPP	para Aminophenyl Monophosphate
PBS	Phosphate Buffered Saline
pIQ	para Iminoquinone
ppm	Parts Per Million
Pt	Platinum
RE	Reference Electrode
RHE	Reversible Hydrogen Electrode
RRDE	Rotating Ring Disc Electrode
SCE	Saturated Calomel Electrode
SD	Standard Deviation
SEM	Scanning Electron Microscopy
SF	Shielding Factor
SHE	Standard Hydrogen Electrode
SiN	Silicon Nitride
SiO_2	Silicon Dioxide
SIRC	Self Induced Redox Cycling
TCA	Trichloramine
THM	Trihalomethanes
Ti	Titanium
TNT	Trinitrotoluene
UV	Ultra Violet
WE	Working Electrode
WHO	World Health Organization

Acknowledgements

I would first like to show my gratitude to my supervisors Dr. James Rohan and Dr. Alan O'Riordan for giving me this opportunity. They have both provided me with unwavering support and encouragement, while also being a source of knowledge and experience, that has proved crucial to me on countless occasions. I first worked with James on the final year project of my bachelor's degree, after which he accepted me back into his group to do my master's research project. In these two projects I believe he got to know me as a person and saw my capabilities as a researcher. To this day I do not know why he brought me back for a PhD, but I am forever grateful. Alan did not supervise my first two projects in Tyndall, so I only met him when he was introduced as the co-supervisor for my PhD. By then it was too late, but I persevered. I believe I am truly lucky to have been supervised by two people who are not just excellent researchers, but genuinely good 'craic' too.

Aside from the guidance of my supervisors, I also had the good fortune to have various post-docs and researchers willing to help me develop my skills in the lab. Dr. Amelie Wahl brought me up to speed on techniques used in electrochemistry, as well as helping me understand how things worked in Tyndall. Like how the purchasing system worked, or that students typically come into work before lunchtime. Dr. Pierre Lovera welcomed me into his lab. (my home for 4 years) and helped me survive an industry project with both his intelligence and his sense of humour. We have had our ups (Barcelona Day one) and downs (Barcelona Day two), but I still believe he truly is the "Catalyst of Greatness". Plus, he does a killer Scottish accent.

A big thanks is needed for each of my friends in Tyndall who kept me sane throughout this by distracting me with various tea breaks, pub sessions, cinema trips, cycles, and hikes. Thanks to Fiona, who has been a phenomenal friend for the entire college experience. I am so glad you ignored my advice to not do a PhD because it would have been weird without you. Just

remember, this is only to pass the time until we grow up and start a business. Caoimhe, thanks for organising basically every activity and being the reason fun things happened. I will never admit it in person, but you are Irish through and through. Niamh, I hope you sing as much in your new job as you did in Tyndall because that always made my day. Also cheers for being the first person to read my thesis and tell me there was some hope. Colm, thanks for answering my stupid electrochemistry questions and always being up for a pint or six. Louise, thanks for showing me that you do not need to drink to have fun on a night out, even if it's a lesson I never put into practise. Benjy, thanks for making sure I never got too big of an ego. Julia, thank you for making sure I actually went running and keeping us safe in Oldcastle. Aidan, for teaching mee how a potentiostat works. Declan, thanks for being just the right amount of distracting. I complain about how much you distracted me while I was writing my master's thesis, but I'd have given anything to have that these last three months. Eoin always enjoyed your stories, but I was most impressed with your invincibility. I have to thank my desk mates, Emma and Anya, for part-taking in my treasure hunts and always being up for a chat, but also for not reporting me to HR due to me not shutting up. Shane (the intern), thanks for not being the worst FYP student ever and for all the music suggestions. Really got me through the writing period. Tyndall has introduced me to so many friends that I could be thanking people forever. However, there is one friend that cannot go unnoticed. While they were not there for the full length of my PhD, they did come into my life at a crucial time and helped me when I needed it most. So, thank you Impala for everything you've done for me.

Of course, not everyone who helped me through this worked in Tyndall. Special thanks to my longest and closest friend Aaron, who was always up for a walk, the rare cycle, or the common gaming session. Big thanks also to my Evergreen Team (Steve, Colm, Sean, Aoife, Becca and Tony) for the sessions. They were few and far between, but let's face it, that was probably for the best.

Massive thanks to Lisa, for your love, support, and encouragement through all of this. Thank you for putting up with me through 9 years of college, keeping me grounded through the stress of project reviews and thesis writing, and for not firing that bottle of sun lotion at my head when I took a work call while we were on holidays in Gran Canaria. I cannot thank you enough for everything you've done for me over the years (most of which were not throwing things at my head when you absolutely should have).

Finally, thanks to my family for giving me all the support I could ask for at every step of the way. To my parents, Mary and John, thank you for the guidance, love, and support you have given me throughout my life. You have always ensured that I had every opportunity to pursue my goals. I have no doubt that I would not be at this point in a PhD without your help. I am also grateful to your respective partners, Colm and Maura, who have always shown me unwavering support throughout. To my (little) brother Keith, thank you not only for your support, but also for always making me laugh. Your incredible sense of humour has always helped me to forget the stressful times. And as a founding member of Brosis, I cannot thank you enough for driving us to see Mary Black on numerous occasions. And to Louise for letting you go. A huge thanks must be given to my sister, Sharon for her love and support, but also for being as immature as I am. It would be incorrect to say that I have been particularly stressed while writing my thesis for these last few months. This is thanks to you. Between our morning coffee walks, playing ball in the house, or flying paper airplanes up and down the stairs, I have been almost entirely stress-free. Without you I would have succumbed to stress and pulled my hair out months ago. Admittedly, I would probably have finished my thesis three months sooner, but it would have been no fun at all. Thank you for not being a proper adult like me. Finally, I'd like to thank my niece and nephew, Hayley and Zach. They have not helped me in any particular way, but they're adorable so they get a mention.

“….it’s a great life”

Chapter 1 Introduction

Electrochemical sensors are attractive alternatives to other sensing technologies (chromatographic, spectroscopic, etc.) due to their simplicity and lower cost. Such sensors can be easily miniaturised, integrated into existing systems and often do not require specialist operators. Electrodes can be simple structures, such as planar metal devices, or more advanced structures, such as nanotubes made of complex materials to facilitate sensing of a wide range of analytes, and for a wide range of applications. These structures can range from single planar disc electrodes, to complex arrays with multiple addressable working electrodes in a variety of shapes and sizes. The main objective of this thesis is to explore how interdigitated electrode arrays, with dimensions less than 1 μm, can be utilised for the electrochemical analysis of water quality.

In this introduction chapter, the fundamental concepts of electrochemistry are discussed. This includes the description of many of the factors that can influence analysis using electrochemical techniques. Each of the core components of an electrochemical cell are described, and the equipment required for analysis. This is followed by a description of generator-collector electrode devices, of which the interdigitated array is one type. Finally, a brief literature review is given for some of the fabrication methods and applications of interdigitated electrode arrays.

1.1 Fundamental Principles of Electrochemistry

The study of electrochemistry is crucial for the advancement of a great number of different technologies. Devices such as batteries, fuel cells and electrochemical sensors are well known examples of the application of electrochemistry. Electrochemical techniques have also facilitated the development of plating technologies that have enabled miniaturised circuits, and electrolysis technologies that can produce hydrogen gas (a green fuel) from water. It is also possible to explain why metals degrade and corrode in certain environments because of electrochemistry, which in turn helps us choose materials that are fit for purpose. At its simplest, electrochemistry is the study of the charge transfer between an electrode and a species in solution when an external voltage or current is applied.[1]

1.1.1 Components of an Electrochemical Cell and Experimental Set-up

While electrochemical cell set-ups can consist of two, three or in some cases four electrodes, the most common type is the three-electrode cell. This consists of a working electrode (WE), a counter electrode (CE) and a reference electrode (RE). Each of these is submerged in an electrolytic solution. The solution may contain a species of interest, or the solution may facilitate analysis of the WE itself. Each electrode is then connected to a potentiostat which is a device that carries out an electroanalytical technique and is discussed further below. When working with ultramicro- (critical dimensions less than the diffusion layer thickness) and nano-electrodes (critical dimension of 100 nm or lower) measurements are sometimes performed within a Faraday cage which is typically made of conductive material and minimises background electrochemical noise. The conductive material allows any electrical interference to be dissipated around the exterior of the cage a preventing electromagnetic noise from reaching the electrolytic cell. Figure 1-1 shows

a schematic representation of how each of these components are set up to facilitate electrochemical analysis. The user interface is commonly a computer, but as potentiostats are becoming smaller and more portable, this can just as easily be a tablet or a mobile phone.

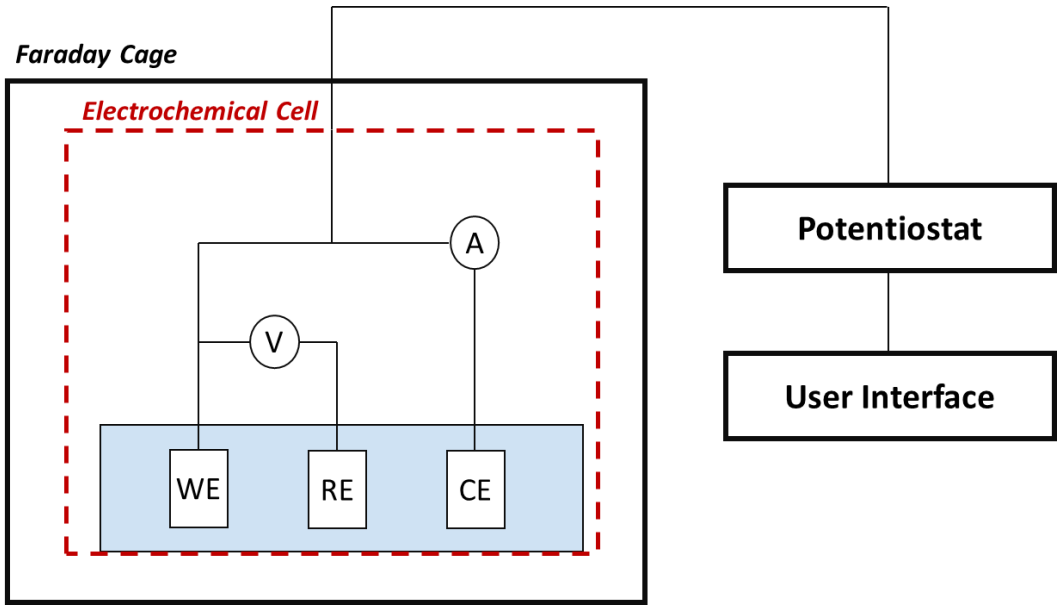

Figure 1-1 Schematic of the set-up for a standard three electrode electrochemical measurement. Everything inside the red dashed box is considered the electrochemical cell

1.1.1.1 *The Working Electrode (WE)*

The WE, sometimes referred to as the indicator electrode, is the electrode where the reaction of interest takes place. The WE needs to be conductive and, when reaction of the electrode is not desired, inert in the potential region of interest. In this thesis, all the electrodes used are made of inert materials to prevent interfering reactions with the species being analysed. Most commonly, noble metals such as gold and platinum and non-metals with good conductivity such as carbon are used. Liquid metals can also be used, such as mercury which was one of the first WE materials used for analysis. The WE must have a clean reproducible surface, so in some cases, electrode pre-treatment is required before analysis can be carried out. The structures of WEs can be quite varied and

depend on the application. Different electrode shapes and sizes can improve various aspects of the electrochemical behaviour. Taking electrochemical sensors as an example, detection of inorganic species can be enhanced by use of porous electrode structures, as the species of interest can penetrate the pores resulting in enhanced sensing.[2] The same electrode would show no benefit for sensing of biomolecules, as these species may be too large to penetrate such pores, resulting in decreased sensing performance.

1.1.1.2 *The Counter Electrode (CE)*

The CE typically acts as a supply or sink of electrons for the WE. As such, it must also be made of conductive materials, and must be larger than the WE to not limit electrochemical reactions. This also enables the flow of current between the WE and the CE which prevents any current flowing through, and polarisation of, the RE. To maintain electroneutrality the CE can also provide the opposite redox reaction to the WE. Because of this, both electrodes need to have a sufficient distance between them so that the redox reactions do not interfere with each other. For an electrochemical sensor, this distance should be at least larger than the distance the excited species can diffuse, but not too large to cause an increase in cell resistance.

1.1.1.3 *The Reference Electrode (RE)*

RE are used to provide a stable and accurate measurement of the WE potential. Therefore, the RE must be an ideal nonpolarizable electrode. Such an electrode does not change its potential upon the application of current, and results from the electrode reaction being extremely fast.[3] REs approach this behaviour for small current values. The reaction governing the RE must also be reversible, such that a potential can be calculated from the Nernst equation. The standard hydrogen electrode (SHE), also referred to as the normal hydrogen electrode (NHE), provides an absolute scale for electrochemical reactions. This

is the electrode against which standard electrode potentials are referenced. The reaction for this electrode has a standard potential of 0 V by convention.

$$2H^+ + 2e^- \rightleftharpoons H_2, \qquad E^\circ_{Pt|H_2,H^+} = 0.000\ V$$

This electrode consists of a platinum wire, submerged in an acid over which hydrogen gas is constantly bubbled. Although it is the standard RE, they can be difficult to work with due to the difficulty in its construction.[4] Alternative REs have been developed that are simpler to use in practice by eliminating the need for constant bubbling of hydrogen. These include, but are not limited to the saturated calomel electrode (SCE) and the silver/silver chloride electrode (Ag/AgCl).[5] The SCE electrode is very stable and is one of the most common REs. It consists of platinum wire submerged in a saturated potassium chloride solution. The wire is also partially submerged in liquid mercury and coated with a mercury, calomel and potassium chloride paste. The reaction that governs the SCE has a standard potential of 0.241 V vs. SHE at 25°C.

$$Hg_2Cl_2 + 2e^- \rightleftharpoons 2Hg + 2Cl^-, E^\circ_{Hg|Hg_2Cl_2} = 0.241\ V \text{ vs. SHE} \qquad \text{Equation 1.1}$$

Unfortunately, due to the use of mercury in this electrode, they are unsafe if broken and difficult to dispose of. As such, non-toxic, environmentally safer alternatives are used such as the Ag/AgCl electrode. This electrode consists of a silver wire, coated with silver chloride submerged in a saturated potassium chloride solution. The reaction that governs this RE has a standard potential of 0.197 V versus SHE at 25°C.

$$AgCl + e^- \rightleftharpoons Ag + Cl^-, E^\circ_{Ag|AgCl} = 0.197\ V \text{ vs. SHE} \qquad \text{Equation 1.2}$$

Both electrodes behave in mostly the same way, in that the activity of the metal ion is determined by the solubility of the metal salt. However, one drawback to both electrode types are that they require a minimum sample volume, typically a few millilitres. If the sample volumes are on a microlitre scale, conventional REs cannot be used. Similarly, reliance on these REs limits the potential for portable electrochemical sensors. To this

end, miniaturised RE for on-chip applications are used to overcome this limitation. Ag/AgCl has been fabricated on chip as a viable alternative. [6] These are somewhat stable, but require regular redeposition of the silver chloride material. An alternative solution is to use pseudo-reference electrode materials, such as platinum.[7] Pseudo REs do not maintain a stable reference potential over long periods of time. Because of this, devices that use a pseudo RE need to be regularly calibrated. Alternatively, an internal reference solution can be used when regularly calibration is not possible. An internal reference solution can be one that contains a well characterised redox couple, so any potential shifts can be accounted for and corrected.

1.1.1.4 *The Potentiostat*

The potentiostat works by maintaining a constant potential difference between the WE and the RE. This is accomplished by applying a current between the WE and the CE. This current value changes depending on the desired potential at the WE. Figure 1-2 shows a schematic representation of the five main components of a potentiostat, one being the electrochemical cell itself.

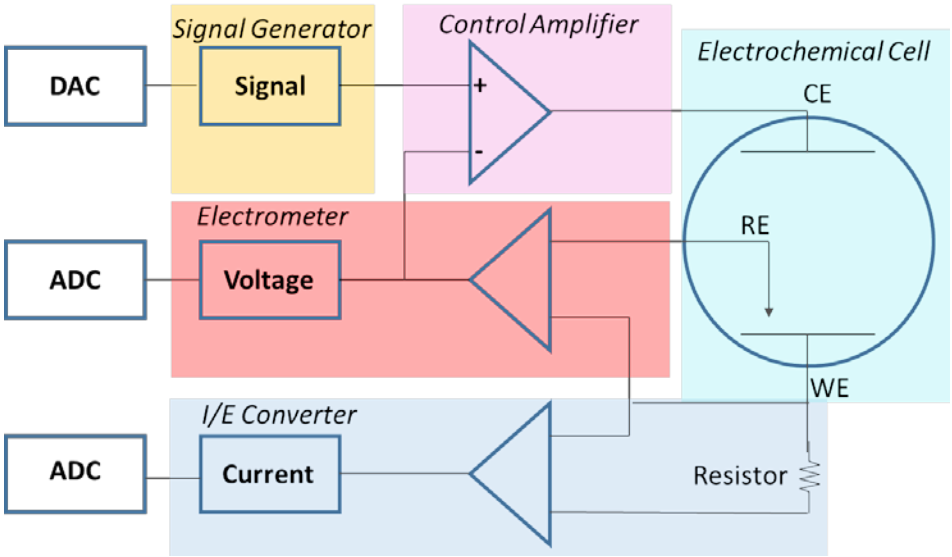

Figure 1-2 Schematic representation of a potentiostat, reproduced from [8]

The signal generator in modern potentiostats is a voltage source controlled by a computer interface. A digital signal from a computer is converted to an analog signal (a voltage) that is applied to the cell. These signals can have varying complexities to suit the electrochemical measurement.

The control amplifier is used to fix the potential of the cell at the desired value. It works by comparing the measured potential of the cell to the desired potential to ensure no deviation is observed. The measured potential is input into the control amplifier at the negative terminal, therefore if the measured potential is higher than the desired, this change is counteracted by the negative feedback.

The electrometer measures the potential between the RE and the WE, which serves two functions in the potentiostat. The first being that it provides a measured potential that feeds into the control amplifier. The second function is that it provides the user with the cell potential measurement at any given time. This voltage can then be converted from analog to a digital signal that is displayed on a computer.

The I/E converter is used to measure the current flowing in the electrochemical cell. This is done by measuring the potential at the WE before and after current flow through a resistor. The potential drop observed as a result of the resistor can be converted to the cell current.

1.1.2 Electron Transfer

In the case of electrochemical charge transfer, the reactions of interest are those that occur at the interface of an electrode and a solution upon application of a potential. The reactions involve the flow of electrons between the electrode and electrolyte or electroactive species in the electrolyte, producing a measurable change in current or potential. These reactions can generate a charged species,[9] convert the species from a

liquid to a gas,[10] form oxides[11], plate materials onto the electrode surface[12] or even remove material from the electrode.[13] These reactions can be termed oxidation (species loses electrons) or reduction (species gains electrons). It is important to note that if one component of the electron transfer reaction is oxidised, the other component is reduced. In this thesis, the heterogeneous electron transfer reactions studied are primarily those between an electrode and an electroactive species in solution. The following section focuses mainly on these types of reactions. These reactions can be described by:

$$O + ne^- \rightleftharpoons R \qquad \text{Equation 1.3}$$

Where O is the oxidised species, R is the reduced species and n is the number of electrons (e^-) used in the reaction. When the electrode causes an oxidation event, it is termed the anode and for a reduction event, it is called the cathode.

For an electron transfer reaction to occur, the energy level of the electrons in the electrode must match that of the vacant orbital in the molecule. Alternatively, the electrode energy levels must be low enough so that it becomes more favourable for an electron in an orbital of a molecule of interest to move to the electrode. A molecular species in solution will have a distinct energy associated with its highest occupied molecular orbital (HOMO), and its lowest unoccupied molecular orbital (LUMO). These are the orbitals that an electron can be taken from or donated to, respectively. The energy required to promote an electron from a HOMO to a LUMO is known as the HOMO-LUMO gap. Concerning solids, metals and conductors do not have discreet energy levels but rather a continuum of energy levels. The Fermi level marks the boundary between occupied and unoccupied states, or for conductors it is the energy level that is half filled by electrons.[14] An electrode in solution with no applied voltage bias does not have the energy required to promote an electron into the LUMO of a species, while simultaneously the electrode energy is

typically not low enough to allow electron transfer from the species to the electrode due to an energy barrier; see figure 1-3(a). Thus, the reactions are thermodynamically unfavourable and will not happen. Upon application of an appropriate voltage bias, the energy levels of the solution are changed with respect to the working electrode; which is maintained at virtual ground. Application of potentials lower than the formal potential of the redox species results in a decrease in the energy of the LUMO w.r.t. the Fermi level. In this case it becomes thermodynamically favourable from an electron to move into the LUMO from the metal resulting in a reduction reaction, Figure 1-3(a). When potentials greater than the formal potential are applied, the energy level of the HOMO increases, such that it becomes favourable for an electron in the HOMO to move into the electrode, resulting in an oxidation reaction, Figure 1-3(b).[3] Figure 1-3 illustrates both the unfavourable, and the favourable conditions for both oxidation and reduction reactions.

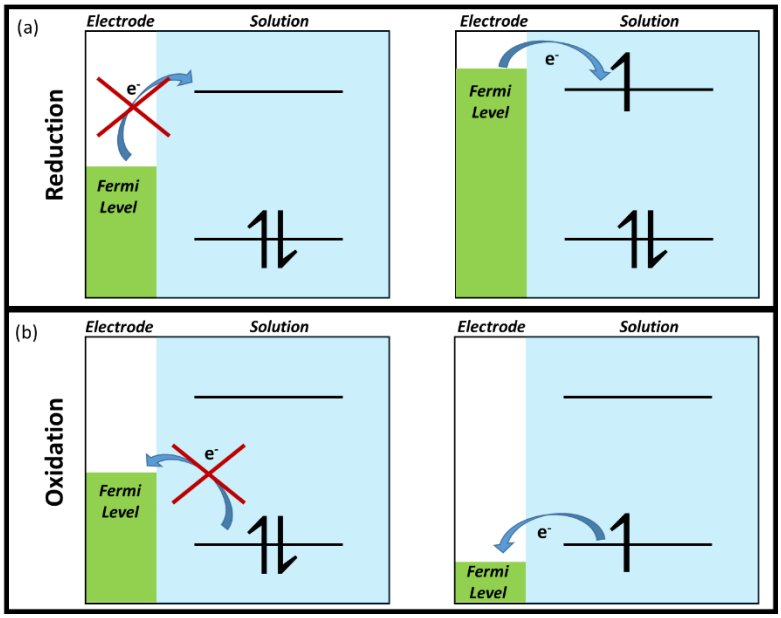

Figure 1-3 Electron transfer and energy levels at the electrode-solution interface during (a) reduction and (b) oxidation reactions.

1.1.3 Faradaic and Non-Faradaic Responses

The oxidation and reduction reactions previously described in section 1.1.2 obey Faraday's Law, which states that the amount of species electrolysed at an electrode is directly proportional to the amount of charge supplied. This is given by the equation:

$$Q = nNF \qquad \text{Equation 1.4}$$

Wherein Q is charge (coulombs, C), n is the number of electrons involved, N is the number of moles (mol) and F is Faraday's constant (96485 C/mol). Thus, the reactions of interest are termed Faradaic processes. However, the measured current by an instrument is not entirely due to the Faradaic response. A portion of the current is attributable to adsorption and desorption processes at the electrode surface, which are not charge transfer reactions and do not obey Faradays law. Thus, these processes are termed non-Faradaic processes.

To help understand what contributes to the non-Faradaic process, it is useful to introduce the concept of an Ideal Polarizable Electrodes (IPE). These are electrodes at which no charge transfer can occur between the electrode and the solution at any applied potential, see Figure 1-4.[3] Real electrodes can behave like IPEs in a certain potential range. In these cases, a current is only seen at extremes of potentials as illustrated in the graph Figure 1-4.

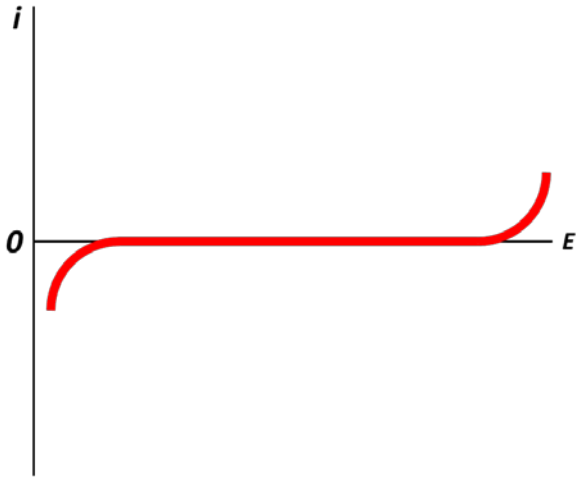

Figure 1-4 Effect of applied potential on an IPE

The behaviour of an IPE in a solution can be directly compared to that of a capacitor. The exception being that for the IPE, the capacitance will be dependent on the potential applied while for a capacitor it is not. This behaviour is then governed by the equation:[15]

$$C = \frac{Q}{E}$$

Where Q is charge (Coulombs, C), E is the potential applied (Volts, V) and C is the capacitance (Farads, F). When a metal is placed in solution, a charge will accumulate at the electrode-solution interface and form an electrical double layer, one layer being the charge from the electrode and the other being the opposing charge from the solution. The formation of this double layer gives rise to a charging current to be passed through the cell. This current value will depend on various factors including electrode material, concentration of electrolyte and type of solvent used.[5] A model of the double layer was initially proposed by Helmholtz, who treated the double layer as a parallel plate. In this model, the charge at the electrode surface is neutralised by a counter-ion in solution a fixed distance away (the Helmholtz plane), and as such the surface charge potential is linearly dissipated with distance.[16]

Gouy and Chapman proposed a diffuse charge model of the double layer, wherein ions are treated as point charges that are non-uniformly distributed in the layer. These ions can diffuse in and out until their counter potential restricts this ability.[17] The most common model used to describe the double layer is the Stern model, which effectively combines both the Helmholtz and Gouy-Chapman models overcoming the limitations of both, see Figure 1-5. In this, the electrode side of the double layer is simply a surface with a charge density of σ_m. The solution side is more complex and consists of multiple zones. The closest zone is the Inner Helmholtz Plane (IHP) and contains specifically adsorbed (counter) ions. The IHP is marked by the centres of the ions and can also contain various solvent molecules and has a charge density of σ_{IHP}. The next zone, the Outer Helmholtz Plane (OHP) consists of non-specifically adsorbed solvated ions that are attracted to the electrode by coulombic forces. The OHP is marked by the centre of these ions and has a charge density of σ_{OHP}. Beyond this is the diffuse layer which extends into the bulk and has a charge of density σ_d.[3] The total charge density of the electrode (σ_m) is equivalent to the total charge density of the solution (σ_s) differing only by sign, thus:

$$\sigma_m = -\sigma_s = -(\sigma_{IHP} + \sigma_{OHP} + \sigma_d) \qquad \text{Equation 1.5}$$

It is this double layer, visualised in Figure 1-5, that leads to the formation of charging currents. These currents form part of the background of an electrochemical measurement. Typically, at low scan rates, they are quite small and can be ignored, however when trying to detect ultra-low concentrations, for example micro- to nano-molar, they can have a relatively large impact and must be accounted for.

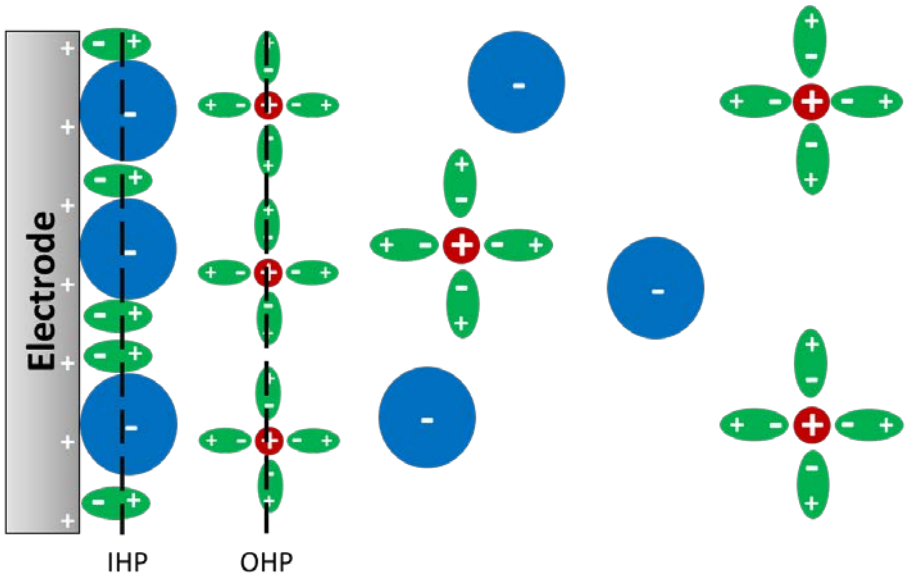

Figure 1-5 Schematic representation of the electric double layer. The blue spheres are anions, red spheres are cations and the green spheres are solvent molecules. Both the Inner Helmholtz Plane (IHP) and Outer Helmholtz Plane (OHP) are labelled.

1.1.4 What Influences a Faradaic Current Response?

The Faradaic response observed from an electrochemical reaction depends on a number of different factors. Figure 1-6 shows the possible steps involved in measuring a current response at an electrode. These include; mass transfer from the bulk solution to the electrode environment; chemical reactions that may occur in the electrode vicinity; surface reactions, such as adsorption and desorption or dipole rearrangements; and finally the electron transfer. The slowest process is the rate determining step and imposes a limit on the electrochemical response. Typically, the most common processes which limit the reactions are the rate of electron transfer and the rate of mass transfer.

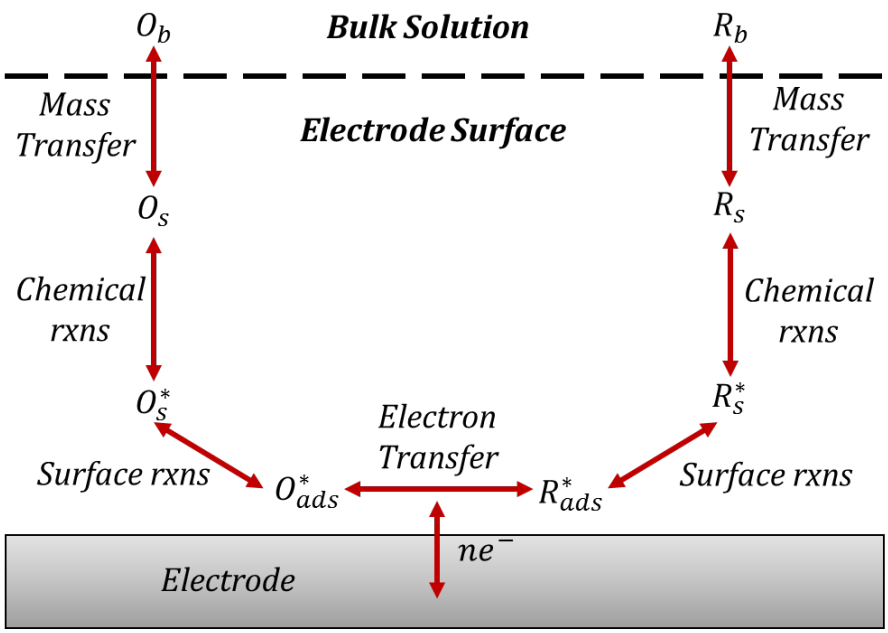

Figure 1-6 Schematic of the steps involved in a Faradaic reaction. O and R are a species in an oxidised and reduced state, respectively. O_b is oxidised species in the bulk solution, O_s is oxidised species at the electrode surface, O_s^* is oxidised species that has been chemically changed and O_{ads}^* is oxidised species that is adsorbed to the surface. The same notation applies to R the reduced species.

1.1.4.1 *Describing Electron Transfer*

As with chemical reactions, electrochemical reactions are associated with a change in Gibbs energy (ΔG). Typically, the change in energy can be calculated by the equation:

$$\Delta G = \Delta G^0 + RTlnK_{eq} \qquad \text{Equation 1.6}$$

Where ΔG^0 is the standard Gibbs energy, R is the universal gas constant, T is temperature and K_{eq} is the equilibrium constant of the reaction. This can also be described by the concentration of products divided by reactants. Gibbs energy can be equated to the cell potential (E) and the standard cell potential (E^0) by the equations:

$$\Delta G = -nFE \qquad \text{Equation 1.7}$$

$$\Delta G^0 = -nFE^0 \qquad \text{Equation 1.8}$$

Negative values of ΔG indicate spontaneous reactions, such as in a galvanic cell. Positive values of ΔG indicate non-spontaneous reactions, and therefore need application of a voltage to proceed. From these equations, the cell potential can be calculated as:

$$-nFE = -nFE^0 + RTln\frac{[R]}{[O]} \qquad \text{Equation 1.9}$$

Which simplifies to:

$$E = E^0 + \frac{2.303RT}{nF} log\frac{[O]}{[R]} \qquad \text{Equation 1.10}$$

This equation is known as the Nernst equation and can be used to determine the ratio of products to reactants at a given applied potential.[3, 15] When a reaction follows this behaviour, it is termed Nernstian and is a reversible reaction. Reversibility in this sense differs from chemical reversibility. A chemical reaction is reversible if the products can reform the reactants under the appropriate conditions. Electrochemical reversibility is determined by the rates at which the forward and reverse reactions occur. When the rates are both fast, the electrochemical reaction is reversible and Nernstian. When the rate of the reverse reaction is significantly slower than the forward, it is deemed irreversible. Reactions that fall in between two are quasi-reversible.

The current measured at an electrode for a simple reversible reaction is dependent on the rate that it progresses. The relation between the two can be described by the current-potential characteristic equation:

$$i = FAk^0[C_O(0,t)e^{\frac{-\alpha F(E-E^0)}{RT}} - C_R(0,t)e^{\frac{(1-\alpha)F(E-E_0)}{RT}}] \qquad \text{Equation 1.11}$$

Where i is current (A), F is Faraday;' constant (C/mol), A is electrode area (cm^2), k^0 is the standard rate constant for the reaction (cm/sec), $C_O(0,t)$ and $C_R(0,t)$ are concentrations of oxidised and reduced species at distance 0 from the electrode at time t (mol) and α is

the transfer coefficient. The rate of the reaction is directly related to the measured current. The value $E - E^0$ is known as the overpotential (η) and is the difference between the standard potential of the reaction and the potential required to drive a reaction. As the reactions described here are reversible, the electrode will experience a cathodic and anodic current. The total current is then a combination of the two. However, at equilibrium the total current is zero, thus:

$$i_c = -i_a = i_0 \qquad \text{Equation 1.12}$$

Where i_0 is referred to as the exchange current which can be described by:

$$i_0 = FAk^0 C_O^{*(1-\alpha)} C_R^{*\alpha} \qquad \text{Equation 1.13}$$

Where C_O^* and C_R^* are bulk concentrations. Substituting this into the current-potential characteristic equation and assuming that mass transfer effects are non-limiting (such that concentration at the electrode and the bulk are equal) gives the equation:

$$i = i_0 [e^{\frac{-\alpha\eta F}{RT}} - e^{\frac{(1-\alpha)\eta F}{RT}}] \qquad \text{Equation 1.14}$$

This is known as the Butler-Volmer equation.[5, 15, 18]

1.1.4.2 *Describing Mass Transfer*

As shown in Figure 1-6, mass transfer also plays a key role in Faradaic current measurements. This can commonly be the rate limiting step as it involves movement of the species from the bulk solution to and from the electrode. A species needs to move into the electrode area for an electron transfer reaction to occur, but also it needs to move away after electron transfer. If the rate of mass transfer is sluggish, fresh analyte will not move into the electrode region and the reacted analyte will not move away. There are three modes in which mass transfer can occur, namely migration, convection, and diffusion.

The total flux of species $J_i(x)$ (mol s^{-1} cm^{-2}) is a combination each of these modes and can be calculated by the Nernst-Planck equation:

$$J_i(x) = -D_i \frac{\delta C_i(x)}{\delta x} - \frac{z_i F}{RT} D_i C_i \frac{\delta \phi(x)}{\delta x} + C_i v(x) \qquad \text{Equation 1.15}$$

where D_i is the diffusion coefficient (cm^2 s^{-1}), $\frac{\delta C_i(x)}{\delta x}$ is the concentration gradient at distance *x*, z_i is the charge, C_i is the concentration (mol cm^{-3}), $v(x)$ is velocity of a unit volume of solution moving in a one dimensional direction and $\frac{\delta \phi(x)}{\delta x}$ is the potential gradient at distance *x*.[1]

Each term in this equation relates to one of the modes of mass transfer. Thus $-D_i \frac{\delta C_i(x)}{\delta x}$ relates to diffusion, $\frac{z_i F}{RT} D_i C_i \frac{\delta \phi(x)}{\delta x}$ relates to migration and $C_i v(x)$ relates to convection. In some cases, it is desirable to reduce the contribution for two of the three terms to simplify this equation. Migration effects are minimised by adding an excess of electrolyte to shield electric field effects, higher than the concentration of the electroactive species. Convection can be mitigated by performing analysis in quiescent solutions. In these cases, mass transport is dependant entirely on diffusion. To minimise diffusion effects, solutions can be stirred, or flowed over the electrode at high rates. In such cases, convection effects become so large that diffusion effects are comparably miniscule.

It is most common however to minimise convection and migration so that diffusion is the only flux so that the equation becomes:

$$-J_O(x) = D_O \frac{\delta C_O(x)}{\delta x} \qquad \text{Equation 1.16}$$

This is known as Fick's law of diffusion. Carrying out an experiment where diffusion effects are the only form of flux, means that the diffusion coefficient becomes an

important parameter. Diffusion is the movement of species from areas of high to low concentration. By definition, the potential applied does not directly impact diffusion. However, the resulting concentration gradient established at the electrode causes flux of species to counter the gradient. A larger gradient will result in more flux; therefore, the potential has an indirect influence on the diffusion of species. If the kinetics of the reaction are extremely fast, then the limiting factor will be the mass transfer. In such a case the current can be calculated by:

$$i = \frac{nFADC^*}{\delta} \qquad \text{Equation 1.17}$$

C^* here refers to the bulk concentration (mol/L). The value δ is known as the diffusion layer thickness (cm). The diffusion layer thickness can be approximated by the following equation:

$$\delta = \sqrt{\pi Dt} \qquad \text{Equation 1.18}$$

Substituting this into Eq. 1.17 gives the Cottrell equation[1, 15]:

$$i(t) = \frac{nFAD^{\frac{1}{2}}C^*}{\pi^{\frac{1}{2}}t^{\frac{1}{2}}} \qquad \text{Equation 1.19}$$

This equation allows for the calculation of the current associated with a diffusionally controlled process, at a given time.

1.1.5 Techniques Used to Study Electrochemical Reactions

The most common methods to study electrode reactions are by using voltammetric techniques. At their most basic, these techniques involve application of a potential and measurement of the resultant current over time. When a constant potential is applied for the duration of the measurement, the technique is known as chronoamperometry and is one of the simplest voltammetric techniques. In most cases, it is more useful to study electrochemical reactions over a range of potential values, wherein the potentials are

swept at a predefined rate. To do this, cyclic voltammetry (CV) is used, which is the primary technique employed in this thesis research. The potential profile and typical measurement of CV is shown in Figure 1-7. If the experiment does not proceed beyond the apex potential shown in Figure 1-7 (a), the measurement is termed a linear sweep voltammogram (LSV).

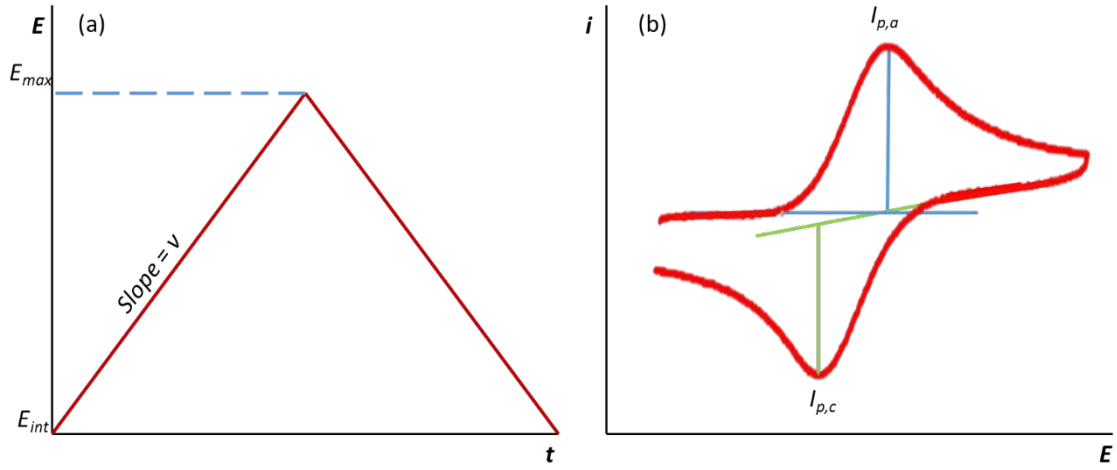

Figure 1-7 Potential profile (a) and current response (b) for a typical cyclic voltammetry measurement. ν is the scan rate of the measurement in V/s. I_{pc} and I_{pa} are the cathodic and anodic peak currents.

CV allows the user to determine if a reaction is reversible based on the ratio of the peak currents, and by applying the Nernst equation. Separation of peak potentials of 0.059 V at 25°C ($\frac{2.302RT}{F}$) indicates full reversibility for a one electron transfer reaction. Furthermore, reaction rates and mechanisms can also be determined using CV. The limiting step of the reaction can also be easily determined based on the shape of the resultant voltammogram, particularly when the species investigated does not undergo a chemical change or surface binding prior to charge transfer. Reactions that give rise to a peak shaped voltammogram in these cases are generally limited by mass transfer to the electrode, thus they are termed diffusion limited. Voltammograms where a current plateau is observed tend to result from steady-state mass transfer, hence these reactions are not

limited by diffusion at the electrode surface. Relationships between peak current and concentration can be established if the diffusion coefficient is known, and similarly the diffusion coefficient can be calculated when the concentrations are known by using the Randles-Sevcik equation:[19]

$$i_p = 0.446nFAC(\frac{nF\nu D_0}{RT})^{\frac{1}{2}} \quad \text{Equation 1.20}$$

This equation does not factor in capacitive currents, however. Their effects can usually be mitigated by background subtraction methods. This equation is used for reversible redox reactions that are limited by mass transfer, such that a peak is observed in a voltammogram.

1.1.6 The Benefits of Smaller Electrodes

This research focuses on the use of ultra-microelectrode devices defined as electrodes with critical dimensions on the micron, or submicron scale.[20] The resulting diffusion layer produced at such electrodes can have a radius larger than the critical dimension of the electrode. In this thesis, the term ultra-micro is used to refer to electrodes with a critical dimension of 1 µm or less, while macro-electrodes are those with a critical dimension of 1 mm or larger. Smaller electrode sizes mean that they require less power, use less materials and have a smaller footprint. With respect to analysis, this means less capacitive charging effects, better detection limits, lower solution resistance effects and lower volumes of solution are required for analysis.[20] One of the major benefits from an electrochemical perspective is the emergence of steady-state behaviour due to enhanced mass transport. At larger electrodes, diffusion to the electrode is limited by mass transfer, unless slow scan rates, for example 10 mV/s or slower are employed. A typical CV measurement is done over a few hundred mV or larger, therefore these scan rates result in long analysis times. By contrast, smaller electrodes exhibit enhanced mass transfer and

steady-state currents are observed at faster scans, reducing overall analysis time. As such, CVs under these conditions tend to result in voltammograms like the one shown in Figure 1-8. This steady-state behaviour can be maintained unless extremely fast scan rates, such as 10 V/s are used.

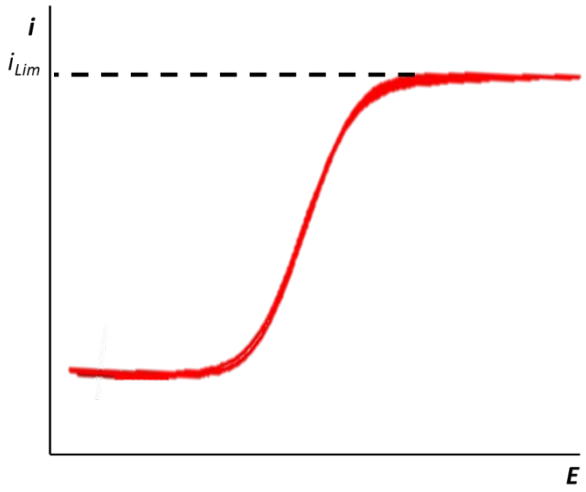

Figure 1-8 Typical CV for steady-state behaviour at a microelectrode for reaction of a solution species. I_{Lim} is the limiting current.

As the currents reach a steady-state (i_{ss}), they can no longer be described by the Randles-Sevcik equation. Steady-state currents are not affected by scan rate but are dependent on the electrode geometry. Therefore different equations are used to describe the behaviour and can be shown simply as:[21]

$$i_{ss} = nFAD_0 m_O C \qquad \text{Equation 1.21}$$

wherein m_O depends on the geometric form of the electrode.

Compared to macro electrodes, microelectrodes produce smaller currents under equivalent conditions. These smaller currents have a greater signal to noise ratio however, as the capacitance effects are much lower at microelectrodes. Microelectrodes can be used in arrays to boost the current signal, without losing the benefits associated with their dimensions. This leads to further consideration of electrode design. If the microelectrodes

are spaced too close together, diffusion layers can overlap and the steady-state behaviour is lost. This can be prevented by using high scan rates; however, this can also result in the loss of steady-state behaviour as previously mentioned. Ensuring that there is adequate space between each electrode can prevent this diffusional overlap, but also increases the overall array footprint. One method to overcome this problem without increasing the array footprint is by using generator-collector devices.

1.1.7 Generator-Collector Electrochemistry

A generator-collector electrochemical cell set-up is one in which there are two working electrodes that can be addressed individually. Typically, the generator electrode produces an activated species by oxidation or reduction, while the collector electrode subsequently reverts the activated species to its ground state. The species can then be cycled between generator and collector multiple times in a process known as redox cycling, shown in Figure 1-9.

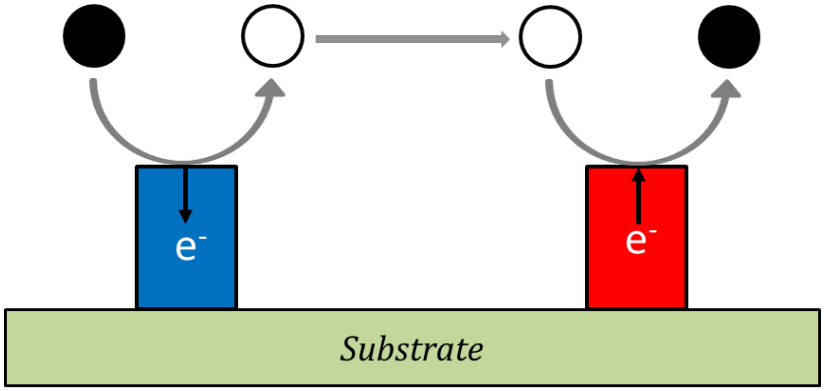

Figure 1-9 Schematic for a typical generator/collector experiment. In this case the reduced species (black) is oxidised (white) at one electrode (blue), and subsequently reduced at the other electrode (red).

One of the earliest used generator-collector electrode systems was the rotating ring-disk electrode developed in 1959. The rotating disk was used as a generator electrode and orthogonal flow brought molecules to the disk electrode surface where they were oxidised

or reduced. The radial flow then transports the activated species outward where they were "collected" by the ring electrode.[22-25] Throughout the 60's and 70's generator-collector research was furthered by creating systems with less complex electrode set-ups. The simplest devices consisted of two electrodes in close proximity to each other, a technique known as twin electrode thin layer electrochemistry.[26-29] Since their emergence, many different configurations of generator-collector devices have been developed, each with their own advantages and specific applications. Figure 1-10 shows a representation of some of the developed generator-collector systems. This is clearly not an exhaustive representation as these devices can be configured in many other arrangements, as described by Barnes et al.[30] Early applications of generator-collector devices assessed reaction rates, pathways and kinetics.[22, 24, 26, 28, 29] These devices are now being employed for sensor applications taking advantage of the second working electrode to facilitate analysis. These will be further discussed later, but examples of this include using the generator electrode to produce an adequate titrant for electrochemical titrations, or by changing local pH to facilitate electroanalysis.[31,32] These techniques require strict control of the distance between generator and collector electrodes. It is also necessary to minimise diffusion of the generated species to the bulk solution. The following section gives a review of interdigitated electrode array (IDE) fabrication techniques and applications, as these are the primary device used in this body of work.

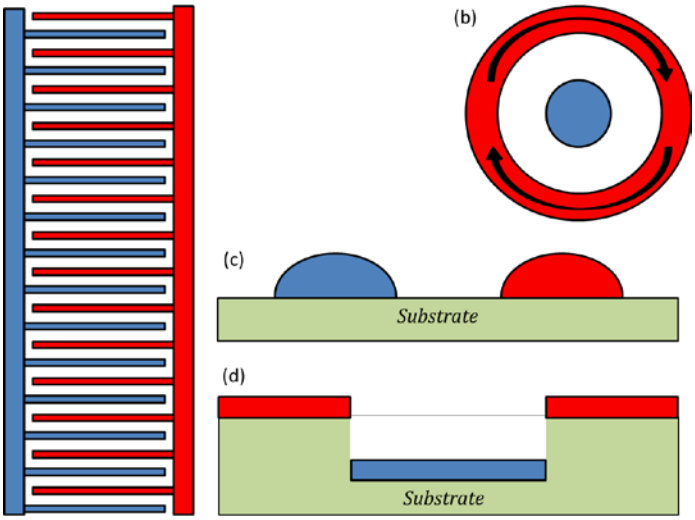

Figure 1-10 Generator-collector devices exist in many different configurations. (a) Interdigitated arrays, (b) rotating ring disk electrodes, (c) dual hemisphere and (d) recessed ring disk electrodes are just some of the many possible device set-ups.

1.1.8 A Review of Interdigitated Electrode Arrays:

IDEs are a type of generator-collector device that facilitate collection of as much generated species as possible within a simple experimental cell.[33] IDEs typically consist of two combs of electrodes separated by a gap, as shown in Figure 1-10(a). At their simplest, IDEs consist of one central generator electrode with a collector electrode on each side known as the triple band set-up.[34, 35] However, it is more common and much more beneficial to have arrays of electrodes in this set-up. IDEs were developed in the 80s and early 90s as arrays of micro- or ultramicroelectrodes.[36-47] In this set-up, the generated species moves to the collector electrode by diffusing across the inter-electrode gap. Unlike the rotating ring-disk electrode, no external driving force is required to move the species away from the generator electrode. However, the species can diffuse in any direction and may not reach the collector in every situation. Therefore, an important parameter that describes how well an IDE performs is the collection efficiency (Φ) which is typically represented as a percentage and calculated using equation 1.22[38, 44]:

$$\Phi = \frac{i_c}{i_g}$$ Equation 1.22

Where (i_c) is the collector current and (i_g) the generator current.

The collection efficiency is the fraction of the generated activated species that reaches the collector. When describing the efficiency of an IDE, a model redox species (e.g. ferrocene monocarboxylic acid) is generally utilised. Typically, CV is used to establish the collection efficiency, wherein the generator electrode is cycled, and the collector held at a constant potential. Recent advances have permitted the application of more complex techniques, such as square wave voltammetry to be employed.[48, 49] The current response is monitored at both electrodes and the measurement is taken in the plateau region. This has been commonly shown in the literature for ferrocene [34, 35, 44, 50-52] and ruthenium based redox probes.[53-55]

The collection efficiency has a strong dependency on the inter-electrode gap. A large gap leads to loss of species and a lower collection efficiency. Similarly electrode width has been shown to have an impact, as wider electrodes result in generated species diffusing perpendicular to the collector electrode.[56] The effects of width and inter-electrode gap have been highlighted by Niwa et al,[44] and are summarised in Table 1-1. It is evident that keeping both the width and the gap between electrodes small improves collection efficiency. While these results are for electrodes on the micron scale, the same effect has been shown at the nanoscale. From a series of experiments done using nano-IDEs of various widths and gaps, it was found that a collection efficiency in excess of 99% was possible with 100 nm width electrodes, separated by a 30 nm gap.[50]

IDE Dimensions		Collection Efficiency	
Electrode Width *µm*	*Inter-Electrode Gap* *µm*	*Ferrocene* *%*	*$Ru(NH_3)_6$* *%*
0.75	0.75	99.1	98.9
1.00	1.00	98.7	98.1
1.50	1.50	98.5	97.8
3.00	2.00	98.0	95.9
5.00	2.00	96.1	95.4
10.00	2.00	93.7	95.0
3.00	5.00	94.2	92.2
5.00	5.00	93.6	91.9
10.00	5.00	90.1	91.6

Table 1-1 Summary of collection efficiencies for ferrocene and ruthenium hexaamine as adapted from Niwa et al.[44]

The height of the electrode can also have an impact on the collection efficiency. Increasing the height results in more species being entrapped between the generator and collector comb of electrodes. Kamrath et al. has shown this, whereby they kept the width and inter-electrode gap constant, but varied the height of each electrode.[57] Collection efficiency increased from 90% to 96% when the electrode height was increased from 0.15 µm to 1.15 µm, keeping all other parameters constant.

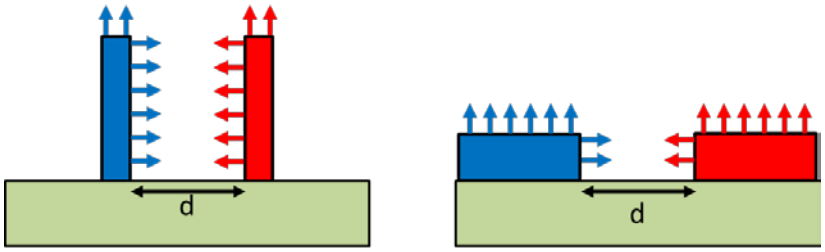

Figure 1-11 Tall and narrow IDEs contain more of the species within the gap and thus have a higher collection efficiency. Short, wide electrodes lose more species to the bulk.

Arrays of microelectrodes are an attractive analytical device because they have an enhanced sensitivity over single electrode devices with the same geometry. This is due to the fact that multiple electrodes working in parallel produce a higher measurable current

so lower limits of detection are achievable.[58-60] The steady-state current expected from a microband electrode can be calculated using this equation:[3]

$$i_{ss} = \frac{2\pi nFAD_0C_0}{w_e \ln(\frac{64D_0t}{w^2})} \quad \text{Equation 1.23}$$

where n is number of electrons involved in oxidation or reduction, F is Faraday's constant, D_0 is the diffusion coefficient of the reactant, C_0 is the initial concentration, t is the time, A is the electrode area and w_e is the electrode width.

The current measured at an array of microbands is typically n times the current for a single microband where n is the number of electrodes in the array. However, this approach only works where the electrodes are diffusionally independent of each other. When the diffusion layers overlap, a shielding effect arises which limits the total current to a fraction of what is expected. The shielding factor (SF) is described by:[38]

$$SF = 1 - \frac{i_{sh}}{\sum_{j=1}^{n} i_j} \quad \text{Equation 1.24}$$

Here the observed shield current (i_{sh}) is divided by the sum of the currents for each individual electrode in the array. A shielded array of electrodes behaves like one larger electrode of width nw and the current is calculated by the equation:[61, 62]

$$i = \frac{nFC_0D_0N(w_e + w_g)l}{(\pi D_0 t)^{1/2}} \quad \text{Equation 1.25}$$

This equation factors in the gap width (w_g) and the length (l) and treats the entire array footprint as the active electrode.

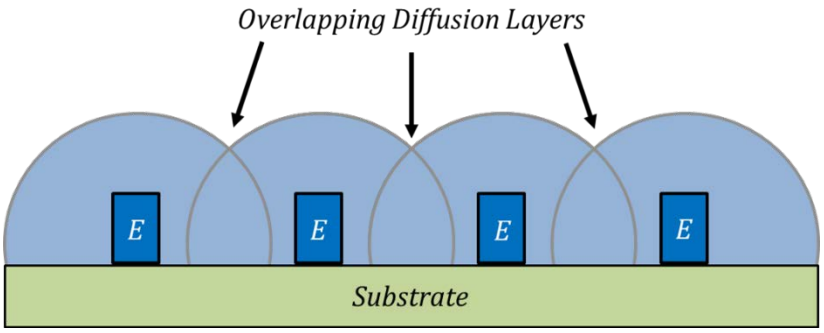

Figure 1-12 Diffusional overlap occurring when the individual electrodes (E) are not spaced far enough apart. The overall diffusion profile becomes more planar than radial.

The benefit of using an IDE instead of a typical array is that the shielding effect can be negated by applying a potential at the collector electrode. This sets up a competing diffusion layer at the collector electrode and prevents diffusional overlap, resulting in a significant increase in signal when compared to single mode use.[44, 55, 63-66] This effect has the advantage of decreasing the sensor footprint. Thus, a higher density of electrodes is achieved in a smaller area, which is ideal for lab-on-a-chip type devices.

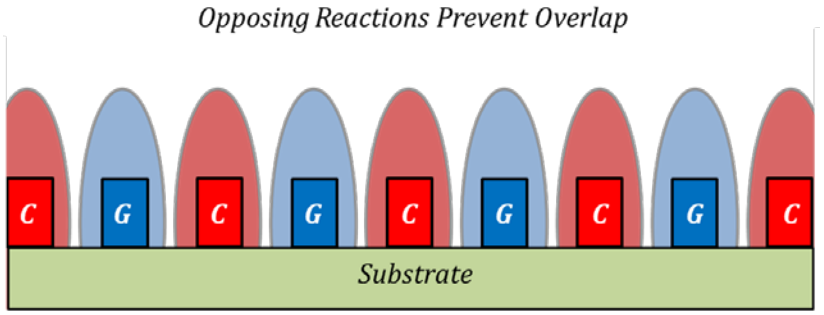

Figure 1-13 Biasing the collector electrode (C) prevents diffusional overlap of the generator electrodes (G), forcing each electrode to be diffusionally independent.

One of the main causes for signal increase, and perhaps the biggest benefit seen when using IDEs, is the phenomenon of redox cycling. This occurs when a one comb of an IDE is biased at the limiting current potential of a reversible species and the other comb is biased at a potential suitable for regeneration of the initial species. The redox species is cycled between the generator and collector electrodes multiple times, as shown in Figure

1-14, leading to an amplification in the current measured.[50-52, 54, 63, 67-75] The more cycles that a molecule undergoes, the higher the measurable current which results in enhanced sensitivity. Table 1-2 shows a comparison of some devices where redox cycling is used to enhance signals. The number of redox cycles is determined by the collection efficiency and can be estimated by the equation:[44]

$$R_c = \frac{1}{(1 - \Phi_1 \Phi_2)} \qquad \text{Equation 1.26}$$

The values Φ_1 and Φ_2 are the collection efficiencies of each comb of the array. However, if the combs are identical (equal width, height and length) then this simplifies to Φ^2.

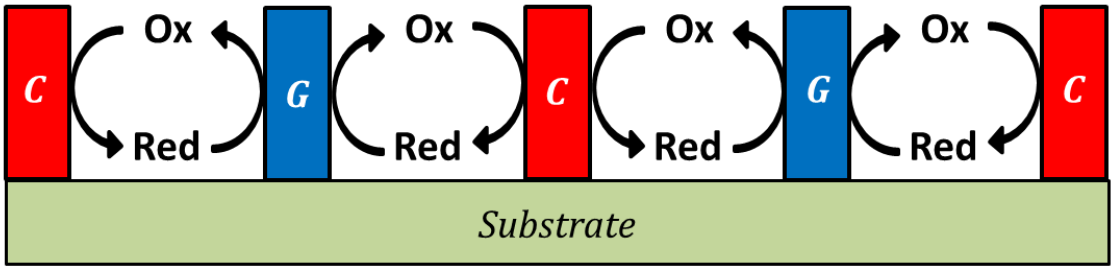

Figure 1-14 Redox cycling occurs when the species is contained between the two combs of generator (G) and collector (C) electrodes. Each oxidation and reduction event contributes to the overall current. More cycling leads to higher currents measured.

Material	E_W	E_G	ϕ	Analyte	Detection Method	Amplification Factor	Ref.
	μm	*μm*	*%*			*x*	
Gold	0.1	0.03	99	FeCpOH	CV	40	[50]
	0.01	11	99	$Fe(CN)_6$	CV with Fluidics	3	[51]
	100	100	45	NO/NO_2	CA Gas Sensing	2	[68]
	10	28	73	pAP	CV (Mesh Electrode)	6	[71]
	0.1	0.2	-	pAP	CV	3000*	[70]
	0.25	0.25	60	Adrenaline	CV	10*	[72]
	0.25	0.25	99	Paracetamol	CV with Fluidics	110	[74]
	10	5	-	TNT	CV	4	[75]
Platinum	3.7	2.4	94.5	Fe(CN)6	CV	11	[52]
	3.7	2.4	-	pAP	CA	8	[52]
	0.8	0.2	95.6	$Ru(NH_3)_6$	CV	48	[54]
	0.8	0.2	60	Dinitrotoluene	CV	2	[54]
	0.06	0.282	99	$Fc(CH_2OH)_2$	CV with Fluidics	400	[63]
Carbon	0.585	1.9	-	Glucose	CA	295	[76]
	0.3	1.9	90	pAP	CV	25	[77]
	0.3	1.65	97	Fe(CN)6	CV	25	[65]

Table 1-2 Comparison of different IDEs used for redox cycling amplification. Amplification factors are based on the increase in current when the collector array is biased on compared to unbiased. * refers to amplification factors measured from detection limits

Enhancement of a signal by redox cycling is only possible when the species reaction is reversible. This means that reversible reactions can be separated from non-reversible reactions in a process described as selective amplification.[74] In a mixture of species, the amperometric signal will be increased when redox cycling is switched on. As this increase can only occur for reversible species, it can be quantified and differentiated from that of the non-reversible species. This allows for both species to be accurately determined. This has been done to separate a reversible biomarker from a non-reversible interfering species. Dopamine was been detected in the presence of ascorbic acid by taking advantage of the dopamine's electrochemical reversibility. Comparison of CVs with and without a collector bias allowed for the separation of the signals for these two compounds.[55] This has also been shown using mixtures of dopamine and potassium ferrocyanide, wherein dopamine's signal was selectively amplified by redox cycling. This was achieved by

biasing the collector electrode at a potentials that enabled the reversal of dopamine oxidation, but not ferrocyanide. [76, 77]

Redox cycling can also be induced without the need for a potential bias at the collector electrode. In this case, the nearby inactive electrode acts as a surface where the activated species can oxidise or reduce. This is known as self-induced redox cycling (SIRC). Typically SIRC is not as efficient as traditional redox cycling, but it does enable an enhancement of current signals seen at the generator.[78-81] As such it is possible to enhance detection of a reversible redox species without the need of a bipotentiostat device, provided that the reaction kinetics are fast enough.

1.1.8.1 *Advances in Fabrication of IDEs*

The simplest approach was developed in the 1980's and involved sandwiching metal foil between insulating films. Typically, platinum or gold foil was used, where the number of electrodes was equal to the number of foils used. The gap was dependent on the thickness of the insulating film and heat curing under pressure helped to minimise this gap.[34, 35] Advances were made to decrease electrode and gap sizes by using conventional lithographic and sputtering techniques,[43, 44, 52, 82] which has since become the most widely used fabrication method. An interesting approach to disposable IDEs with fast fabrication times was achieved by printing the desired electrode design in black ink. This was then transferred onto a conventional CD and acted as a blocking area during an acid etch. The ink prevented gold from being etched and thus upon removing the ink an IDE remained, as illustrated in Figure 1-15.[83] The benefit of this approach is that IDEs can be made relatively cheaply, without requiring complex machinery or expensive substrates. The typical considerations when designing and fabricating IDEs are the interelectrode gap

distance and the electrode size,[84] as they generally dominate the collection efficiency and sensitivity.

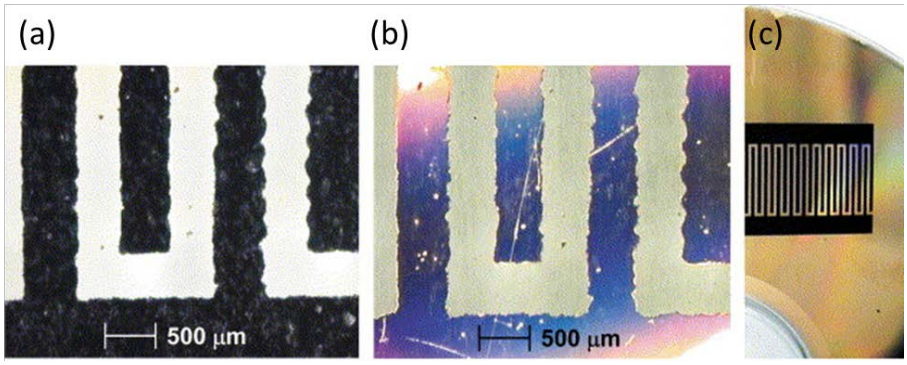

Figure 1-15 IDE etched onto the surface of a CD[83]. (a) The desired design in ink transferred onto the gold surface. (b) The fabricated IDE after etching and removal of ink. (c) The design shown on the CD

In the last ten years, the majority of research using IDEs has been on micron scale lab-on-chip type devices. The most popular method of fabricating these devices has been a top-down approach onto substrates like silicon. A general lift-off procedure for fabricating a metal IDE is as follows and is illustrated in Figure 1-16. First, a substrate is chosen and insulated, as necessary. Then a photoresist is coated over the substrate and UV lithography is used to write the IDE pattern. The exposed photoresist is subsequently removed, and the desired metal is sputtered or evaporated onto the device. Typically, a metal adhesion layer is deposited with the desired metal. The remaining photoresist is removed along with the excess metal. A passivation layer is then deposited as needed and the device is ready to be used.

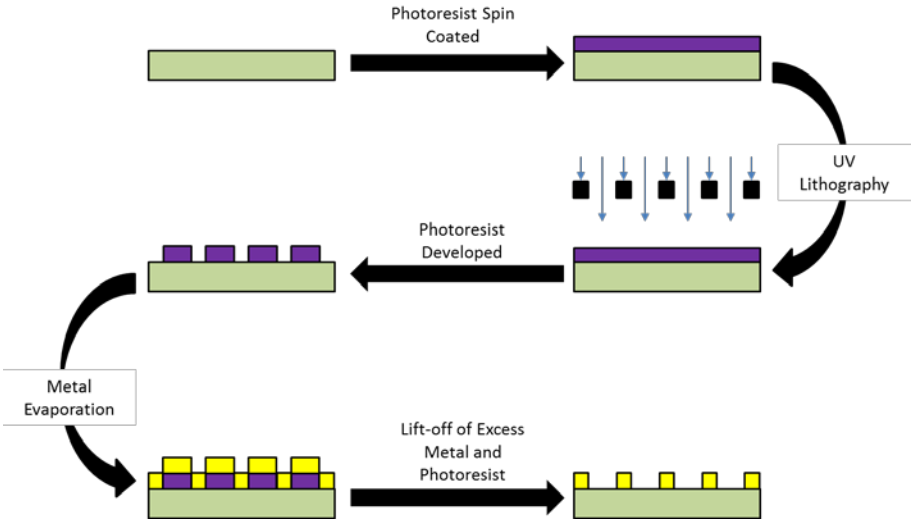

Figure 1-16 Typically process flow for lift off based fabrication of IDEs. The UV lithography step can be replaced with electron beam lithography for nano-sized devices.

The most commonly used substrate is silicon,[85-91] however glass, quartz and even thermoplastics have been routinely used.[92-98] A slight modification to the above method is to put down the metal layer before the photoresist and to use UV lithography to pattern the electrode gaps. The metal is then etched where the photoresist has been exposed resulting in the formation of gaps.[99, 100] This method however runs the risk of etching exposed metal under the photoresist, which affects reproducibility of the electrodes. The main benefit of the standard lithographic techniques is the ease of scaling up production. IDEs produced lithographically can be fabricated at wafer scale meaning that a high throughput is obtained. Lithographic masks can be complex, enabling multiple different designs on one single wafer. This can be extremely useful where factors such as electrode height and gap width may need to be varied. Recent advances in electron beam lithography have allowed for nanowire and nanogap based IDEs to be fabricated with the same degree of reproducibility as the micro- and ultramicro-electrode equivalents. Resolutions of less than 5 nm have been achieved[101] with emerging electron beam lithographic techniques which have been used to fabricate nano-IDE devices.[102-105] Generally, electron beam lithography is used to write the IDE pattern while UV

lithography is still used to pattern connection tracks and contact pads. The benefits to using nano-electrodes are enhanced sensitivity and signal to noise ratio. Moreover, minimising the gap size to create nano-gaps facilitates enhanced collection efficiency and as a result, a significant increase in redox cycling, as shown in Table 1-2. Furthermore, using nano-electrodes means that a higher density of electrodes can be achieved in the same footprint as a micro-electrode array. Finally, advanced lithographic techniques have also permitted the fabrication of electrodes of different heights. Typically, the collector comb is a taller set of electrodes which results in further enhancement of the collection efficiency. Morita at al. has shown this using carbon electrodes, where the electrode width and gap were fixed at 15 µm and 5 µm respectively, but the height was varied from 10 nm to 5 µm.[106] Collection efficiency increased from 90% to 96% across this range of heights.

An interesting way to use conventional UV lithographic techniques to generate nanogap IDEs is to exploit the undercutting effect, which results from non-uniform deposition on a substrate when using sputtering techniques (Figure 1-17). In this case, standard lithographic techniques are used to create a basic structure for the IDEs. An insulating layer, typically SiO_2, is then sputtered down on the substrate. This layer typically deposits more at the top of the structure resulting in a mushroom cloud type deposition at each IDE finger. A subsequent metal deposition results in the formation of the desired IDE structure. Alternatively, this undercut can be achieved by depositing the metal before the photoresist and under etching the metal after patterning.[107-109] This route offers a cheaper approach to fabricating nanogap IDEs, as it eliminates the need for electron beam lithography. However, one limitation is that the electrode width will be significantly larger than the gap and therefore collection efficiency is sacrificed.

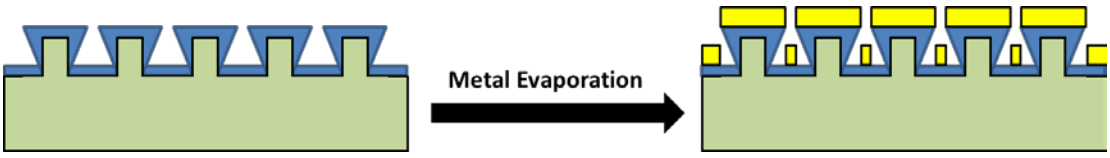

Figure 1-17 Undercutting occurs when sputter deposition of an insulation layer (typically SiO_2) results in non-uniform coating on the substrate. Subsequent metal deposition results in separate interdigitated electrodes, while the metal deposited between the gaps is sacrificial

Carbon based electrodes are very attractive due to their wide potential window and lower cost of fabrication. They are also known to have low electrical resistivity, which is useful for electrochemical sensing applications.[110, 111] They can be used to detect redox species that are active outside of the potential range possible for bare metal based electrodes. For the most part, fabrication of carbon IDEs follows the same initial steps. This involves choosing a substrate, depositing a photoresist and patterning with lithography (UV or electron beam). For metal IDEs, a metal deposition step is required after the lithographic pattern development. For carbon IDEs, the photoresist can effectively become the electrode. Pyrolysis of the device converts the photoresist into a glassy carbon electrode. This approach has been frequently used in recent years[65, 76, 77, 112-115] to fabricate carbon IDEs with complex structures that are more difficult to achieve with metal based techniques. One example of this has been shown by Sharma et al, wherein a carbon IDE was fabricated with a suspended carbon mesh above the array. The mesh was functionalized with antibodies, and the IDE was used to cycle a produced species in the presence of a biomarker.[77] This method is also cheaper and does not require metal patterning and lift-off. The pyrolysis step also has a unique benefit. The conversion of photoresist to glassy carbon results in shrinkage of the electrode dimensions. This means that UV lithography can be used to pattern electrodes that subsequently become significantly smaller than its resolution typically allows. UV lithography can allow for a minimum feature size of about 50 nm[116] and pyrolysis has demonstrated shrinkage of up

to 60%,[65] therefore the minimum feature size can actually become 20 nm. This however has the drawback that the inter electrode gap becomes larger than the pattern defined which can lead to a decrease in collection efficiency. It should also be noted that the pyrolysis step limits the substrate choice to those compatible with the high temperatures (up to 900 °C) required to create the glassy carbon electrodes.

The development of cheap fabrication methods for disposable sensors is a growing research topic. These devices typically are not complex structures but can be made rapidly without advanced fabrication tools. One such method involves printing conductive ink (gold, silver, carbon etc.), onto a substrate typically producing multiple devices in a matter of minutes.[117-121] Most commercial printers can be fitted with an appropriate ink. Specialised printers can also be used with better resolution and compatibility with complex inks. Typically, these are still relatively cheap by comparison with common fabrication equipment. Recently, IDEs were fabricated using an Epson Inkjet printer (ET-2550 EcoTank) for impedimetric detection of bacteriophages.[122] This particular printer was commercially available for an average of €500, with the ink itself being made by the researchers. Devices resulting from this fabrication technique are usually used for biosensing,[123] because biosensors are commonly non-reusable, therefore cheap fabrication methods are paramount. Conventional printers have a resolution of about 600 dots per inch (DPI). This equates to a minimum feature size of roughly 40 µm. Therefore, the electrode size and gap are limited to minimum values of 40 µm, however this may not always be reliably achieved as many factors affect the ink. With varying ink conditions, feature sizes can be double the predicted value.[122] High resolution printers may push the feature size down to roughly 10 µm, and have inbuilt temperature regulators, but such

printers are more expensive, such as the Fujifilm Dimatrix Materials Printer DMP-2850 which can cost up to €40,000. [124]

A more advanced method has been developed that attempts to bridge the gap between printed and lithographic fabrication techniques by creating a mold to define the IDE structure and subsequently stamping it into a substrate, called nanoimprint lithography. The mold itself may be created using UV or electron beam lithography, however in most cases this is the only required lithographic step. The mold is then heated and stamped into the substrate to create the desired IDE structure.[125-128] By definition, the substrate chosen needs to be sensitive to the heat applied as the design is effectively melted into the substrate. However, work has been done where a silicon substrate has been used by coating it with a thermally sensitive layer. This method can also be used as a lift-off free approach by utilising the undercut method previously described to create the electrodes. This method has the benefit of fewer lithographic steps while still having the high resolution required for ultramicro- and nano-electrodes. A disadvantage, however, is that the mold degrades over time. Depending on the degree of reproducibility desired, the mold may need to be changed frequently.

1.1.8.2 *Sensing Approaches with IDEs*

The earliest analytical applications of IDE devices were to study fundamental parameters of molecules in solution or electrode materials. These included the study of kinetics and reaction rates,[26, 28] establishing diffusion coefficients,[37, 129-131] determining the activities of various enzymes[46] and even monitoring transfer of ions across liquid-liquid interfaces.[132] The major development towards creating sensors based on IDEs came from using the redox cycling phenomenon to boost trace analysis. At their simplest, these sensors were used to detect compounds such as iron[67] and nitrogen oxide gas[68] dissolved

in suitable solvents. Gradually, this technique was applied to more complex molecules such as long chain organic compounds, enzymes and hormones.[45, 72, 75, 133, 134]

Major improvements to sensing with IDEs can be attributed to advancements in fabrication. Reducing electrode sizes results in better signal to noise ratios and lower capacitive background, thus enhanced sensitivities for trace analysis. Reducing gap sizes means that collection efficiencies can be increased, which can give rise to an increase in the number of redox cycling events for such a sensor. The combination of nanowire and nanogap in an IDE device has recently been shown capable of sensing iron in mains water with a detection limit of 0.01 μM, when using cyclic voltammetry, due to redox cycling enhancement. The same device had a detection limit of 0.44 μM in non-redox cycling mode.[105] Within the last ten years this approach has been used to boost detection limits of IDE based biosensors. The basic approach for this is to modify the IDE substrate with target antibodies and then incubate the substrate with a solution containing the target biomarker as illustrated in Figure 1-18. The biomarker will bind specifically to the antibody, after which a subsequent antibody linked to an enzyme can attach to the bound biomarker. The enzyme catalyses the production of a redox species, which can then be detected using the IDE. The amount of redox species produced is related to the amount of the biomarker that binds and gives a quantitative measurement. This approach can also be coupled with microfluidics where the fluidic channel is modified with the relevant antibodies and enzymes, and then a solution containing the redox probe is passed through the channels terminating at the electrode surface.

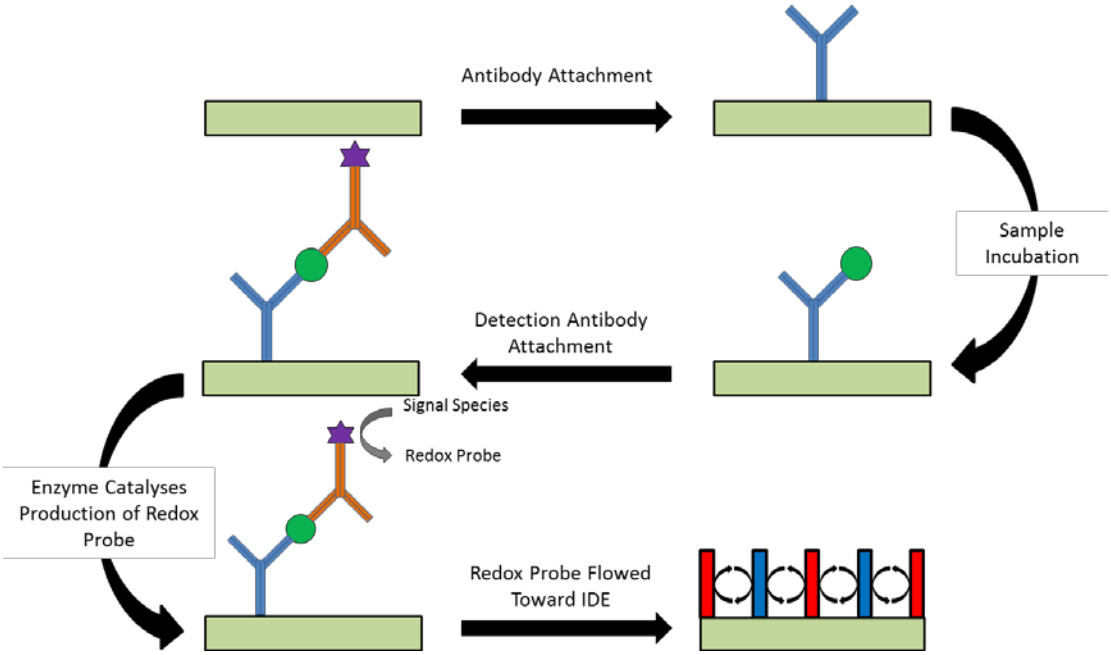

Figure 1-18 Process flow for a redox-cycling based biosensor. The amount of redox probe produced is directly proportional to the amount of antigen in the sample. This provides a quantitative measurement of the biomarker being investigated.

Perhaps the most common redox probe used in recent years for this biosensing approach is para-aminophenol (pAP). This species is produced from para-aminophenol phosphate (pAPP) by the enzyme alkaline phosphatase.[135-137] This enzyme can be attached as a label for many antibodies so it can be applied to the detection of a wide variety of biomarkers. One advantage of using pAP is that the precursor pAPP is not redox active, therefore it does not interfere with the amperometric detection. The pAP species is oxidised to para-iminoquinone (pIQ) which can be easily reduced back to the pAP species enabling redox cycling, see Figure 1-19. Again, advances in nanofabrication have enabled sensitive detection of pAP due to the reduction in electrode and gap sizes. IDEs for pAP detection have been shown to have a fourteen times amplification in current resulting from redox cycling compared to conventional, non-interdigitated arrays[138]. This method has been used to develop sensors for enterobacteriaceae (detection limit of 10 colony forming units/ml)[139], arcinoembryonic antigens (detection limit of 0.01 ng/ml)[140], cortisol (detection limit of 1 ng/ml)[93], DNA (detection limit of 0.1 nM)[100] and cardiac antigens

(detection limit of 0.4 pg/ml)[77]. Disposable biosensors have been developed that have a pAP detection limit of 10 nM.[107] This low detection limit can facilitate early diagnosis of diseases where pAP can be used as the biomarker. These devices are not limited to pAP however as other redox molecules can be produced by enzymatic reactions of labelled antibodies, such as 3,3',5,5' tetramethylbenzidine[95, 97] and 4-aminophenyl[141]. The attraction of this type of biosensing is that simple amperometric techniques are used for each of these sensors. CV and chronoamperometry coupled with redox cycling provide sufficient sensitivity that more complex techniques are not required.

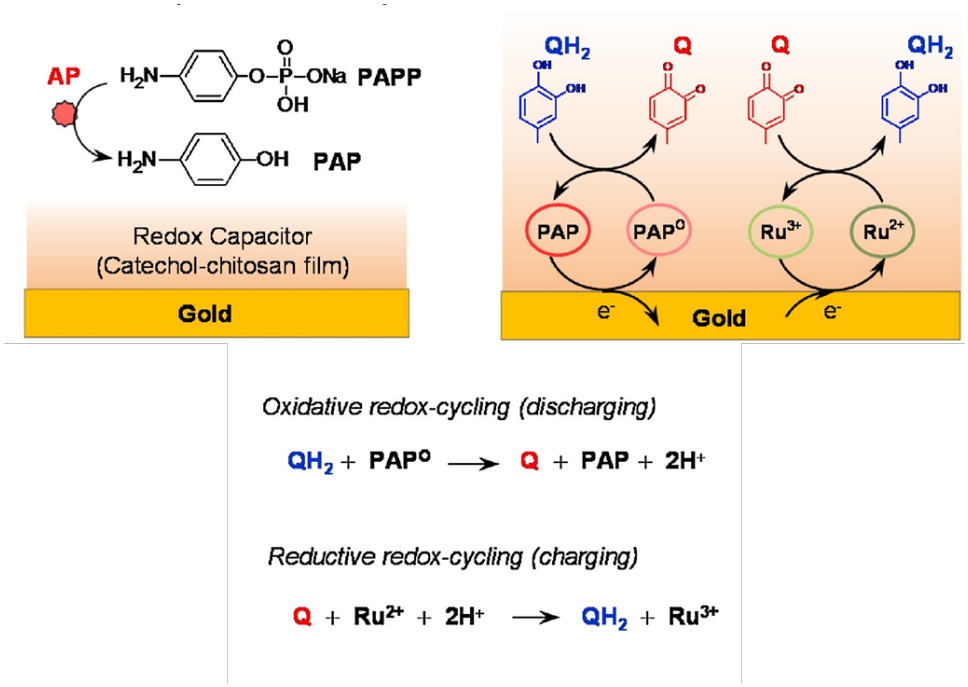

Figure 1-19 An example of how pAP can be used as a redox cycling biomarker [136]

In recent years, advances have been made to selectivity as well as sensitivity when using IDE based sensors. Selective amplification of redox over non-redox species means that one can separate out the activity of one species from the other. An example of where this can be applied is in the removal of ascorbic acid as an interferent for analysis in blood serum. Ascorbic acid is present in serum samples and oxidises readily at positive potentials. As a result, it commonly interferes when measuring the oxidation current of a

target analyte.[142] However, this oxidation of ascorbic acid is irreversible and so it does not undergo redox cycling at an IDE. Therefore, in a sample containing ascorbic acid and a reversible analyte, quantification of both species is possible using two approaches. This first approach involves taking a measurement with and without biasing the second comb of the IDE. The increase in signal when the comb is biased results from redox cycling amplification and the concentrations can be determined. The second, and the simpler approach is to monitor the current at the second electrode. The current at the second electrode is attributed only to the reversible species so quantification is simple. This approach has been more popular in recent years as fewer steps are required. This has been used for the selective detection of paracetamol (detection limit of 10 μM)[74] and dopamine (detection limit of 0.62 μM).[103, 142, 143]

Moving away from amperometric biosensors, IDEs have also been utilised for detection using electrochemical impedance spectroscopy (EIS). This type of measurement takes advantage of the small gap sizes between the combs of electrodes, as the smaller gap gives a better response[86]. EIS also has the benefit of not requiring any labelling for the detection method. Generally, a specific antibody is bound to the electrode surface which captures the specific biomarker. This causes an increase (or decrease) in impedance which is measured and used to quantify the amount of biomarker present. In this case, the electrochemical set-up is typically two electrode mode. For IDEs one comb is used as the working electrode and the other comb is used as the counter electrode. The prevalence of nano-gap IDEs has enabled ultra-low detection of bacterial cells[144], cardiovascular disease targets (detection limit of >10 ng/ml)[86], celiac disease targets (detection limit 50 pg/ml)[102], DNA (detection limit ~0.1 nM)[126] and HPV disease targets (detection limit of 0.1 fM)[145].

A similar idea is used in semiconductor IDE based gas sensors. IDEs are a useful geometry as they allow for high surface area with a small overall footprint. These work typically by having a gas permeable membrane between each comb of electrodes, with the resistivity measured between the combs as gas is exposed to the system[146]. Ultramicro- and nano-gaps have facilitated the detection of NH_3 (detection limit of 3 ppm)[89, 117, 147], acetone (detection limit of 3 ppm)[148] and NO_2 (detection limit of 5 ppm).[90] Alternatively, gas sensors can be set up with a liquid membrane that dissolves the target gas and be analysed using redox cycling as has been shown for oxygen [149]

Many groups have shown novel approaches to detection with IDEs that are not as frequently used but offer alternative analysis techniques. A method has been shown for the detection of glucose that involves modifying one comb of electrodes with the enzyme glucose oxidase. Glucose reacts with the enzyme to produce glucose oxidase in a solution that also contains ferri-ferrocyanide. The glucose oxidation simultaneously causes the reduction of ferricyanide. The unmodified electrode comb is biased at a potential that oxidises ferrocyanide and therefore the oxidation current is proportional to the amount of glucose present.[76] A novel technique has been developed to differentiate dopamine from norepinephrine by alternating the gap width. Both species are reversible redox molecules, so it is not possible to separate them by conventional methods. However their respective rate constants are different and by varying the gap between the electrode combs, one species can effectively be 'silenced'.[150] A simple pH probe has also been developed using IDEs. In this case, a current is measured as a potential difference of 1 V is applied across the combs of electrodes. This results in the migration of H^+ and OH^- ions to the negative and positive terminals respectively. A current measurement gives an indication of pH and has been shown to have a tolerance of ±0.1.[99]

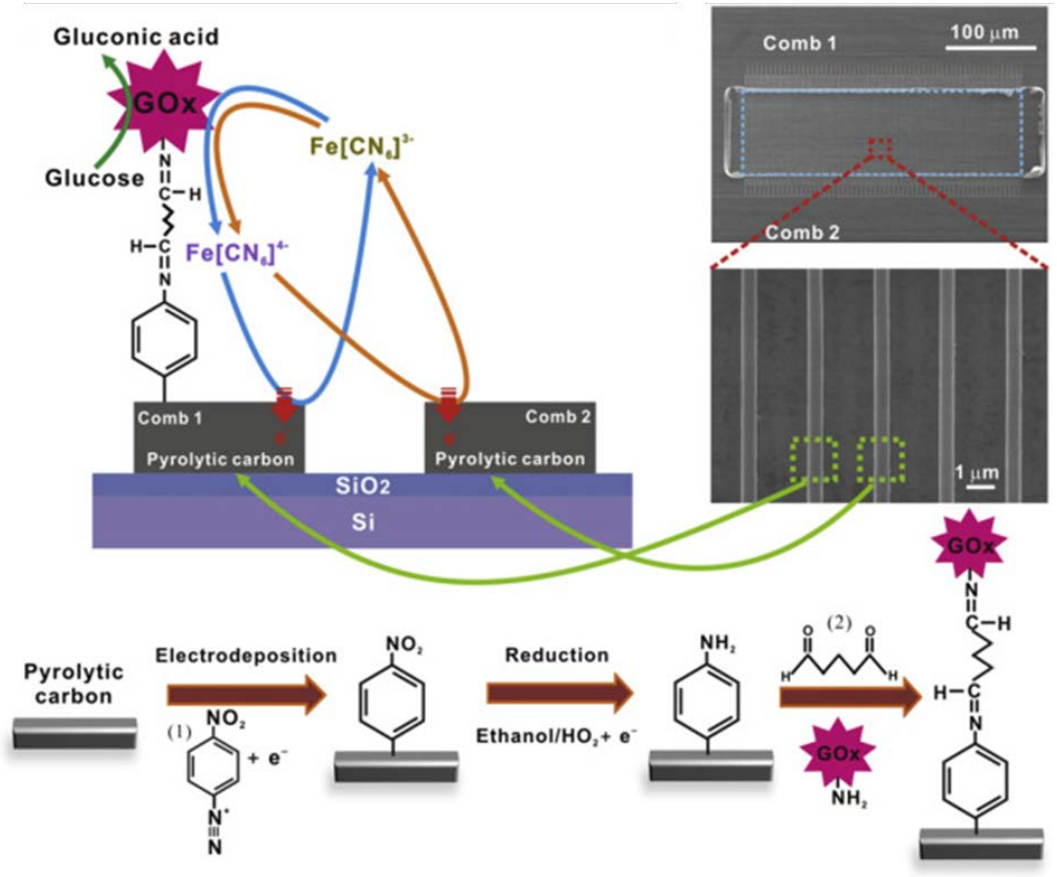

Figure 1-20 Top: Schematic showing hoe ferri-ferrocyanide is used as a probe for glucose concentration by redox cycling. Bottom: Schematic of the deposition process required to bind the biomolecule to the electrode surface[76]

1.1.8.3 *Future Prospects for IDEs*

With advances in fabrication techniques, sensitivity to analytes has increased dramatically and overall device footprint has decreased. Wafer-scale fabrication techniques have enabled different configurations to be extensively characterised and manufactured at lower costs. It is evident that research in fabrication aims to lower the costs associated with making a device, but also to make devices with more exotic structures that can facilitate analysis. Sensing applications of IDEs have shown an increasing focus on bio-sensing. This can be attributed to advanced fabrication methods, but also to advances in bio-functionalisation of electrode surfaces. The drive to get the inter-electrode gap as small as possible will likely result in the fabrication of devices with

sub nanometer gaps, which will permit single molecule analysis. Current devices have seen gaps between electrodes of sub 100 nm[151] and even going as low as 20 nm.[152]

1.2 References

1. A. J. Bard and L. R. Faulkner, in *Electrochemical Methods: Fundamentals and Applications*, Wiley, 2000, ch. Introduction and Overview of Electrode Processes, pp. 1 - 43.

2. E. Seker, M. L. Reed and M. R. Begley, *Materials*, 2009, **2**, 2188-2215.

3. A. J. Bard and L. R. Faulkner, in *Electrochemical Methods: Fundamentals and Applications*, Wiley, 2000, ch. Introduction and Overview of Electrode Processes, pp. 87 - 136.

4. T. J. Smith and K. J. Stevenson, in *Handbook of Electrochemistry*, ed. C. G. Zoski, Elsevier, Amsterdam, 2007, pp. 73-110.

5. C. M. A. Brett and A. M. O. Brett, in *Electroanalysis* Oxford Universisty Press, 1998, ch. 2, pp. 8 - 37.

6. N. Rohaizad, C. C. Mayorga-Martinez, F. Novotný, R. D. Webster and M. Pumera, *Electrochemistry Communications*, 2019, **103**, 104-108.

7. B. K. K. Kasem and S. Jones, *Platinum Metals Review*, 2008, **52**, 100-106.

8. Understanding the Specifications of your Potentiostat, http://www.gamry.com/application-notes/instrumentation/understanding-specs-of-potentiostat/, (accessed 08/04/2020).

9. D. Bao, B. Millare, W. Xia, B. G. Steyer, A. A. Gerasimenko, A. Ferreira, A. Contreras and V. I. Vullev, *The Journal of Physical Chemistry A*, 2009, **113**, 1259-1267.

10. M. Carmo, D. L. Fritz, J. Mergel and D. Stolten, *International journal of hydrogen energy*, 2013, **38**, 4901-4934.

11. K. Ogura, S. Haruyama and K. Nagasaki, *Journal of The Electrochemical Society*, 1971, **118**, 531-535.

12. K. Twomey, L. Nagle, A. Said, F. Barry and V. Ogurtsov, *BioNanoScience*, 2015, **5**, 55-63.

13. S. Cherevko, A. A. Topalov, I. Katsounaros and K. J. J. Mayrhofer, *Electrochemistry Communications*, 2013, **28**, 44-46.

14. A. Kahn, *Materials Horizons*, 2016, **3**, 7-10.

15. M. Ciobanu, J. P. Wilburn, M. L. Krim and D. E. Cliffel, in *Handbook of Electrochemistry*, ed. C. G. Zoski, Elsevier, Amsterdam, 2007, pp. 3-II.

16. J. Koryta, J. Dvořák and L. Kavan, in *Principles of electrochemistry*, Wiley, 1993, pp. 198 - 244.

17. J. O. M. Bockris and A. K. Reddy, in *Modern electrochemistry 2B: electrodics in chemistry, engineering, biology and environmental science*, Springer Science & Business Media, 2000, vol. 2, pp. 771 - 1034.

18. A. J. Bard and L. R. Faulkner, in *Electrochemical Methods: Fundamentals and Applications*, Wiley, 2000, ch. Introduction and Overview of Electrode Processes, pp. 44 - 86.

19. N. Elgrishi, K. J. Rountree, B. D. McCarthy, E. S. Rountree, T. T. Eisenhart and J. L. Dempsey, *J. Chem. Educ.*, 2017, **95**, 197-206.

20. R. J. Forster and T. E. Keyes, in *Handbook of Electrochemistry*, ed. C. G. Zoski, Elsevier, Amsterdam, 2007, pp. 155-171.

21. A. J. Bard and L. R. Faulkner, in *Electrochemical Methods: Fundamentals and Applications*, Wiley, 2000, ch. 5, pp. 156 - 225.

22. A. Frumkin, L. Nekrasov, B. Levich and J. Ivanov, *Journal of Electroanalytical Chemistry (1959)*, 1959, **1**, 84-90.

23. A. Frumkin and L. Nekrasov, *Dokl. Akad. Nauk SSSR*, 1959, **126**, 115.

24. L. N. Nekrasov, *Faraday Discussions of the Chemical Society*, 1973, **56**, 308-316.

25. G. Zhao, D. M. Giolando and J. R. Kirchhoff, *Anal. Chem.*, 1995, **67**, 1491-1495.

26. L. B. Anderson and C. N. Reilley, *Journal of Electroanalytical Chemistry (1959)*, 1965, **10**, 538-552.

27. L. B. Anderson, B. McDuffie and C. N. Reilley, *Journal of Electroanalytical Chemistry (1959)*, 1966, **12**, 477-494.

28. B. McDuffie, L. B. Anderson and C. N. Reilley, *Anal. Chem.*, 1966, **38**, 883-890.

29. S. J. Konopka and B. McDuffie, *Anal. Chem.*, 1970, **42**, 1741-1746.

30. E. O. Barnes, G. E. M. Lewis, S. E. C. Dale, F. Marken and R. G. Compton, *Analyst*, 2012, **137**, 1068-1081.

31. D. Bustin, S. Jursa and P. Tomčík, *Analyst*, 1996, **121**, 1795-1799.

32. T. L. Read, E. Bitziou, M. B. Joseph and J. V. Macpherson, *Anal. Chem.*, 2014, **86**, 367-371.

33. T. A. Postlethwaite, J. E. Hutchison, R. Murray, B. Fosset and C. Amatore, *Anal. Chem.*, 1996, **68**, 2951-2958.

34. B. Fosset, C. Amatore, J. Bartelt and R. M. Wightman, *Anal. Chem.*, 1991, **63**, 1403-1408.

35. J. E. Bartelt, M. R. Deakin, C. Amatore and R. M. Wightman, *Anal. Chem.*, 1988, **60**, 2167-2169.

36. C. E. Chidsey, B. J. Feldman, C. Lundgren and R. W. Murray, *Anal. Chem.*, 1986, **58**, 601-607.

37. B. J. Feldman, S. W. Feldberg and R. W. Murray, *The Journal of Physical Chemistry*, 1987, **91**, 6558-6560.

38. T. V. Shea and A. J. Bard, *Anal. Chem.*, 1987, **59**, 2101-2111.

39. T.-Y. Ou, S. Moldoveanu and J. L. Anderson, *Journal of Electroanalytical Chemistry and Interfacial Electrochemistry*, 1988, **247**, 1-16.

40. K. Aoki, *Journal of Electroanalytical Chemistry and Interfacial Electrochemistry*, 1989, **270**, 35-41.

41. K. Aoki and M. Tanaka, *Journal of Electroanalytical Chemistry and Interfacial Electrochemistry*, 1989, **266**, 11-20.

42. O. Niwa, M. Morita and H. Tabei, *Journal of Electroanalytical Chemistry and Interfacial Electrochemistry*, 1989, **267**, 291-297.

43. A. Aoki, T. Matsue and I. Uchida, *Anal. Chem.*, 1990, **62**, 2206-2210.

44. O. Niwa, M. Morita and H. Tabei, *Anal. Chem.*, 1990, **62**, 447-452.

45. R. Hintsche, M. Paeschke, U. Wollenberger, U. Schnakenberg, B. Wagner and T. Lisec, *Biosensors and Bioelectronics*, 1994, **9**, 697-705.

46. U. Wollenberger, M. Paeschke and R. Hintsche, *Analyst*, 1994, **119**, 1245-1249.

47. B. J. Seddon, H. H. Girault and M. J. Eddowes, *Journal of Electroanalytical Chemistry and Interfacial Electrochemistry*, 1989, **266**, 227-238.

48. G. E. M. Lewis, S. E. C. Dale, B. Kasprzyk-Hordern, E. O. Barnes, R. G. Compton and F. Marken, *Electroanalysis*, 2012, **24**, 1726-1731.

49. M. Li, S.-Y. Xu, A. J. Gross, J. L. Hammond, P. Estrela, J. Weber, K. Lacina, T. D. James and F. Marken, *ChemElectroChem*, 2015, **2**, 867-871.

50. K. Ueno, M. Hayashida, J.-Y. Ye and H. Misawa, *Electrochemistry Communications*, 2005, **7**, 161-165.

51. T. R. L. C. Paixão, E. M. Richter, J. G. A. Brito-Neto and M. Bertotti, *Electrochemistry Communications*, 2006, **8**, 9-14.

52. S. K. Kim, P. J. Hesketh, C. Li, J. H. Thomas, H. B. Halsall and W. R. Heineman, *Biosensors & bioelectronics*, 2004, **20**, 887-894.

53. A. J. Bard, J. A. Crayston, G. P. Kittlesen, T. Varco Shea and M. S. Wrighton, *Anal. Chem.*, 1986, **58**, 2321-2331.

54. A. E. Cohen and R. R. Kunz, *Sensors and Actuators B: Chemical*, 2000, **62**, 23-29.

55. W. R. Vandaveer, D. J. Woodward and I. Fritsch, *Electrochimica Acta*, 2003, **48**, 3341-3348.

56. J. Min and A. J. Baeumner, *Electroanalysis*, 2004, **16**, 724-729.

57. R. R. Kamath and M. J. Madou, *Anal. Chem.*, 2014, **86**, 2963-2971.

58. Š. Komorsky-Lovrić, in *Electroanalytical Methods: Guide to Experiments and Applications* ed. F. Scholz, Springer, 2003, pp. 273-290.

59. G. Wittstock, *Analytical and bioanalytical chemistry*, 2002, **372**, 16-17.

60. S. Szunerits and L. Thouin, in *Handbook of Electrochemistry*, ed. C. G. Zoski, Elsevier, Amsterdam, 2007, pp. 391-XI.

61. J. Huangxian, C. Hongyuan and G. Hong, *Journal of Electroanalytical Chemistry*, 1992, **341**, 35-46.

62. K. Stulík, C. Amatore, K. Holub, V. Marecek and W. Kutner, *Journal*, 2000, **72**, 1483.

63. M. A. G. Zevenbergen, D. Krapf, M. R. Zuiddam and S. G. Lemay, *Nano Letters*, 2007, **7**, 384-388.

64. T. R. L. C. Paixão, R. C. Matos and M. Bertotti, *Electrochimica Acta*, 2003, **48**, 691-698.

65. J. I. Heo, D. S. Shim, G. T. Teixidor, S. Oh, M. J. Madou and H. Shin, *Journal of The Electrochemical Society*, 2011, **158**, J76.

66. A. Wahl, K. Dawson, J. MacHale, S. Barry, A. J. Quinn and A. O'Riordan, *Faraday Discussions*, 2013, **164**, 377-390.

67. J. Polonsky, M. Rievaj and D. Bustin, *Chem. Anal.(Warsaw)*, 1997, **42**, 445.

68. K. Toda, S. Hashiguchi, S. Oguni and I. Sanemasa, *Analytical Sciences*, 1997, **13**, 981-986.

69. P. Tomčík, P. Jenčušová, M. Krajčíková, D. Bustin, A. Manová and M. Čakrt, *Journal of Electroanalytical Chemistry*, 2006, **593**, 167-171.

70. A. K. Samarao, M. J. Rust and C. H. Ahn, *IEEE Sensors Journal*, 2007, DOI: 10.1109/ICSENS.2007.4388481, 644-647.

71. H. Sato, K. Yoshimine, T. Otsuka and S. Shoji, *Journal of Micromechanics and Microengineering*, 2007, **17**, 909-914.

72. K. Hayashi, J.-i. Takahashi, T. Horiuchi, Y. Iwasaki and T. Haga, *Journal of The Electrochemical Society*, 2008, **155**, J240.

73. J. Randhahn, B. Spilker, J. Flehr, H. Grabow, A. Neudeck, P. Jeroschewski and H. Beikirch, *Journal of Electroanalytical Chemistry*, 2008, **613**, 109-117.

74. E. D. Goluch, B. Wolfrum, P. S. Singh, M. A. Zevenbergen and S. G. Lemay, *Analytical and bioanalytical chemistry*, 2009, **394**, 447-456.

75. S. A. Trammell, F. Velez, P. T. Charles and A. Kusterbeck, *Analytical Letters*, 2008, **41**, 2634-2645.

76. D. Sharma, Y. Lim, Y. Lee and H. Shin, *Anal Chim Acta*, 2015, **889**, 194-202.

77. D. Sharma, J. Lee and H. Shin, *Biosensors & bioelectronics*, 2018, **107**, 10-16.

78. C. Ma, L. P. Zaino Iii and P. W. Bohn, *Chemical Science*, 2015, **6**, 3173-3179.

79. T. Horiuchi, O. Niwa, M. Morita and H. Tabei, *Journal of The Electrochemical Society*, 1991, **138**, 3549-3553.

80. T. Horiuchi, O. Niwa, M. Morita and H. Tabei, *Anal. Chem.*, 1992, **64**, 3206-3208.

81. M. Morita, O. Niwa and T. Horiuchi, *Electrochimica Acta*, 1997, **42**, 3177-3183.

82. M. Kudera, H. A. O. Hill, P. J. Dobson, P. A. Leigh and W. S. McIntire, *Sensors*, 2001, **1**, 18-28.

83. D. Daniel and I. G. R. Gutz, *Electrochemistry Communications*, 2003, **5**, 782-786.

84. E. O. Barnes, G. E. M. Lewis, S. E. C. Dale, F. Marken and R. G. Compton, *Journal of Electroanalytical Chemistry*, 2013, **703**, 38-44.

85. S. Barry, K. Dawson, E. Correa, R. Goodacre and A. O'Riordan, *Faraday Discuss*, 2013, **164**, 283-293.

86. K. V. Singh, A. M. Whited, Y. Ragineni, T. W. Barrett, J. King and R. Solanki, *Analytical and bioanalytical chemistry*, 2010, **397**, 1493-1502.

87. S. Partel, S. Kasemann, P. Choleva, C. Dincer, J. Kieninger and G. A. Urban, *Sensors and Actuators B: Chemical*, 2014, **205**, 193-198.

88. S. Nadzirah, N. Azizah, U. Hashim, S. C. B. Gopinath and M. Kashif, *PloS one*, 2015, **10**, e0139766.

89. R. Prajesh, V. Goyal, V. Saini, J. Bhargava, A. Sharma and A. Agarwal, *Materials Research Express*, 2018, **5**, 096415.

90. C. Kamble and M. Panse, *Materials Chemistry and Physics*, 2019, **224**, 257-263.

91. R. H. Prasad, U. Hashim, K. L. Foo, T. Adam and M. Shafiq, *Advanced Materials Research*, 2013, **832**, 517-521.

92. H. F. Hawari, N. M. Samsudin, A. Y. M. Shakaff, Y. Wahab, U. Hashim, A. Zakaria, S. A. Ghani and M. N. Ahmad, *Sensors and Actuators B: Chemical*, 2013, **187**, 434-444.

93. Y. Ueno, K. Furukawa, K. Hayashi, M. Takamura, H. Hibino and E. Tamechika, *Analytical Sciences*, 2013, **29**, 55-60.

94. H. Ohnuki, T. Wako, B. Mecheri, H. Wu, D. Tsuya and H. Endo, *Japanese Journal of Applied Physics*, 2019, **58**, SBBG16.

95. G. Y. Lee, J. H. Park, Y. W. Chang, S. Cho, M. J. Kang and J. C. Pyun, *Anal Chim Acta*, 2017, **971**, 33-39.

96. H. Wan, H. Yin and A. J. Mason, *Sensors and actuators. B, Chemical*, 2017, **242**, 658-666.

97. G. Y. Lee, J. H. Park, Y. W. Chang, S. Cho, M. J. Kang and J. C. Pyun, *ACS sensors*, 2018, **3**, 106-112.

98. Y. Bai, Y. Li, S. Xia, J. Sun, C. Bian and J. Tong, *Micro & Nano Letters*, 2014, **9**, 862-865.

99. R. D. A. A. Rajapaksha, U. Hashim, S. C. B. Gopinath and C. A. N. Fernando, *Microsystem Technologies*, 2017, **24**, 1965-1974.

100. I. J. Chen and I. M. White, *Biosensors & bioelectronics*, 2011, **26**, 4375-4381.

101. R. M. M. Hasan and X. Luo, *Nanomanufacturing and Metrology*, 2018, **1**, 67-81.

102. K. V. Singh, D. K. Bhura, G. Nandamuri, A. M. Whited, D. Evans, J. King and R. Solanki, *Langmuir : the ACS journal of surfaces and colloids*, 2011, **27**, 13931-13939.

103. N. Alayo, C. Fernández-Sánchez, A. Baldi, J. P. Esquivel, X. Borrisé and F. Pérez-Murano, *Microchimica Acta*, 2016, **183**, 1633-1639.

104. D. Sharon, P. Bennington, C. Liu, Y. Kambe, B. X. Dong, V. F. Burnett, M. Dolejsi, G. Grocke, S. N. Patel and P. F. Nealey, *Journal of The Electrochemical Society*, 2018, **165**, H1028-H1039.

105. A. J. C. Wahl, I. P. Seymour, M. Moore, P. Lovera, A. O'Riordan and J. F. Rohan, *Electrochimica Acta*, 2018, **277**, 235-243.

106. M. Morita, K. Hayashi, T. Horiuchi, S. Shibano, K. Yamamoto and K. J. Aoki, *Journal of The Electrochemical Society*, 2014, **161**, H178-H182.

107. J. S. Shim, M. J. Rust and C. H. Ahn, *Journal of Micromechanics and Microengineering*, 2013, **23**, 035002.

108. S. Partel, C. Dincer, S. Kasemann, J. Kieninger, J. Edlinger and G. Urban, *ACS Nano*, 2016, **10**, 1086-1092.

109. V. Matylitskaya, S. Kasemann, G. Urban, C. Dincer and S. Partel, *Journal of The Electrochemical Society*, 2018, **165**, B127-B134.

110. M. A. T. Gilmartin and J. P. Hart, *Analyst*, 1995, **120**, 1029-1045.

111. R. L. McCreery, *Chemical Reviews*, 2008, **108**, 2646-2687.

112. J. I. Heo, Y. Lim and H. Shin, *Analyst*, 2013, **138**, 6404-6411.

113. F. Liu, G. Kolesov and B. A. Parkinson, *Anal. Chem.*, 2014, **86**, 7391-7398.

114. F. Liu, G. Kolesov and B. A. Parkinson, *Journal of The Electrochemical Society*, 2014, **161**, H3015-H3019.

115. J. Lee, D. Sharma, Y. Lim and H. Shin, *Sensors and Actuators B: Chemical*, 2018, **267**, 467-475.

116. T. Ito and S. Okazaki, *Nature*, 2000, **406**, 1027.

117. P. Teerapanich, M. T. Z. Myint, C. M. Joseph, G. L. Hornyak and J. Dutta, *IEEE Transactions on Nanotechnology*, 2013, **12**, 255-262.

118. G. Ibáñez-Redín, R. H. M. Furuta, D. Wilson, F. M. Shimizu, E. M. Materon, L. M. R. B. Arantes, M. E. Melendez, A. L. Carvalho, R. M. Reis, M. N. Chaur, D. Gonçalves and O. N. Oliveira Jr, *Materials Science and Engineering: C*, 2019, **99**, 1502-1508.

119. D. Wang, Q. Chen, H. Huo, S. Bai, G. Cai, W. Lai and J. Lin, *Food Control*, 2017, **73**, 555-561.

120. J. Zhang, L. Huang, Y. Lin, L. Chen, Z. Zeng, L. Shen, Q. Chen and W. Shi, *Applied Physics Letters*, 2015, **106**, 143101.

121. R. Wang, J. Lum, Z. Callaway, J. Lin, W. Bottje and Y. Li, *Biosensors*, 2015, **5**, 791-803.

122. G. Rosati, A. Cunego, F. Fracchetti, A. Del Casale, M. Scaramuzza, A. Toni, S. Torriani and A. Paccagnella, *Chemosensors*, 2019, **7**.

123. R. Tortorich, H. Shamkhalichenar and J.-W. Choi, *Applied Sciences*, 2018, **8**, 288.

124. Fujifilm Dimatrix Materials Printer DMP-2850, https://www.fujifilmusa.com/products/industrial_inkjet_printheads/deposition-products/dmp-2800/, (accessed 20/04/2020).

125. S. Partel, S. Kasemann, V. Matylitskaya, C. Thanner, C. Dincer and G. Urban, *Microelectronic Engineering*, 2017, **173**, 27-32.

126. L. E. Delle, V. Pachauri, A. Vlandas, M. Riedel, B. Lägel, R. Lilischkis, X. T. Vu, P. Wagner, R. Thoelen, F. Lisdat and S. Ingebrandt, *Sensors and Actuators B: Chemical*, 2018, **265**, 115-125.

127. E. Noviana, K. J. Klunder, R. B. Channon and C. S. Henry, *Anal Chem*, 2019, **91**, 2431-2438.

128. K.-S. Chou and C.-H. Lee, *Advances in Materials Science and Engineering*, 2014, **2014**, 5.

129. M. Wittek, G. Möller, M. J. Johnson and M. Majda, *Anal. Chem.*, 2001, **73**, 870-877.

130. H. Nishihara, F. Dalton and R. W. Murray, *Anal. Chem.*, 1991, **63**, 2955-2960.

131. B. J. Feldman and R. W. Murray, *Inorganic Chemistry*, 1987, **26**, 1702-1708.

132. A. Vuorema , H. Meadows, N. B. Ibrahim , J. Del Campo, M. Cortina-Puig, M. Y. Vagin, A. A. Karyakin, M. Sillanpää and F. Marken, *Electroanalysis*, 2010, **22**, 2889-2896.

133. V. A. T. Dam, W. Olthuis and A. van den Berg, *Analyst*, 2007, **132**, 365-370.

134. A. Bange, J. Tu, X. Zhu, C. Ahn, H. B. Halsall and W. R. Heineman, *Electroanalysis*, 2007, **19**, 2202-2207.

135. Z. J. Zhang and S. S. Sun, *Journal of Electroanalytical Chemistry*, 2016, **778**, 80-86.

136. K. Yan, Y. Liu, Y. Guan, N. Bhokisham, C.-Y. Tsao, E. Kim, X.-W. Shi, Q. Wang, W. E. Bentley and G. F. Payne, *Colloids and Surfaces B: Biointerfaces*, 2018, **169**, 470-477.

137. X. Su, N. Tayebi, G. M. Credo, K. Wu, O. H. Elibol, D. J. Liu, J. S. Daniels, H. Li, D. A. Hall and M. Varma, *ACS sensors*, 2018, **3**, 1773-1781.

138. S. Partel, M. Mayer, P. Hudek, C. Dinçer, J. Kieninger, G. A. Urban, K. Motzek and L. Matay, *Microelectronic Engineering*, 2012, **97**, 235-240.

139. O. Laczka, C. García-Aljaro, F. J. del Campo, F. X. M. Pascual, J. Mas-Gordi and E. Baldrich, *Analytica Chimica Acta*, 2010, **677**, 156-161.

140. T. Yasukawa, Y. Yoshimoto, T. Goto and F. Mizutani, *Biosensors and Bioelectronics*, 2012, **37**, 19-23.

141. D. Lee, S. Lee, J. Rho, W. Jang, S. H. Han and T. D. Chung, *Biosensors & bioelectronics*, 2018, **101**, 317-321.

142. A. Oleinick, F. Zhu, J. Yan, B. Mao, I. Svir and C. Amatore, *ChemPhysChem*, 2013, **14**, 1887-1898.

143. F. Zhu, J. Yan, M. Lu, Y. Zhou, Y. Yang and B. Mao, *Electrochimica Acta*, 2011, **56**, 8101-8107.

144. M. Varshney and Y. Li, *Biosensors & bioelectronics*, 2009, **24**, 2951-2960.

145. N. A. Parmin, U. Hashim, S. C. B. Gopinath, S. Nadzirah, Z. Rejali, A. Afzan, M. N. A. Uda, V. C. Hong and R. Rajapaksha, *Mikrochimica acta*, 2019, **186**, 336.

146. S. P. Lee, *Sensors (Basel, Switzerland)*, 2017, **17**, 683.

147. Z. Du, C. Li, L. Li, H. Yu, Y. Wang and T. Wang, *Journal of Materials Science: Materials in Electronics*, 2010, **22**, 418-421.

148. Q. N. Minh, H. Tong, A. Kuijk, F. van de Bent, P. Beekman and C. M. van Rijn, *RSC advances*, 2017, **7**, 50279-50286.

149. R. Gondosiswanto, D. B. Hibbert, Y. Fang and C. Zhao, *Anal Chem*, 2018, **90**, 3950-3957.

150. M. Hu and I. Fritsch, *Anal Chem*, 2016, **88**, 5574-5578.

151. T. Terse-Thakoor, P. Ramnani, C. Villarreal, D. Yan, T.-T. Tran, T. Pham and A. Mulchandani, *Biosensors and Bioelectronics*, 2019, **126**, 838-844.

152. L. Le Thi Ngoc, M. Jin, J. Wiedemair, A. van den Berg and E. T. Carlen, *ACS Nano*, 2013, **7**, 5223-5234.

Chapter 2 Enhanced Iron Sensing in Generator-Collector Mode at Interdigitated Nanowire Electrode Arrays

This work has been published in Electrochimica Acta, 2018, 277, 235 - 243

2.1 Introduction

Recent advances in micro and nanofabrication techniques[1, 2] have enabled the fabrication of structures with controllable dimensions in the ultramicro- nanoscale. These have facilitated the development of novel devices such as electrochemical sensors for a wide range of applications including environmental, healthcare and security sensing.[3-6] For example, gold nanoelectrodes with critical dimensions less than 100 nm have been fabricated on silicon-based substrates with top-down approaches such as electron beam,[7, 8] nano[9] or focused ion beam lithography[10] and then combined with optical lithography to integrate on-chip interconnection tracks and on-chip counter and (pseudo)-reference electrodes.[11, 12] Nanoelectrodes by comparison with state-of-the-art microelectrodes display significantly improved electro-analytical characteristics arising from further enhanced mass transport, i.e., their critical dimensions are considerably smaller than the analyte diffusion layers formed during electroanalysis resulting in the fast establishment of steady-state analyte mass transfer by radial diffusion.[13-15] Furthermore, nanoelectrode arrays may be diffusionally independent under well-defined conditions such that the current is proportional to the number of nanoelectrodes present.[16]

However, there are some limitations and we have shown that such arrays require micron-scale inter-electrode spacing for diffusional independence which limits the number of nanowires per unit area[17, 18]. They may also experience relatively large charging currents (especially at high scan rates) and in such scenarios to identify changes in faradaic currents it is necessary to digitally subtract background currents from the overall recorded signals which then adds to the complexity of the system and analysis[19, 20]. To overcome these limitations, nanoelectrode arrays may be designed to enable redox cycling (RC) based analysis, i.e., repetitive analyte redox reactions occurring between adjacent

electrodes. The basic concept of RC and its use for signal amplification has been well documented.[21-27] Typically, RC relies on two individually addressable working electrodes whereby one electrode, the generator, may be biased at one potential, while at the same time the other electrode, the collector, may be biased with a different potential. A number of electrode configurations supporting RC have been reported, including: combined rotating-microdisc electrodes,[28] paired microband electrodes[29] recessed dual-ring nanopores[26] and interdigitated electrode arrays.[30] In the case of the latter arrays N generator electrodes are typically surrounded by N+1 collector electrodes with an inter-electrode distance on the order of micrometres to nanometres thus enabling efficient analyte diffusion and collection under generator-collector (GC) control.[22, 23, 31]

RC is optimised with enhanced signal amplification when the analyte redox reaction is fully reversible. Effectively, in GC mode, reversible electroactive species cycles back and forth between the generator and collector, which provides a fresh (regenerated) supply of analyte to the electrodes. This RC gives rise to significant current amplification over electrode arrays operating in non-GC mode.[29, 30, 32] Furthermore, holding the generator or collector at constant potentials during data analysis minimises background charging currents. Thus, nano-IDEs operating in GC mode are promising electrochemical sensing devices as they demonstrate advantageous electrochemical properties when compared to microelectrodes[26] and they may be fabricated at higher density.

Iron concentration in drinking water varies worldwide depending on several factors, such as the iron salts used as coagulating agents in water-treatment plants or the pipe material used for water distribution. In Europe the permitted limit for iron in drinking water, based on the World Health Organisation guidelines is 200 $\mu g.L^{-1}$ (3.6 µM)[33]. Spectrophotometric techniques, e.g., inductively coupled plasma mass spectrometry, are widely used to monitor iron content in drinking water,[34] however based on the

experimental complexity of the analysis equipment it is generally restricted to lab environments. By contrast, electrochemical techniques, particularly with the development of nano-IDEs, offer the possibility for rapid and portable methods of trace iron determination in aqueous environments.

In this work, we report on the fabrication of fully functional gold nano-IDEs (~100 nm wide, ~50 nm high, ~45 μm long and with ~500 nm spacing) on a Si/SiO_2 chip substrate. The arrays comprise two individually addressable interdigitated comb-like structures designated as working electrode 1 (WE1, generator) and working electrode 2 (WE2, collector).

Following fabrication, electrochemical characterisation was performed in ferrocene monocarboxylic acid (FCA) in 10 mM phosphate buffered saline at pH 7.4 (PBS) in non-GC (WE1 or WE2 connected) and in GC mode (WE1 was swept while a constant potential was applied to WE2). In non-GC mode, the closely spaced nano-IDEs effectively behave as microelectrodes with diffusion to the whole array area rather than hemispherical diffusion to each nanowire.[35] By contrast, in GC-mode, the nano-IDEs displayed significantly enhanced electrochemical behaviour arising from RC between adjacent nanowires and localised diffusion to each individual nanowire. At nano-IDEs the local environment at the generator electrode can also be altered significantly by the potential imposed at the collector electrode leading to very different electrochemical responses in identical solutions. Simulations of analyte diffusion to validate the electrochemical response were in excellent agreement with experimental results, providing further insight into the molecular RC. To demonstrate the advantages of nano-IDEs their suitability towards iron sensing for water quality analysis was also assessed.

2.2 Experimental

2.2.1 Interdigitated Nanowire Device Fabrication.

On-chip devices containing gold interdigitated nanowire electrode arrays, a gold counter and a platinum pseudo-reference electrode were fabricated using a combination of electron-beam and photolithography processes on Si/SiO_2 substrates as described in detail previously.[17] Interdigitated nanowires were patterned in resist by direct beam writing and metal evaporation (Ti/Au 5/50 nm) followed by standard lift-off techniques. Alignment marks were patterned along with this first metal layer to facilitate accurate positioning of subsequent optical lithography masks. Photolithography, metal evaporation (Ti/Au 10/90) and lift-off procedures were then employed to overlay electrical interconnection tracks including peripheral probe pads. Two macroscale gold electrodes were also deposited during this process, one of which was used as a counter electrode. A further metal deposition step (Ti/Pt 10/90 nm) onto one of these macroscale electrodes was undertaken to create an on-chip pseudo-reference electrode. A silicon nitride layer (~500 nm thick) was deposited to passivate the entire chip and windows selectively opened to contact the gold nano-IDEs, the gold counter and platinum pseudo-reference electrodes. Openings were also patterned above peripheral contact pads to permit electrical connection.

2.2.2 Structural and Electrical Characterisation.

Optical micrographs were acquired using a calibrated microscope (Axioskop II, Carl Zeiss Ltd.) with a charge-coupled detector camera (CCD; DEI-750, Optronics). SEM images were obtained using a calibrated field emission FEI Quanta FEG 650 at beam voltages between 5 and 30 kV. Two-point electrical measurements were performed using

a probe station (Model 6200, Micromanipulator Probe Station) with a Keithley 2400 source meter and dedicated LabVIEW™ programme.

2.2.3 Electrochemical cell and analysis.

To perform electrochemical analysis and to complete device packaging, chips were mounted in a custom-built electrochemical cell as described elsewhere, which is also shown in Appendix A.1.[12] Spring loaded probes (PM4J micro probe, CRIMP or PLUG SOCKET for PM4 series and a pre-wired RM4T-W700 terminal, Coda Systems Ltd.) made contact to the on-chip working, counter and pseudo-reference electrodes and (bi)potentiostat. The sample reservoir accommodated 150 µL solution with a chemical resistant O-ring seal (Polymax Ltd.), 4.5 mm in diameter. All electrochemical experiments were performed at room temperature (20°C) using a CHI760C bipotentiostat under PC control and Faraday Cage CHI200C (CH Instruments). All CVs were performed in triplicate, the data shown in each case is the third scan unless otherwise specified.

Prior to electrochemical experiments, electrodes were cleaned by sequential immersion for 10 minutes each in acetone and iso-propyl alcohol, followed by a thorough rinse with deionised water and dried with a filtered stream of nitrogen. Cyclic voltammetry (CV) measurements were recorded in 0 – 1 mM FCA in 10 mM PBS (pH 7.4) solutions. Standard solutions were prepared using iron (II) chloride tetrahydrate and tap water acidified with HCl. Finally, the iron content in tap water was measured using a standard addition technique. Tap water aliquots were diluted 1:10 in deionised water and spiked with 0.1 – 0.5 µM of iron. Both the deionised water and the iron stock solution were acidified to pH 3 with HCl to ensure that the tap water samples were also adequately acidified. All chemicals were purchased from Sigma Aldrich and used as received. Solutions were prepared using deionised water (18.2 MΩ cm, ELGA Pure Lab Ultra).

2.2.4 Finite-Element Simulations.

All simulations were performed by Dr Amelie Wahl in the Electrochemical Materials and Energy group. FCA concentration profiles at nano-IDEs used in non-GC and in GC modes were simulated using the commercial software package Comsol Multiphysics® 5.1. The objectives of these simulations were to explore the effect of altering connected and non-connected electrodes on the diffusional behaviour of the nano-IDEs and examine the influence of the collector electrode potential on redox reactions taking place at the generator for a range of scan rates. The simulations were based on our approach reported previously[7, 15, 17]. The models were implemented to mirror experimental conditions in 1 mM FCA in 10 mM PBS as described above. The electron transfer process of FCA/FCA^+ is reversible, with both the oxidised and reduced forms soluble in solution with the associated diffusion coefficients assumed equal (5.4×10^{-6} $cm^2.s^{-1}$), i.e., the sum of the concentration of both species is constant over the diffusion space and is assumed equal to the sum of their bulk concentration. An experimentally determined value of 0.15 V (vs. Pt) was employed for E^0, the formal potential of FCA/FCA^+. A simplified two-dimensional model known as the diffusion domain approach was adopted. In this approach, each nanowire was modelled as a 50 × 100 nm rectangle located at the centre of a much larger rectangle (space domain). The space domain area was selected to be large enough to ensure bulk-like conditions at the external boundaries remained unaffected by the electrochemical processes occurring at the electrodes. Simulations were resolved iteratively until a convergence error less than 2% was achieved.

2.3 Results and Discussion

2.3.1 Structural and Electrical Characterisation.

Structural characterisation of gold nano-IDEs was performed using a combination of optical and scanning electron microscopy (SEM). Figure 2-1(a) presents a schematic diagram showing the entire chip layout, while Figure 2-1(b) is an optical image of the central area of the chip where the electrodes are located. Each chip contains twelve nano-IDEs symmetrically located around a semi-circular gold counter electrode (CE) and a semi-circular platinum pseudo-reference electrode (PRE). Arrays comprise two individually addressable comb-like structures, WE1 and WE2 interdigitated nanowires, see Figure 2-1(c) and (d). Each interdigitated nanowire device, either WE1 or WE2 or both could be biased selectively vs. the on-chip CE and PRE using the spring-loaded probes in the custom-made sample holder.

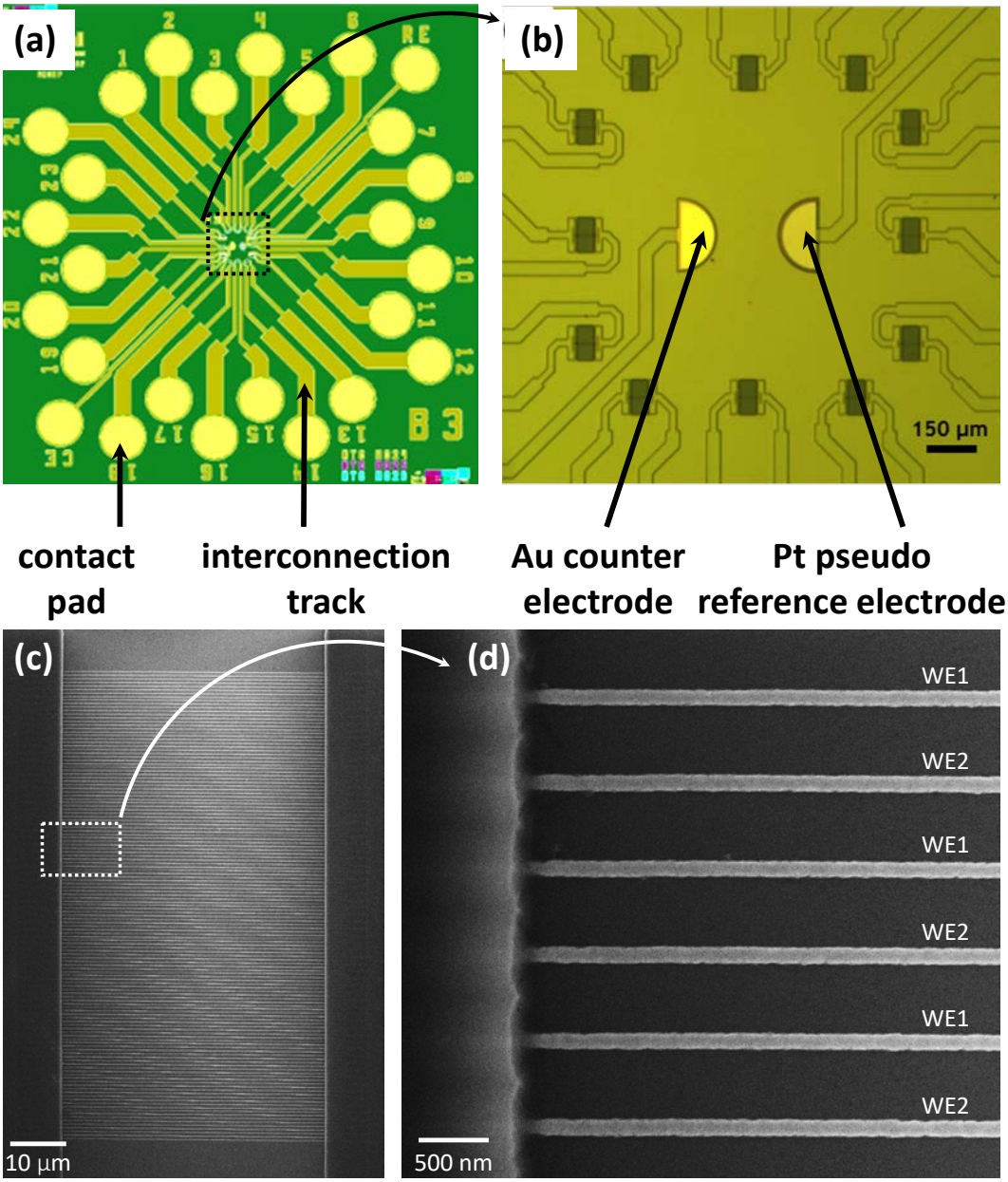

Figure 2-1 (a) Plan schematic diagram of a chip. (b) Optical micrograph highlighting the central area containing twelve gold interdigitated nanowire WE1-WE2 devices located around a gold CE and a platinum PRE. (c) SEM of gold interdigitated nanowire WE1-WE2 electrode arrays. (d) Higher magnification of (c).

SEM characterisation demonstrated that no residual passivation layer remained on the electrode surface and excellent connection between the nanowire electrodes and the overlaid interconnection tracks. Nanowires have a proud rectangular cross-sectional shape (as opposed to being inlaid or recessed) and the passivation window defined their electrochemically active length (typically 45 µm). Their dimensions are ~100 nm in

width and ~50 nm in height as previously reported[7, 12, 15] with an inter-nanowire distance of ~500 nm. Standard two-point *IV* measurements in air were undertaken as a quality control check to ensure electrical isolation between WE1 and WE2 prior to electrochemical analysis (data not shown). All functioning devices yielded very high resistances (~10 GOhm) typical of an open circuit response.

2.3.2 Simulations and Electrochemical Analysis.

FCA was selected as a model molecule for a completely reversible single electron redox process[36]. The black line in Figure 2-2(a) shows the characteristic sigmoidal CV for a single gold nanowire electrode (~100 nm wide, ~50 nm high and ~45 μm long); the current reaches a highly reproducible time-independent steady-state on the order of 1.0 nA. The corresponding simulations show that the diffusion layer thickness is much larger than the nanowire electrode dimensions throughout the cycle, in particular when the potential reaches the mid (0.15 V) and end (0.45 V) potentials as presented in Figure 2-2(c) and (d), respectively.

Equivalent CVs were also obtained at gold interdigitated nanowire arrays in non-GC mode at WE1 (red line) and WE2 (blue line). Both CVs have the same shape with the current reaching a highly reproducible diffusion-limited oxidation peak with an average of about 9.5 nA. In fact, as expected they almost perfectly overlap, thereby demonstrating the nearly identical electrochemical behaviour of the two sides of the interdigitated arrays. However, while the electrode area of either side of the interdigitated nanowire arrays (~6 x 10^{-6} cm^2) is significantly (~70 times) larger than that of a single nanowire (~9 x 10^{-8} cm^2), the current only increased by a factor of ~9.5. This arises from overlap of the individual diffusion layers at each nanowire over the timeframe of the experiment for the closely spaced nanowires. Corresponding simulated concentration profiles are shown in

Figure 2-2(d)-(e) which confirm the diffusional overlap i.e., planar diffusion to the whole array[37, 38]. Consequently, in non-GC mode, WE1 and WE2 behave more as single microelectrodes occupying the same area as the overall array and thus may be considered as microelectrodes of width 80.5 μm (i.e., the distance separating the outer two nanowires in the array) and length 45 μm. There remains a contribution of each nanowire to the diffusion flux and therefore the current achieved given the actual area of the nanowire electrodes is higher than would be predicted by diffusion control to a microelectrode which would be expected to yield a limiting current less than 7 nA.

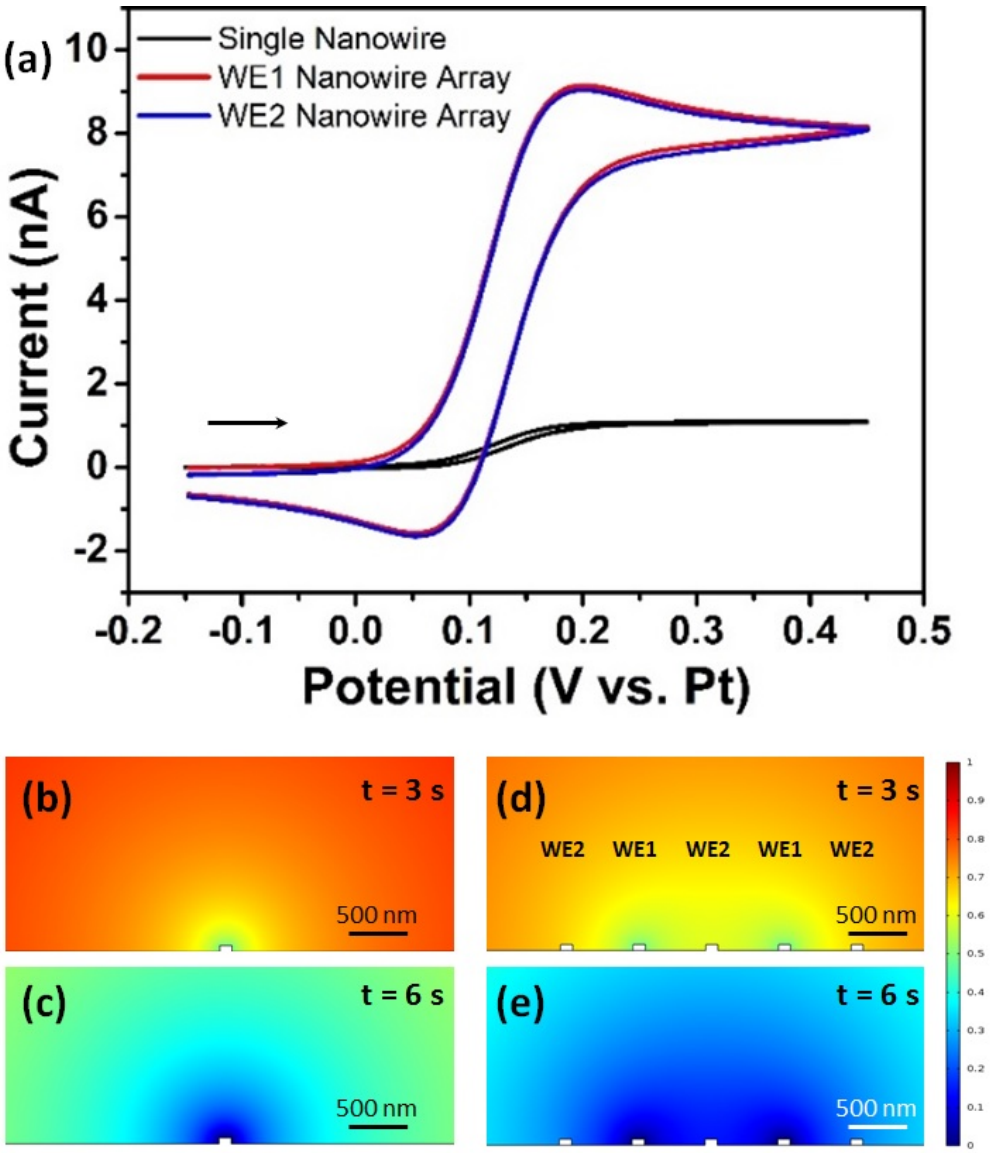

Figure 2-2 (a) Typical CVs for 1 mM FCA in 10 mM PBS between -0.15 and 0.45 V at 100 $mV.s^{-1}$. Signals were obtained at a single gold nanowire electrode (black line) and at gold nanowire interdigitated electrode arrays with 500 nm inter-nanowire spacing. Arrays were used in non-GC mode: the potential of WE1 was swept while WE2 was disconnected (red line) and vice-versa (blue line). (b) and (c) Cross-sectional views of 2D simulations of FCA concentration profiles at a single nanowire electrode respectively at t = 3 s (0.15 V) and 6 s (0.45 V) at 100 $mV.s^{-1}$. (d) and (e) are the equivalent cross-sectional representations at nanowire interdigitated electrode arrays with 500 nm inter-nanowire spacing in non-GC mode.

CVs were then recorded in GC mode. As presented in Figure 2-3(a), when WE2 was held at -0.15 V (reducing potential for FCA^{+}), the current measured at WE1 (solid red line) and at WE2 (dashed red line) are essentially the inverse of each other. FCA redox currents at WE1 and WE2 reach a reproducible steady-state current ~7 times higher than the non-

GC mode, thereby demonstrating improved individual nanowire behaviour. The currents are proportional to the number of nanowires in the arrays, i.e., every nanowire within WE1 and WE2 behaves as a single electrode[22, 39]. As the nanowires are only 500 nm apart and WE2 maintains conditions favourable to the reduction of FCA^+ species, RC occurs between WE1 and WE2 as depicted in the schematic of Figure 2-3(f), thus leading to the significant increase in current. The depletion of redox species at WE1 creates local concentration gradients that shuttle redox species between WE1 and WE2, unlike single electrodes or arrays employed in non-GC mode where the electrochemical response relies solely on mass transfer from the bulk solution.

2.3.3 Effect of Collector Potential.

In the GC mode CV experiments, species oxidised at WE1 were collected and reduced at WE2. Under these conditions, the WE2 collection efficiency, $\phi_{WE2(-0.15)}$, is defined as the ratio of the cathodic limiting current (absolute value) at WE2 to the anodic limiting current at WE1[23]. The maximum efficiency (98.5 %) for this electrode arrangement may be obtained when all nanowires in the WE1 and WE2 arrays behave complementary to each other (i.e., not perturbed by bulk species nor by charging currents) such that it is equal to the ratio of the number of nanowires within each array. A 92.7% collection efficiency was measured, which demonstrates that redox species effectively diffused in cycles between the generator and collector, however a small percentage escaped to the bulk solution. These observations were further investigated by the associated simulated concentration profiles. As shown in Figure 2-3(b)-(c), while species produced at WE1 largely diffused to WE2 (and vice-versa) a minority also diffused back into the bulk solution, vertically and at the outer nanowires. The diffusion layer established at WE1 necessitates an interaction with the bulk solution (see arrows). This behaviour is more

apparent when the potential at WE1 reaches 0.45 V (t = 6 s) compared to that at 0.15 V (t = 3 s) as the diffusion layer increases with time.

By contrast, when the collector electrode WE2 was set to 0.45 V (oxidising potential), the resulting electrochemical behaviour (green lines; Figure 2-3(a)) is the inverse of that described previously. However, the current increase is not as efficient as that described above, i.e., the amplification vs. the non GC-mode is slightly lower (~ factor of 6.5). This is probably due to the imposition of 0.45 V at WE2 creating an environment where a low oxidation current (approximately 5.5 nA) is seen for bulk species oxidation at WE1 when the potential reaches 0.45 V. The WE2 collection efficiency, $\phi_{WE2(0.45\ V)}$, was found to be 92.5%, i.e., the opposite redox process is as effective. Consequently, the number of RC, N_{RC}, for each FCA molecule may be determined as follows:

$$N_{RC} = \frac{1}{1-[\phi_{WE2(-0.15)}\,\Phi_{WE2(0.45)}]} \qquad \text{Equation 2.1}$$

Solving this equation yielded a value of ~7 for N_{RC}, which correlates extremely well with the observed current amplification when using GC mode compared to non-GC at 100 $mV.s^{-1}$ and indicates that the current amplification arises from a RC process between WE1 and WE2. Effectively, as the nanowires are close to each other and WE2 continuously oxidises the FCA species it creates an environment around the nanowires rich in FCA^+ while the bulk solution is FCA. This shows that for a simple open electrode arrangement as opposed to the more complex nano-well type electrodes, in a bulk solution of FCA, the environment of the electrode can be altered by controlling the collector electrode potential and the reacted product, in this case FCA^+, can be detected with an amplified signal as a result of RC. The simulated concentration profiles are again in excellent agreement with experimental observations: Figure 2-3(d)-(e) show bulk/reductive species are readily oxidised at WE2 and a constant supply of oxidative species is maintained at WE1; when

the potential at WE1 reaches 0.45 V (t = 6 s) a very small oxidation current is recorded at both electrodes but since both are at positive potentials there is no RC or hemispherical diffusion field and the current is more like the case in non-GC mode shown in Figure 2-2(a).

The collector electrode WE2 was also poised at the intermediate value of 0.15 V, see purple lines in Figure 2-3(a). This biasing condition is between the completely oxidised and reduced extremities described previously. At t = 0 s, the applied potential at WE2 is sufficient to oxidise some FCA molecules which diffuse to and are reduced at WE1. Thus, a RC process is again established but the measured current at both electrodes is lower due to the lower applied potential differential. As the applied potential increases at WE1, the measured current decreases. At t = 3 s, WE1 reaches 0.15 V and a similar situation to Figure 2-3(a) (green lines) arises in that all oxidisable FCA molecules are depleted and negligible current is measured at WE1 or WE2. As the CV continues and the applied bias to WE1 increases beyond 0.15V, the RC process again begins but this is inverted compared to that at lower potentials. At t = 6 s, FCA molecules oxidised at WE1 diffuse to and are reduced at WE2. This situation arises since at 0.15 V WE2 may oxidise FCA or reduce FCA^+ with equal feasibility. This demonstrates that judicious selection of the collector electrode bias can selectively alter the chemistry of the local environment in close proximity to the electrodes. This can be utilised to selectively remove interferent species while the RC process enhances the analyte signal.

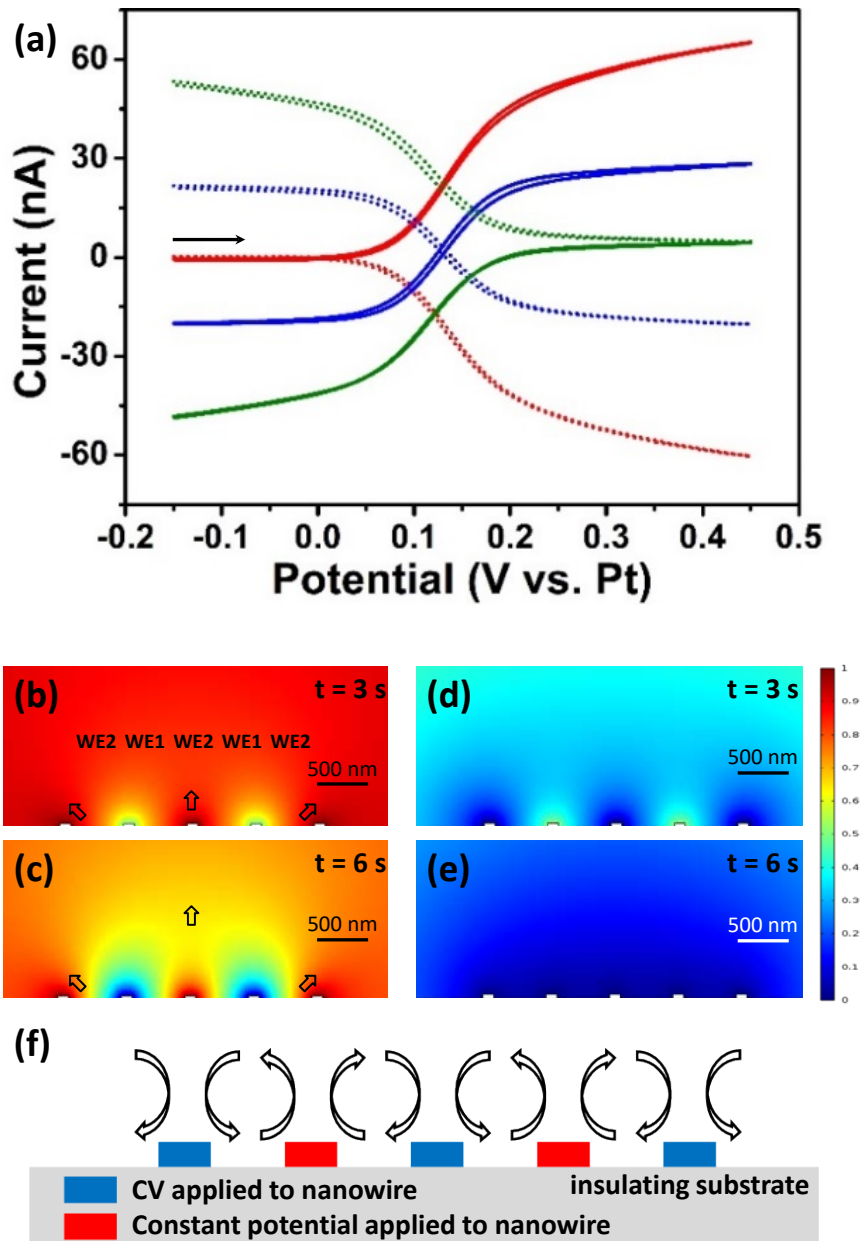

Figure 2-3 (a) Typical CVs for 1 mM FCA in 10 mM PBS from -0.15 to 0.45 V at 100 $mV.s^{-1}$. CV signals were obtained at gold INEAs with 500 nm inter-nanowire spacing. Arrays were used in GC mode: the potential of WE1 was swept while the potential of WE2 was held at -0.15 V (red lines), 0.15 V (blue lines) or 0.45 V (green lines). The current was measured at both WE1 (solid lines) and WE2 (dashed lines). Corresponding cross-sectional view of 2D simulations of FCA concentration profiles during the CV in GC mode at 100 $mV.s^{-1}$ at t = 3 s and 6 s, respectively, with the collector potential (b, c) -0.15 V and (d, e) 0.45 V. (f) Schematic diagram of RC at interdigitated nanowire array in GC mode.

2.3.4 Effect of Scan Rate.

CVs in 1 mM FCA in 10 mM PBS in GC-mode with WE2 biased at -0.15 V were repeated for a range of scan rates. As presented in Figure 2-4(a), interdigitated gold nanowire electrodes typically display sigmoidal CVs (only results for 5 and 5000 $mV.s^{-1}$ are shown for clarity) with the current reaching a highly reproducible time-independent steady-state at both WE1 (solid lines) and WE2 (dashed lines) arising from the RC process. Of note, the slight hysteresis in the WE1 currents is associated with charging currents which are more pronounced at higher scan rates. This clearly indicates that the rate of FCA replenishment was sufficient at WE1 regardless of the analysis time (on the order of 100 ms at 5000 $mV.s^{-1}$ and 100 s at 5 $mV.s^{-1}$), while bulk-like conditions remained unchanged at WE2. In other words, at high scan rates both the generator and collector currents may reach steady-state within a hundred milliseconds, thus opening the door for the investigation of electron-transfer processes over extremely short electrolysis times. Furthermore, the corresponding simulated concentration profiles are in excellent agreement with experimental observations as no significant differences are observed between that at 5, 100 and 5000 $mV.s^{-1}$, Figure 2-3(c) and Figure 2-4 (b)-(c).

As briefly discussed above, high signal-to-noise ratios were achieved, unlike conventional electrodes for which faradaic signals may become swamped by background currents especially at high scan rates. Background currents principally arise from an electrical double layer of positively charged species which forms at the electrode surface when a potential bias is applied. The redox analyte must diffuse through this layer for electron transfer to occur[20, 40], thus it is critical to assess charging currents contributions and understand their origin. To this end, CV experiments were undertaken in 10 mM PBS solution only without the redox active FCA. At WE1 (generator), the non-faradaic currents increased linearly with increasing scan rates from less than 0.1 nA at 5 $mV.s^{-1}$

to about 5.6 nA at 5000 $mV.s^{-1}$ (average of forward and reverse scans) yielding a very low capacitance (on the order of 1 nF), while at WE2 (collector) the background contributions are significantly lower (<0.3 nF); see Figure 2-5. While the potential of the collector electrode is fixed (i.e., no charging currents should be observed), the measured contributions may be originating from the generator: the double layer formed at WE1 may be detected by WE2. This would explain the slight differences in current observed in the presence of FCA. The redox species must diffuse through the electrical double layer (which is more pronounced at high scan rates) to react at WE1 and diffuse back through that layer to react at WE2 and vice-versa in cycles.

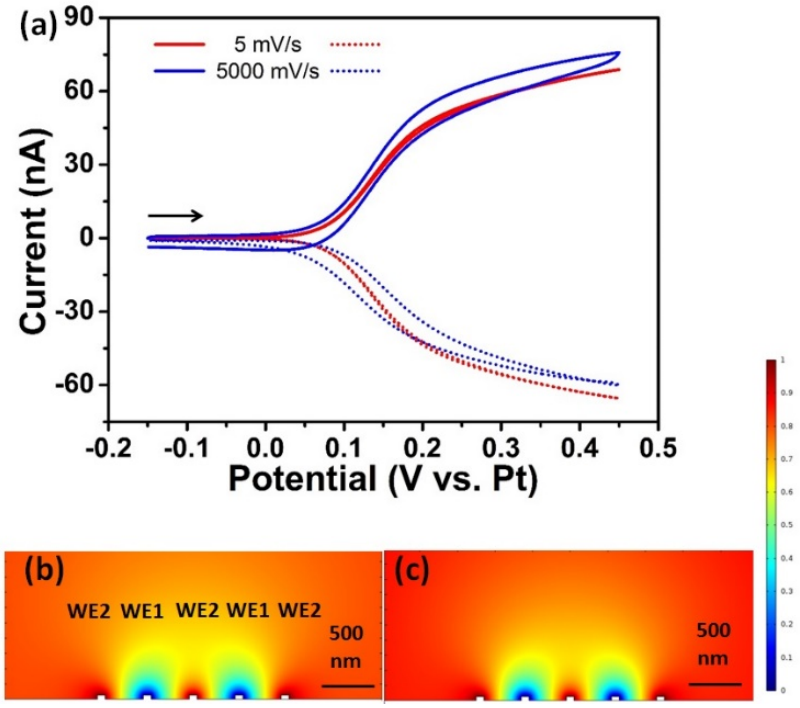

Figure 2-4 (a) Typical CVs at gold nanowire interdigitated electrode arrays with 500 nm inter-nanowire spacing in 1 mM FCA in 10 mM PBS between -0.15 and 0.45 V (vs. Pt) at 5 and 5000 $mV.s^{-1}$. Arrays were used in GC mode: the potential of WE1 was swept while the potential of WE2 was held at -0.15 V. The current was measured at both WE1 (solid lines) and WE2 (dashed lines). (b)-(c) Cross-sectional view of 2D simulations of FCA concentration profiles corresponding to CVs when the potential at WE1 reaches 0.45 V and was swept at 5 and 5000 $mV.s^{-1}$, respectively.

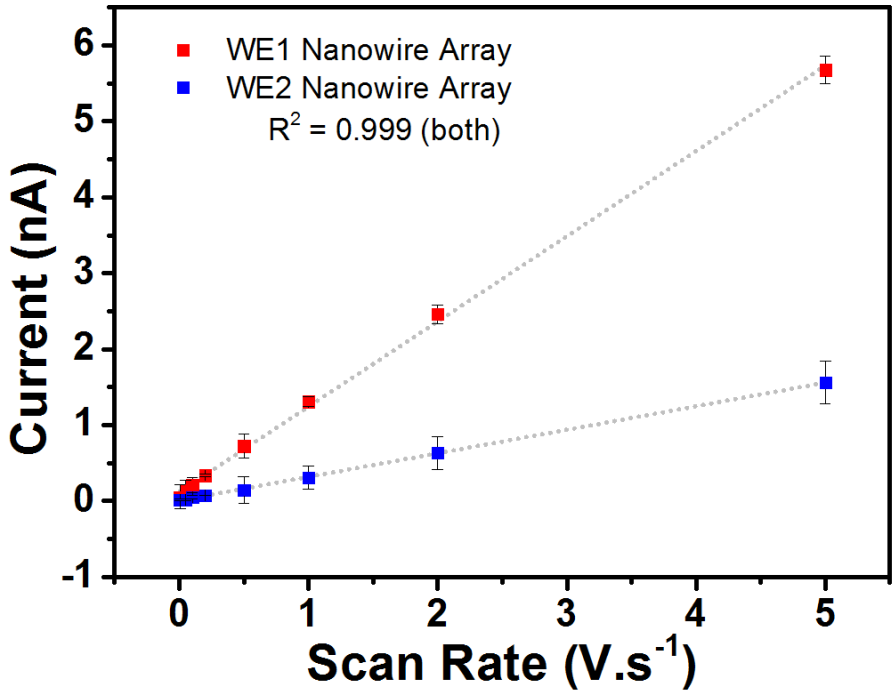

Figure 2-5 Average of forward and reverse non-faradaic currents at WE1 (red squares) and WE2 (blue squares) vs. scan rate (for WE1) from typical CVs in 10 mM PBS only (without redox active FCA) at a gold nanowire interdigitated electrode array with 500 nm inter-nanowire spacing. The array was used in GC mode: the potential of WE1 was swept from -0.15 to 0.45 V for the scan rates shown while the potential of WE2 was held at -0.15 V.

Digital subtraction of the background currents from the overall recorded signals (not shown) further demonstrates that CVs at WE1 and WE2 consisted essentially of faradaic currents, i.e., only signals at WE1 were slightly affected by charging currents for high scan rates ($\geq$ 2000 mV.s^{-1}). The slight distortions of the fast sweep CVs caused collection efficiencies to drop from $\geq$ 90% ($<$ 2000 mV.s^{-1}) to about 80% ($\geq$ 2000 mV.s^{-1}). Furthermore, it is also known that charging currents may become more pronounced with decreasing analyte concentration. However, the same collection efficiencies with respect to scan rate (within experimental error) were observed for 0.1 – 1 mM FCA in 10 mM PBS.

2.3.5 Effect of Analyte Concentration.

CVs in GC-mode over a range of scan rates and with WE2 biased at -0.15 V were undertaken in triplicate in 0.1, 0.2, 0.5, 0.75 and 1 mM FCA in 10 mM PBS solutions in order to further study the sensitivity of gold interdigitated nanowire electrodes. All recorded signals were sigmoidal and exhibited highly reproducible current magnitudes (data not shown). Figure 2-6 shows that steady state currents were proportional to FCA concentration from 0.1 to 1 mM (R^2 = 0.978) at both WE1 (red squares) and WE2 (blue squares) at 100 $mV.s^{-1}$. Furthermore, this behaviour was observed for all scan rates with only small variations observed in the slopes and intercepts which are likely due to interferences caused by the charging currents discussed above. This shows that high signal-to-noise ratios were achieved even at high scan rates, thus permitting rapid (within milliseconds) quantitative analysis to be undertaken and both the generator and collector currents can be used for calibration purposes.

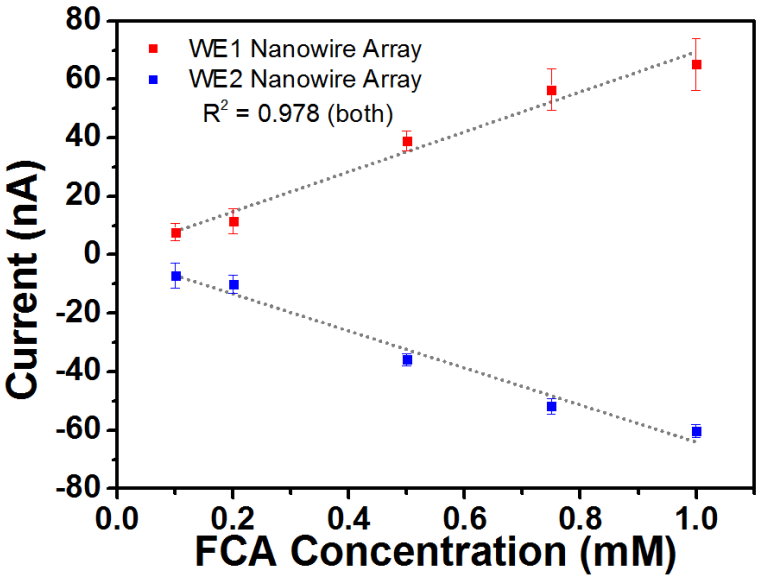

Figure 2-6 Quasi steady-state currents measured at WE1 (red squares) and WE2 (blue squares) vs. FCA concentration. CVs in 0-1 mM FCA in 10 mM PBS were obtained in GC mode at gold nanowire interdigitated arrays with 500 nm inter-nanowire spacing. The potential of WE1 was swept from -0.15 to 0.45 V at 100 $mV.s^{-1}$ while the potential of WE2 was held at -0.15 V.

2.3.6 Iron Detection.

To explore the suitability of fully integrated gold INEAs towards future sensing applications, CV measurements in GC mode were undertaken for a range of iron concentrations in HCl solutions across an applied potential range of 0.2 to 1.0 V (vs. Pt) at 100 $mV.s^{-1}$. The potential at WE2 was held at a reductive potential (0.4 V vs. Pt), i.e., a potential established experimentally to be favourable to the RC of Fe^{3+}/Fe^{2+} between WE1 and WE2. Iron was selected as the analyte of choice due to its reversible electrochemical properties and its importance in environmental and health applications.[41-43] It is commonly found in both its ferrous and ferric states, which are soluble in acidic aqueous solutions but precipitate at neutral pH and above.[43] As HCl has been found to facilitate the reversible redox processes of Fe^{3+}/Fe^{2+}, it was selected as the background electrolyte.[44] To this end, 1 mM (pH 3), 10 mM (pH 2) and 100 mM (pH 1) HCl solutions were investigated. 1 mM HCl was found to give rise to the maximum iron oxidation peak and thus was chosen as the background electrolyte. No damage to the nanowire electrodes arising from the presence of the acidic aqueous media was observed, however cycling from over -0.9 to 0.8 V (i.e., outside hydrogen evolution and prior to gold dissolution[44]) in 1 mM HCl prior to each measurement in iron solution was required as a surface activation step to obtain stable reproducible signals.

CV studies in GC mode were performed at the optimised conditions in 0-40 µM Fe^{2+} (0-2234 $\mu g.L^{-1}$) in 1 mM HCl solutions. As seen in Figure 2-7(a), on the forward scan at WE1 a well-defined oxidation peak at around 0.6-0.7 V was typically recorded in the absence of iron. This peak arises from oxide layer formation at the gold surface,[44] for which a corresponding reduction peak was recorded on the reverse scan at about 0.2-0.3 V. No additional peaks were recorded in the presence of iron other than the increase in the anodic pre-peak at ~0.7 V for increasing iron concentrations. Low coverage gold

oxides (which are reformed during the activation step in 1 mM HCl) are known to effectively promote electron transfer[45] and thus the analytical signal of iron is actually the difference between the recorded analyte signal and the background oxide formation current. This was demonstrated across a range of iron concentrations, see Figure 2-7(b). The oxidation peak currents at WE1 were found to be directly proportional to the iron concentration (R^2 = 0.995) with the intercept equal to the oxide formation current in 1 mM HCl and collection efficiencies on the order of 60%.

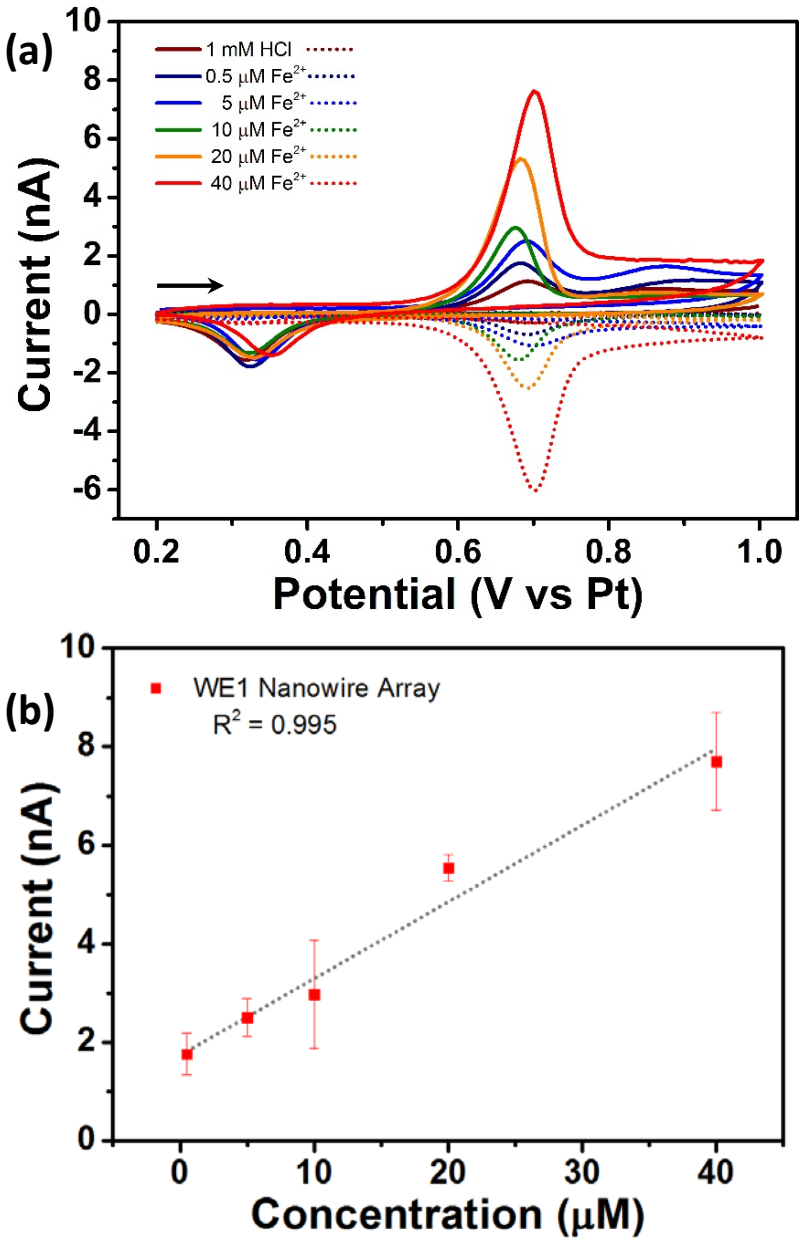

Figure 2-7 (a) Typical CVs (vs. Pt) in 0-40 μM Fe^{2+} in 1 mM HCl (pH 3) between 0.2 and 1.0 V at 100 $mV.s^{-1}$ for gold nanowire interdigitated electrode arrays with 500 nm inter-nanowire spacing. Arrays were used in GC mode: the potential of WE1 was swept while the potential of WE2 was held at 0.4 V (vs. Pt). The current was measured at both WE1 (solid lines) and WE2 (dashed lines). (b) Peak currents measured at WE1 vs. Fe^{2+} concentration.

The peak behaviour is likely due to the compact gold oxide formation as the sweep is continued to higher positive potentials which ultimately inhibits the continuing reaction for the iron species. The gold reduction peak at WE1 was found to be very reproducible for all solutions, which strongly supports that the oxidation of iron (II) occurs around the

same potential as gold oxide formation. The presence of an increasing current at the collector electrode for the reduction of the reacted Fe^{3+} demonstrates that it remains in solution and can be detected within the applied voltage range for this solution. The lower collection efficiencies (~60%) compared to that for FCA/FCA^{+} may be attributed to a weaker reversibility of the Fe^{2+}/Fe^{3+} couple.

Based on the obtained calibration curves and multiple replicates in the background solution, the Limit of Detection (LOD) was calculated to be on the order of 0.01 µM (0.6 $\mu g.L^{-1}$) by using Equation 2.2:

$$LOD = \frac{3.3\sigma_B}{m} \qquad \text{Equation 2.2}$$

Where σ_B is the standard deviation of the blank samples and m is the slope of the calibration curve. To overcome any matrix effects arising from the unknown tap water composition, the iron content was measured using a standard addition technique. In this approach, measurements were carried out for a range of tap water aliquots diluted 1:10 in deionised water spiked with 0.1-0.5 µM iron and acidified to pH 3 with HCl. As can be seen in Figure 2-8(a), recorded signals display the same shape as that in Figure 2-7(a), in particular the gold reduction peak was approximately of the same magnitude as previously seen for all solutions. However, the position of the peaks shifted by about 0.1 V (likely due to the slight variability of the platinum quasi-reference electrode), consequently the potential window was adjusted accordingly. As depicted in Figure 2-8(b), the peak currents at WE1 were also found to be directly proportional to the iron concentration ($R^2 = 0.995$) yielding an average iron content of 2.4 ± 1.0 µM.

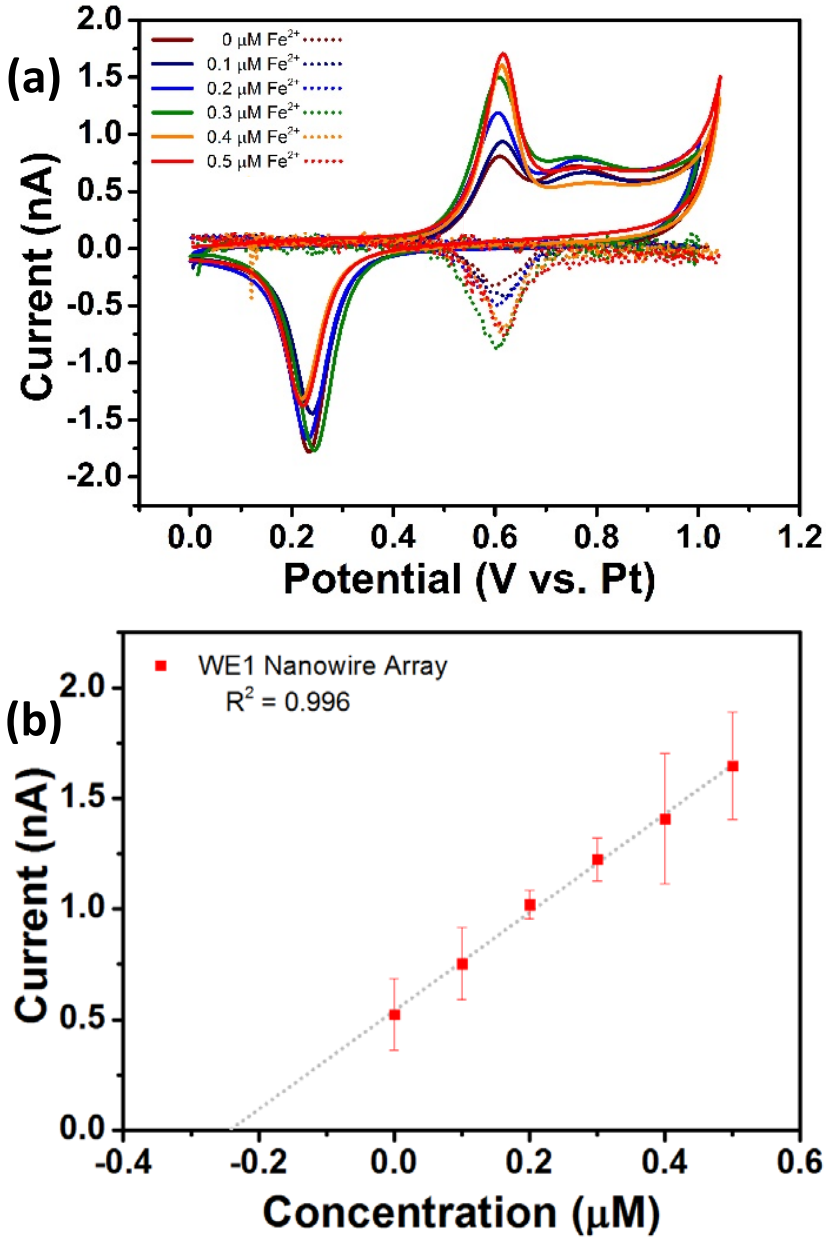

Figure 2-8 (a) Typical CVs (vs. Pt) between 0 and 1 V at 100 $mV.s^{-1}$ in aliquots of tap water 1:10 diluted, spiked with 0.1-0.5 µM Fe^{2+} and acidified to pH 3 with 1 mM HCl for gold nanowire interdigitated electrode arrays with 500 nm inter-nanowire spacing. Arrays were used in GC mode: the potential of WE1 was swept while the potential of WE2 was held at 0.4 V (vs. Pt). The current was measured at both WE1 (solid lines) and WE2 (dashed lines). (b) Peak currents measured at WE1 vs. Fe^{2+} concentration.

2.4 Conclusions

Interdigitated gold nanowire electrode arrays with reproducible dimensions (~100 nm wide, ~50 nm high, ~45 μm long and ~500 nm spacing) were fabricated on a Si/SiO_2 chip substrates. When employed in GC mode, interdigitated arrays displayed significantly enhanced electrochemical behaviour arising from a RC process, e.g., fast establishment (within a hundred milliseconds at 5000 $mV.s^{-1}$) of steady-state conditions, increased signal to noise ratios and increased sensitivity while also allowing quantitative detection at much lower concentrations. Simulations of analyte diffusion of the system were in excellent agreement with experimental results. Both simulations and experiments showed that for a relatively simple interdigitated nanowire array in an open solution the environment of the electrodes could be altered such that the product of the electrochemical detection can be detected with an amplified signal in GC mode analysis. The neighbouring nanoelectrode can therefore act as a switch for electrochemical responses depending on its imposed potential which opens up a wider range of detection capability for the already versatile electrochemical approach. Finally, the suitability of gold INEAs towards iron sensing was demonstrated in the 0.5 to 40 μM (28-2234 $\mu g.L^{-1}$) concentration range with an LOD on the order of 0.01 μM (0.6 $\mu g.L^{-1}$), which is well below the 200 $\mu g.L^{-1}$ permitted concentration limit for iron in drinking water in Europe.

2.5 References

1. A. Biswas, I. S. Bayer, A. S. Biris, T. Wang, E. Dervishi and F. Faupel, *Adv. Colloid Interface Sci.*, 2012, **170**, 2-27.

2. K. Dawson and A. O'Riordan, in *Annual Review of Analytical Chemistry, Vol 7*, eds. R. G. Cooks and J. E. Pemberton, 2014, vol. 7, pp. 163-+.

3. C. K. Chua and M. Pumera, *Electrophoresis*, 2013, **34**, 2007-2010.

4. V. Gubala, L. F. Harris, A. J. Ricco, M. X. Tan and D. E. Williams, *Anal. Chem.*, 2012, **84**, 487-515.

5. S. Barry, K. Dawson, E. Correa, R. Goodacre and A. O'Riordan, *Faraday discussions*, 2013, **164**, 283-293.

6. C. Robinson, N. Creedon, R. Sayers, E. Kennedy and A. O'Riordan, *Analytical Methods*, 2020, **12**, 2655-2660.

7. K. Dawson, A. Wahl, R. Murphy and A. O'Riordan, *The Journal of Physical Chemistry C*, 2012, **116**, 14665-14673.

8. A. Montrose, N. Creedon, R. Sayers, S. Barry and A. O'riordan, *J. Biosens. Bioelectron*, 2015, **6**, 1-7.

9. S. E. F. Kleijn, A. I. Yanson and M. T. M. Koper, *Journal of Electroanalytical Chemistry*, 2012, **666**, 19-24.

10. S. Rauf, M. J. A. Shiddiky, A. Asthana and K. Dimitrov, *Sensors and Actuators B: Chemical*, 2012, **173**, 491-496.

11. C. Duarte-Guevara, V. V. Swaminathan, M. Burgess, B. Reddy, E. Salm, Y.-S. Liu, J. Rodriguez-Lopez and R. Bashir, *Analyst*, 2015, **140**, 3630-3641.

12. K. Dawson, A. Wahl, S. Barry, C. Barrett, N. Sassiat, A. J. Quinn and A. O'Riordan, *Electrochimica Acta*, 2014, **115**, 239-246.

13. A. Molina, J. Gonzalez, M. C. Henstridge and R. G. Compton, *The Journal of Physical Chemistry C*, 2011, **115**, 4054-4062.

14. D. W. M. Arrigan, *Analyst*, 2004, **129**, 1157-1165.

15. A. Wahl, S. Barry, K. Dawson, J. MacHale, A. J. Quinn and A. O'Riordan, *Journal of The Electrochemical Society*, 2014, **161**, B3055-B3060.

16. N. Godino, X. Borrisé, F. X. Muñoz, F. J. del Campo and R. G. Compton, *The Journal of Physical Chemistry C*, 2009, **113**, 11119-11125.

17. A. Wahl, K. Dawson, J. MacHale, S. Barry, A. J. Quinn and A. O'Riordan, *Faraday Discussions*, 2013, **164**, 377-390.

18. C. Schopf, A. Wahl, A. Martin, A. O'Riordan and D. Iacopino, *J. Phys. Chem. C*, 2016, **120**, 19295-19301.

19. K. Dawson, A. Wahl, A. Pescaglini, D. Iacopino and A. O'Riordan, *Journal of the Electrochemical Society*, 2014, **161**, B3049-B3054.

20. C. G. Zoski, *Handbook of Electrochemistry*, Elsevier Science Bv, Amsterdam, 2007.

21. A. J. Bard, J. A. Crayston, G. P. Kittlesen, T. Varco Shea and M. S. Wrighton, *Anal. Chem.*, 1986, **58**, 2321-2331.

22. K. Aoki, M. Morita, O. Niwa and H. Tabei, *Journal of Electroanalytical Chemistry and Interfacial Electrochemistry*, 1988, **256**, 269-282.

23. O. Niwa, M. Morita and H. Tabei, *Anal. Chem.*, 1990, **62**, 447-452.

24. M. Paeschke, U. Wollenberger, C. Köhler, T. Lisec, U. Schnakenberg and R. Hintsche, *Analytica Chimica Acta*, 1995, **305**, 126-136.

25. M. Paeschke, U. Wollenberger, T. Lisec, U. Schnakenberg and R. Hintsche, *Sensors and Actuators B: Chemical*, 1995, **27**, 394-397.

26. D. Han, L. P. Zaino, K. Y. Fu and P. W. Bohn, *J. Phys. Chem. C*, 2016, **120**, 20634-20641.

27. E. Kätelhön, B. Hofmann, S. G. Lemay, M. A. G. Zevenbergen, A. Offenhäusser and B. Wolfrum, *Anal. Chem.*, 2010, **82**, 8502-8509.

28. S. Han, J. Zhai, L. Shi, X. Liu, W. Niu, H. Li and G. Xu, *Electrochemistry Communications*, 2007, **9**, 1434-1438.

29. M. G. Straver, M. Odijk, W. Olthuis and A. van den Berg, *Lab on a Chip*, 2012, **12**, 1548-1553.

30. B. Wolfrum, E. Katelhon, A. Yakushenko, K. J. Krause, N. Adly, M. Huske and P. Rinklin, *Accounts Chem. Res.*, 2016, **49**, 2031-2040.

31. D. Han, L. P. Zaino, K. Fu and P. W. Bohn, *The Journal of Physical Chemistry C*, 2016, **120**, 20634-20641.

32. D. Han, Y.-R. Kim, C. M. Kang and T. D. Chung, *Anal. Chem.*, 2014, **86**, 5991-5998.

33. W. H. Organization, *Journal*, 2004, **1**.

34. X. Pu, B. Hu, Z. Jiang and C. Huang, *Analyst*, 2005, **130**, 1175-1181.

35. A. J. Bard and L. R. Faulkner, in *Electrochemical Methods: Fundamentals and Applications*, Wiley, 2000, ch. Introduction and Overview of Electrode Processes, pp. 87 - 136.

36. Y. H. Lanyon, G. De Marzi, Y. E. Watson, A. J. Quinn, J. P. Gleeson, G. Redmond and D. W. M. Arrigan, *Anal. Chem.*, 2007, **79**, 3048-3055.

37. R. G. Compton, G. G. Wildgoose, N. V. Rees, I. Streeter and R. Baron, *Chem. Phys. Lett.*, 2008, **459**, 1-17.

38. N. V. Rees and R. G. Compton, *Chemical Communications*, 2010, **46**, 4238-4248.

39. J. H. Thomas, S. K. Kim, P. J. Hesketh, H. B. Halsall and W. R. Heineman, *Analytical Biochemistry*, 2004, **328**, 113-122.

40. A. J. Bard and L. R. Faulkner, 2000.

41. J. M. Gorell, C. C. Johnson, B. A. Rybicki, E. L. Peterson, G. X. Kortsha, G. G. Brown and R. J. Richardson, *Neurotoxicology*, 1999, **20**, 239-247.

42. A. Bradman, B. Eskenazi, P. Sutton, M. Athanasoulis and L. R. Goldman, *Environmental Health Perspectives*, 2001, **109**, 1079-1084.

43. E. S. Gurzau, C. Neagu and A. E. Gurzau, *Ecotoxicology and Environmental Safety*, 2003, **56**, 190-200.

44. E. A. Zakharova, E. E. Elesova, G. N. Noskova, M. Lu and R. G. Compton, *Electroanalysis*, 2012, **24**, 2061-2069.

45. L. D. Burke, *Gold Bull*, 2004, **37**, 125-135.

Chapter 3 Electrochemical Detection of Free-Chlorine in Water Samples Facilitated by in-situ pH Control using Interdigitated Microelectrodes

*This work has been published in Sensors and Actuators B: Chemical, 2020, p*128774

https://doi.org/10.1016/j.snb.2020.128774

3.1 Introduction

The pH of a solution is an important factor in aqueous chemical reaction mechanisms. The pH can influence the reaction rate, or whether a reaction even occurs. Many electrochemical reactions are also impacted by pH. For example; electrochemical deposition[1], polymerization[2] and sensing[3] all require a carefully controlled pH to achieve the desired outcome. In sensing applications, pH variations can lead to a shift in the redox potential or can even convert the species of interest into an inactive conjugate acid or base. In a laboratory environment, buffers are typically utilized to negate the effects of pH variability. However, with commercial sensors an end user cannot be expected to adjust sample pH before taking a measurement. For this reason, many commercially available test kits include some form of reagent to simplify and standardize the analysis. These reagents can induce a colour change essential for colorimetric testing, but also buffer the sample to a pH appropriate to the reactions of interest[4]. Reagents can be expensive, environmentally unacceptable and in some cases potentially hazardous to the operator. Moreover, they impose undesirable additional process steps for the end-user. Electrochemical-based sensing is attractive as it typically does not require reagent addition and can be used in-line; meaning a trained operator is not required to perform the measurements. In-line sensors can be modified for selectivity to particular analytes under the expected conditions of the sample matrix. In most applications, solution pH is either strictly controlled or does not deviate significantly. An example is the glucose bio-electrochemical sensor, commonly used for diabetes monitoring. These sensors detect glucose in blood, which is a complex matrix with a pH of 7.4[5]. If the blood pH varies from this value the sensors may not work precisely at the time of greatest clinical need.

Chlorine disinfection steps are employed for both potable and non-potable water systems and, in each case, knowing the concentration of residual chlorine at the end of the

distribution systems is a legal requirement. Residual chlorine is defined as the sum of the concentrations of both chlorine species, hypochlorous acid (HOCl) and hypochlorite (OCl^-).[6-8] Disinfection processes typically involve bubbling chlorine gas, or adding a salt such as sodium hypochlorite (NaOCl) to the water, Both processes result in the formation of hypochlorous acid as shown by the reaction schemes:[9]

$$Cl_2 + H_2O \leftrightarrow HOCl + HCl \qquad \text{Equation 3.1}$$

$$NaOCl + H_2O \leftrightarrow HOCl + NaOH \qquad \text{Equation 3.2}$$

The concentration of residual chlorine in a water system must be carefully monitored since too low a value may result in ineffective disinfection and pathogens remaining in the system, while too high may lead to reactions with organic compounds forming, e.g., trihalomethanes, which have been linked to cancer,[10] respiratory problems[11] and other adverse health effects.[12] As a result, the WHO has guidelines that specify the appropriate concentrations of chlorine in drinking water.[13]

Residual chlorine typically exists as a mixture of HOCl and OCl^-, the exact ionic ratio being dependent on solution pH. Drinking water has an acceptable pH range of 6.5 to 9.5.[14] While this relatively broad pH range is suitable for human consumption, it can greatly affect the signal output from a sensor. In this pH range the chlorine ion ratio can switch from predominantly HOCl to predominantly OCl^- species; which have very different reactivities at different sensors.[15] Figure 3-1 shows the relationship between pH and HOCl to OCl^- ratio.[16] The most common method of detecting residual chlorine is by a colorimetric technique using N,N-diethyl-p-phenylenediamine (DPD). This involves the reaction between the amine group of DPD and chlorine which produces a pink coloured compound.[17] Chlorine concentration can then be quantified based on the colour intensity. Similar methods have been developed based on fluorescence, chemiluminescence and other colorimetric techniques that show high selectivity with

limits of detection in the ppb range.[6-8, 18-20] Although some of these methods mitigate the issue of pH variation, they can be difficult to deploy in-line as required in water distribution networks. They also typically require the addition of a "reagent", which in most cases is not reusable. In contrast, it is well known that electrochemical methods permit detection of other analytes without the need for additional reagents, for example, in medtech[21, 22] and environmental sectors.[23]

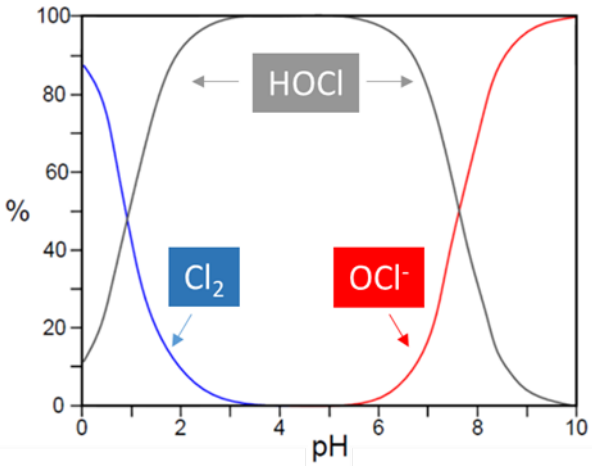

Figure 3-1 Distribution of residual chlorine as a function of pH

Free-chlorine sensors have been described in the literature employing cyclic voltammetry,[24-26] linear sweep voltammetry,[27, 28] and chronoamperometry[29-34] as detection methods. Chlorine concentration is probed by measuring the reduction of either hypochlorous acid or hypochlorite according to the following reactions:[27]

$$HClO + H^+ + 2e^- \rightarrow Cl^- + H_2O \qquad \text{Equation 3.3}$$

$$ClO^- + H_2O + 2e^- \rightarrow Cl^- + 2OH^- \qquad \text{Equation 3.4}$$

However, conventional electrochemical measurement of free-chlorine in water faces two main challenges. Firstly, as described above, the ratio of the chlorine reactants present in a measuring environment is pH sensitive. While electrochemical methods can work well in highly controlled pH environments, with water, the pH is likely to vary considerably. The second challenge is that hypochlorite is the dominant species at near neutral pH's,

and electrochemical reduction of hypochlorite occurs in the same potential region as dissolved oxygen.[35 36] Consequently, dissolved oxygen is a ubiquitous interferent limiting the effectiveness of electrochemical sensors.[32] By contrast, hypochlorous acid (HOCl) reduction occurs around 0.3 V (versus a saturated calomel electrode, SCE) outside of the oxygen reduction potential window. Thus, novel solutions are required to mitigate the effects of pH variability when using electrochemical based detection methods.

Prior work has shown that pH can be controlled *in-situ* using a ring disc electrode arrangement. In this work, hydrolysis of water was used to produce protons at an anode ring which diffused to the sensing disc electrode. This resulted in a lower pH environment at the electrode surface compared to the bulk solution. Acidic conditions facilitate the detection of mercury, so this method enables optimum detection without addition of acidic reagents.[37]. In acidic conditions, water is split by the following mechanism:[38]

$$\boldsymbol{Cathode}: 2H^+ + 2e^- \rightarrow H_2 \qquad \text{Equation 3.5}$$

$$\boldsymbol{Anode}: 2H_2O \rightarrow O_2 + 4H^+ + 4e^- \qquad \text{Equation 3.6}$$

In basic conditions, the mechanism becomes:

$$\boldsymbol{Cathode}: 2H_2O + 2e^- \rightarrow 2OH^- + H_2 \qquad \text{Equation 3.7}$$

$$\boldsymbol{Anode}: 4OH^- \rightarrow O_2 + 2H_2O + 4e^- \qquad \text{Equation 3.8}$$

An acidic medium can be made more basic by consumption of protons in a reduction reaction, or alternatively more acidic by production of protons in an oxidation reaction (depending on the potential imposed at an electrode). It is important to note that the pH change is strongest close to the electrode and diminishes with increasing distance from the electrode.

An important factor to consider is how quickly the pH environment is established. This is dependent on the diffusion of protons as they ultimately cause the pH change. The

diffusion coefficient of protons has been experimentally calculated to be 9.31 x 10^{-5} cm^2/s by Lee.[39] The majority of the work done in these experiments are on electrode arrays with gaps of approximately 100 µm. It is important that we know how long it takes for the protons to bridge this gap, as it will be factored into the quiet time of the experiment. Modifying the calculation for diffusion layer thickness gives the equation:

$$\frac{\delta^2}{\pi D} = t \qquad \text{Equation 3.9}$$

From this equation it was calculated that protons will diffuse far enough to encapsulate the sensing electrode 100 µm away in 0.342 seconds.

The electrochemical measurements in this work are performed on a generator-collector type device composed of two combs of interdigitated electrode arrays. The working electrodes are spaced 10 µm apart while the counter electrode is 1.1 mm away from the region of interest. By imposing an appropriate potential at one ("protonator") comb of electrodes, a pH change occurs in the local environment that tailors the pH at the other ("sensor") comb. That comb can then be used to perform sensing in conditions that differ from the bulk solution. It is vital that the counter electrode is relatively well removed spatially from the interdigitated combs. This ensures that the consumption of protons does not occur too close to the sensing electrode, which would inevitably prevent pH control. Using this approach, a local environment is created that is more acidic (or basic) than the bulk conditions. We apply this method to sensing of free-chlorine in the hypochlorous acid ionic form by electrochemically shifting the pH at a sensor to more acidic conditions. Consequently, at low pH all free-chlorine ions exists as hypochlorous acid, facilitating a more sensitive analysis, that is also removed from the dissolved oxygen interferent reduction potential region. The close spacing of the electrode combs ensures that pH control is established by the rapid diffusion of protons, so additional solution acidification, convection or fluidic forces are not required. Thus, this approach has the

potential for deployment as in-line analysis process, required, for example, in water distribution systems

3.2 Experimental

3.2.1 Electrode Fabrication:

Silicon chip based devices were fabricated using methods similar to those described by Dawson et al.[40-42] Each chip consisted of two combs of gold working interdigitated electrodes, platinum pseudo reference and gold counter electrodes were also employed on-chip. In brief, chips were designed to interface with external electronics via a microSD port to facilitate facile electrical connection. All the devices were fabricated on 4-inch silicon wafers bearing a thermally grown 300 nm silicon dioxide layer. Blanket metal evaporations of Titanium (10 nm) and Gold (100 nm) using a Temescal FC-2000 E-beam evaporator and lift-off technique yields interdigitated microband (55 µm x 1 µm x 60 nm) structures with gaps between the combs of 1, 2 and 10 µm. A second metal evaporation and lift-off process yields the interconnection tracks, contact pads and the gold counter electrode (90 µm x 7 mm). Finally, a third metal evaporation was performed to create the platinum pseudo reference electrode. To prevent unwanted interactions along the connection tracks, silicon nitride, which acts as an insulting layer was deposited by plasma-enhanced chemical vapour deposition. Photolithography and dry etching were utilised to selectively open windows (45 µm x 100 µm) in the insulating SiN layer over the microband electrodes for exposure to the electrolyte. Openings were also created over the counter and pseudo-reference electrodes and the contact pads. Each device contains six interdigitated electrode arrays (sensors) which are separated by 0.94 mm. Once the sensor fabrication was completed, each wafer was diced into 28 separate chip devices.

A custom-made holder cell was fabricated to allow measurement in small electrolyte volumes (~50 µL to 5 mLs). The cell was constructed from an aluminium base and a Teflon lid. Spring loaded probes (Coda Systems Ltd. PM4J Plain Radius Microprobes)

were inserted into the lid in position above the peripheral contact pads, to permit electrical connection to external potientiostats. The cell was assembled with a Viton O-ring embedded in the lid to forma seal around the on-chip electrodes. Viton O-rings were chosen for their chemical resistance. The inner diameter of the O-ring was 7 mm with a cross section of 1.6 mm to allow an opening large enough to expose all six sensors, counter and reference electrodes on the device to the electrolyte.

3.2.2 Electrode Characterisation:

Each chip was inspected using optical microscopy to identify any obvious defects or faults. Prior to any electrochemical characterisation chips were cleaned by immersion in acetone, then iso-propyl alcohol and finally de-ionized water, each for a period of ten minutes. The chips were dried in a flow of nitrogen and placed in the chip holder. Electrochemical analysis was performed using an Autolab Bipotentiostat (MAC80150 with BA Module, Metrohm). Cyclic voltammograms (CV) were performed from 0 V to 0.6 V at 50 mV/s in 1 mM ferrocene carboxylic acid (FCA, Sigma Aldrich, 97%). All CVs were performed in triplicate, with the data shown being the third scan unless otherwise specified. During these scans, the second interdigitated comb of electrodes were held at 0 V. The reference electrode used for each experiment was an external SCE (Note, vs. SCE means the external electrode was used). As a result, the sample volumes in each measurement was approximately 8 mLs.

3.2.3 Buffer preparation and Electrode Characterisation:

A series of buffers of differing pH was used to study the gold oxide reduction reaction. 0.1 M citric acid (Riedel-de Haën, 99.5% anhydrous) and 0.2 M sodium phosphate dibasic (Merck, 99% anhydrous) were mixed in appropriate ratios to yield buffers with pH values

of 3.6, 4.6 and 7.6, respectively. 0.2 M sodium phosphate dibasic and 0.2 M sodium phosphate monobasic (Sigma Aldrich, 99%) were mixed to make a pH 8.6 buffer, while 0.1 M sodium carbonate (Sigma Aldrich, 99%) and 0.1 M sodium bicarbonate (Sigma Aldrich, 99.5%) were mixed to yield a pH 10.8 buffer. Voltammetric analysis was performed in each buffer over the potential range 0 to 1.2 V (versus SCE) at 50 mV/s.

3.2.4 pH Adjustment in Water Samples:

Deionised water samples and artificial drinking water (ADW) samples were used to assess the ability of the microarray to control pH. ADW was prepared by dissolving 1 g of sodium bicarbonate, 0.0654 g of magnesium sulphate (Sigma Aldrich, 99.5% anhydrous), 0.3414 g calcium sulphate dehydrate (Honeywell, 99%), 0.007 g potassium phosphate dibasic (Fluka, 98%), potassium phosphate monobasic (Sigma Aldrich, 99%) and 0.01 g sodium nitrate (Sigma Aldrich, 99%) in 10 L of deionised water. For in-situ pH control, voltammograms were per-formed in both DI and ADW samples by scanning the sensing comb of the IDE array from 0.2 V to 1.2 V (versus SCE) at 50 mV/s with the protonator comb biased at 1.65 V (which is in the oxygen evolution region) to protonate (acidify) the local environment of the sensing electrodes.

3.2.5 Diffusion Simulations:

Simulations were performed by Benjamin O'Sullivan in the NanoTechnology Group. Diffusion simulations of proton concentration in the vicinity of the protonator electrodes were undertaken according to Fick's second law. A model was designed to simulate generation at and diffusion of protons from the protonator electrodes using finite element analysis (FEA) software, COMSOL Multiphysics 5.3, in line with the galvanostatic model shown by Read et al.[37] The geometry of the model consisted of a 5 mm square box

as the experimental domain, and two sets of interdigitated 1 µm wide microband electrodes (14 protonator electrodes and 13 sensing electrodes), separated by 2 µm. A flux of protons was applied at the surface of the protonators, by applying a fixed anodic current, where the flux was assumed to be proportional to the current applied at the electrodes. The initial pH value was set to 7. The proton diffusion coefficient used for the simulation was 9.31×10^{-5} cm^2 s^{-1}.

3.2.6 Detection of Free-Chlorine Without In-situ pH Control:

Initial scans were performed in various concentrations of free-chlorine in ADW at pH 3 (acidified using HCl) to establish the appropriate linear sweep voltammetry (LSV) parameters. Working samples were prepared by diluting Milton Sterilising Fluid (2% Sodium Hypochlorite) to the required concentrations. The concentration of free-chlorine was measured using a commercial free-chlorine colorimeter (Pocket Colorimeter II 58700-00 with Cl2 Test Kit, DPD method). The samples were acidified using 0.1 M HCl to ensure the dominant chlorine ion species was hypochlorous acid. LSV potential parameters were determined to be 0.95 V to 0.2 V (versus SCE) with a 50 mV/s scan rate. Scans were also performed using the same LSV parameters at pH 8.5 to establish the detection of free-chlorine when the sample is a mixture of hypochlorous acid and hypochlorite.

3.2.7 Detection of Free-Chlorine With pH Control:

The same samples of chlorine in ADW used for the tests at pH 8.5 were used for the experiments using pH control. The LSV parameters were as before with the addition of a bias of 1.65 V imposed on the protonator comb of electrodes to acidify the local environment.

3.3 Results and Discussion

3.3.1 Device Characterisation:

Devices were fabricated with varying inter-electrode comb spacing (1, 2 and 10 µm). Each comb of interdigitated electrodes can be addressed separately allowing for generator-collector type sensing applications. Figure 3-2(A) shows an image of a silicon chip device which consists of six sensors and on-chip counter and reference electrodes. Each sensor comprised of two interdigitated electrode combs, a protonator and sensor comb, respectively. Figure 3-2(B) shows a higher magnification image of a sensor with a 2 µm gap between electrode combs. The protonator comb (left hand side) contains 14 electrodes, while the sensor comb (right hand side) has 13 electrodes. The passivation is opened directly over the interdigitated combs of electrodes which is evident by the darker blue coloured rectangular window. This prevents unwanted electrochemical reactions occurring along the interconnection tracks. It is also clear that the electrodes do not touch the opposite side of the array which indicates that there is no electrical short in the device so dual mode generator-collector type electrochemical measurements are possible.

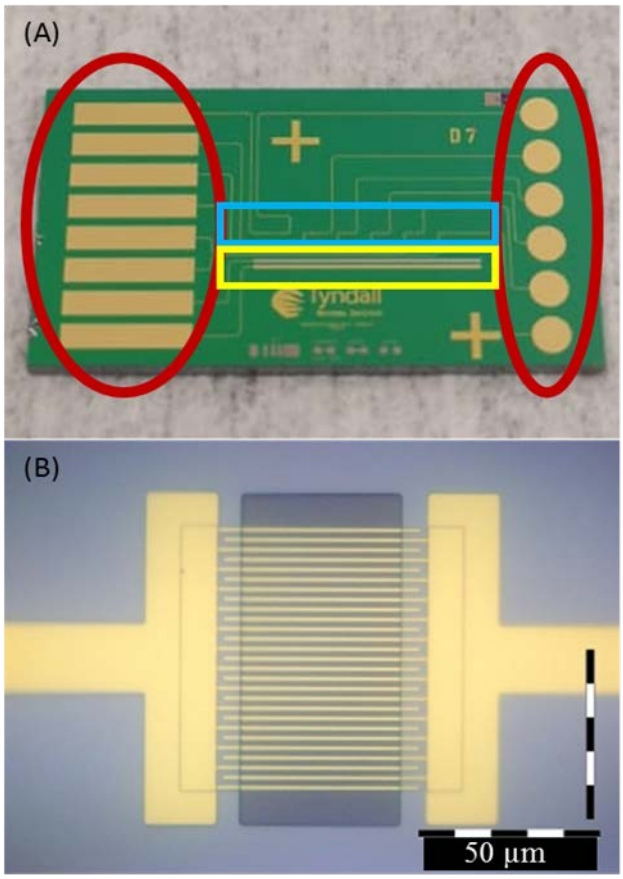

Figure 3-2 (A) Photograph of the full silicon chip (9.68 mm by 17.42 mm). The contact pads are circled in red; the sensors are in the blue box and both the counter and reference electrodes are in the yellow box. (B) 50 x magnification of a single sensor array highlighting where the gold IDEs make contact to the gold pads.

Following on from optical inspection, sensors were electrochemically characterized using FCA. Single microbands and IDEs of each gap width were characterised in single mode initially. Figure 3-3 shows the CV of each electrode type in FCA. The single microband showed a steady state current of approximately 1.4 nA. As the gap width decreased, the measured current increased due to increased electrode surface area. The 10 µm gap electrode measured 5 nA, the 2 µm gap measured 10 nA and the 1 µm gap measured 11.5 nA. However, the currents observed for each array should have been higher in theory. The 10 µm gap array had 4 generator electrodes, thus based on the single electrode current, this should have shown 5.6 nA (measured 5.36 nA). Similarly, the 2 µm had 13 generators, so a current of 18.2 nA was expected (measured 9.91 nA). Finally, the 1 µm

gap had 20 generators so a current of 28 nA was expected (measured 11.38 nA). The reason for the lower currents is diffusional overlap. The electrodes were not spaced far enough apart to ensure diffusional independence; therefore, the arrays began to act as larger single electrodes. This was highlighted by the change in shape of the CVs. It was seen that the scans became more peak shaped at the smaller gaps indicating that these scans had overlapping diffusion fields at this sweep rate and more of a peak-shaped transient response rather than a plateau steady-state current. The 10 µm gap still exhibited more steady-state than-peak shaped behaviour as each generator was separated enough to allow for diffusional independence over this timeframe.

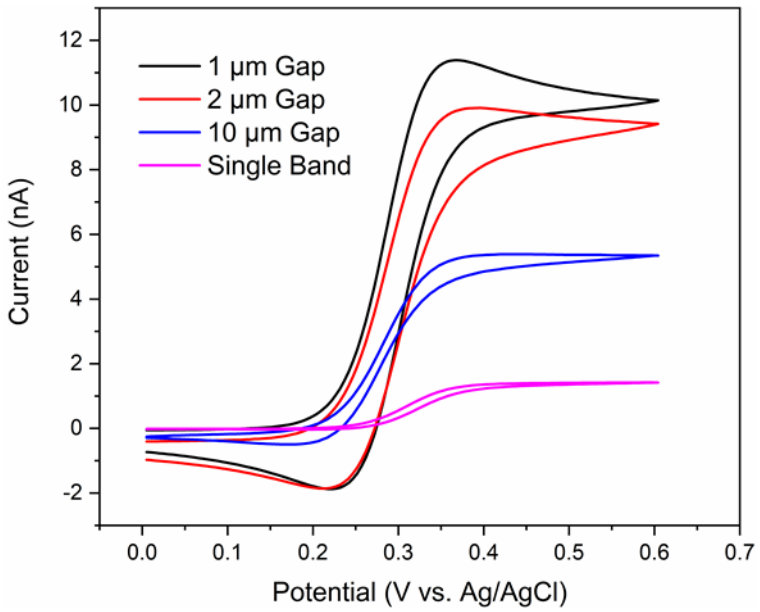

Figure 3-3 Comparison of FCA scans on different electrode arrays in single mode and a single electrode. CVs were performed from 0 to 0.6 V at 50 mV/s.

Both the 1 µm and 2 µm gap arrays were further characterised in single mode at various scan rates. Figure 3-4 and Figure 3-5 show the effect that varying the scan rate had on both array types. The slower scan rates exhibited a quasi-steady state behaviour, displaying a plateau rather than a peak shape. As the scan rate was increased, the behaviour changed significantly, and peaks were observed rather than plateaus. This effect was more pronounced in the 1 µm gap array as greater overlap occurred.

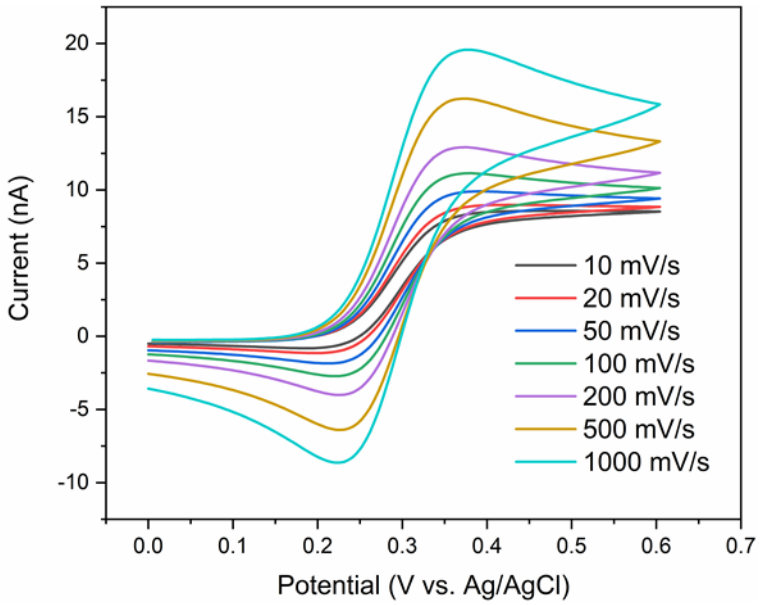

Figure 3-4 Comparison of scans on a 2 µm gap IDE in FCA. CVs were performed from 0 V to 0.6 V at various scan rates in single mode.

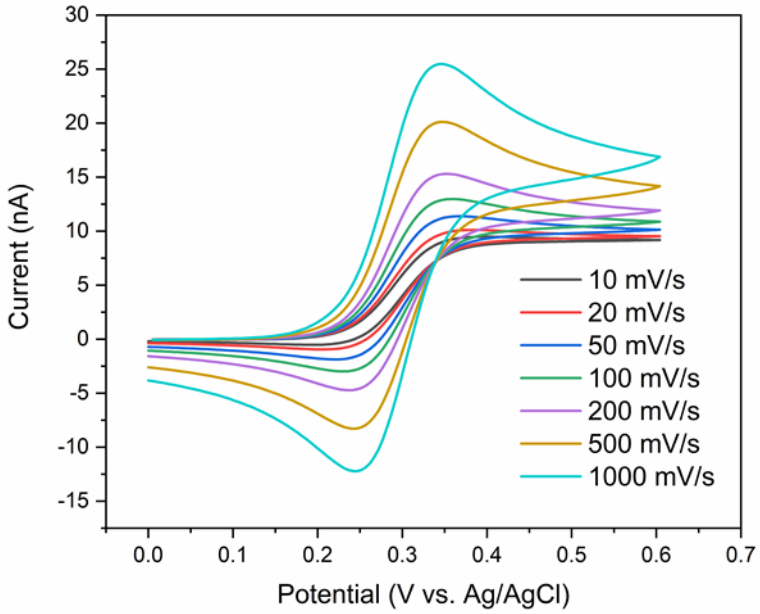

Figure 3-5 Comparison of scans on a 1 µm gap IDE in FCA. CVs were performed from 0 V to 0.6 V at various scan rates in single mode.

Each IDE was then further characterised in generator-collector mode. The general procedure for this was to bias the collector electrode at various potentials and scan the generator at a fixed scan rate. Subsequently, the collector was held at a fixed bias while the scan rates were adjusted. Figure 3-6 shows how the generator currents were influenced

by the collector bias. The bias potentials chosen were 0 V, 0.3 V and 0.6 V. These potentials allowed FCA to be in the ground state, partially oxidised, or fully oxidised prior to switching on the generator. Imposing any bias at the collector electrode forces each generator to act individually, therefore the current measured should be a multiple of the single microband current. Taking the 0 V bias scan as the example, the oxidation current was predicted to be 5.6 nA, calculated by multiplying the current at a single band by the number of generator electrodes. The measured current was 7 nA however. The discrepancy between the two figures is explained by redox cycling. The collection efficiency was determined to be 42.86%, thus using Equation 2.1, it was calculated that 1.23 redox cycling events occurred.

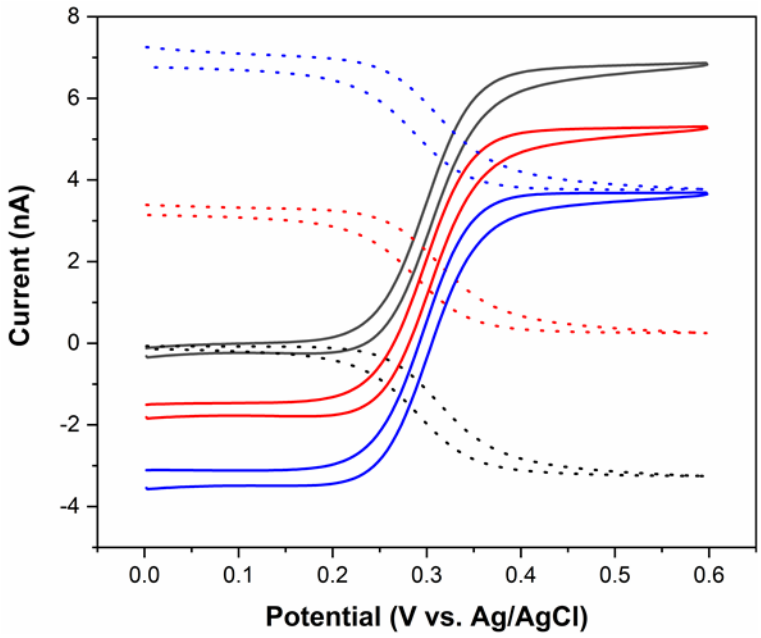

Figure 3-6 10 µm gap IDE in generator-collector mode. The solid lines are the generator scans, the dashed lines are the collector scans. CVs were performed from 0 to 0.6 V at 50 mV/s with the collector biased at 0 V (black), 0.3 V (red) and 0.6 V (blue).

Ultimately it was determined that the collection efficiency was too low for the 10 µm gap array. Figure 3-7 shows the result of varying the scan rate while the collector was biased at 0 V. It was found that the collection efficiency decreased dramatically as the scan rate was increased from 10 mV/s to 1000 mV/s. At faster scan rates the diffusion layer

thickness does not become as large as for the slower scan rates. As the gap between generator and collector electrodes is relatively large, less species crosses this gap resulting in the lower collection efficiencies. The highest measured collection efficiency was 42.86% at the slowest scan rates. The scan at 1000 mV/s showed significant hysteresis between the forward and the reverse scans because of increased capacitative effects. The collector scan at 1000 mV/s was found to have a dramatically different behaviour than for the other scan rates. Typically, the collector scan appears to be a mirror image of the generator, albeit at lower currents. For this scan however, the forward and reverse scans cross over each other and a current plateau is only observed on the reverse sweep. It was theorized that this effect was due to the timescale of this experiment being too short to allow for adequate diffusion of FCA across the gap. Therefore, the generator electrode was on the reverse sweep by the time a sufficient concentration of oxidised FCA was available to establish a steady state at the collector. As such, the distance between the generator and collector electrodes results in an apparent lag being observed at the collector at this scan rate.

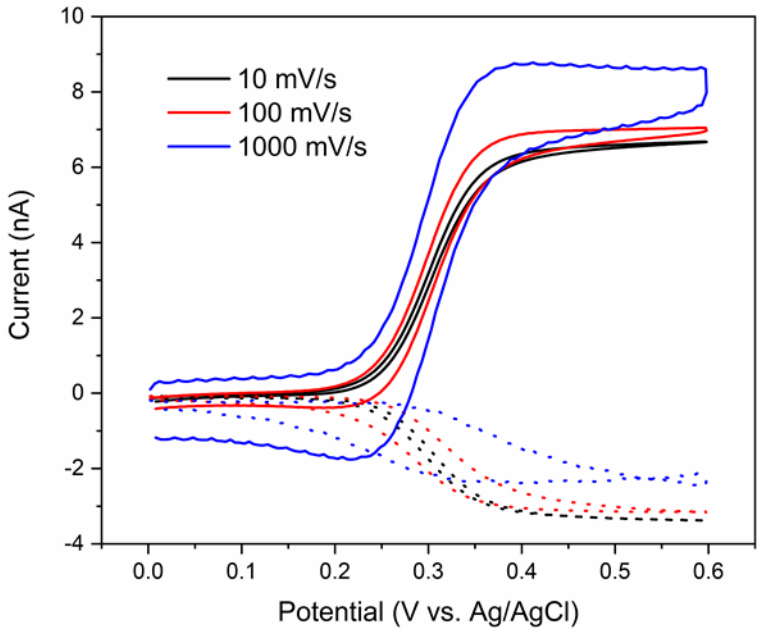

Figure 3-7 10 µm gap IDE in generator-collector mode. CVs were performed from 0 to 0.6 V at various scan rates with the collector (dashed lines) biased at 0 V.

It was therefore concluded that the 10 µm gap arrays were insufficient for the desired analysis. The 1 µm and 2 µm gap arrays were found to be more promising devices. Figure 3-8 and Figure 3-9 show how the 2 µm and 1 µm gap, respectively, behaved in generator collector mode. In both cases, a significant improvement was observed compared to the equivalent tests on the 10 µm gap arrays. The measured collection efficiency for the 2 µm gap array was 82.78%, and therefore the number of redox cycles was calculated to be 3.18. Similarly, the 1 µm gap array showed a collection efficiency of 91.14% and the number of redox cycles was determined to be 5.9. In chapter 2 it was found that using an IDE with electrodes 100 nm in width and separated by a 500 nm gap, a collection efficiency of 92.7% was possible. The 1 µm gap IDE, considering the electrodes are ten times the width of the nano-IDE and the gap is twice as large, show a comparably high collection efficiency. It appears from Figure 3-6, Figure 3-8 and Figure 3-9 that the smaller gaps show less hysteresis between forward and reverse scans, indicating less capacitative effects. However, the capacitance is unchanged but redox cycling causes the Faradaic component to increase, thus giving the appearance of decreased capacitance. Comparison of Figure 3-9 with the equivalent test performed on the 500 nm nano IDE (shown in chapter 2) shows that the measured currents are almost the same. Converting the limiting current for the scans with the collector biased at 0 V to current density shows that the nanowires are more sensitive, however. The 1 µm gap arrays, having a surface area of 990 μm^2 have a current density of 58.9 A/m^2. The 500 nm gap arrays, having a surface area of 603 μm^2 have a current density of 107.8 A/m^2. The benefits of nanowires certainly account for some of this improved current density, but the enhanced redox cycling due to the smaller inter-electrode gap also helps to improve this sensitivity.

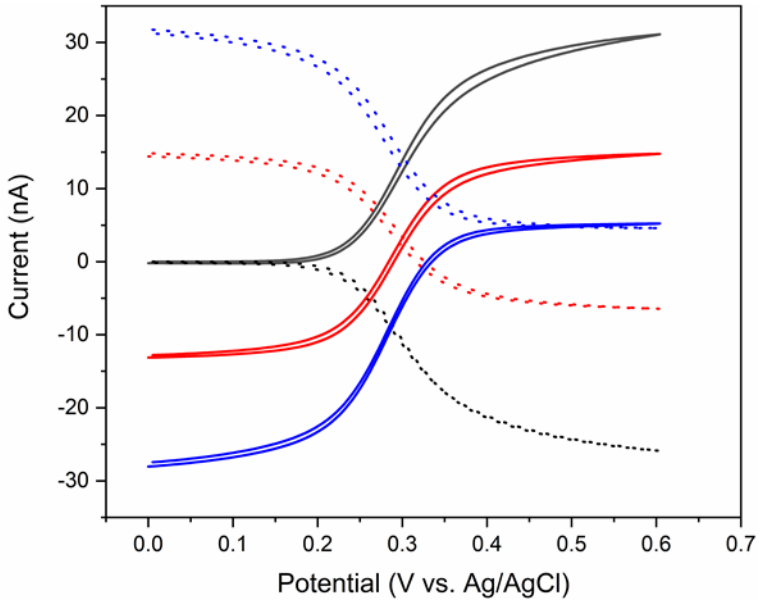

Figure 3-8 2 µm gap IDE in generator-collector mode. The solid lines are the generator scans, the dashed lines are the collector scans. CVs were performed from 0 to 0.6 V at 50 mV/s with the collector biased at 0 V (black), 0.3 V (red) and 0.6 V (blue).

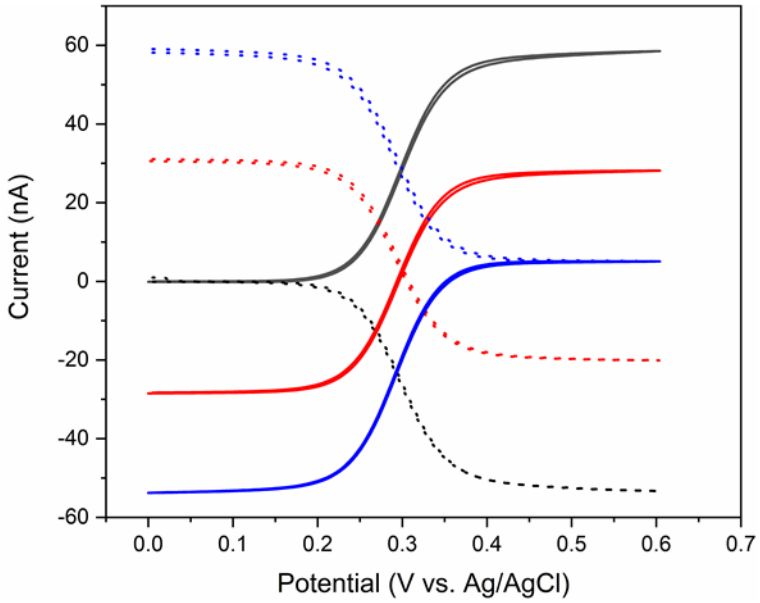

Figure 3-9 1 µm gap IDE in generator-collector mode. The solid lines are the generator scans, the dashed lines are the collector scans. CVs were performed from 0 to 0.6 V at 50 mV/s with the collector biased at 0 V (black), 0.3 V (red) and 0.6 V (blue).

No significant loss of collection efficiency with increasing scan rate was observed for the smaller gap IDEs as shown in Figure 3-10 and Figure 3-11. The 1 µm and 2 µm gap IDEs permit the diffusion of the oxidised species from the generator to the collector at faster scan rates, as the species needs to cover a shorter distance. As such, the smaller gaps

enable faster analysis without any loss of sensitivity. While the 1 µm gaps were found to have the greatest performance in terms of collection efficiency, it was ultimately decided that the 2 µm gap arrays would be used for pH control experiments. These were chosen as the larger gap minimised any cross reaction between the production of protons and detection of hypochlorous acid.

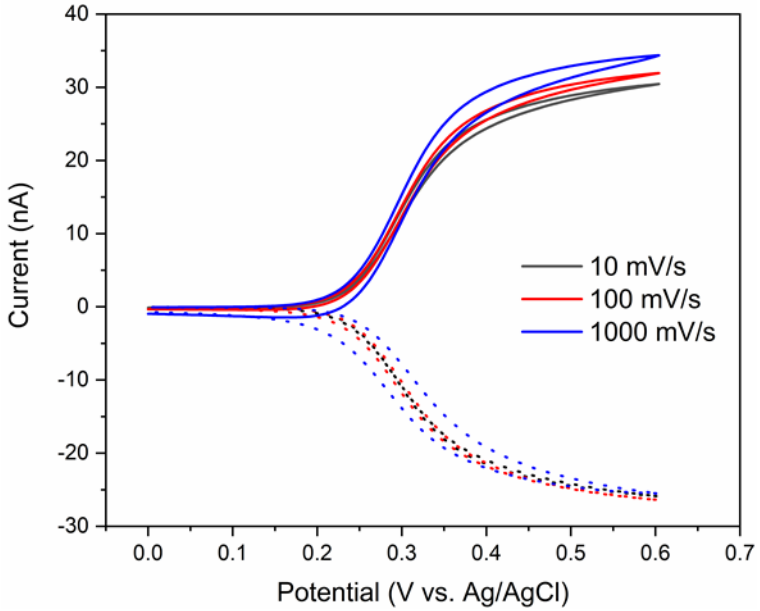

Figure 3-10 2 µm gap IDE in generator-collector mode. CVs were performed from 0 to 0.6 V at various scan rates with the collector (dashed lines) biased at 0 V.

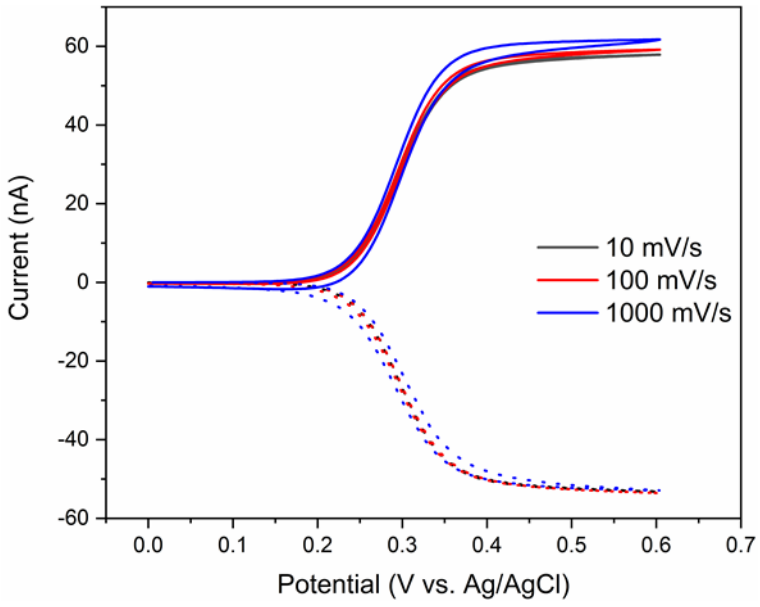

Figure 3-11 1 µm gap IDE in generator-collector mode. CVs were performed from 0 to 0.6 V at various scan rates with the collector (dashed lines) biased at 0 V.

3.3.2 pH Dependence of Gold Oxide Reduction Peak:

The gold oxide reduction peak was used as a probe for the pH condition of the electrodes. Gold oxide reduction is known to occur in 1 M H_2SO_4 at 1.18V vs. RHE[39] and the gold oxide reduction process is well documented.[43]

$$2Au + 3H_2O \rightleftarrows Au_2O_3 + 6H^+ + 6e^- \qquad \text{Equation 3.10}$$

In alkaline solutions the oxide reduction peak potential occurs around 0.05V vs. SCE.[44]

$$2Au + 6OH^- \rightleftarrows Au_2O_3 + 3H_2O + 6e^- \qquad \text{Equation 3.11}$$

The relationship between the gold oxide peak potential thus varies approximately in a Nernstian response of 59 mV/pH unit.[45] An oxide was formed on a gold electrode by scanning to a sufficiently positive potential, typically around 1.2 V. The electrode was then swept cathodically to the initial potential and the position of the oxide reduction peak was noted. This procedure was repeated at different pH values in a series of buffers to establish the linearity of the technique. Figure 3-12 (A) shows the oxide reduction peaks for the different buffer solutions. In each case, four replicate scans were performed to determine reproducibility. As expected, the oxide peaks shifted to more positive potentials at lower pH values. The oxide peak potential values for different pH's were reproducible (SD of 6.32×10^{-4} V for greatest error) over multiple scans as confirmed by the negligible error bars for the calibration in Figure 3-12(B) fitted using a linear regression approach. The calibration plot indicates a strong linearity with an $R^2 = 0.998$. The oxide approach to pH analysis shows a sensitivity of 67.78 mV/pH, indicated by the slope of the linear fit. The slight deviation from Nerstian behaviour may be due to the utilization of a fixed upper limit for oxide formation in the solutions of different pH. As mentioned, the error was very low for each data point, so the error bars are not well defined. The error was calculated as three times the standard deviation between scans, which is used for each calibration.

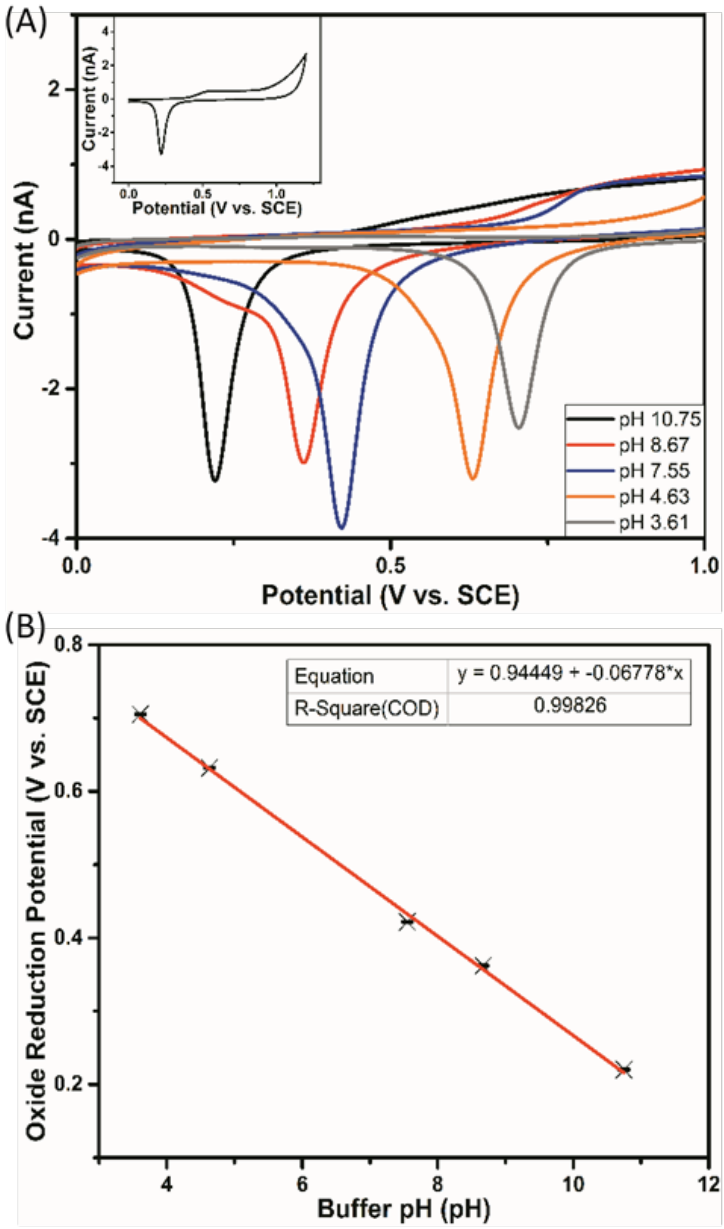

Figure 3-12 (A) CVs of one electrode comb in a series of pH buffers from 0 to 1.2 V at 50 mV/s. For these scans, the second electrode was left unbiased to prevent any interference. The inset shows the full scan used to take a measurement. (B) Calibration plot of oxide peak reduction potential vs. pH. A linearity fit of 0.998 is determined for this calibration plot. Error calculated from standard deviation of multiple scans (n=3).

3.3.3 Simulation of pH Control at Interdigitated Electrodes:

To determine the viability of the proposed in-situ pH control method using interdigitated electrodes, a simulation study was performed to elucidate the diffusion of H^+ ions away from a protonator electrode with 2 µm separations. The simulation model was employed to determine the best electrode configuration for pH control and to establish some of the conditions necessary to tailor the local pH to the acidic values required. Figure 3-13 (A) shows the pH in the environment of the electrodes after applying a current of 1 µA for 10 ms. The image shows a 2-D cross-section of a 1.2 mm by 1.8 mm area through the interdigitated array. It can be seen that although the bulk pH value remains at its initial value (in this case pH 7.0), in the locality of the electrodes the pH has begun to drop from pH 7 to below 5 (see inset – zoom in showing a 6 µm by 16 µm area around the electrodes). The estimated diffusion layer thickness (see Equation 3.9) for these conditions was 0.0017 cm, while simulation shows a thickness of 0.006 cm. Figure 3-13 (B) shows the situation 100 ms after the current bias was applied. The diffusion layer thickness has increased and the local environment at the electrodes has decreased to below pH 4. Again the predicted diffusion layer thickness was 0.0054 cm while the simulation shows a thickness of 0.016 cm. Figure 3-13 (C) shows the local environment 1 s after the current bias was applied. The diffusion layer thickness has increased further and the local environment at the electrodes is now at pH 3 (Inset). The predicted thickness was 0.0171 cm with the simulation showing a thickness of 0.05 cm. This suggests that within 1 second from switching on the pH control, the local pH environment should be sufficiently low to convert all residual chlorine to hypochlorous acid ionic form.

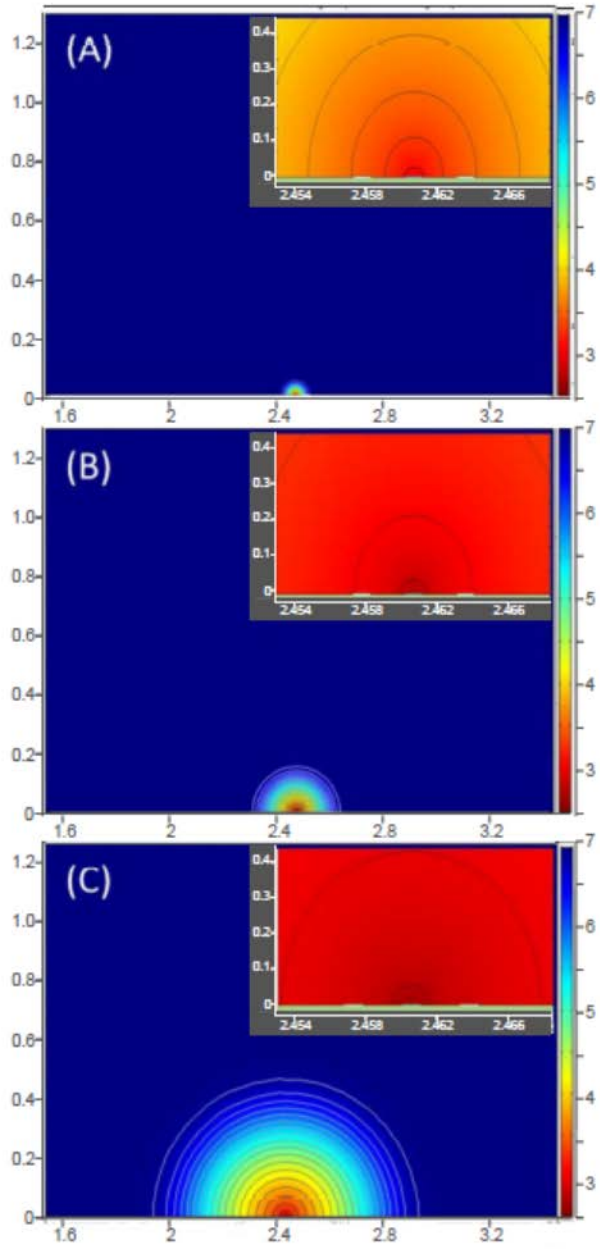

Figure 3-13 Simulation of an interdigitated array of electrodes with a current of 1 µA applied to the inner electrode. Simulations show the local pH 10 ms (A), 100 ms (B) and 1000 ms (C) after current imposition. The insets are a higher magnification of the 3 electrodes highlighting the local pH environment. The colour gradient represents the pH, the legend of which is shown on the right. The insets also show the silicon substrate (light green colour). The axis for each simulation is given in millimetres. The pH range is indicated on the right hand side of the figures.

3.3.4 Evaluation of in-situ pH Control of Deionised Water and Artificial Drinking Water:

As previously discussed, the location of the gold oxide reduction peak was used to determine the parameters required for pH control in non-buffered matrices. Deionised water samples were used initially to minimize complications arising from buffering capacity and interfering species. The samples were made slightly basic (pH 8.5) using 10 mM NaOH, as water splitting is not efficient at neutral pH. Tests were performed in triplicate where the sensing comb was swept anodically from 0 – 1.2 V while the protonator remained unbiased. A gold oxide was formed on the electrode and subsequently reduced on the cathodic sweep. The location of the reduction peak maximum was observed at ~ 0.27 V, see Figure 3-14. The protonator electrode was then biased at a constant positive potential of 1.65V (vs. SCE) to induce a local pH change and the sensor electrode again swept from 0 -1.2 V. These results are shown in Figure 3-14, where the gold oxide reduction peak of the sensor electrode was observed to shift anodically to 0.75 V; a shift of 480 mV. Using the data presented in Figure 3-12(B) it is estimated that the induced pH change was from pH 9.8 to pH 2.9 at the "sensor" electrode; a drop of ~6 pH units.

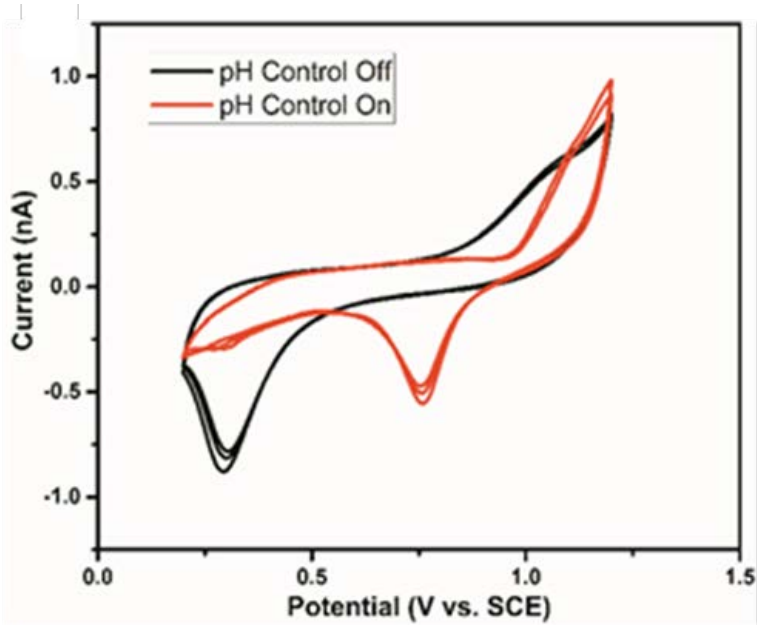

Figure 3-14 CVs at gold "sensor" IDEs over the range 0.2 to 1.2V vs SCE at a sweep rate of 50 mV/s in deionised water performed in triplicate. Initial pH is 8.5, and the oxide reduction peak is seen at approximately 0.27 V (black). By biasing the second electrode at 1.65 V the oxide reduction peak shifts to 0.75 V (red).

Tests were then repeated in ADW to determine the effectiveness of pH control in real sample conditions. ADW contains significant concentrations of sodium bicarbonate which was expected to buffer the pH at around 8.5. Using the same parameters as described above, it was found that pH control was still possible under these buffered conditions, see Figure 3-15. The pH shift is not as large as for deionised water, which was expected, but it was still sufficient to decrease the pH. The oxide reduction peak in this case appears at 0.68 V, which was estimated to be pH 3.8. While not as acidic as the deionised water sample, this pH still enables a near total conversion to HOCl (see Figure 3-1). By adjusting the protonator potential further, the pH change can be tailored to the required value of 3.0.

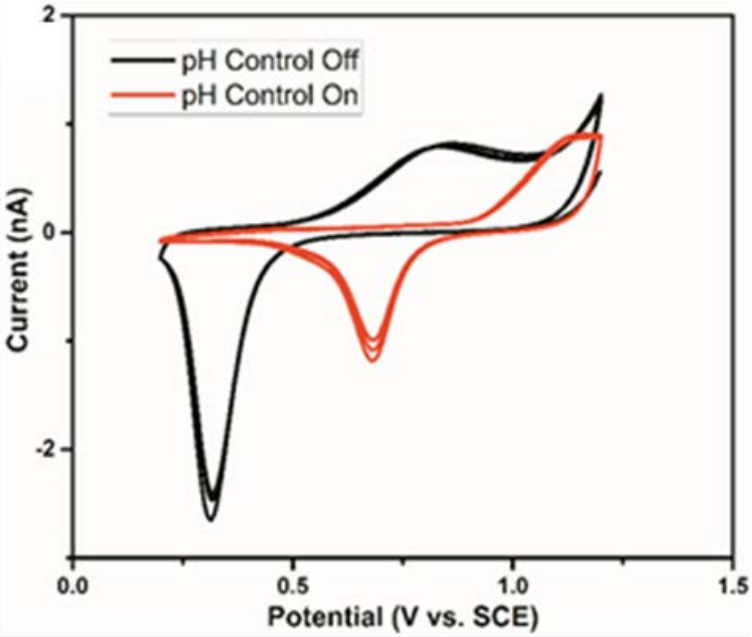

Figure 3-15 CVs at gold "sensor" IDEs over the range 0.2 to 1.2V vs SCE at a sweep rate of 50 mV/s in ADW performed in triplicate. Initial pH is 8.5, and the oxide reduction peak is seen at approximately 0.27 V (black). By biasing the second electrode at 1.65 V the oxide reduction peak shifts to 0.68 V (red).

3.3.5 Free-Chlorine Detection Using pH Control:

Samples of hypochlorous acid (made by diluting a hypochlorite stock in ADW and acidifying with 10 mM HCl) were assessed using the interdigitated electrodes to establish the appropriate detection window. LSV was again used as the detection method and it was found that scanning from 0.95 V to 0.2 V at 50 mV/s was optimal for detection of free-chlorine. A series of low concentration (0.3 - 2 ppm) hypochlorous acid standards (pH of approximately 8.5) were prepared and their respective concentrations confirmed using a commercial DPD method. Figure 3-16 shows typical LSV scans obtained at a senor electrode while the protonator electrode remained un-biased. Under these conditions, the free-chlorine will exist as both hypochlorous acid and hypochlorite, with the latter being the predominant species. Voltammograms recorded for the 0.35 and 0.7 ppm standards overlapped entirely, as the currents associated with each are quite low, and could not be differentiated from each other. A well-defined plateau current for the reduction was not

observed making it difficult to determine the appropriate potential at which to take a reading for calibration purposes. A second plateau associated with hypochlorite reduction would be expected outside of this potential window at more cathodic potentials in the oxygen reduction region. Consequently, dissolved oxygen would interfere with the analysis by providing higher currents and thus false positive readings.

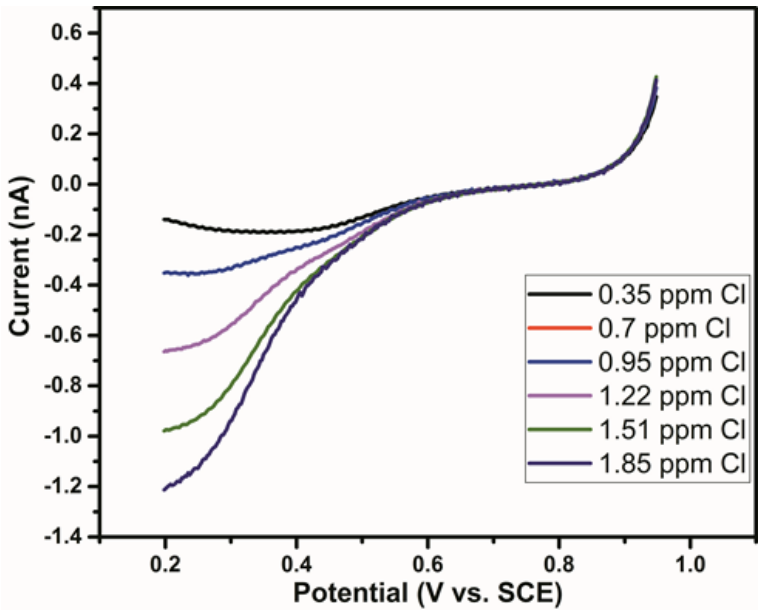

Figure 3-16 LSVs at gold IDEs over the range 0.95 to 0.2V vs SCE at a sweep rate of 50 mV/s in various concentrations of chlorine, measured by the DPD method in ADW at pH 8.

The equivalent tests were then undertaken in newly prepared standard solutions acidified to pH 3 using 0.1 M HCl. The equivalent LSV scans are presented in Figure 3-17. Much higher currents (compared to Figure 3-16) for similar concentrations were observed. This higher sensitivity allowed clear discrimination between the lower concentration standards. Furthermore, a well-defined plateau region between 02 -03 V was observed enabling facile calibration. Finally, as the free-chlorine existing entirely as hypochlorous acid, the problems associated with dissolved oxygen as an interferents were removed.

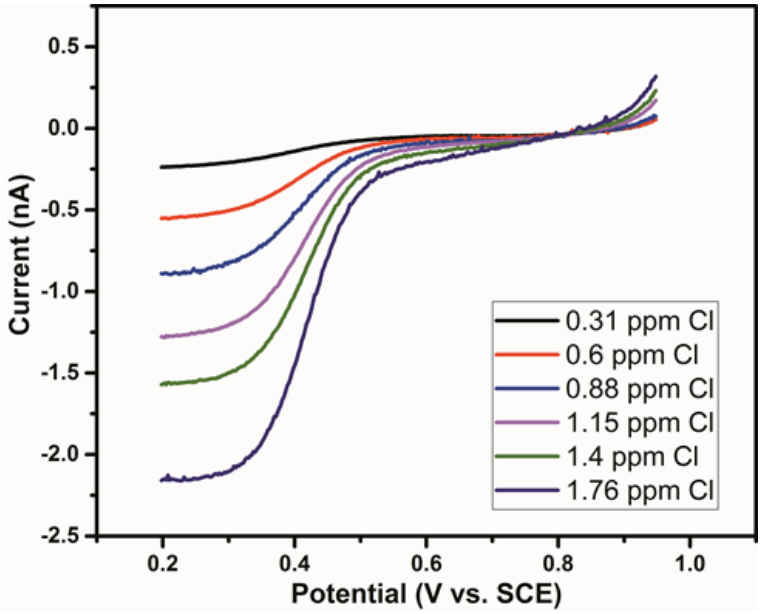

Figure 3-17 LSVs at gold IDEs over the range 0.95 to 0.2V vs SCE at a sweep rate of 50 mV/s in various concentrations of chlorine, measured by the DPD method in ADW at pH 3.

Following the successful demonstration of decreasing pH increasing chlorine detection sensitivity, the protonator potential established for pH control in blank water samples was then applied to the initial free-chlorine standards at pH 8.5. Figure 3-18 shows the equivalent scans (to Figure 3-16) performed with the protonator biased at 1.65 V. A significant increase in signal current was observed for each scan performed; similar to Figure 3-17. Figure 3-19 shows the associated calibration curve fitted using a linear regression technique exhibiting good linearity with a $R^2 = 0.969$ and a measured detection limit of 0.01 ppm using Equation 2.2. Measurements were undertaken in triplicate to determine the error. A second reduction event was observed in the pH control results, occurring at approximately 0.6 V. While not fully understood, it is possible that this may arise as a result of chlorine (Cl_2) formation. As shown in Figure 3-1, it is possible for Cl_2 to form in extremely acidic pH conditions, typically below pH 3. While the parameters used should create a pH 3.8 environment, it is possible that the pH is lower than this. This second reduction was not seen in the samples that had been chemically adjusted, as the samples could not become more acidic.

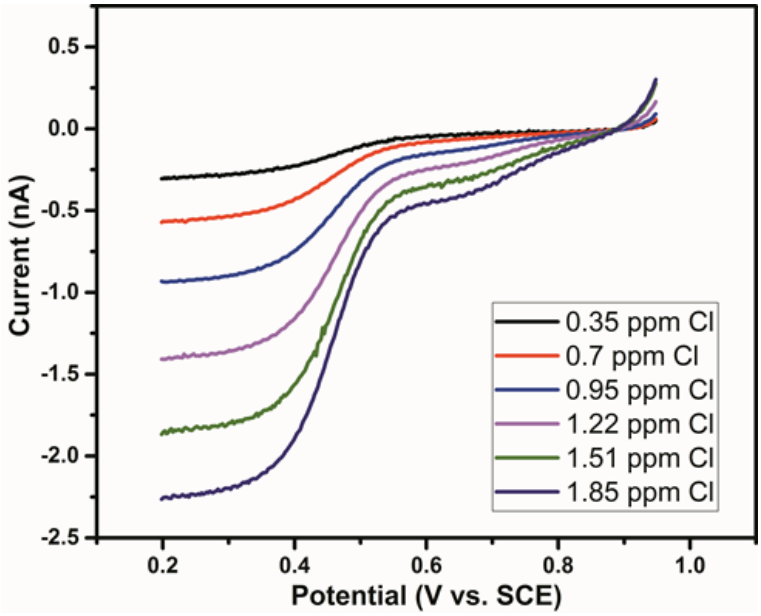

Figure 3-18 LSVs at gold IDEs over the range 0.95 to 0.2V vs SCE at a sweep rate of 50 mV/s in various concentrations of chlorine, measured by the DPD method in ADW at pH 8. A bias of 1.65 V was applied at the protonator electrode.

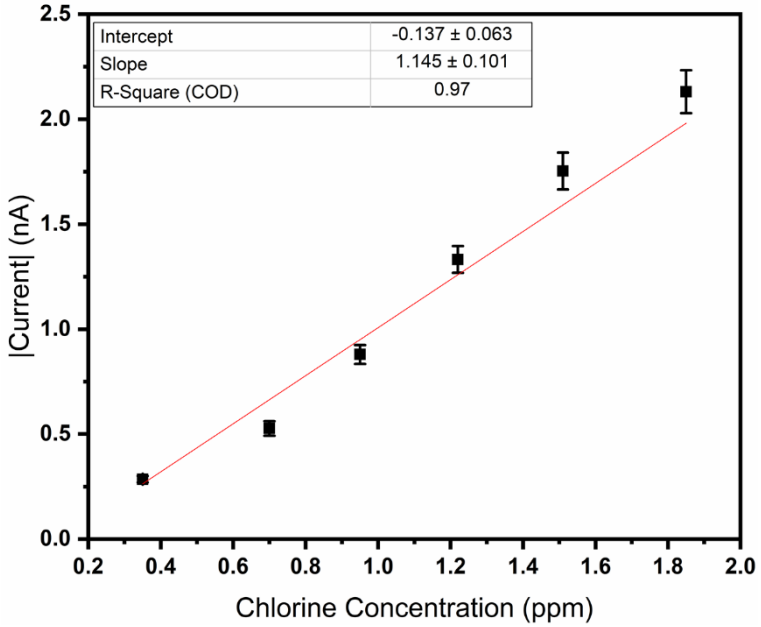

Figure 3-19 Calibration plot for LSVs in ADW with the protonator biased at 1.65 V. Error calculated from standard deviation of multiple scans (n=3).

3.3.6 Detection of Free-Chlorine in Tap Water Samples:

To confirm the potential of these sensors for water distribution applications, measurements of residual free-chlorine were undertaken in tap water samples. For this work, the protonator was again biased at 1.65 V. The sensing electrodes were biased at

1.2 V, to generate the gold oxide and the potential of the gold oxide reduction peak observed by scanning cathodically used to confirm pH ~3.0 of the solution in the region of the sensing electrode. A standard addition approach was used to determine the unknown concentration of residual chlorine in tap water. An initial measurement was performed in tap water, i.e., an 'unknown' sample. Subsequent scans were then performed in tap water samples that had been spiked with residual chlorine stock solution to form 'unknown' + 0.5, 1.5, 2.5, 3.5 and 4.5 ppm of chlorine. The resulting scans are shown in Figure 3-20(A). It was found that while pH 3 conditions were achieved in tap water, the HOCl reduction occurred at a less positive potential and did not reach a steady state. This was thought to be a result of some unknown component of tap water slowing the kinetics of the HOCl formation, which needs to be investigated further. However, Figure 3-20(B) shows that linearity was maintained and allowed for quantification of the unknown. The concentration of the base tap water sample was determined by extrapolating the linear fit to the x-axis, which has been highlighted in Figure 3-20(B) The value recorded by this method was 0.33 ppm. The actual concentration was determined using the commercial DPD method, which yielded a concentration of 0.31 ppm. In this regard, both methods provided the same result within experimental error thereby confirming the efficacy of the in-situ pH control method.

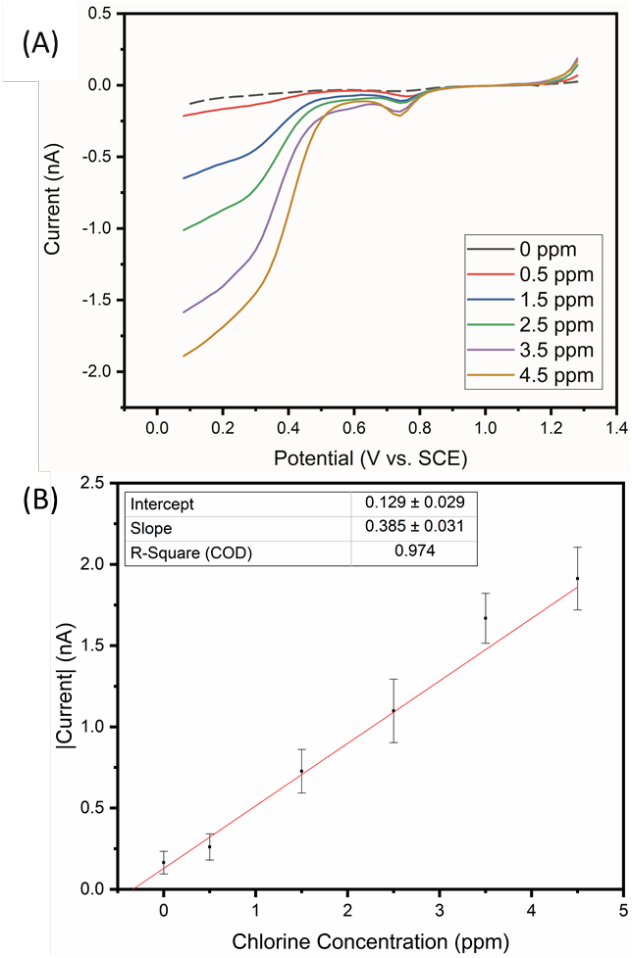

Figure 3-20 LSVs at gold IDEs from 1.2 V to 0 V at a sweep rate of 50 mV/s. (A) Scans of various concentrations of chlorine in tap water. The dashed line represents the unknown sample. (B) Calibration plot for the scans shown in background subtracted (A). Error calculated from standard deviation of multiple scans (n=3).

3.4 Conclusions

We have shown that electrochemical pH control is an effective approach to detecting residual chlorine concentration in real water samples. Finite element simulations and subsequent electrochemical characterization, using gold interdigitated microelectrode arrays in buffered samples, demonstrated the feasibility of this technique. By designing the sensing electrode to be close to the protonator electrode, the local pH at the sensing electrode can be tailored to pH 3 thereby converting all free-chlorine into the hypochlorous acid species. Effective chlorine detection was shown in buffered artificial drinking water samples using in-situ pH control and an enhanced signal response, compared to measurements without pH control, was demonstrated. Finally, tap water samples were measured using the in-situ pH control method and the results correlated excellently (within experimental error) with a commercial instrument. This work shows the possibility of an electrochemical approach to reagent-free, in-line sensing of chlorine required for water distribution networks.

3.5 References

1. C. M. Shen, X. G. Zhang and H. L. Li, *Materials Science and Engineering: B*, 2001, **84**, 265-270.
2. H. Okamoto and T. Kotaka, *Polymer*, 1998, **39**, 4349-4358.
3. P. Bumroongsakulsawat and G. H. Kelsall, *Electrochimica Acta*, 2014, **141**, 216-225.
4. Chlorine Test Kits https://www.hach.com/chlorinetestkits, (accessed 15/02/2019, 2019).
5. J. Wang, *Chemical Reviews*, 2008, **108**, 814-825.
6. M. Szili, I. Kasik, V. Matejec, G. Nagy and B. Kovacs, *Sensors and Actuators B: Chemical*, 2014, **192**, 92-98.
7. Y. Dong, G. Li, N. Zhou, R. Wang, Y. Chi and G. Chen, *Anal. Chem.*, 2012, **84**, 8378-8382.
8. T. Lu, L. Zhang, M. Sun, D. Deng, Y. Su and Y. Lv, *Anal. Chem.*, 2016, **88**, 3413-3420.
9. AWWA, *Water Chlorination and Chloramination Practices and Principles*, American Water Works Association, 2nd Edition edn., 2011.
10. R. D. Morris, A.-M. Audet, I. F. Angelillo, T. C. Chalmers and F. Mosteller, *American Journal of Public Health*, 1992, **82**, 955-963.
11. B. Nemery, P. Hoet and D. Nowak, *European Respiratory Journal*, 2002.
12. R. L. Jolley, H. Gorchev and D. Hamilton Jr, *Water chlorination: environmental impact and health effects. Volume 2*, Ann Arbor Science Publishers, Inc., Ann Arbor, MI, 1978.
13. WHO, Monochlorine in Drinking Water, https://www.who.int/water_sanitation_health/water-quality/guidelines/chemicals/chloramine-background.pdf, (accessed 26/04/2020).
14. WHO, *pH in Drinking Water*, 2007.
15. F. Arslan, in *Nobel Metals*, IntechOpen, 2012, DOI: 10.5772/32641.
16. M. Deborde and U. von Gunten, *Water Research*, 2008, **42**, 13-51.
17. D. L. Harp, *Current Technology of Chlorine Analysis for Water and Wastewater*, U.S.A., 2002.
18. K. Singh and S. K. Mehta, *Analyst*, 2016, **141**, 2487-2492.
19. V. V. Apyari, M. O. Gorbunova, A. V. Shevchenko, A. A. Furletov, P. A. Volkov, A. V. Garshev, S. G. Dmitrienko and Y. A. Zolotov, *Talanta*, 2018, **176**, 406-411.
20. L. Lu, J. Zhang and X. Yang, *Sensors and Actuators B: Chemical*, 2013, **184**, 189-195.
21. S. Sharma, A. El-Laboudi, M. Reddy, N. Jugnee, S. Sivasubramaniyam, M. El Sharkawy, P. Georgiou, D. Johnston, N. Oliver and A. E. G. Cass, *Analytical Methods*, 2018, **10**, 2088-2095.

22. C. Barrett, K. Dawson, C. O'Mahony and A. O'Riordan, *ECS Journal of Solid State Science and Technology*, 2015, **4**, S3053-S3058.

23. I. Seymour, B. O'Sullivan, P. Lovera, J. F. Rohan and A. O'Riordan, presented in part at the 2019 IEEE SENSORS, 27-30 Oct. 2019, 2019.

24. D. R. Kumar, S. Kesavan, T. T. Nguyen, J. Hwang, C. Lamiel and J.-J. Shim, *Sensors and Actuators B: Chemical*, 2017, **240**, 818-828.

25. M. Murata, T. A. Ivandini, M. Shibata, S. Nomura, A. Fujishima and Y. Einaga, *Journal of Electroanalytical Chemistry*, 2008, **612**, 29-36.

26. F. Kodera, M. Umeda and A. Yamada, *Japanese Journal of Applied Physics*, 2005, **44**, L718-L719.

27. F. Kodera, S.-y. Kishioka, M. Umeda and A. Yamada, *Japanese Journal of Applied Physics*, 2004, **43**, L913-L914.

28. M. Jović, F. Cortés-Salazar, A. Lesch, V. Amstutz, H. Bi and H. H. Girault, *Journal of Electroanalytical Chemistry*, 2015, **756**, 171-178.

29. J. Muñoz, F. Céspedes and M. Baeza, *Microchemical Journal*, 2015, **122**, 189-196.

30. S. Thiagarajan, Z.-Y. Wu and S.-M. Chen, *Journal of Electroanalytical Chemistry*, 2011, **661**, 322-328.

31. O. Ordeig, R. Mas, J. Gonzalo, F. J. Del Campo, F. J. Muñoz and C. de Haro, *Electroanalysis*, 2005, **17**, 1641-1648.

32. T. Soundappan, K. Haddad, S. Kavadiya, R. Raliya and P. Biswas, *Applied Nanoscience*, 2017, **7**, 645-653.

33. R. Olivé-Monllau, J. Orozco, C. Fernández-Sánchez, M. Baeza, J. Bartrolí, C. Jimenez-Jorquera and F. Céspedes, *Talanta*, 2009, **77**, 1739-1744.

34. P. Salazar, M. Martín, J. L. González-Mora and A. R. González-Elipe, *Talanta*, 2016, **146**, 410-416.

35. M. Eryilmaz and I. M. Palabiyik, *Tropical Journal of Pharmaceutical Research*, 2013, **12**, 123-126.

36. G. Lindbergh and D. Simonsson, *Journal of The Electrochemical Society*, 1990, **137**, 3094-3099.

37. T. L. Read, E. Bitziou, M. B. Joseph and J. V. Macpherson, *Anal. Chem.*, 2014, **86**, 367-371.

38. J. Rossmeisl, A. Logadottir and J. K. Nørskov, *Chemical Physics*, 2005, **319**, 178-184.

39. S. H. Lee and J. C. Rasaiah, *The Journal of Chemical Physics*, 2011, **135**, 124505.

40. K. Dawson, A. Wahl, R. Murphy and A. O'Riordan, *The Journal of Physical Chemistry C*, 2012, **116**, 14665-14673.

41. K. Dawson, M. Baudequin, N. Sassiat, A. J. Quinn and A. O'Riordan, *Electrochimica Acta*, 2013, **101**, 169-176.

42. K. Dawson, A. Wahl, S. Barry, C. Barrett, N. Sassiat, A. J. Quinn and A. O'Riordan, *Electrochimica Acta*, 2014, **115**, 239-246.

43. L. Burke and P. Nugent, *Gold Bull*, 1997, **30**, 43-53.

44. L. C. Nagle and J. F. Rohan, *Electrochemical and Solid-State Letters*, 2005, **8**, C77-C80.

45. L. D. Burke, M. E. Lyons and D. P. Whelan, *Journal of Electroanalytical Chemistry and Interfacial Electrochemistry*, 1982, **139**, 131-142.

Chapter 4 Removal of Oxygen Interference in the Electrochemical Detection of Monochloramine using in-situ pH Control at Interdigitated Microelectrodes

4.1 Introduction

Chloramines are a family of compounds that are analogous to ammonia with chlorine taking the place of one, or more hydrogens. The simplest of these is monochloramine (MCA) which has the formula NH_2Cl. Dichloramine (DCA) forms when a solution of MCA is acidified, or when the chlorine content of a solution containing MCA is increased. Similarly trichloramine (TCA), sometimes called nitrogen trichloride, forms when a solution of DCA is further acidified or has the chlorine content increased significantly.[1] Figure 4-1 shows the structure of each chloramine compound and the conditions required to form the more complex species.

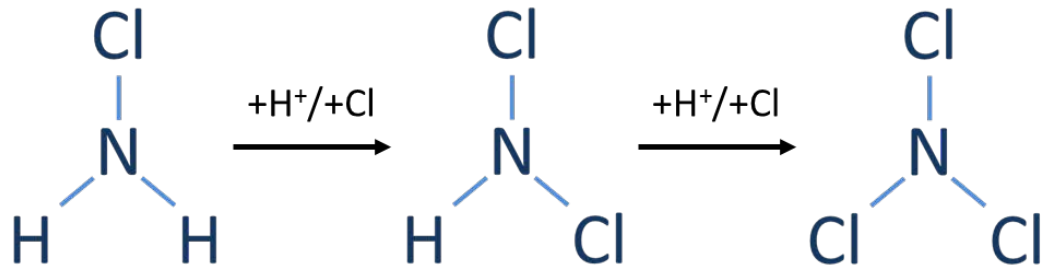

Figure 4-1 Monochloramine (left), dichloramine (centre) and trichloramine (right). Increasing the chlorine concentration or making the solution more acidic favours the production of di and trichloramines.

MCA is formed by reacting hypochlorous acid (HOCl) with ammonia (NH_3) in aqueous solution. This is a two-step reaction where ammonium hypochlorite is initially formed and subsequently rapidly breaks down according to the following the equations:[1, 2]

$$HOCl + NH_3 \rightarrow NH_4OCl \qquad \text{Equation 4.1}$$

$$NH_4OCl \rightarrow NH_2Cl + H_2O \qquad \text{Equation 4.2}$$

The formation of DCA and TCA proceed by reaction of the previous chloramine, thus DCA cannot be formed unless MCA has been produced and TCA cannot be formed unless DCA has been produced. The main factor that influences the formation of the subsequent

chloramines is the chlorine to nitrogen ratio (Cl_2:N). A Cl_2:N of approximately 3:1 will ensure that production of MCA occurs, however the optimum value is 5:1.[3, 4] Above this value the following reactions dominate[5]:

$$HOCl + NH_2Cl \rightarrow NHCl_2 + H_2O \qquad \text{Equation 4.3}$$

$$HOCl + NHCl_2 \rightarrow NCl_3 + H_2O \qquad \text{Equation 4.4}$$

Further addition of chlorine after the formation of TCA results in the decomposition to nitrogen oxides and nitrogen gas and an excess of chlorine. It is also possible to cause the formation of DCA and TCA at Cl_2:N ratios below 5:1 by changing the pH. To ensure a maximum of MCA pH values above 6.5 are required. As the pH values become more acidic, the concentration of MCA in solution decreases and DCA concentration increases until it predominates. Similarly, further acidification leads to TCA becoming the dominant species. The ratio of these has been illustrated by Wolfe et al. and is shown in Figure 4-2.[3]

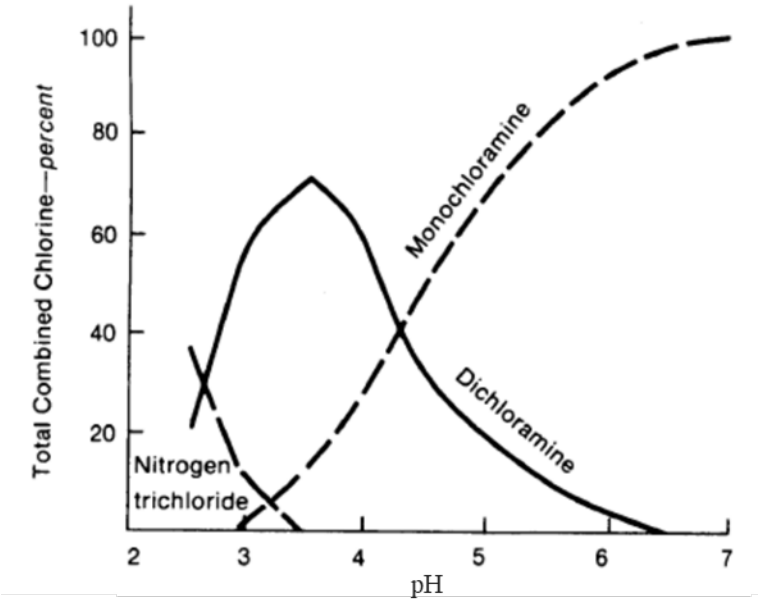

Figure 4-2 Ratios of MCA, DCA and TCA as a function of pH (Taken from Reference 3)

In each case, the chloramine species reacts with itself to produce the more chlorinated chloramine and ammonium, as shown in the following equations:[6]

$$2NH_2Cl + H^+ \rightarrow NHCl_2 + NH_4^+ \qquad \text{Equation 4.5}$$

$$3NHCl_2 + H^+ \rightarrow 2NCl_3 + NH_4^+ \qquad \text{Equation 4.6}$$

It is important to note that three moles of MCA are required to produce one mole of TCA when using pH to convert the chloramine species. The significance of this will be discussed later.

The reason for the interest in MCA is its prevalence in water systems. Chloramines can be formed as a by-product of the water disinfection process. Treatment with HOCl is the most common form of disinfection. However as shown in Equation 4.1, the HOCl reacts with amines present in water systems, producing chloramines. The presence of these chloramines can result in the decrease of residual chlorine, which then results in inadequate disinfection of water. The ability to quantify the chloramines formed from initial disinfection, will determine the quantity of chlorine to be added at the start of the treatment process to counteract the chloramine formation in the system. However some water system utility companies, particularly in North America are switching to MCA as their disinfectant source.[7] This can lead to confusion as there are vastly different conditions needed to optimise disinfection in both systems. This is highlighted in Figure 4-3, which shows how chlorine is used in a water system that contains 1 mg/L ammonia.[4] The key difference is that a system using chlorine is not sufficiently disinfecting until a minimum dose of 9 mg/L chlorine is achieved. However, for a chloraminated system, it needs to be maintained at 5 mg/L or the MCA is lost. It should be noted that while TCA can be produced after the breakpoint, it is typically very unstable and breaks down to free

chlorine. Also, after the breakpoint MCA and DCA may still be present in trace amounts and are considered combined chlorine.

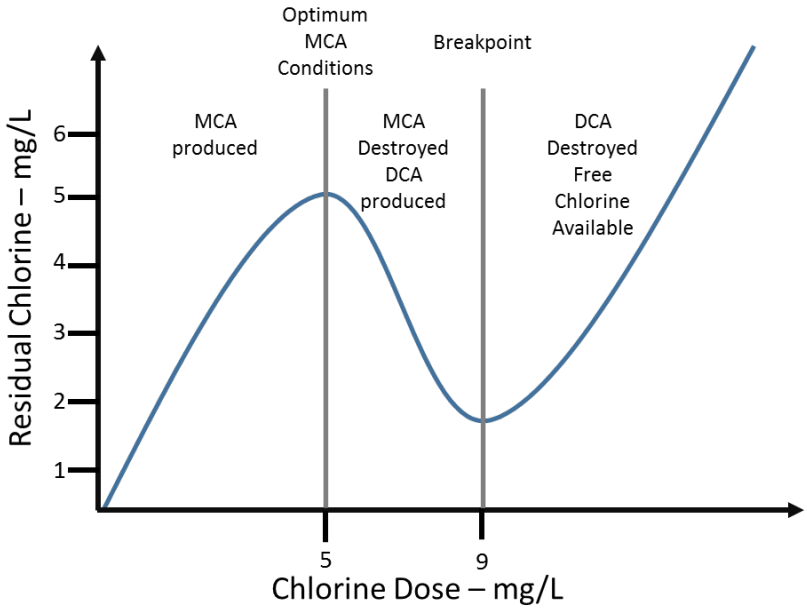

Figure 4-3 Chlorination/Chloramination breakpoint curve taken from reference.[4] 1 mg/L ammonia is present in solution during chlorine dosing. Optimum MCA disinfection occurs when 5:1 Cl_2:N ratio is achieved. For chlorination, a minimum of 9:1 Cl_2:N is required before adequate disinfection can occur.

While many factors need to be considered when disinfecting with MCA, there are benefits to its use in water systems. It has been shown that MCA hydrolyses at a much slower rate than hypochlorous acid, and is far more stable in UV light.[8, 9] This means that the chlorine residual is more persistent and thus a more widespread and longer lasting disinfection is achieved. It has also been found to better penetrate biofilms, resulting in superior biocidal activity.[10] Perhaps a more significant advantage is that MCA results in less toxic by-products. Water that has been treated with hypochlorous acid can result in the formation of trihalomethanes (THM).[11, 12] These THMs have been shown to have mutagenic, cytotoxic and genotoxic effects, so minimization of their prevalence is desirable[13]. MCA treated water has been shown to have significantly lower concentrations of resulting THMs.[14] Treatment with MCA does have its disadvantages, most typically the formation

of DCA and TCA. Both are less powerful disinfectants than MCA and can lead to unpleasant tastes and smells in the water system. More significantly, the subsequent breakdown of TCA can lead to the formation of nitrates and nitrites. High concentrations of these can lead to nitrification of the water system which is hazardous to aquatic life.[15-17] Low concentrations result in poor disinfection, but they can also be an indicator of high concentrations of organic matter in the system.[18] Because of this, MCA levels need to be monitored in water systems. The typical concentration expected in a chloraminated system ranges from 0.6 mg/L to 5 mg/L,[19] and requires routine analysis to ensure it stays within this range.

Many methods exist to determine MCA concentrations, such as; spectrophotometry, chemical titrations, gas chromatography, liquid chromatography and mass spectrometry.[6, 20, 21] The DPD method described for chlorine in chapter 3 is also applicable, as MCA is a combined chlorine species. The DPD method permits measurement of total chlorine and free chlorine, therefore it can be assumed that the MCA concentration is the difference between the two figures. A simple commercially available alternative to this is to use a test kit specific for MCA, such as the one sold by the Hach company.[22] This is a colorimetric test kit wherein a reagent containing phenate is added to the MCA solution and reacts to form an indophenol, which is green in colour.[23] The intensity of the green colour correlates with the concentration of MCA. The issue with these methods, however, is that a skilled operator is required to do the analysis, and additional reagents are needed that are environmentally undesirable. They also require sampling of the water system by an operator to remove an adequate volume for measurement. This increases the time and the cost associated with carrying out a measurement. Quantification by use of an electrochemical method would simplify this analysis as no additional reagents are

required, and the device can be deployed and accessed remotely. To this end, a great deal of research has gone into developing electrodes suitable for MCA quantification.

The electrochemical analysis of MCA is undertaken by measuring the current associated with the reduction of MCA to ammonium and chloride. This is a one-step, two electron reduction as shown in Equation 4.7: [20, 24]

$$NH_2Cl + 2H^+ + 2e^- \leftrightarrow Cl^- + NH_4^+ \qquad \text{Equation 4.7}$$

This is a relatively simple reduction reaction and can be done on a variety of electrode materials such as gold, platinum and even carbon. One of the major issues with electrochemical quantification of MCA is that dissolved oxygen in the solution is an interferent.[20, 25, 26] Dissolved oxygen undergoes reduction in the same electrochemical window that is used for the analysis of MCA. However, there is little information indicating cross reactivity in the literature. For a solution containing dissolved oxygen and MCA, the total current is the sum of the currents associated with each reduction thus, if the concentration, and associated current of oxygen is known, then MCA can be easily quantified. In real water samples oxygen concentrations may not always be known, so those measurements need to be performed simultaneously. As MCA will interfere additional methods are required to deconvolute the signal. This requires additional equipment and an operator to go to the source, which defeats the purpose of employing an electrochemical method. Subsequently a technique that can measure MCA free of dissolved oxygen interference is required.

In this chapter, a novel method for interferent-free MCA quantification is presented. This was carried out by using and subsequently refining the pH control method discussed in Chapter 3.[27] Given that MCA can be converted to DCA and TCA by making the solution

more acidic, and that the electro-reduction reactions for both of these species have been shown to occur at more positive potentials than MCA, described by the reactions:[24]

$$NHCl_2 + 3H^+ + 4e^- \rightarrow NH_4^+ + 2Cl^- \qquad \text{Equation 4.8}$$

$$NCl_3 + 4H^+ + 6e^- \rightarrow NH_4^+ + 3Cl^- \qquad \text{Equation 4.9}$$

which are outside the oxygen reduction potential window and thus remove it as an interferent. Therefore, pH control can again solve this detection issue although this is not as straightforward as converting hypochlorite to hypochlorous acid. That reaction involved the protonation of hypochlorite, which is a fast reaction, whereby the limiting step was the diffusion of H^+ ions to modify the pH conditions. In the case of MCA detection, the formation of DCA is required. It has been determined that the conversion of MCA to DCA occurs via a protonated MCA intermediate as follows:[28, 29]

$$NH_2Cl + H^+ \leftrightarrow NH_3Cl^+ \qquad \text{Equation 4.10}$$

$$NH_3Cl^+ + NH_2Cl \leftrightarrow NHCl_2 + NH_4^+ \qquad \text{Equation 4.11}$$

The first reaction occurs rapidly while the second reaction tends to progress slower. A reaction rate of between 230 and 270 $M^{-1}.s^{-1}$ for this step has been determined.[3, 30] However, these figures apply to DCA formation in neutral to basic pH values. Acidic conditions catalyse this reaction and permit a faster reaction rate[31] but the determination of this rate is problematic due to the short lifetime of DCA. As a result, more consideration needs to be given to the experimental parameters. The reaction rate may be increased by the constant supply of protons. DCA formation is typically associated with an increase in pH through the proton consumption and ammonium ion production steps. With pH control protons are continuously supplied and the required pH value is maintained throughout the experiment driving the reaction to produce more DCA.

It is desirable that all the MCA is converted to DCA to ensure accurate concentration estimates. From Figure 4-2, a pH value of 3 is required to ensure that the solution is

entirely DCA. The pH window wherein a solution consists of at least 95% DCA is pH 2.3-4.2.[6] The optimum pH value at the median of this range ≈ pH 3.2 which eliminate the interference of the other chloramines. TCA is potentially a more significant interferent being more likely than MCA to be present in acidic conditions. However, the rate of formation of TCA is almost 100 times slower than DCA (3.4 $M^{-1}.s^{-1}$) so it is not expected that a significant concentration will be formed[3]. The reduction of TCA occurs at potentials more positive than DCA reduction, and thus outside of the oxygen reduction window. Therefore, if a detectable concentration is produced, it too can be quantified and related to the MCA concentration of the water system.

This chapter describes the optimisation of parameters and refinement of materials for the amperometric detection of MCA facilitated by pH control. The elimination of oxygen as an interferent is shown, and the influence of other common interferents anticipated in water is also investigated. The method was finally applied to water samples of varying buffering capacities and conductivities to investigate its effectiveness under non-ideal conditions.

4.2 Experimental Materials and Methods

4.2.1 Electrode Fabrication and Characterisation

Electrodes were fabricated, cleaned, and characterised as described in chapter 3.

4.2.2 Preparation of MCA Stock Solutions

Stock solutions of 200 ppm MCA were made and diluted with the relevant matrix to make MCA working samples. The MCA stock solution was prepared by slowly mixing a 1:1 ratio of sodium hypochlorite (NaOCl, 5% Milton Sterilising Fluid) and ammonium chloride (NH_4Cl, Sigma Aldrich >99%). The NaOCl was prepared by diluting a 5% bleach solution in DI water and adjusting to pH 8.3 with 1M NaOH. The NH_4Cl was dissolved in DI water and adjusted to pH 8.3 using 1 M HCl. The slow mixing ensures that NH_3 is in excess, which promotes the formation of MCA. The solution was then let sit for 5 minutes to ensure that the reaction was complete.

4.2.3 Measurement of MCA by the Colorimetric Test

Colorimetric measurement of MCA concentration was performed on the stock solution, and subsequent diluted working solutions to determine the concentration. This was undertaken as MCA can degrade over time, but more significantly the hypochlorous acid content of bleach also can drop over time. The stock therefore may not always be 200 ppm depending on when the bleach was purchased. A commercial test kit was employed to determine the concentrations of the MCA solutions. The Hach colorimeter and indophenol method was used for this quantification. 10 mls of the MCA stock solution was added to a clean sample vial. This was put into the colorimeter and a blank

measurement was taken. Monochlor F reagent was then added to the sample vial. This reagent was purchased as a pre-weighed sachet of powder, the entire contents of which were added to the sample. As the reagent reacted with the sample, the solution gradually became green with a maximum colouration achieved after a 5-minute reaction time. This was then put back into the colorimeter and a measurement was taken. This method is only sensitive to concentrations between 0.5 ppm and 5 ppm MCA, so dilutions were required to determine the concentration of stock solutions.

4.2.4 Initial Measurements on Microdisc Arrays

Initial electrochemical analysis of high concentration MCA solutions was carried out using a CHI potentiostat (660C) and CHI Faraday cage. A three electrode cell set up was used with a gold microdisc array working electrode, platinum wire counter electrode and a saturated calomel electrode (SCE) reference. The electrodes were scanned using CV from 0.4 V to -0.8 V at 50 mV/s for 3 cycles, the data shown being from the third cycle. Working samples with concentrations of between 20 ppm and 200 ppm MCA were made by diluting the stock solution with the appropriate volume of DI water. A sample of 1.75 mM hypochlorous acid was also scanned to compare its behaviour to MCA under the same conditions. Scans were also performed on samples of MCA with high and low concentrations of oxygen to determine its influence on the analysis. High concentration oxygen solutions were MCA sample solutions used as prepared. Other samples were purged with nitrogen gas for 20 minutes prior to any electrochemical measurement to minimise the effect of oxygen.

4.2.5 Electrochemical Analysis of Acidified MCA Solutions

Solutions of MCA in DI water were acidified to pH 3 to determine the electrochemical behaviour of DCA on the IDEs. Sulphuric Acid (0.1 M H_2SO_4) was used to reduce the solution pH to the required value. The pH of each solution was confirmed with a pH meter (Hach). Electrochemical analysis of the acidified samples was performed using an Autolab potentiostat (MUX 101 with BA module) in a Faraday cage. The working electrode used was an IDE array with 1 µm wide electrodes separated by 2 µm gaps. The counter was an on-chip platinum electrode and the reference was a SCE. CVs were performed from 1.2 V to 0.2 V at 50 mV/s in triplicate, with the data shown being from the third scan. Scans were also performed at intermediate pH values to determine the pH dependence of DCA formation.

4.2.6 pH Control in MCA Solutions at µIDE Arrays

Electrochemical analysis of MCA solutions via pH control was carried out using an Autolab bipotentiostat in a Faraday cage. The same electrochemical parameters were used as in section 4.2.5, initially. The starting potential was reduced to 0.95 V for later work. The protonator electrode was held at 1.65 V or 1.75 V depending on the matrix conditions. Working samples were made by diluting the MCA stock solution with DI water or ADW (described in chapter 3). Typical concentrations of 0.5 to 5 ppm MCA were used, with 10 ppm samples used to study the upper detection limit.

4.2.7 Platinum Plating on the Protonator Electrode

Platinum plating was carried out on one comb of the IDE array to enhance protonator performance. This was achieved by biasing the comb at -0.5 V vs. SCE in a commercial Platinum dihydrogen dinitrosulphatoplatinum (DNS) bath (Johnson Matthey) wherein the

platinum is in the 2+ oxidation state. Plating times from 6 to 12 seconds were investigated but ultimately 8 second depositions were used.

4.2.8 Effects of Interferents and Matrix Composition on MCA Detection

High alkalinity solutions of MCA were prepared by the addition of sodium bicarbonate (0.84g/500ml ADW stock). High conductivity samples were made by the addition of 0.1 M sodium sulphate until the desired conductivity was reached. In this case the working solutions were directly adjusted as opposed to the stock solutions. MCA sample solutions were also spiked with 1 ppm each of iron, copper and phosphate (as iron (II) chloride, copper sulphate and sodium phosphate monobasic) to determine their effect on the MCA analysis. The final interferent investigated was free chlorine (as OCl^-/HOCl). This was achieved by diluting the hypochlorous acid stock used in the preparation of MCA solutions, and subsequently using this to spike the MCA working solutions.

4.3 Results and Discussion

4.3.1 MCA Calibration and Effect of Oxygen on Microdisc Arrays

Initial work was carried out using microdisc arrays and high concentrations of MCA. The microdisc arrays had been well characterised from prior work and allowed for the understanding of MCA electrochemistry. The microdisc arrays were gold, 20 µm in diameter and separated by 500 µm gaps. The solutions were purged with nitrogen, to remove oxygen. The samples were made up to be 20, 50, 100, 150 and 200 ppm MCA, however upon measurement with the colorimeter it was found that these concentrations were lower than predicted. It was possible that the HOCl stock used to make these solutions had a lower than expected concentration, as HOCl can degrade in UV light. The measured values of MCA were 18.2, 47.5, 91, 140 and 189 ppm. Figure 4-4 shows CV scans for the range of MCA concentrations. The reduction begins at 0 V and proceeds via an irreversible single step reaction. The calibration shown in Figure 4-5 uses the measured concentrations of MCA rather than the predicted values and shows a good linearity (R^2 = 0.995) for MCA response. As all the other conditions were kept constant, this shows that MCA concentration is directly proportional to the measured current. The predicted current can be calculated using the equation for the limiting current at a microdisc:[32]

$$i_{lim} = (4nFDr)C \qquad \text{Equation 4.12}$$

Where n is the number of electrons, F is Faradays constant, D is the diffusion coefficient C is the bulk concentration and r is the radius of the microdisc. The linearity was expected as the limiting current is directly proportional to the concentration. The equation of the line can therefore be used to describe the relationship between current and concentration:

$$y = mx + c \qquad \text{Equation 4.13}$$

In this case, y is the absolute measured current and x is the MCA concentration. The slope gives us the sensitivity of the sensor, which in this case was 0.01 µA/ppm. The slope accounts for the bracketed portion of Equation 4.12, therefore the diffusion coefficient can be estimated by using the equation:

$$D = \frac{m}{4nFr} \qquad \text{Equation 4.14}$$

The slope first needed to be converted to SI units, so 0.01 µA/ppm became 0.5148 A/mol.cm^{-3}. This slope accounted for an array of 56 microdiscs, so the equivalent for one microdisc became 0.0092 A/mol.cm^{-3}. Factoring this into Equation 4.14 gives a diffusion coefficient of 1.19x10^{-5} cm^2/s. The recorded intercept (c) gives a measure of the background current in this measurement. It was known that oxygen would interfere with measurement of MCA, therefore a relatively large background current was expected, as these tests were undertaken in solutions saturated with oxygen. Interestingly, the intercept value (0.558 µA) corresponds with the change in current observed for a MCA CV before and after purging (~0.6 µA) as shown in Figure 4-7.

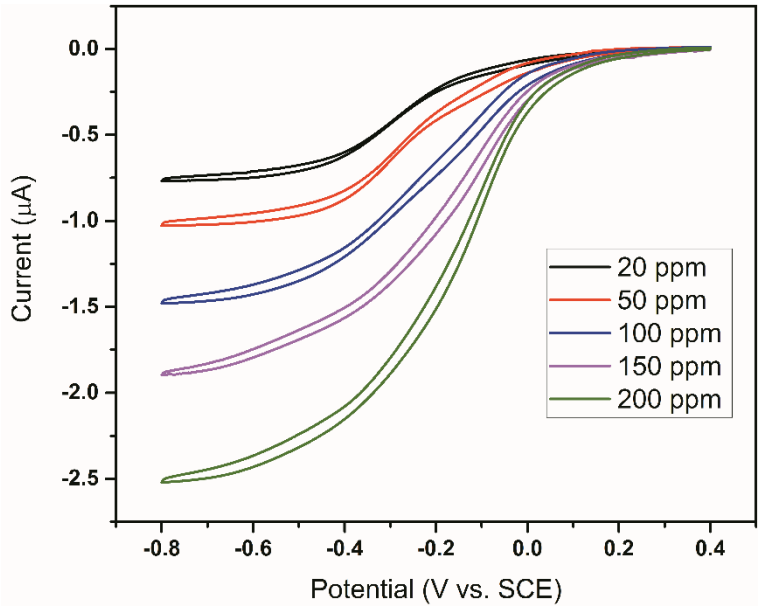

Figure 4-4 Various MCA concentrations scanned on a microdisc array. CVs were performed from 0.4 V to -0.8 V at 50 mV/s.

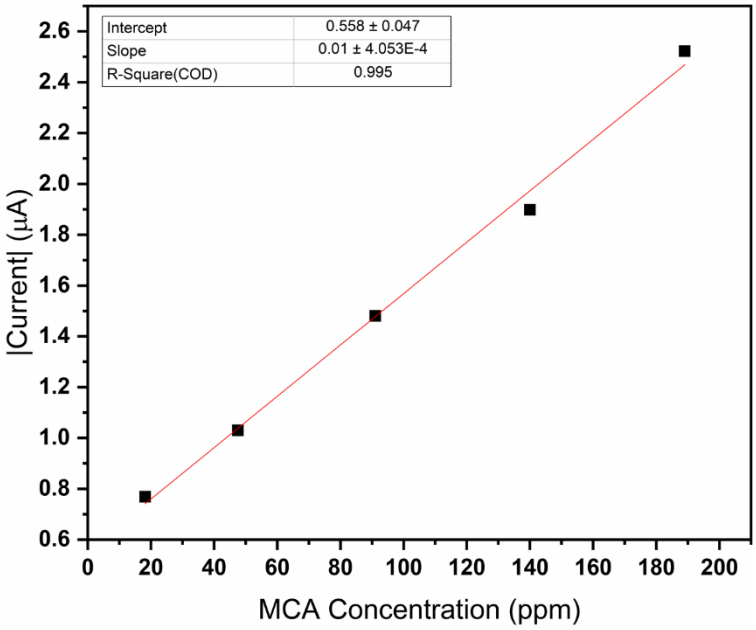

Figure 4-5 Calibration of MCA at the microdisc array.

To confirm that MCA is the species contributing to the amperometric response, CVs were performed in solutions of free chlorine (as hypochlorite). This was also used to determine if there was any interference possible from solutions where free chlorine may be present. It was found that the onset of reduction for free chlorine occurs at more positive potentials than MCA as shown in Figure 4-6. While the plateau currents occur around the same potentials, the earlier onset is enough for the differentiation of the two species. However, if a mixture of the two were present, it is more likely that additional MCA (or perhaps DCA) would be formed rather than a mixture of the two.

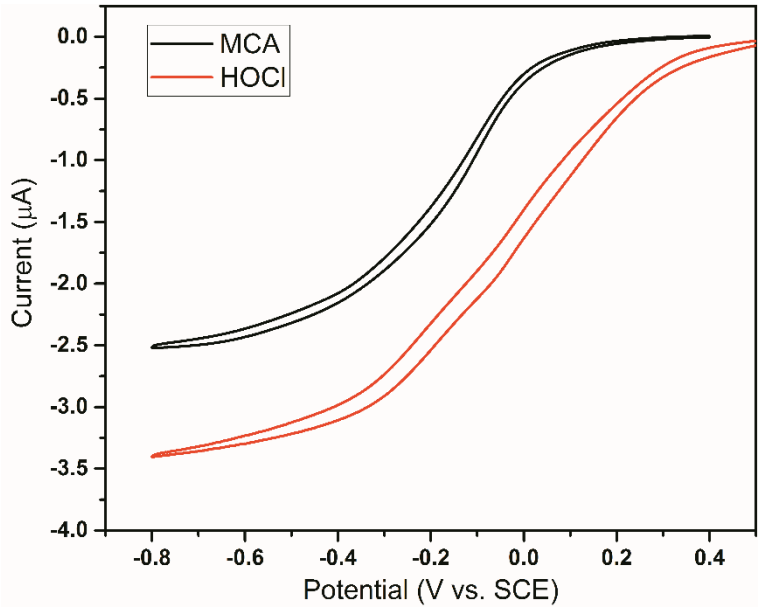

Figure 4-6 Comparison of 200 ppm concentrations of MCA (black) and the hypochlorous acid stock (red). The hypochlorous acid was scanned from 0.6 V to -0.8 V at 50 mV/s as the onset of reduction was earlier than for MCA.

It is clear that MCA has activity in the same window as oxygen reduction. The onset of reduction for both reactions is at approximate the same potential (≈ 0.1 V). The significance of oxygen interference is shown in Figure 4-7, where high (200 ppm MCA) and low (50 ppm MCA) concentration samples are tested with and without oxygen present. The saturated samples have approximately 9 ppm O_2 (0.3 mM) and the purged samples have below 1 ppm (0.033 mM). A decrease in current response of approximately 0.6 µA is attributable to the oxygen reduction. This is significant as it accounts for 23% of the signal seen in the 200 ppm sample and almost 50% of the 20 ppm sample. Considering that the desired MCA detection range is 0.5 to 5 ppm, an oxygen signal will effectively mask any reliable MCA reduction data measured in this window. Similarly, if any discernible MCA signal is measurable, the variability of oxygen concentration will deleteriously impact the ability to accurately calibrate the detection method. It can also be seen in the lower MCA concentration samples that a current shoulder is evident at approximately -0.2 V. This is most likely the production of peroxide as part of the two

step oxygen reduction mechanism (see chapter 5). The production of peroxide further complicates this analysis as it has been known to interact with chloramines, and as such can cause unwanted side reactions.

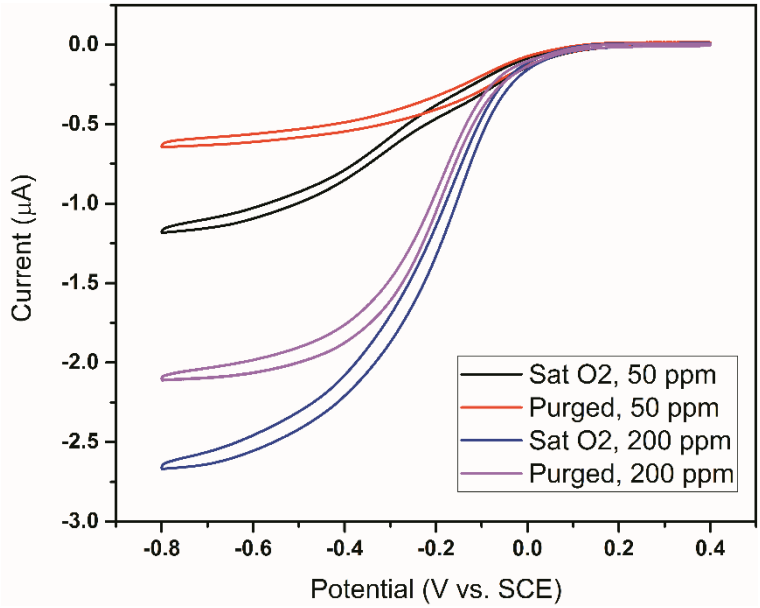

Figure 4-7 Comparison of MCA scans at microdisc arrays in solutions of high and low oxygen content.

4.3.2 Acidified MCA Samples on µIDE Arrays – DCA Detection

MCA samples were acidified and allowed to convert to DCA by waiting approximately 10 minutes. These samples were tested using one comb of the gold µIDE arrays to determine the electrochemical response of DCA. It was found that the onset of reduction of DCA occurred at approximately 0.6 V, which is 500 mV more positive than the onset of oxygen reduction. A plateau was reached at 0.3 V and was stable on multiple cycles. The results of these LSVs are shown in Figure 4-8. Although not necessary for DCA, the scans started at 1.2 V in each case. This starting potential was chosen to generate a gold oxide that could subsequently be reduced, and therefore give an indication of pH. In this case, the reduction peak was seen at 0.8 V indicative of a pH 3 solution. This was not needed for the chemically pH adjusted samples but gave a direct comparison to the electrochemically pH adjusted samples that followed. A calibration plot is shown in

Figure 4-9 which illustrates good linearity (R^2 = 0.99) and a sensitivity to DCA of approximately 0.5 nA/ppm. Again, linearity was expected as the only component of the solution that was changed was MCA concentration, which was previously shown to be directly proportional to the measured current. The equation that is used to predict the current at a band electrode differs from the microdisc, which is:[33]

$$i_{lim} = \frac{nFlC2\pi D}{ln\frac{64Dt}{w^2}} \qquad \text{Equation 4.15}$$

This is a more complex equation which includes the band length (l) and width (w) as well as time (t). It remains however, that the current is directly proportional to the concentration, illustrating the origin of the linearity. Comparison of the sensitivities of MCA detection at the microdisc array and the IDE would indicate that the microdisc array is more sensitive (10 nA/ppm vs. 0.5 nA/ppm), even with removal of oxygen as an interferent. However, the microdisc array had a surface area of 17,593 μm^2, while the IDE had a surface area of 175.5 μm^2. Conversion of the sensitivities to current density showed that the microdisc array had a sensitivity of 0.568 A/m^2/ppm, while the IDE had a sensitivity of 6.411 A/m^2/ppm. The intercept was also significantly lower at 0.094 nA as the interference due to oxygen was eliminated. For the microdisc array, the intercept current accounted for approximately 74% of the current measured for the lowest MCA concentration. The intercept current on the IDE accounted for only 16% of the lowest measured current, highlighting that less interference was observed. All these results are recorded in terms of MCA concentration, as that is how the solutions are measured by the colorimeter. The DCA concentrations should, in theory, be exactly half the MCA concentration (Equation 4.5).

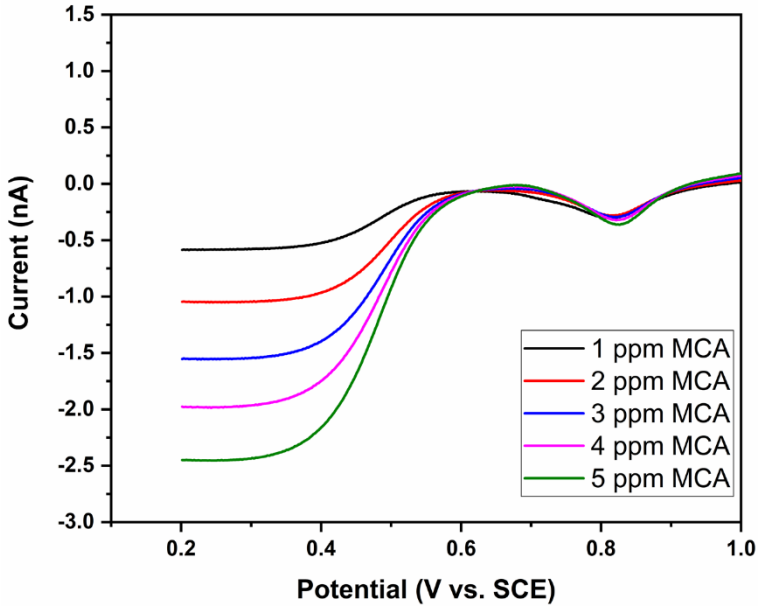

Figure 4-8 LSVs performed in various concentrations of MCA that had been acidified to pH 3. Scans were performed from 1.2 V to 0.2 V at 50 mV/s.

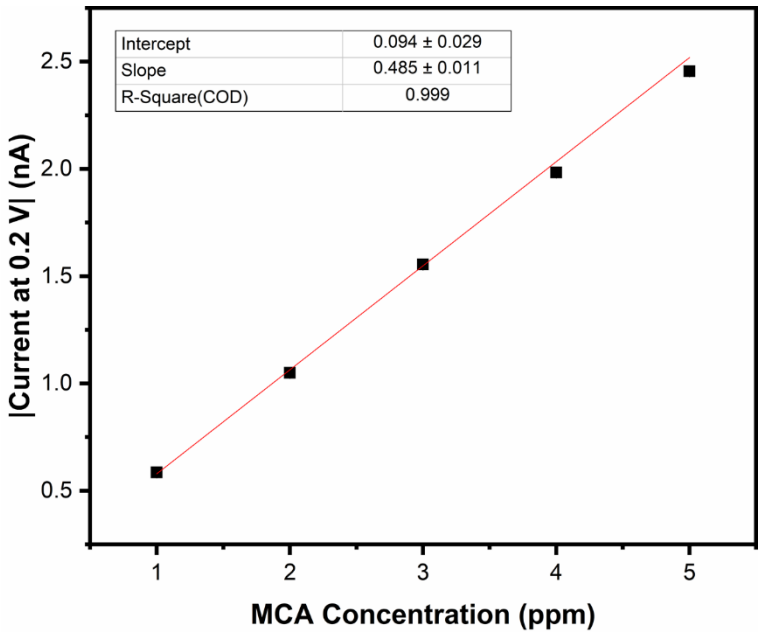

Figure 4-9 Calibration plot for LSVs of MCA at pH 3

4.3.3 Initial pH Control Experiments and Proof of DCA Formation

Based on the parameters established from tests performed at pH 3, equivalent tests were performed in pH 8 solutions. In these solutions, the chloramine should exist 100% as

MCA. It was found that using this potential window (1.2 V to 0.2 V) no activity for MCA was observed. This was expected as at this pH, the solutions exist primarily as MCA, which is not active in this region. The results of these scans, shown in Figure 4-10, do show some interesting activity for the oxide formation and reduction. Oxide formation was expected around 1.1 V based on analysis in blank solutions (see chapter 3). However, the peak at 1.1 V seems to increase with MCA concentration. This was initially thought to be the result of some oxidation of MCA; however, it was determined to be the result of some interaction between chlorine and gold. This also explains why the oxide reduction intensity decreased with increasing MCA. Less oxide can be formed when interactions between gold and chlorine dominate and the reduction reflects this. The shift of the oxide reduction potential is attributed to the slight change in pH of the higher concentration MCA samples. MCA decomposition results in the release of H^+, higher concentrations of MCA results greater production of H^+ when decomposition occurs. This typically does not influence the pH in drinking water, as the presence of ions contributes to some buffering capacity. As these solutions were made in DI water only, therefore no ions were present, there was no buffering capacity and so the effect on pH was more significant.

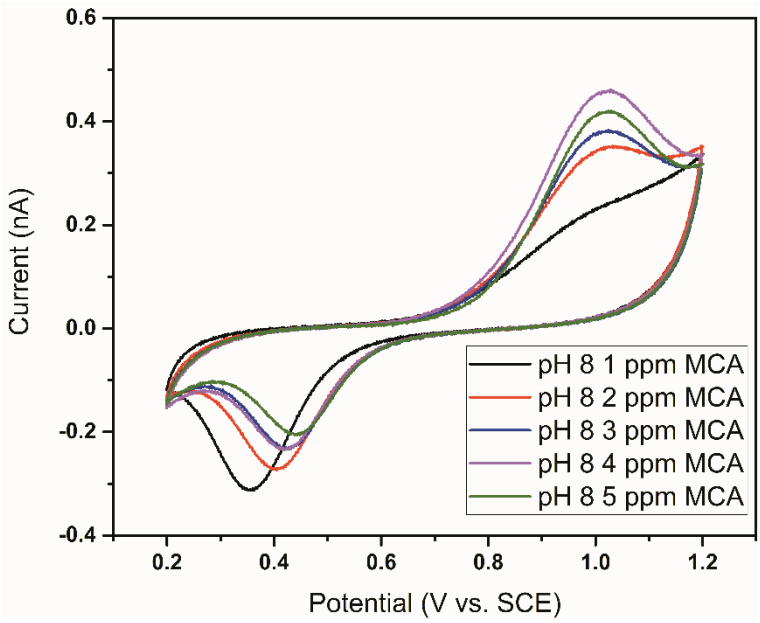

Figure 4-10 CVs of various concentrations of MCA at pH 8. Aside from gold oxide formation and reduction, no event is observed.

The oxide reduction peak potential was again used to determine the local pH of the solution. It was expected that a potential of 0.75 V for the oxide reduction indicated a pH 3 environment. Various protonator potentials were tested, but it was again found that a value of 1.65 V was sufficient to drive the pH down to the required value. These parameters were applied to various sample concentrations of MCA. The results, in Figure 4-11 show that the local MCA was successfully converted to DCA based on the electrochemical activity. The CV data consisted of three consecutive cycles. It was found that the oxide reduction for the first cycle was seen at 0.67 V and the DCA reduction was lower than expected. From the pH 3 solution measurements, 1 ppm MCA was expected to have a reduction current of -0.5 nA, but the measured current was -0.35 nA. This may be due to the timeframe of the experiment being insufficient to generate a pH 3 solution, and not adequately producing DCA. Subsequent scans, however, showed the desired behaviour and overlapped entirely. From this it was determined that a 20 second quiet time before scanning would allow for the system to equilibrate. The calibration shown in Figure 4-12 portrays a good linearity to DCA (R^2 = 0.99) and a sensitivity of

approximately 0.5 nA/ppm, just as for the samples at pH 3. Again, it is important to point out that the concentrations are represented in terms of MCA. It was expected that the resultant currents would be lower, as the timeframe of the experiment would be too slow to allow for sufficient conversion to DCA. However, the sensitivities show that equivalent concentration of DCA is detected in the chemical and electrochemical pH adjustment methods. This indicates that the pH control as well as changing the pH may facilitate the conversion to DCA at a faster rate. A comparison of the scans with and without pH control for a 2 ppm sample is shown in Figure 4-13.

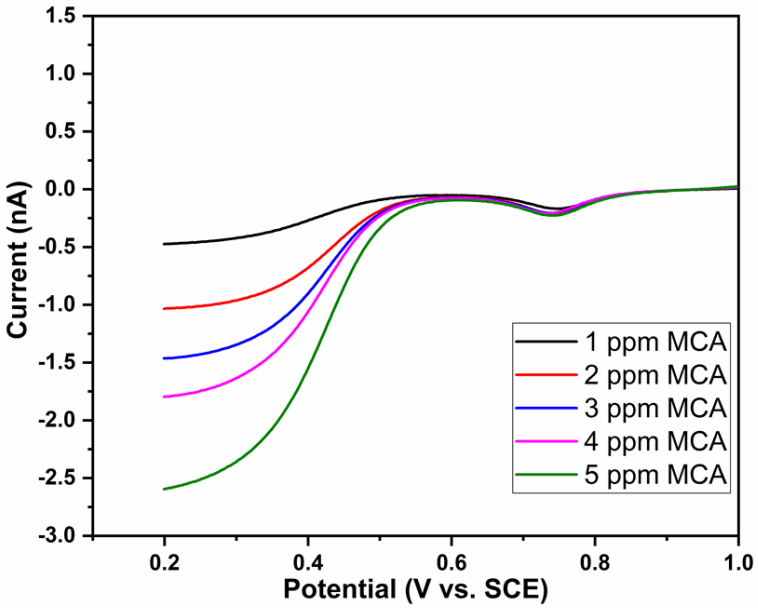

Figure 4-11 Comparison of various concentrations of MCA in DI water with pH control applied. This was achieved by biasing the protonator electrode at 1.65 V while scanning the working electrode from 1.2 V to 0.2 V, at 50 mV/s.

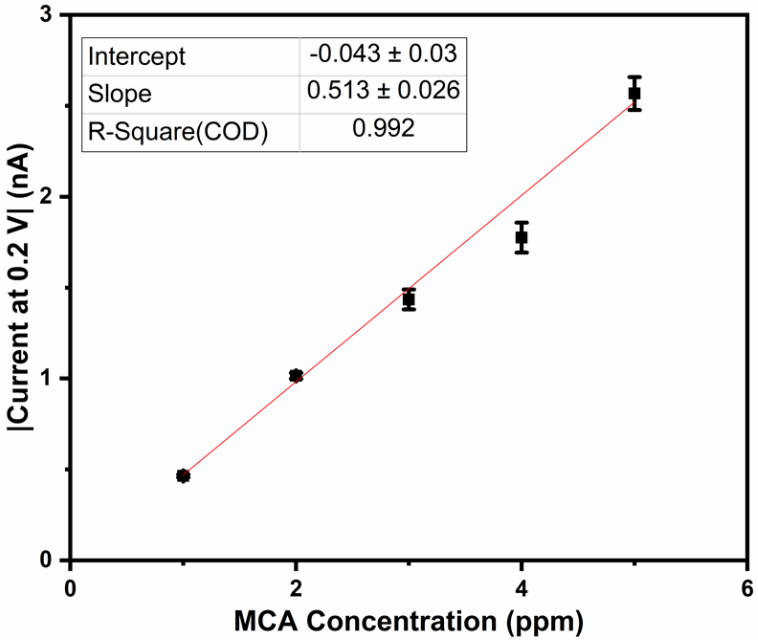

Figure 4-12 Calibration of MCA detection in DI water with pH control

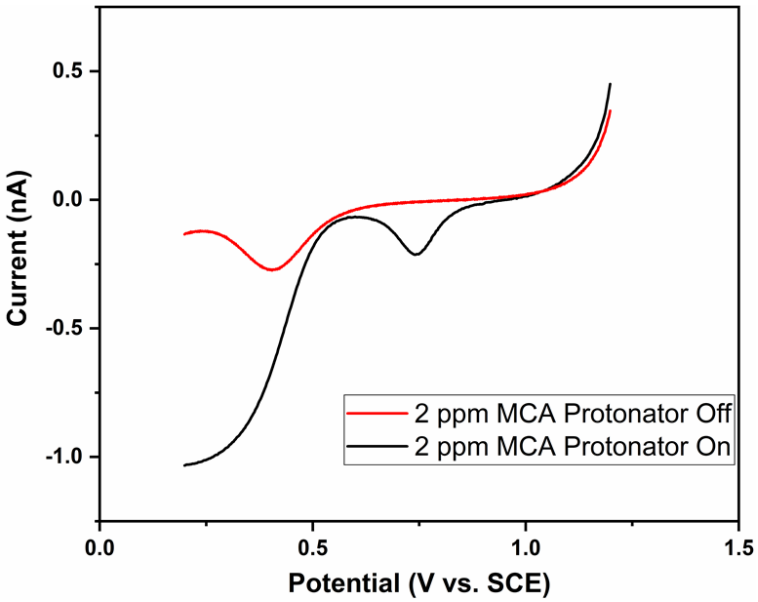

Figure 4-13 Comparison of a 2 ppm MCA scan with (black) and without (red) pH control applied. Error was calculated from the standard deviation of multiple scans (n=3).

To eliminate any doubt that DCA was being formed, experiments were carried out to remove any obvious possible alternatives. The potential window was extended for the scans when the protonator was switched off. This was undertaken to assess whether the pH shift caused additional peaks to appear that are normally outside the window. Figure 4-14 shows the result of this extended scan in a 2 ppm MCA sample. Other than the onset

of oxygen reduction, no reduction event was observed that resembled the current plateau observed in Figure 4-13. Oxygen reduction and MCA reduction are starting to occur but nothing that could be mistaken for DCA. The second test carried out was a scan in an equivalent concentration of free chlorine. As the protonator is held at such high potentials, the possibility that MCA was being destroyed resulting in free chlorine as opposed to DCA had to be investigated. Figure 4-15, however, shows that the onset of reduction for free chlorine is more positive than DCA, and can be dismissed as a possible source of interference.

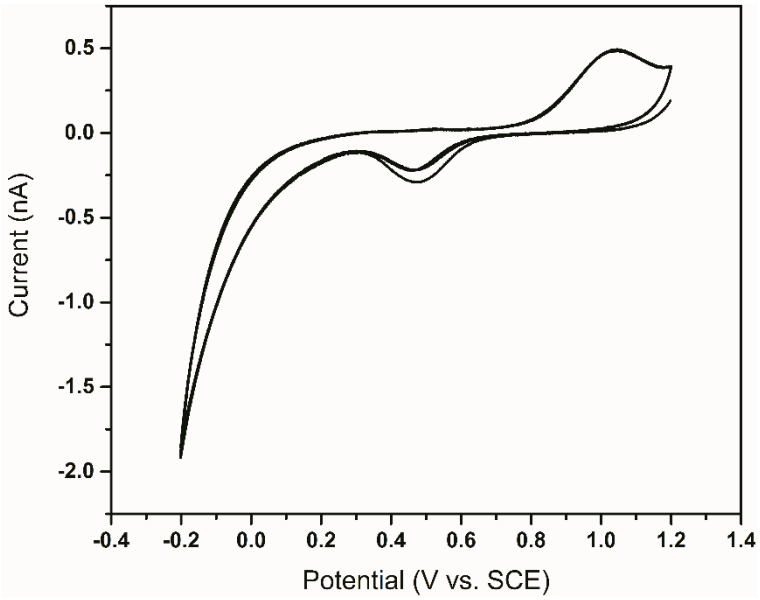

Figure 4-14 Extended potential window for a 2 ppm sample of MCA with no pH control applied. No plateau is observed beyond 0.2 V.

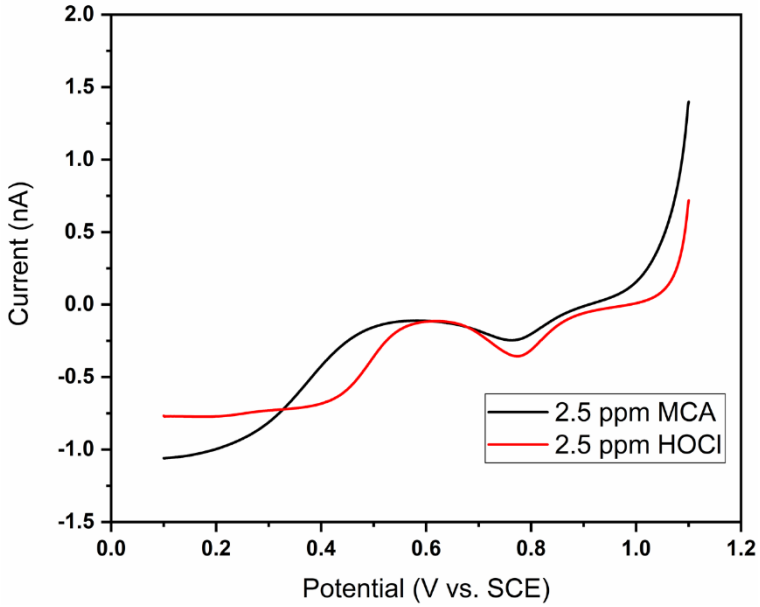

Figure 4-15 Comparison of equivalent concentrations of MCA (black) and hypochlorous acid (red) under pH control conditions.

This method was developed to remove oxygen as an interferent in MCA detection, therefore it was necessary to evaluate the detection method at various oxygen concentrations. It was not expected that oxygen would interfere, as the window used is outside that where oxygen reduction typically occurs, but side reactions are not necessarily ruled out. Figure 4-16 shows quite clearly that oxygen has no impact on the amperometric detection of MCA using pH control. The saturated (8.78 ppm O_2) and purged (0.52 ppm O_2) samples of 5 ppm MCA show no variation, and in fact, completely overlap. This was repeated on samples with MCA concentrations of 1 – 4 ppm, and the same effect was observed.

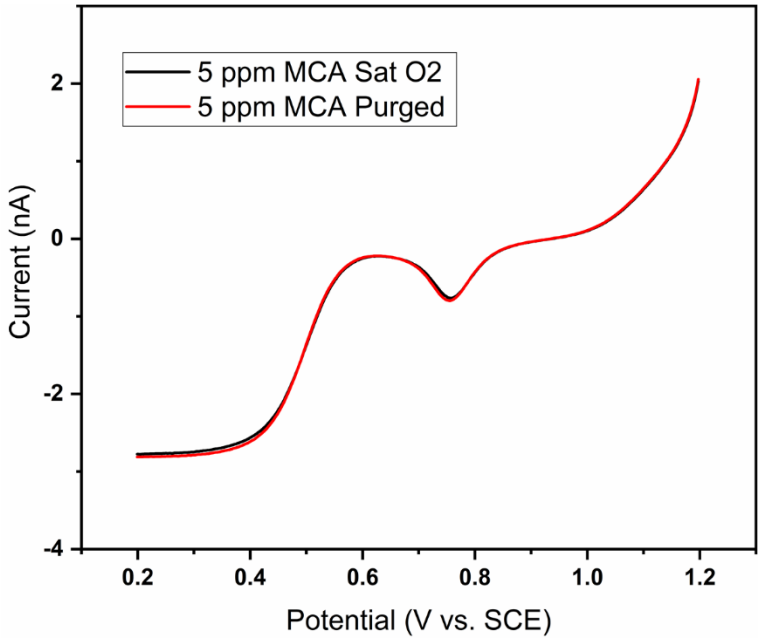

Figure 4-16 Comparison of 5 ppm MCA scans with high (black) and low (red) concentrations of oxygen. No interference from oxygen is observed.

4.3.4 Protonator Stability and Platinum as a Protonator Material

Over multiple tests it was found that the stability of the pH control decreased. This was noted by the movement of the gold oxide reduction peak under the same parameters. Upon inspection it was found that the gold protonator became discoloured and in some cases lifted off the device entirely. The gold electrodes were held at high potentials for extended periods of time in chlorine-based solutions, harsh conditions for long term use. Platinum was investigated as a possible alternative protonator material, as it is more stable in chlorine solutions than gold, and has been shown to evolve oxygen at lower potentials than gold[34]. To test its performance versus gold, both materials were scanned in ADW. The electrodes were cycled multiple times from 0 V to 1.65 V (the protonator potential used so far) to monitor the current measurements with time. Figure 4-17 shows the results of both sets of scans. The results are summarised in Figure 4-18. There is a large difference in the currents measured for both materials, and it was found that platinum outperforms gold. The gold electrode performance degrades from the first cycle and

exhibits a gradual decrease from scan three. Platinum also degrades with time, however due to the much larger initial current measurement, this degradation did not become significant as quickly as gold. Over 10 scans it was found that platinum showed a 1.7 % decrease in current, while gold showed a 7.9 % decrease. It was also shown that platinum increases in current for the first few scans. The protonator potential required for pH control is also lower for platinum than for gold. To get a current of 20 µA on gold, a potential of 1.65 V was required, whereas for platinum the same current is obtained at approximately 1.57 V.

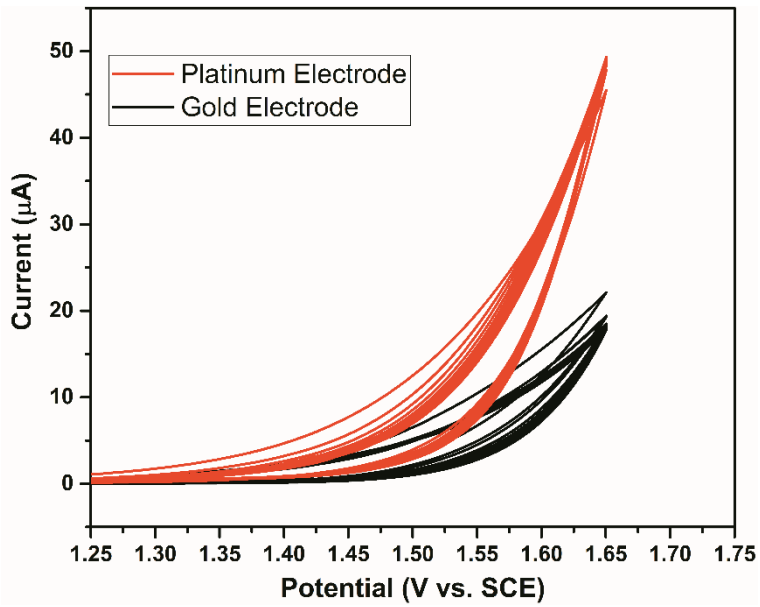

Figure 4-17 Multiple cycles of platinum (red) and gold (black) in ADW samples. CVs were performed from 0 V to 1.65 V multiple times to determine the protonating ability of both materials.

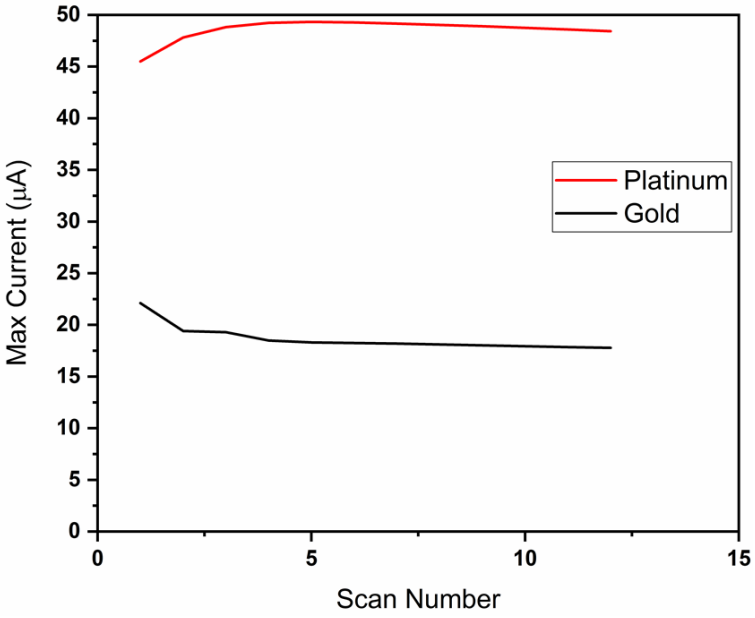

Figure 4-18 Degradation of the max current seen at 1.65 V for both platinum (red) and gold (black). Gold has a lower current, and degrades quicker than platinum.

Platinum was subsequently electrodeposited onto one comb of the µIDE array. This resulted in a mixed metal array where the gold comb was used as the detector and platinum as the protonator. Electrodeposition was carried out by chronoamperometry and a typical scan is shown in Figure 4-19. The first two seconds of this scan show a significant discharging current. This is a resulted of the charging current associated with a potential bias being imposed at an electrode surface. As the potential did not change, no further charge was observed after the initial potential bias. The thickness of the resulting deposition was calculated in several steps. Firstly, the chronoamperogram was integrated to give the total charge passed (Q), which was 34.93 µC. This was used to determine the mass (m) of platinum deposited using Faradays law shown in Equation 4.16.

$$Q = nF\left(\frac{m}{M_w}\right) \qquad \text{Equation 4.16}$$

The number of electrons passed (n) was 2, as platinum is in the 2+ state in the DNS bath. From this it was established that 3.531×10^{-8} g of platinum was deposited. It was then

possible to determine the thickness (T) of the deposit by knowing the density (D) of platinum (21.447×10^6 g/m^3) and using Equation 4.17.

$$D = \frac{m}{A\,x\,T} \qquad \text{Equation 4.17}$$

Where A is the surface area of the electrodes, estimated to be 756 µm^2. The product of surface area and thickness represents volume of the platinum deposit. It was calculated that the deposition thickness was 167.5 nm.

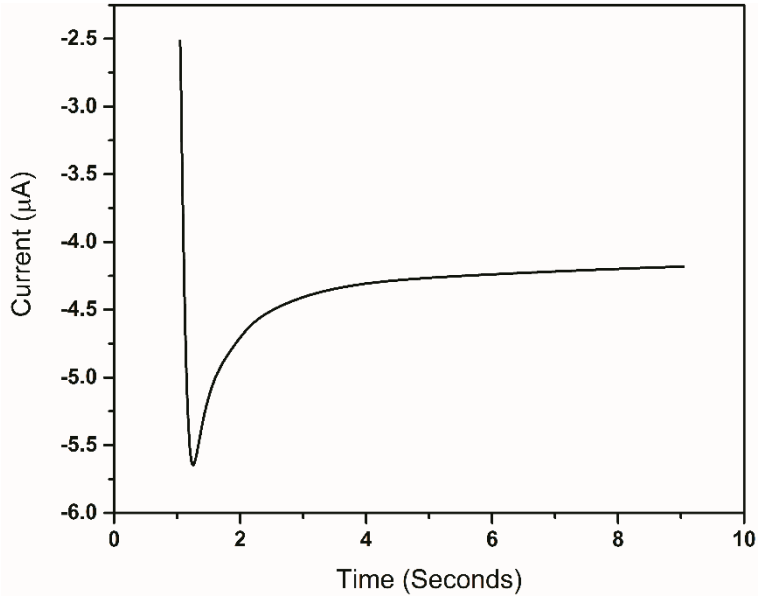

Figure 4-19 Chronoamperometric plating of platinum on one comb of the gold IDE array. This was done by holding the electrode at -0.5 V for 8 seconds.

Following electrodeposition, a series of characterisation steps were carried out to examine the platinum deposited. The devices were inspected optically at 50x magnification. Figure 4-20 shows images captured before and after platinum deposition. Figure 4-20 (b) shows that the platinum plated only on one comb of electrodes. A slight silver colour was

observed on the plated comb, which is contacted from the left-hand side contact in the image.

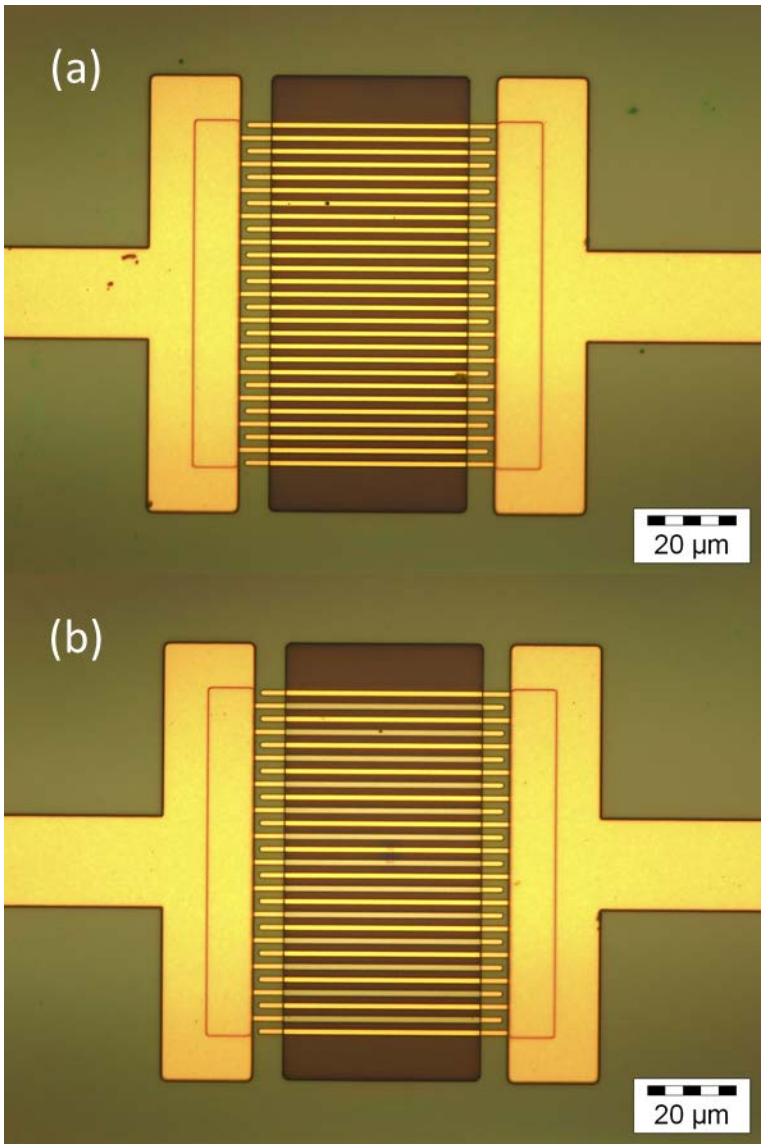

Figure 4-20 Optical images at 50 x magnification of an array (a) before plating and (b) after plating.

Scanning electron microscopy (SEM) allowed for accurate determination of the platinum deposition thickness. Figure 4-21 (a) shows a typical SEM image of an untreated IDE. The average electrode width was found to be 1.06 µm with an inter-electrode gap of ~ 2 µm. Following plating, SEM characterisation showed that the average electrode width increased by 0.24 µm as shown in Figure 4-21 (b) or 0.12 µm on either side of the

electrode indicating a Pt deposit thickness of 120 nm, which is lower than predicted by the chronoamperogram.

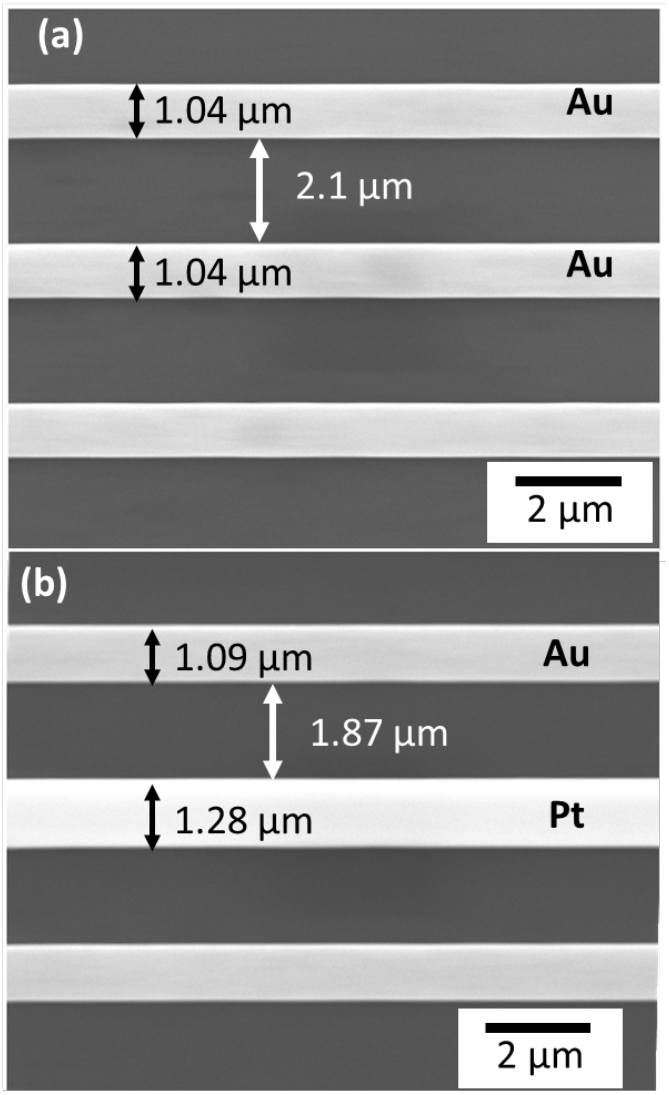

Figure 4-21 SEM images showing the change in electrode width and inter-electrode gap as a result of plating. (a) Array prior to plating (b) after plating.

Energy dispersive x-ray (EDX) spectroscopy was performed on each comb of an IDE following electrodeposition. Figure 4-22 (a) shows the EDX spectra for the unplated comb and (b) shows the equivalent spectra for the plated comb. The unplated comb mainly showed peaks attributed to the gold metal electrode. Titanium and silicon peaks were also observed, which were attributed to the adhesion layer and substrate respectively. For the plated comb, many of the same peaks were observed, with the

addition of a new platinum peak. This confirmed that platinum was present due to successful deposition. The gold peaks are still present in this EDX spectra however, as the x-rays used in EDX can penetrate the platinum and reach the underlying gold, therefore both materials were observed. Analysis of the spectra was carried using the EDX software, by setting the detector to be sensitive to only gold and platinum. Prior to plating, the gold peaks accounted for 100% of the spectra, as expected. After plating however, gold accounted for only 39% of the spectra, while platinum accounted for 61%. Considering the gold thickness does not change, the 39% still accounts for 100 nm of gold. Therefore 100% is equivalent to a thickness of 256 nm, meaning that the platinum thickness is 156 nm. This value is in good agreement with the value calculated from the chronoamperogram.

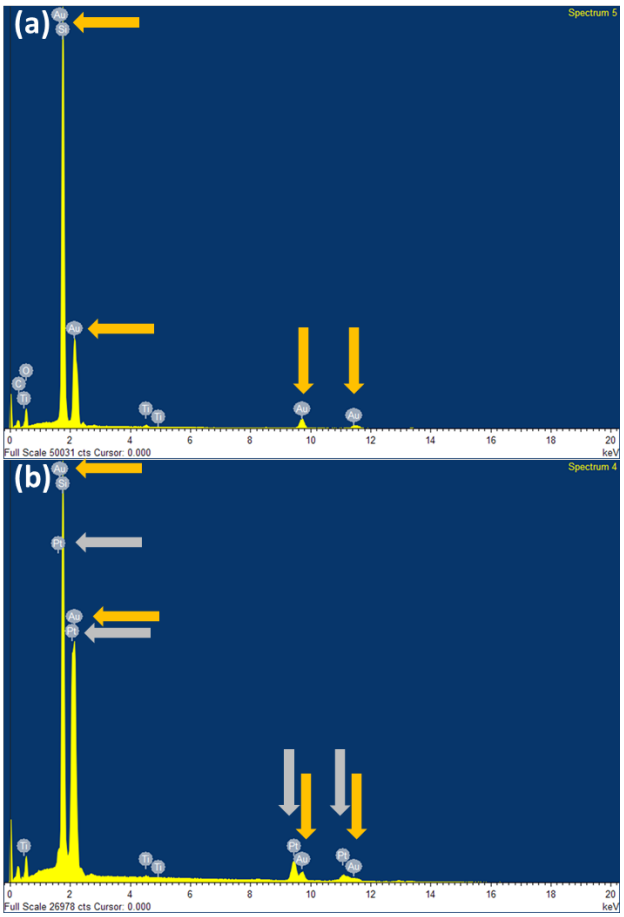

Figure 4-22 EDX Spectra obtained on (a) a bare gold array and (b) a platinum plated array. The orange arrows indicate a gold peak, while the grey arrows indicate a platinum peak.

4.3.5 Calibration of DCA in ADW and Refinement of Parameters

Having chosen an appropriate electrode material and determined the parameters for MCA detection by pH control, real sample matrices were analysed. This employed the use of ADW which consists of the typical components expected in potable water. It was found that the detection of DCA was still possible in ADW and the protonator potential did not need to be adjusted. Unfortunately, it was found that the interaction between gold and chlorine, as mentioned previously, was found to cause destruction of the electrodes. The peak shown at 1.1 V in Figure 4-23 increased with multiple scans and repeated analysis. This peak was found to be linear with MCA concentration initially when the electrode area was undergoing slight changes. Eventually, this peak reached a maximum current after which no electrochemical signal was obtained, and upon visual inspection, the electrode was seen to be completely gone. This method as a possible sensing approach was only viable if regular redeposition of gold was performed between scans, which was unfeasible. The electrodes in low concentrations of MCA survived for more cycles, but the higher concentrations resulted in electrode dissolution in less than 15 cycles or 7 nm of gold per cycle.

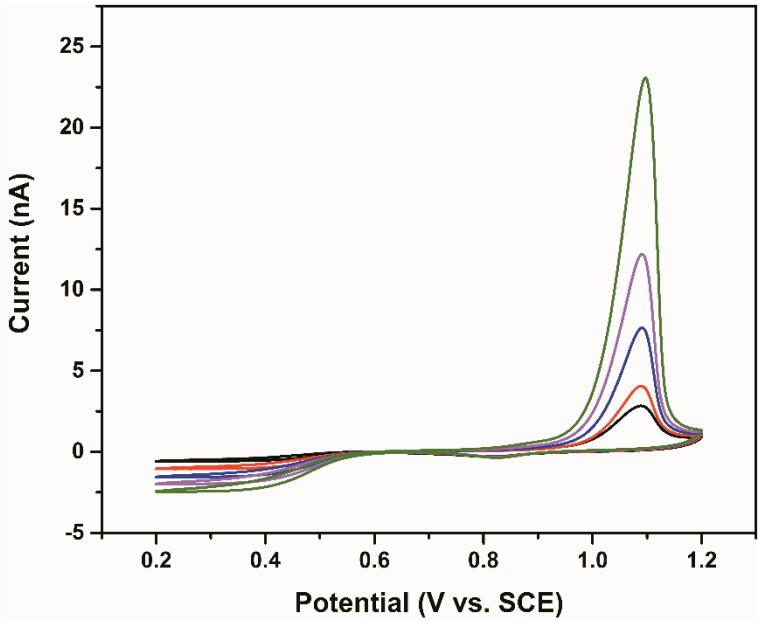

Figure 4-23 Comparison of multiple concentrations of MCA showing the full sweep parameters. The oxidation event at 1.1 V was found to lead to destruction of the electrode.

To combat this, the parameters for detection were slightly refined. The cause of electrode loss was the oxidation event at 1.1 V. Initially it was required to scan this far positive as generation of the gold oxide was necessary to determine local pH, and thus adjust the protonator potential. However, the protonator potential required never changed for the MCA samples, so it was not always necessary to generate the gold oxide. Thus the scan can be started and stopped at a potential before the gold chloride is formed, preserving the electrode for longer. The adjusted start potential chosen was 0.95 V, and scans for this are shown in Figure 4-24. The smaller window also means that the overall analysis time is shortened by 10 seconds per scan. The calibration (Figure 4-25) shows a good linearity ($R^2 = 0.99$), however the sensitivity is slightly lower (0.347 nA/ppm) than for the previous tests in DI. This could be a result of matrix effects, but it is more likely that it is due to the smaller potential window used. The electrode surface may have been slightly cleaned by the formation and reduction of the surface gold oxide. Anything that may have bound to the surface while the electrode was sitting in solution is effectively removed with the oxide. This may have given a cleaner surface on which to detect DCA. It is also possible

the formation of gold chloride and its subsequent dissolution removes the outermost layer of the gold electrode. While this means that the electrode was losing material, it also left the electrode surface less contaminated. This can be advantageous as for long term testing, fouling is expected. Sacrificing the outermost layer of gold can remove the fouled gold and leave a clean electrode with which to do analysis. This of course limits the number of uses the electrode has, but the goal for these devices is in real water testing. In such an application, single measurements are taken on a weekly or fortnightly basis, so long-term use can still be achieved.

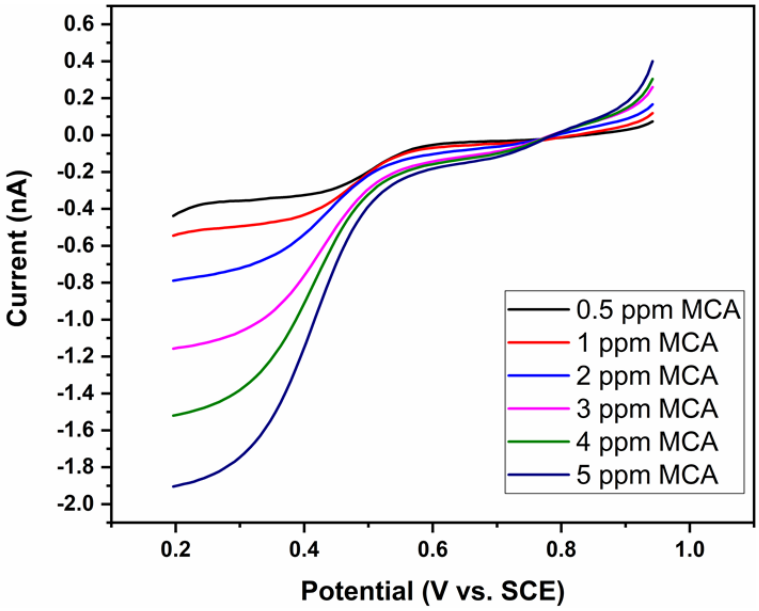

Figure 4-24 Calibration of MCA samples made in ADW using the adjusted parameters. Scans were performed by sweeping the electrode from 0.95 V to 0.2 V at 50 mV/s.

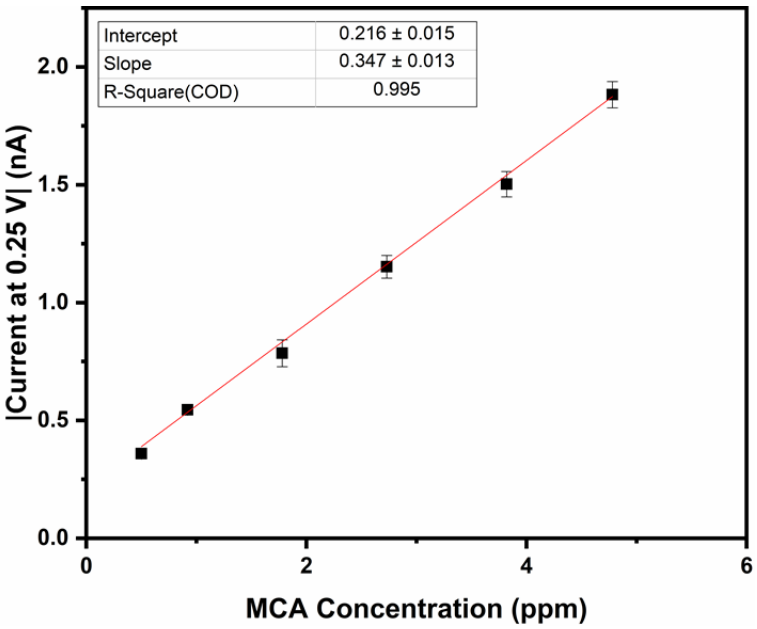

Figure 4-25 Calibration plot for MCA in ADW using the new parameters. Error was calculated from standard deviation of multiple scans (n=3).

Work up to this point focused on the MCA range expected in most water systems. As such, concentrations between 0.5 ppm and 5 ppm MCA were investigated. While the test method was found to be promising in this range, it is possible that a water system may present with an extreme concentration of MCA. It was therefore necessary to investigate a high concentration of MCA outside of the typical range. For this, a concentration of 10 ppm MCA in ADW was chosen. This is significantly above the upper limit for water systems and would be highly unlikely in any system. The main purpose of this test was to investigate if the detection method would hold up in an extreme case scenario. The scans, seen in Figure 4-26 and subsequent calibration, Figure 4-27, show that 10 ppm can be accurately measured and fits in with the trend for the previous MCA samples. The significance of the accurate measurement of the 10 ppm sample is that, higher concentrations of MCA can be converted to DCA within the same timeframe. Therefore, the quiet time used to ensure adequate conversion of MCA to DCA is sufficient to ensure that a very high concentration of MCA in a water system is not under estimated as a result of poor conversion.

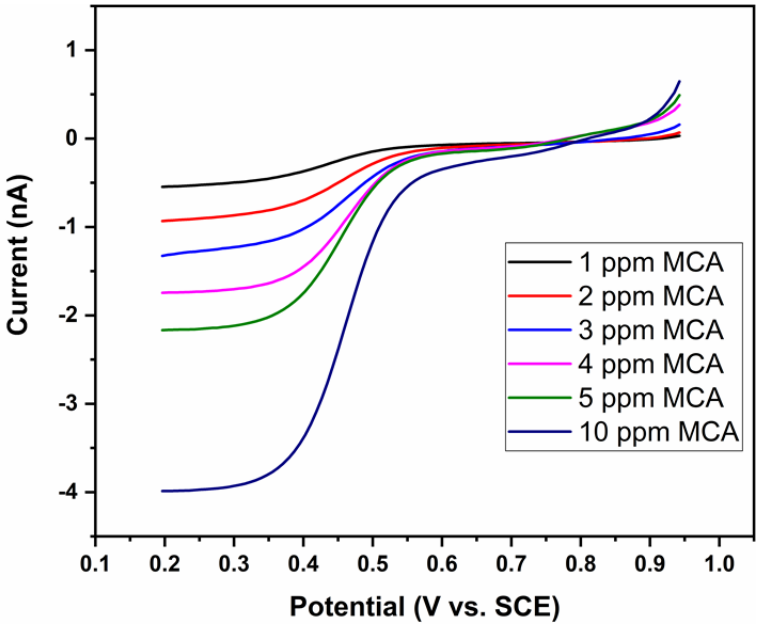

Figure 4-26 The high range of MCA detection was investigated by performing a scan in a 10 ppm MCA sample. Similar behaviour was seen as for the lower concentrations.

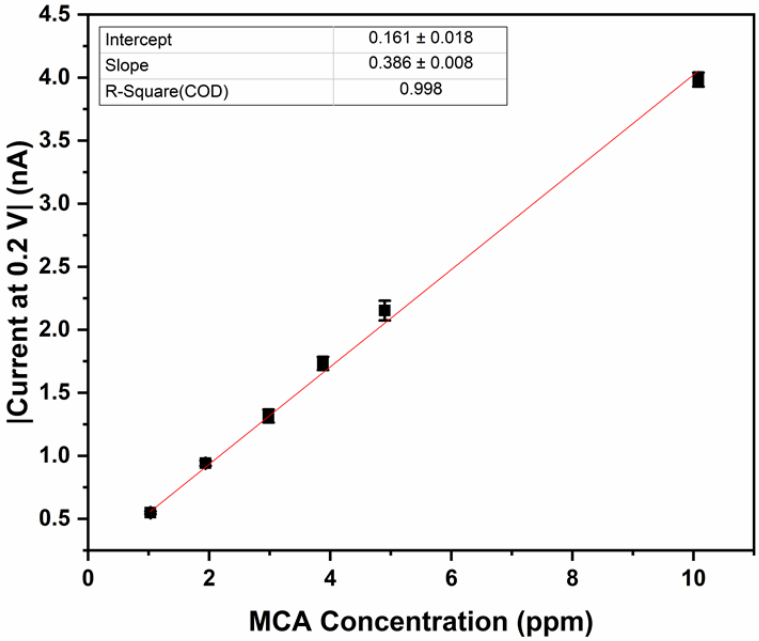

Figure 4-27 Calibration plot including the higher concentration of MCA. Linearity is maintained with the 10 ppm sample. Error was calculated from standard deviation of multiple scans (n=3).

4.3.6 Matrix Effects – High Alkalinity and High Conductivity

Certain components of a water system are strictly regulated, such as concentrations of residual chlorine and heavy metals. As other components have less of an impact on the consumer, they can be present over a greater range of concentrations. While these may

have no impact on the quality of the water, they can impact the efficiency of the pH control detection method. The biggest concern is the alkalinity, which can lead to a buffering of the water system. High alkalinities can arise from the erosion of carbonate-based rocks, which depends on the area from which the water is sourced. While this does not pose a health concern, it can dramatically change the pH control performance. Samples of ADW with 500 ppm alkalinity, made by adding sodium bicarbonate to the stock solution, were tested with the pH control method to cause an acid shift in the local pH. The main adjustment that was required to facilitate this was an increase of the platinum protonator potential to 1.7 V. Figure 4-28 shows that adequate pH control was achieved with these parameters. The shift in the oxide reduction potential of 0.4 V indicates that a drop in local pH, from pH 9 to pH 3.25, was achieved.

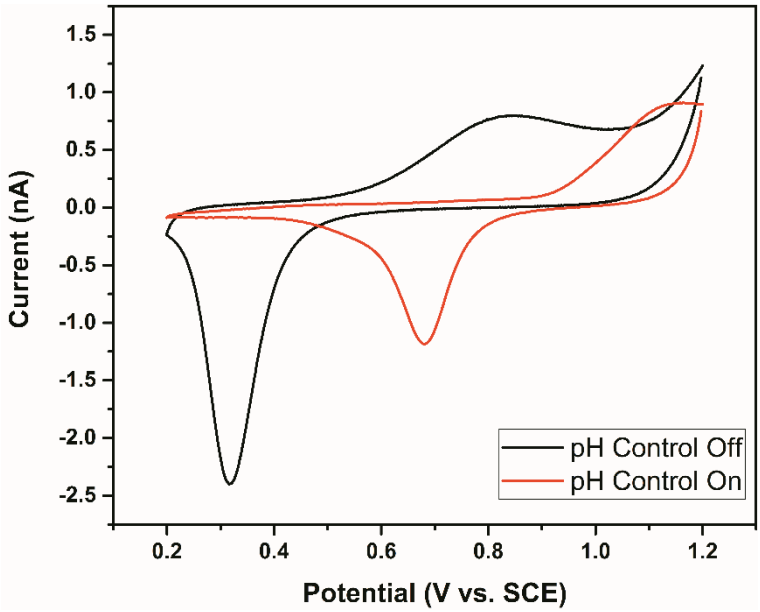

Figure 4-28 CVs in high alkalinity ADW with pH control off (black) and on (red). The solution was driven to pH 3 by applying a protonator potential of 1.7 V at the protonator and sweeping the detector from 1.2 V to 0.2 V at 50 mV/s.

Following the establishment of parameters in the 500 ppm alkalinity, the test was then applied to samples containing various concentrations of MCA. For this set of tests, the original parameters (1.2 V to 0.2 V) were used to ensure that the pH was maintained

throughout. The MCA detection was shown to behave the same as for the unmodified ADW samples, and is shown in Figure 4-29. The resultant calibration (Figure 4-30) also shows that the good linearity is maintained (R^2 = 0.99). The sensitivity has increased (0.53 nA/ppm) over the previous scans with the adjusted parameters. This is due to the formation and reduction of the surface oxide, which provides further support that this acts as a cleaning step. The formation of the gold chloride (oxidation at 1.1 V) is not as significant in the higher alkalinity samples, therefore the enhancement is most likely due to the oxide effects.

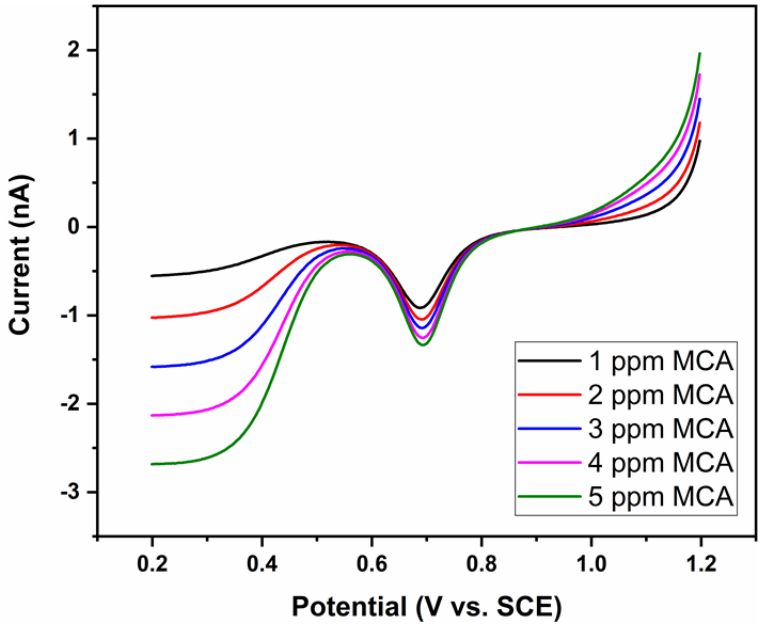

Figure 4-29 LSVs of various concentrations of MCA in the high alkalinity (500 ppm) ADW samples. Original pH control parameters were used to determine if pH 3 was still achieved.

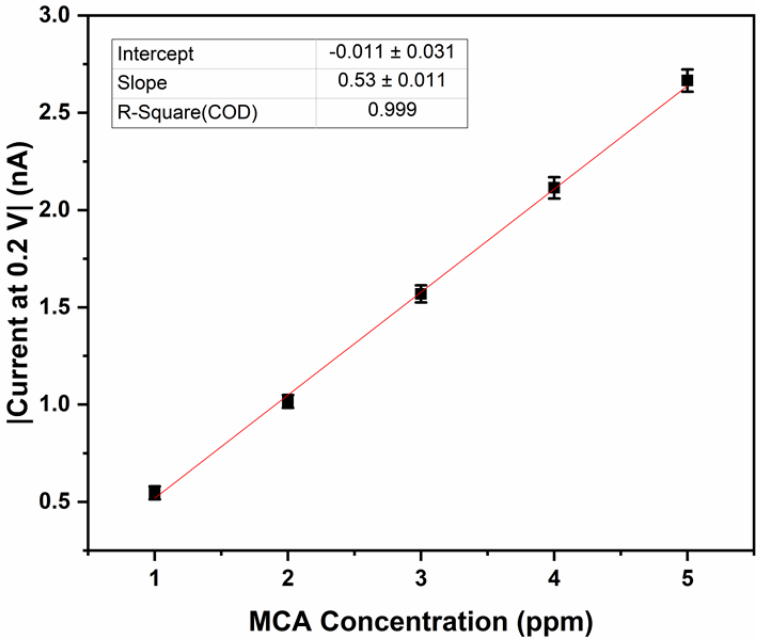

Figure 4-30 Calibration of MCA in 500 ppm alkalinity samples. Error was calculated from standard deviation of multiple scans (n=3).

Alkalinity was further increased from 500 ppm to 1000 ppm (via sodium bicarbonate addition), again to an extreme case to determine the suitability of the test in more harsh conditions. It was found that the protonator had to be pushed to a higher potential (1.75 V) in order to achieve the required pH. After the stability shown for pH control in the 500 ppm sample, the adjusted parameters (0.95 V to 0.2 V) were used for a 1000 ppm alkalinity sample. Even though the formation of gold chloride was not as significant in the higher alkalinity samples, it is still not desirable, so the adjusted parameters were preferred. The same DCA reduction behaviour is seen in Figure 4-31, and linearity is maintained (R^2 = 0.99) in the calibration, see Figure 4-32. The sensitivity has dropped again to 0.363 nA/ppm since the surface oxide was not formed and removed immediately prior to DCA analysis.

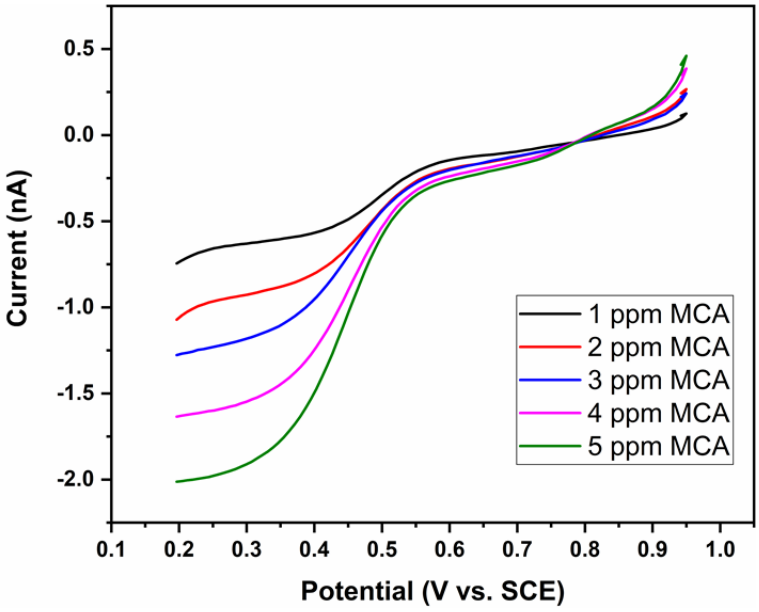

Figure 4-31 Alkalinity of the MCA samples was increased to 1000 ppm and the adjusted parameters (0.95 V to 0.2 V) were used to determine the upper limit of alkalinity. Protonator potential was increased to 1.75 V

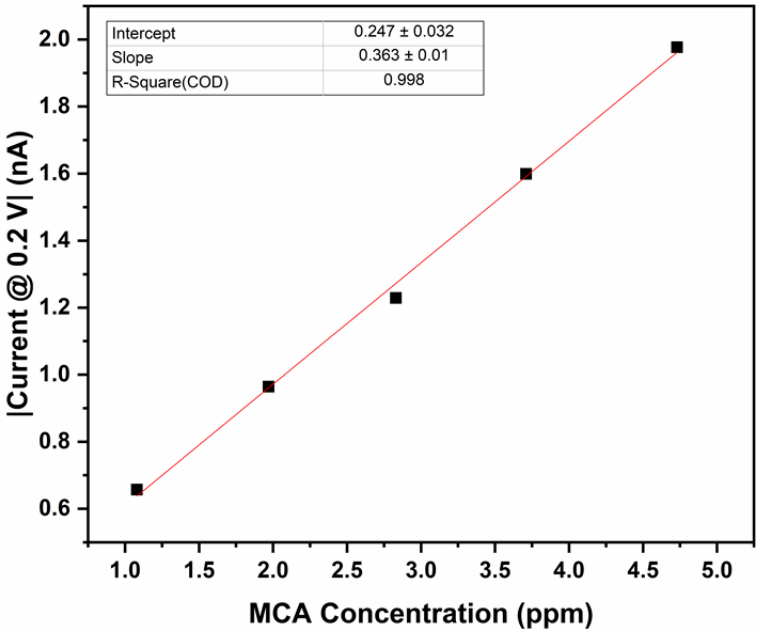

Figure 4-32 Calibration for the 1000 ppm alkalinity samples of MCA.

Another major parameter that may have an influence on the detection is the conductivity on the sample matrix. A wide variety of conductivities were tested throughout the previous work. The lowest conductivity tested was 147 µS/cm, while the highest was 2000 mS/cm. Low conductivities were measured for MCA samples in DI water and

medium to high values were measured in the ADW and high alkalinity ADW samples. Drinking water typically has a conductivity in the range 0.5-5 mS/cm, and detection in this range did not have much of an impact on the analysis. To test the extremes, samples with conductivities of 2000 mS/cm were made up and subjected to the pH control parameters. It was found that even for the upper extremes of conductivity, MCA detection was still possible. It was not expected that conductivity would have a significant impact, so only 3 samples were tested, shown in Figure 4-33. Instead of doing an entire calibration series, these three points were added to an existing calibration plot for ADW to see how well they fit the trend. Figure 4-34 shows that the linearity was only slightly affected (R^2 = 0.98) and the sensitivity remained the same (0.35 nA/ppm).

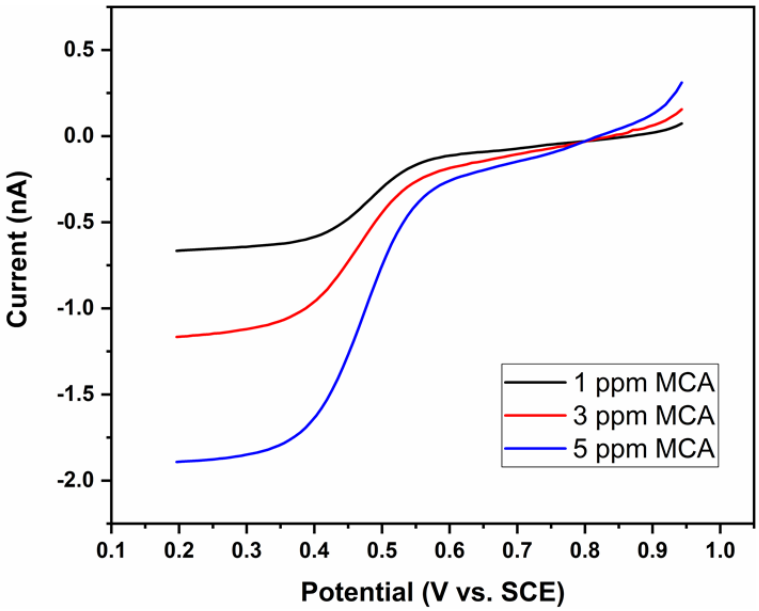

Figure 4-33 Scans of MCA in high conductivity ADW. Conductivity of 2000 mS/cm was used and the adjusted parameters were used. The protonator was held at 1.65 V.

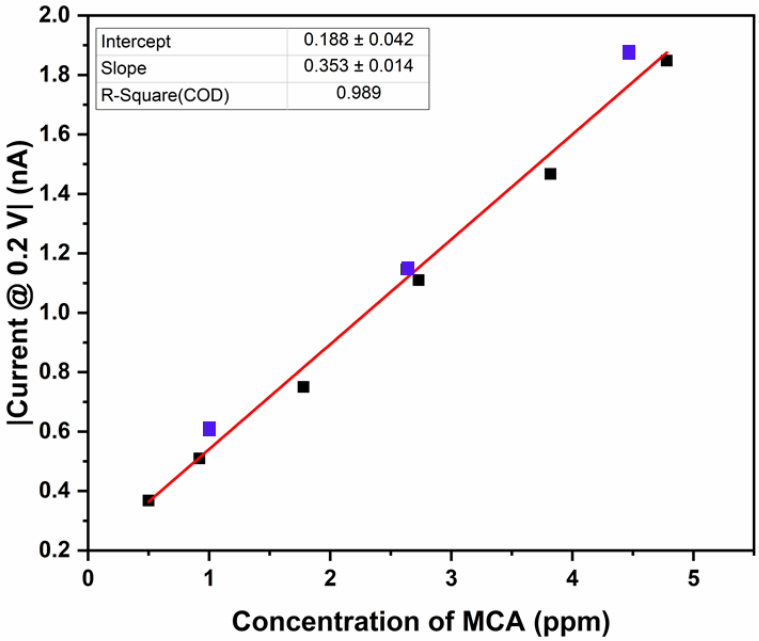

Figure 4-34 The current values for the high conductivity samples were put into an existing calibration for regular ADW samples. The three points from the high conductivity samples (shown in blue) fit to the calibration and maintained linearity.

4.3.7 Effect of Iron, Copper, Phosphate and Chlorine on DCA Detection

While there is the potential to have a wide range of different interferents present, it is important to focus on the more common ones to determine their effect on MCA detection. These were limited to species that were expected in real water samples, but not necessarily part of typically drinking water. These included iron, copper, and phosphates. To determine how they would affect the analysis, samples of 2.4 ppm MCA were spiked with 1 ppm of each. The worst-case scenario was used again, as 1 ppm is considered the upper limit of concentration for each of these in water. It was found that no significant activity was observed in terms of detection of each of these species, as shown in Figure 4-35. However, an increased current was measured in the presence of each species, as shown in Figure 4-36. A 4.6% increase over the expected current for a 2.5 ppm MCA sample

was observed for iron. For phosphate and copper the increase was found to be 3.5% and 2.4% respectively.

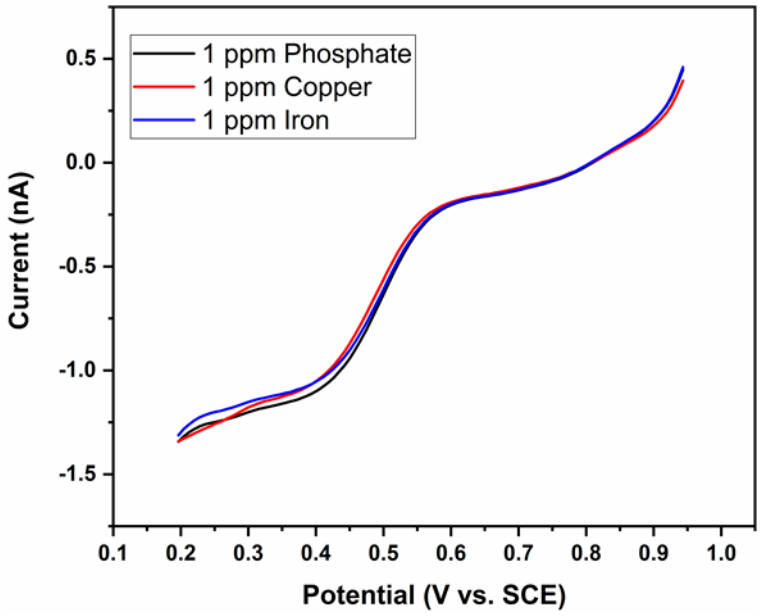

Figure 4-35 Comparison of 3 samples of 2.4 ppm MCA, each spiked with 1 ppm each of phosphate, copper and iron. No significant interference is seen for any of these species.

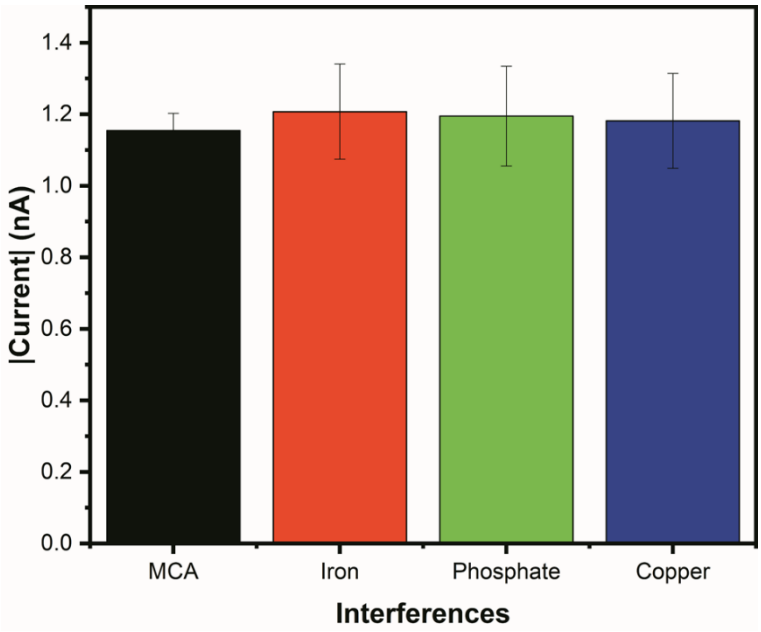

Figure 4-36 Comparison of the measured MCA current with the average currents of the scans in the presence of each interferent.

Free chlorine itself can also be quite a significant interferent for MCA detection. In laboratory-based experiments, however, it can be difficult to determine how much of an

effect it may have. This is because of the difficultly associated with creating a mixture of both MCA and free chlorine on a small scale. Free chlorine added to a solution of MCA with an excess of ammonia will just produce more MCA. Free chlorine added to a solution of MCA alone will ultimately produce DCA. This of course can happen in the water system too, so it is rare that MCA and free chlorine will be present in the same mixture. Again, thinking of the worst-case scenario, a method was investigated that could separate the two signals. It has been shown that free chlorine has activity, although low at pH 8 (chapter 3). For example, a 1 ppm solution of free chlorine in ADW shows a reduction current of -0.7 nA. Figure 4-37 shows that DCA is not present in solutions until at least pH 5, and in no significant concentration until a pH of about 4. The method devised in this work to separate the two signals is to first take a measurement with no pH control to determine the free chlorine signal. Then take a measurement with pH control to determine the signal of free chlorine and MCA. Subtraction of the free chlorine signal from the total will yield the MCA value.

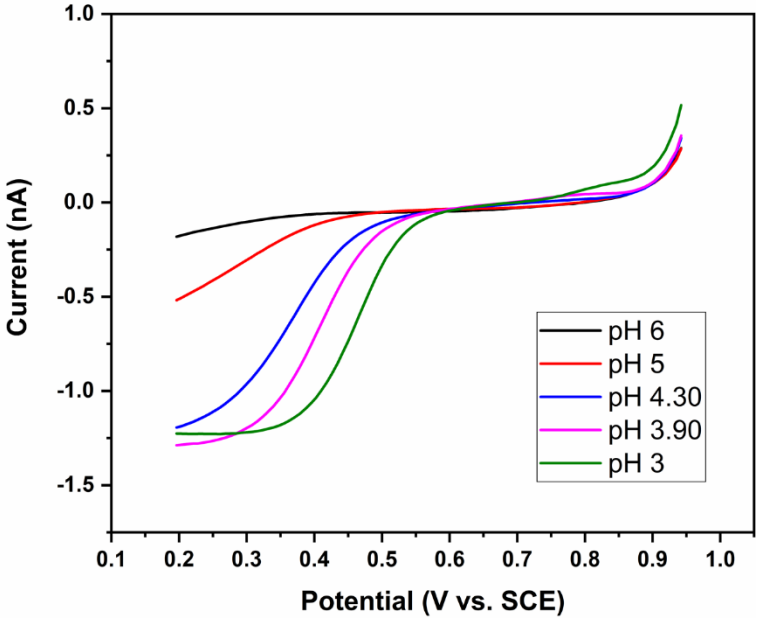

Figure 4-37 pH dependence on the formation of DCA from MCA. 2.5 ppm samples of MCA were adjusted with 0.1 M H_2SO_4 and LSVs were recorded at various pH values.

4.3.8 Accuracy of Detection Method and Limit of Detection

To determine the accuracy and precision of the detection method, five samples of 2 ppm MCA were tested using the pH control method. The current values for each of these were noted and converted to predicted MCA concentrations using the calibration line equation for MCA in ADW:

$$y = 0.4318x + 0.0381 \qquad \text{Equation 4.18}$$

The measured MCA values were obtained using the colorimetric test method. Similarly the predicted current was calculated by putting the measured MCA values into Equation 4.18:

$$x = \frac{y - 0.0381}{0.4318}$$

The results for this are summarised in Table 3 and show very low variation between the predicted and measured currents, with the largest variation being 4.61% or 90 ppb when comparing concentration and 4.62% when comparing current.

Measured MCA *ppm*	**Predicted MCA** *ppm*	**Variation** *%*	**Measured Current** *nA*	**Predicted Current** *nA*	**Variation** *%*
2.09	2.143	2.439	-0.964	-0.941	2.381
1.97	2.045	3.663	-0.921	-0.889	3.533
1.97	2.035	3.179	-0.917	-0.889	3.081
1.92	1.885	1.816	-0.852	-0.867	1.767
2.01	1.917	4.611	-0.866	-0.906	4.621

Table 3 Variation of measured and predicted values for MCA in ADW

This analysis was also done using the high alkalinity samples and the equations:

$$y = 0.3626x + 0.2468 \qquad \text{Equation 4.19}$$

which becomes:

$$x = \frac{y - 0.2468}{0.3626}$$

These results are summarised in Table 4 and again show very little variation between measured and predicted values (maximum variation was 6.6% for concentration, 6.3% for current).

Measured MCA *ppm*	**Predicted MCA** *ppm*	**Variation** *%*	**Measured Current** *nA*	**Predicted Current** *nA*	**Variation** *%*
1.97	2.100	6.600	-0.964	-0.913	6.300
1.98	2.029	2.478	-0.921	-0.917	2.074
1.95	2.014	3.277	-0.917	-0.905	2.718
1.96	1.948	0.603	-0.852	-0.909	0.517
1.96	1.943	0.861	-0.866	-0.909	0.740

Table 4 Variation of measured and predicted values for MCA in 1000 ppm alkalinity MCA

The limit of detection was determined by first performing 7 replicate measurements in a 0.5 ppm sample of MCA in ADW. The standard deviation (σ) of these measurements was calculated in terms of nA and multiplied by 3.14 to ensure a 99% confidence in the resulting detection limit. This value was subsequently divided by the slope of the calibration curve to determine a concentration value. The resulting limit of detection was calculated to be 0.03 ppm. This is far below the lowest value of the required MCA range in water, which is 0.5 ppm MCA.

4.4 Conclusions and Future Work

In this chapter, we have demonstrated that reliable, reagent-free detection of MCA was achieved by using a pH control method. The developed sensor was calibrated between 0 and 5 ppm MCA, which is the typical range expected in potable water, showing both accuracy and precision in measurements, with deviations of less than 6%. The lowest measured concentration was 0.5 ppm, with a detection limit calculated at 0.03 ppm MCA. The upper extreme was tested using a 10 ppm MCA sample, which was quantified with no loss of sensor performance. This range of concentrations far surpass the anticipated limits of potable water, indicating that the developed sensor is more than suitable for real world applications.

The greatest anticipated challenge facing the use of pH control in real water samples is the inherent buffering capacity of water due to its alkalinity. In this work, we have evaluated the detection method at a potential worst-case scenario for alkalinity wherein the concentration of carbonates was 1000 ppm and found that sensor performance was not impacted. Similarly, the variability of conductivity in water samples was not found to impact the analysis. The presence of common interferents in water, showed little to no impact on the detection method and MCA was still quantifiable in the presence of such compounds.

This pH control method was initially shown in chapter 3 using a gold-gold IDE. It was found in this chapter that the protonator performance was significantly improved by depositing platinum on the electrode. As platinum better catalyses the evolution of oxygen from water, the required protonator potential was decreased from 1.65 V to 1.55 V.

4.5 References

1. J. F. T. Berliner, *Journal of the American Water Works Association*, 1931, **23**, 1320-1333.
2. M. K. Silva, I. C. Tessaro and K. Wada, *2nd Mercosur Congress on Chemical Engineering*, 2005.
3. R. L. Wolfe, N. R. Ward and B. H. Olson, *Journal of the American Water Works Association*, 1984, **76**, 74-88.
4. AWWA, *Water Chlorination and Chloramination Practices and Principles*, American Water Works Association, 2nd Edition edn., 2011.
5. I. Weil and J. C. Morris, *Journal of the American Chemical Society*, 1949, **71**, 1664-1671.
6. B. Piela and P. K. Wrona, *Journal of the Electrochemical Society*, 2003, **150**, E255-E265.
7. L. J. Rose, E. W. Rice, L. Hodges, A. Peterson and M. J. Arduino, *Applied and Environmental Microbiology*, 2007, **73**, 3437-3439.
8. R. G. Rice and M. Gomez-Taylor, *Environmental Health Perspectives*, 1986, **69**, 31-44.
9. G. C. White, in *White's Handbook of Chlorination and Alternative Disinfectants*, 2009, pp. 174-229.
10. W. H. Lee, D. G. Wahman, P. L. Bishop and J. G. Pressman, *Environmental Science & Technology*, 2011, **45**, 1412-1419.
11. G. J. Kirmeyer and A. R. Foundation, *Optimizing Chloramine Treatment*, American Water Works Association, 2004.
12. R. D. Morris, A.-M. Audet, I. F. Angelillo, T. C. Chalmers and F. Mosteller, *American Journal of Public Health*, 1992, **82**, 955-963.
13. L. de Castro Medeiros, F. L. S. de Alencar, J. A. Navoni, A. L. C. de Araujo and V. S. do Amaral, *Environmental Science and Pollution Research*, 2019, **26**, 5316-5332.
14. AWWA, *Journal of the American Water Works Association*, 2008, **100**, 110-124.
15. R. L. Wolfe, E. G. M. III, M. K. Davis and S. E. Barrett, *Journal of the American Water Works Association*, 1988, **80**, 109-114.
16. R. L. Wolfe, N. I. Lieu, G. Izaguirre and E. G. Means, *Applied and Environmental Microbiology*, 1990, **56**, 451-462.
17. AWWA, *Nitrification Prevention and Control in Drinking Water*, American Water Works Association, 2013.
18. P. J. Vikesland, K. Ozekin and R. L. Valentine, *Environmental Science & Technology*, 1998, **32**, 1409-1416.
19. WHO, Monochlorine in Drinking Water, https://www.who.int/water_sanitation_health/water-quality/guidelines/chemicals/chloramine-background.pdf, (accessed 26/04/2020).

20. V. V. Rajasekharan, B. N. Clark, S. Boonsalee and J. A. Switzer, *Environmental Science & Technology*, 2007, **41**, 4252-4257.

21. S. Kinani, B. Richard, Y. Souissi and S. Bouchonnet, *TrAC Trends in Analytical Chemistry*, 2012, **33**, 55-67.

22. Hach, DR300 Pocket Colorimeter, Monochlor/Free Ammonia, https://www.hach.com/dr300-pocket-colorimeter-monochlor-free-ammonia-with-box/product?id=55321383873&callback=qs, (accessed 07/01/2020).

23. D. L. Harp, *Water Environment Research*, 2000, **72**, 706-713.

24. P. K. Wrona, *Journal of Electroanalytical Chemistry*, 1998, **453**, 197-204.

25. W. H. Lee, J. G. Pressman, D. G. Wahman and P. L. Bishop, *Sensors and Actuators B: Chemical*, 2010, **145**, 734-742.

26. W. H. Lee, D. G. Wahman and J. G. Pressman, *Ionics*, 2015, DOI: 10.1007/s11581-015-1454-7.

27. I. Seymour, B. O'Sullivan, P. Lovera, J. F. Rohan and A. O'Riordan, *Sensors and Actuators B: Chemical*, 2020, **325**, 128774.

28. P. P. Fehér, M. Purgel, A. Lengyel, A. Stirling and I. Fábián, *Dalton Transactions*, 2019, **48**, 16713-16721.

29. V. C. Hand and D. W. Margerum, *Inorganic Chemistry*, 1983, **22**, 1449-1456.

30. *The Chemistry of Disinfectants in Water: Reactions and Products*, National Academies Press (US), 1980.

31. R. L. Valentine and C. T. Jafvert, *Environmental science & technology*, 1988, **22**, 691-696.

32. A. J. Bard and L. R. Faulkner, in *Electrochemical Methods: Fundamentals and Applications*, Wiley, 2000, ch. Introduction and Overview of Electrode Processes, pp. 87 - 136.

33. A. J. Bard and L. R. Faulkner, in *Electrochemical Methods: Fundamentals and Applications*, Wiley, 2000, ch. 5, pp. 156 - 225.

34. L. Coustan, G. Shul and D. Bélanger, *Electrochemistry Communications*, 2017, **77**, 89-92.

Chapter 5 Quantification of Dissolved Oxygen using Generator-Collector Mode at an Interdigitated Microelectrode Array

5.1 Introduction

5.1.1 The Significance of Dissolved Oxygen:

Dissolved Oxygen (DO) refers to the amount of gaseous oxygen that a water system contains. DO arises primarily from two main processes: photosynthesis and diffusion from the atmosphere. Photosynthesis by aquatic plant life results in the production of oxygen, thus greater amounts of plant life results in higher DO levels. Diffusion occurs when oxygen moves from the atmosphere into the water system. Agitated water systems will dissolve more oxygen by diffusion, therefore flowing and tidal water systems are expected to have higher DO concentrations than stagnant or quiescent waters. Many environmental factors influence how much DO water can contain. Temperature, salinity and altitude are just some of the natural factors that can limit the DO concentration.[1] Keeping environmental factors constant, water typically has between 4 and 10 mg/L DO.

This consistent DO concentration is vitally important for the survival of fish and other aquatic life. While larger marine mammals get their oxygen from air, fish breathe by taking in DO through their gills. As the biology of fish can be quite variable, there is no minimum DO concentration that suits all types of fish. As water passes over the thin walls of the gills, dissolved oxygen moves into the blood and travels to the cells. Generally, it has been found that most species can survive in water with DO concentrations between 6 and 10 mg/L (parts per million, ppm). Below this value, smaller fish begin to die. Water with concentrations below 2 ppm is deemed hypoxic and is unsuitable for fish.[2] This is why warm, stagnant waters typically have no fish while colder, moving waters have an abundance. Fish kills, which are events wherein large numbers of fish in a water system die, occur when the DO drops dramatically from the typical value. Dramatic and

unexpected decreases in DO concentration typically result from contamination of the water source. The most common contaminants are bacteria and organic matter.[3, 4] Bacteria consume oxygen from biological processes while organic matter may be broken down by microbes, which also consume oxygen in the process. Nutrient run-off from fertilizers is also a source of contamination that can dramatically reduce DO in water.[5] The nitrates and phosphates promote the growth of aquatic plant life and algae. When these plants die, they are also broken down by microbes and thus consume oxygen, as illustrated in Figure 5-1.[6, 7]

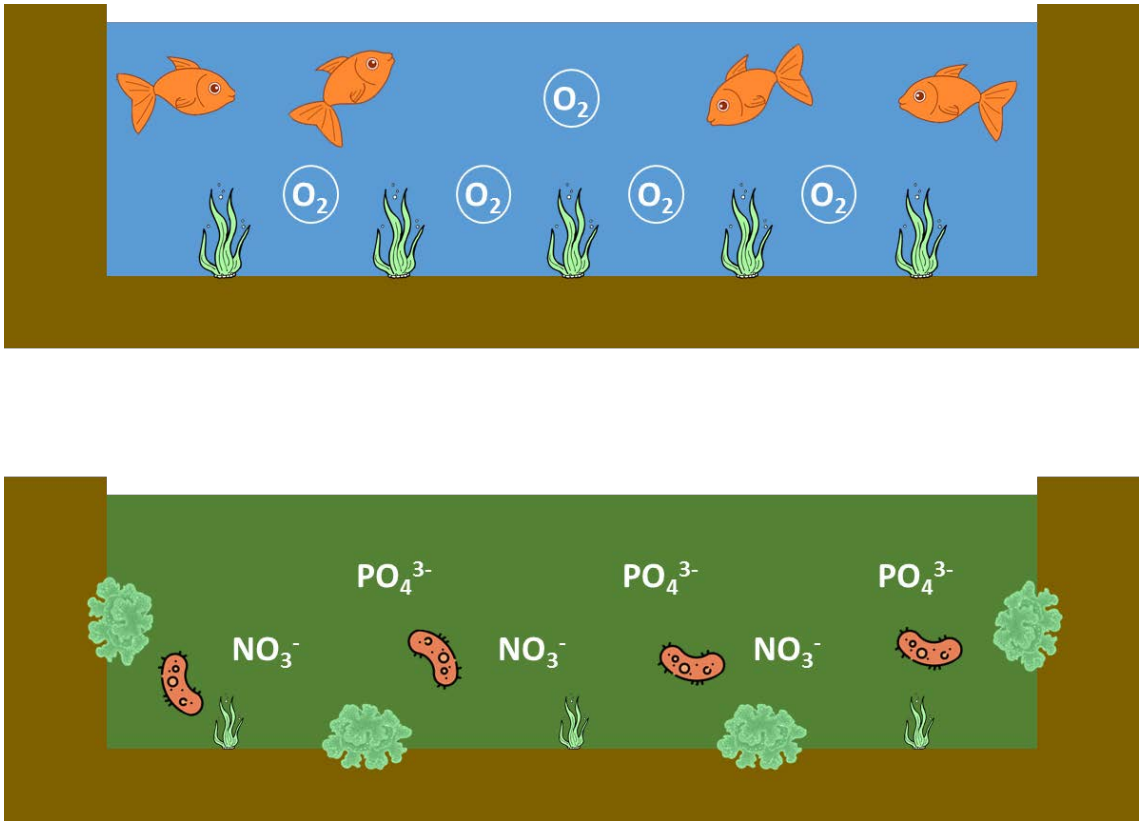

Figure 5-1 Top: Schematic of a healthy water system showing adequate dissolved oxygen and marine life. Bottom: Schematic of an unhealthy system with no dissolved oxygen due to nitrates, phosphates, bacteria, and algal blooms.

From this, it is evident that DO can be an indicator of the overall health of the water system. A decrease in DO or the presence of pollutants becomes apparent quickly in river and lake waters, due to the fish kills. For potable water, however, this is not as readily

apparent. Therefore, it is necessary to actively monitor drinking water systems to ensure that it is safe to consume. Regular monitoring of DO in drinking water can establish a baseline of normal "healthy" conditions. Significant deviations from this normal behaviour can therefore indicate an issue, most likely due to some contamination. Due to the importance of DO as a quality indicator, many methods exist to quantify its concentration in water.

5.1.2 Typical Approaches to DO Quantification

The most common lab-based method for quantifying DO is the Winkler Titration method. This involves the stepwise addition of multiple reagents that ultimately results in iodine formation, the concentration of which is determined by titration with thiosulfate and is directly proportional to the amount of oxygen present.[8, 9] Although accurate, this method requires multiple reagents and specialist knowledge to obtain a DO measurement. Samples must also be sealed to prevent atmospheric oxygen from influencing the measurement. The sampling method itself may also cause the DO concentration to increase or decrease, leading to inaccurate measurements. Reagent-free alternatives to DO sensing are frequently based on optical or electrochemical detection mechanisms. These approaches can also be used to develop portable DO sensors facilitating on-site analysis.

Optical based DO sensors typically operate by measurement of the luminescence response of a molecule in the presence of oxygen. Blue light is absorbed by the molecule which causes an excitation to a higher energy state. This energy is released again as red light which is measured by a photodiode. Collision of the excited species with oxygen results in the transfer of energy and subsequently quenches the emission of light. Higher

concentrations of oxygen mean less luminescence, so a quantitative measure can be obtained as represented in the schematic of Figure 5-2.[10] Commercial sensors based on this technique do not require the addition of any reagent. The luminescent species, typically an organic molecule, is provided as part of the overall device. This simplifies the analysis and permits sensor use by non-specialised personnel. A drawback however is that luminescent species needs to be replenished over time and can be influenced by environmental factors, such as temperature and pH.

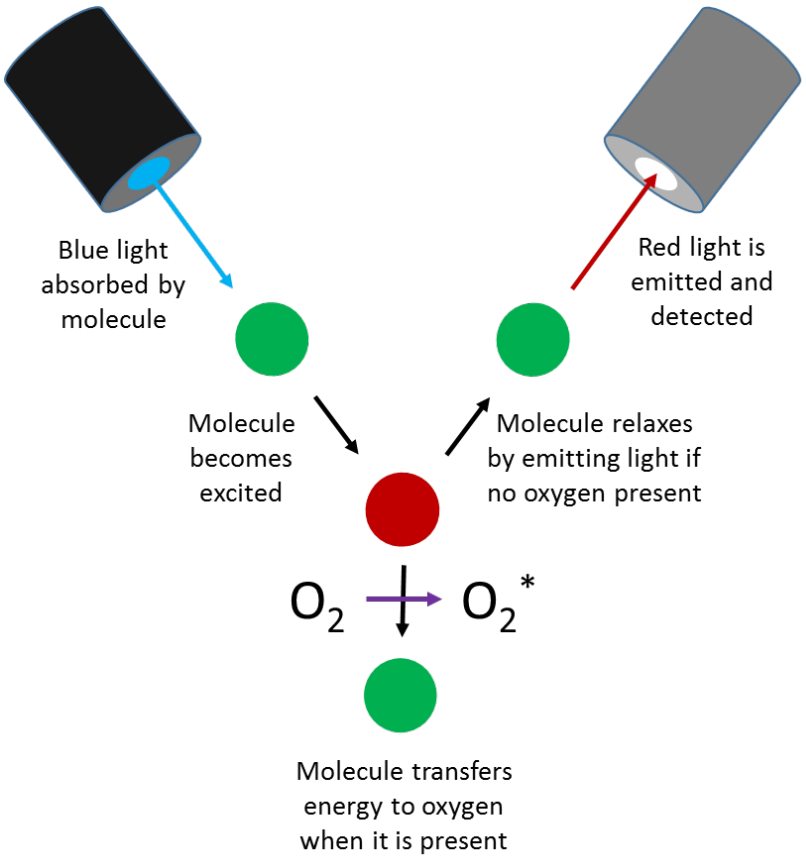

Figure 5-2 Schematic representation of the optical DO probe showing how the production of an excited oxygen species (O_2*) results in less light being detected.

Electrochemical approaches to DO sensing, typically involve measurement by direct reduction of oxygen at an electrode surface. The reaction that governs this is shown in Equation 4.17:[11, 12]

$$O_2 + 4H^+ + 4e^- \rightarrow 2H_2O \qquad \text{Equation 5.1}$$

The most popular of these sensors is the Clark membrane configuration, which was invented in 1959 and is represented by the schematic in Figure 5-3.[13] This approach incorporates an oxygen permeable membrane behind which electrodes and electrolyte are placed. Applying the appropriate potential results in oxygen reduction, the current of which is directly proportional to the concentration.[14] The membrane acts to ensure that only oxygen reaches the electrode surface. The oxygen reduction reaction, which occurs at cathodic potentials, is subject to interference from other species, particularly in a complex matrix like water. While this is certainly less expensive than the optical method, issues arise when trying to miniaturise the sensor device due to the requirement for a membrane. Miniaturisation is important to facilitate portability, but also to minimise consumption of oxygen. Reduction of oxygen is a destructive process, see equation 5.1, as the oxygen is irreversibly reduced to water therefore, larger electrodes may inadvertently change the DO concentration. However, complex fabrication methods are required for the membrane at smaller scales, and as a result a lot of research focuses on improving these methods.[10, 15-17] Elimination of the membrane would make miniaturisation of devices significantly easier, but also opens the potential for interferents, such as chlorine, adversely affecting DO detection. In this work, we propose a method to quantify DO using IDEs. In this approach, hydrogen peroxide (H_2O_2), produced as an intermediate species in oxygen reduction, is used as an indicator of overall DO concentration. This method permits facile, interference-free DO quantification, without the need for an oxygen permeable membrane, consequently enabling miniaturisation.

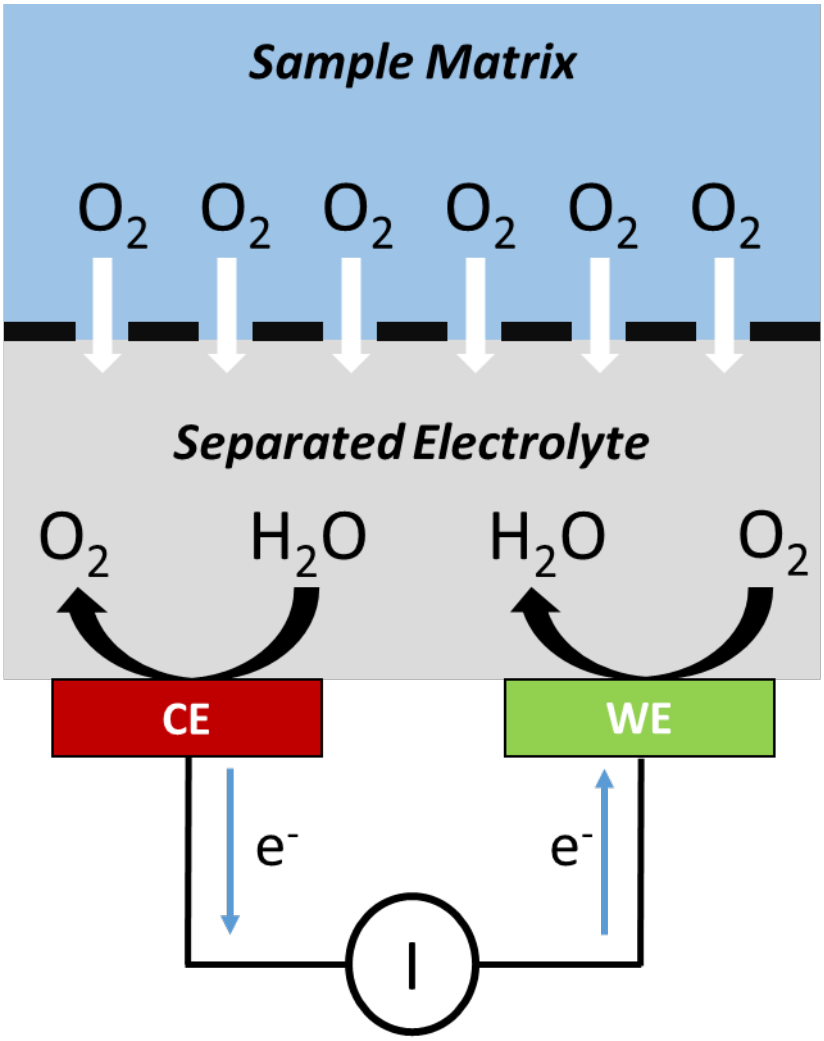

Figure 5-3 Schematic representation of the interface between the Clark electrode surface and the sample solution. The gas permeable membrane facilitates the transfer of oxygen gas only to the inner electrolyte

5.1.3 The Oxygen Reduction Reaction

To understand the sensing approach taken in this work, it is first necessary to explain the Oxygen Reduction Reaction (ORR). Equation 4.17 shows the summarised one-step pathway for reduction of oxygen. This is just one pathway for the ORR however, which has been studied extensively with respect to fuel cell technology. The Proton Exchange Membrane fuel cell uses hydrogen as a fuel but is limited by the large overpotential associated with oxygen reduction. Therefore materials are being studied that can replicate this reaction at lower overpotentials.[18] The one step pathway involves four electrons per

molecule of oxygen, resulting in a high current flow. The alternative to this is the two-step pathway, wherein hydrogen peroxide is produced as an intermediate and is subsequently reduced to water. This pathway is shown by Equation 5.2 and Equation 5.3.[19, 20]

$$O_2 + 2H^+ + 2e^- \rightleftharpoons H_2O_2 \qquad \text{Equation 5.2}$$

$$H_2O_2 + 2H^+ + 2e^- \rightleftharpoons 2H_2O \qquad \text{Equation 5.3}$$

Production of hydrogen peroxide is seen as an interferent in fuel cell research, thus great efforts go to choose materials and conditions that prevent its production. In this work, the production of hydrogen peroxide is vital to the sensor performance, so materials and conditions that promote the two-step pathway are required.

Two common materials employed for probing the ORR are gold and platinum. The consensus in the literature is that gold electrodes facilitate the two-step pathway, while platinum electrodes facilitate the one-step pathway. Sarapuu et al have shown that the reaction pathway for gold, for both bulk and ultra-thin film electrodes favour the two step pathway.[21] Similarly Tammeveski et al have shown that bulk and ultra-thin film platinum electrodes favour the one-step pathway.[22] To understand why this is the case, a more detailed explanation of the oxygen reduction reaction is required. The mechanism for the two step reaction is typically referred to as the peroxo mechanism, while the one step reaction is referred to as the metal oxide mechanism.[23] The peroxo mechanism is shown in equations 5.4 – 5.7.[24] In this mechanism, the bond between the oxygen atoms is not broken until both atoms have been protonated, therefore hydrogen peroxide exists as an intermediate species, which can desorb from the surface into solution.

$$O_2 + e^- \rightarrow O_2^- \qquad \text{Equation 5.4}$$

$$O_{2(ads)}^- + 2H^+ + e^- \rightarrow H_2O_{2(ads)} \rightleftharpoons H_2O_2 \qquad \text{Equation 5.5}$$

$$H_2O_{2(ads)} + H^+ + e^- \rightarrow H_2O + OH_{(ads)}$$ Equation 5.6

$$OH_{(ads)} + H^+ + e^- \rightarrow H_2O$$ Equation 5.7

The subscript (ads) means that the species is adsorbed on the electrode surface where the reaction takes place. The production of the superoxide anion, shown in equation 5.4 is the subject of some debate, as it may occur by either an inner-sphere or outer-sphere mechanism. An outer-sphere mechanism involves electron transfer from a species that may not directly interact with the electrode surface. By contrast, an inner-sphere mechanism requires adsorption of some component of the electroactive species.[25]

The metal oxide mechanism differs from the peroxo mechanism, in that the bond between the oxygen atoms is broken before both oxygen atoms have been protonated, therefore hydrogen peroxide typically is not produced as an intermediate species. This mechanism can be further subdivided into associative and dissociative oxygen reduction, depending on when the oxygen bond cleavage occurs. The associative mechanism is: [26, 27]

$$O_{2(ads)} + H^+ + e^- \rightarrow HO_{2(ads)}$$ Equation 5.8

$$HO_{2(ads)} + H^+ + e^- \rightarrow H_2O + O_{(ads)}$$ Equation 5.9

$$O_{(ads)} + H^+ + e^- \rightarrow OH_{(ads)}$$ Equation 5.10

$$OH_{(ads)} + H^+ + e^- \rightarrow H_2O$$ Equation 5.11

While the dissociative mechanism is:[26, 27]

$$O_{2(ads)} \rightarrow 2O_{(ads)}$$ Equation 5.12

$$2O_{(ads)} + 2H^+ + 2e^- \rightarrow 2OH_{(ads)}$$ Equation 5.13

$$2OH_{(ads)} + 2H^+ + 2e^- \rightarrow 2H_2O$$ Equation 5.14

While matrix effects, such as pH and temperature can impact which mechanism is observed, for the purposes of this thesis, the electrode effects will be focused on solely the peroxo mechanism. In this case, the interaction between oxygen and the electrode

will determine how the reaction progresses. The peroxo pathway typically occurs when there is weak interaction between the electrode and oxygen. Therefore, peroxide is measurable in the solution as it is weakly bound to the electrode surface. Gold typically shows this behaviour as it is known for its weak adsorption ability.[28] Weak surface adsorption means that the cleavage of the oxygen bonds is energetically unfavourable, as the surface does not provide an adequate catalytic site. Thus, the oxygen bonds are not broken until both oxygen sites have been protonated. The metal oxide pathway is characteristic of electrode materials that show strong adsorption ability for oxygen. In such cases, little to no peroxide is observed as the surface binding is strong, so dissociation is unfavourable. Platinum typically shows this behaviour, as it catalyses the cleavage of the oxygen bonds.

It is easy to assume that using a gold electrode will result in production of hydrogen peroxide, while use of a platinum electrode results generally in no hydrogen peroxide being produced. This however is not always the case as the electrode surface morphology can dramatically change the oxygen reduction activity. For example, different crystal structures of gold can result in greater production of hydrogen peroxide, while different crystal structures of platinum can result in lower overpotentials for oxygen reduction.[29] Certain crystal structures can also result in a reversal of the expected behaviour. For example, oxygen reduction on the gold (100) single crystal surface proceeds via the metal oxide $4e^-$ pathway.[30, 31] This is because the orientation of gold atoms facilitates the side-on adsorption of oxygen, which makes it energetically favourable to cleave the oxygen bonds. As most gold crystal structures reduce oxygen via the peroxo mechanism, it can be expected that polycrystalline gold electrodes behave in this way also. Electrode preconditioning needs to be considered also, as this can significantly impact the oxygen reduction reaction. For example platinum electrodes can be made to proceed via the two-

step pathway, which is typically uncommon, provided pre-treatment to form a surface oxide on the electrode is carried out prior to analysis.[21, 32] In this case, many of the catalytic platinum sites are blocked to oxygen, therefore side-on adsorption is not possible. The resulting end-on adsorption makes it energetically unfavourable to cleave the oxygen bonds, and the peroxo mechanism dominates. As with gold, polycrystalline platinum electrodes tend to follow the general trend of oxygen reduction. However, as some crystal structures may facilitate the peroxo mechanism, trace amounts of hydrogen peroxide can be expected when using platinum electrodes. Increasing the electrochemically active surface area, typically by roughening the electrode or making nanostructures, tends to help catalyse the formation of hydrogen peroxide.[33, 34]

The detection of hydrogen peroxide during oxygen reduction has classically been achieved using a rotating ring disc electrode (RRDE) configuration.[35-37] These are used to push the produced hydrogen peroxide to the ring electrode by convection forces, ensuring maximum collection of the produced hydrogen peroxide. Typically, the collection efficiencies are quite low in comparison to generator-collector experiments done using a redox couple. Collection efficiencies of 15-25% are considered desirable in these experiments. Detection of hydrogen peroxide is dependent on the dissociation from the generator electrode. Therefore, high collection efficiencies are not typically expected. The RRDE set-up however, can be quite complex and cannot be miniaturised for portable sensing applications. An alternative to the RRDE for the detection of produced hydrogen peroxide is the interdigitated electrode array (IDE). In this set-up, detection at the collector is governed by diffusion of hydrogen peroxide, rather than by convection. This has been shown to be a viable approach by Postlethwaite et al. [38] The major drawback being a lower observed collection efficiency by comparison. While low collection

efficiencies are expected for this reaction, the IDE method shown by Postlethwaite had a hydrogen peroxide collection efficiency of just 5%. However, by working with IDEs having smaller electrode gaps and widths, such as 1 μm for both dimensions, this efficiency can be increased significantly. The IDE approach also has the major benefit in that it also permits redox cycling, i.e., where the same molecule can be reduced and oxidised a number of times. In the RRDE set-up, at the ring collector electrode the product of oxidised hydrogen peroxide (i.e., oxygen) is pushed away by the prevailing convection forces from the disc electrode. In the IDE set-up, it can diffuse back to the generator electrode to be reduced again, thus improving sensitivity.

In this chapter, oxygen reduction to hydrogen peroxide is investigated, using both gold and platinum IDEs, to determine which material has a better performance at this scale. Fabrication of single metal IDEs requires fewer processing steps than a mixed metal IDE, therefore sensor devices comprising of two IDEs were fabricated as either gold-gold or platinum-platinum. While gold is anticipated as being the superior metal, platinum may have the appropriate behaviour at the ultra-micro scale to suit the desired detection method. These experiments were also performed in generator-collector mode to oxidise any hydrogen peroxide produced. Subsequently, each metal's ability to oxidise hydrogen peroxide was also tested to establish the preferred collector material. Parameters were established for the appropriate sensing technique, including the relevant pre-treatment steps. Finally, this method was applied to river water samples using a custom-built portable miniature potentiostat device, which had been developed specifically for this analysis.

5.2 Experimental Materials and Methods

5.2.1 Electrode Fabrication and Characterisation

Electrodes were fabricated, cleaned, and characterised as described in chapter 3. Unless otherwise stated, each array in this work had a 1 µm gap between the generator and the collector electrodes and the electrodes were 1 µm wide. Each device had 20 generator and 21 collector electrodes per array.

5.2.2 Electrochemical Oxygen Reduction on Gold and Platinum Electrodes – Initial Calibration with µIDEs

Electrochemical oxygen reduction was carried out in artificial drinking water (ADW). ADW was allowed to saturate with oxygen through exposure to air at room temperature (~17 ºC). Low concentration oxygen samples were prepared by purging the ADW solutions with nitrogen for 30 minutes. After purging, the ADW samples were covered with parafilm which contained a small perforation. This allowed oxygen to dissolve back into solution, albeit at a slow rate. It was found that oxygen typically re-dissolved at rate of approximately 1 ppm per 3 minutes when the concentration was between 0 and 4 ppm. After 4 ppm was reached, the rate slowed down to 1 ppm per 7 minutes until a 6 ppm concentration was reached. To bring the solution back to saturated concentrations, oxygen had to be bubbled into the solution, as the time to reach saturation by diffusion was considerably longer. This resulted in ADW solutions with various oxygen concentration between fully purged (~0.5 ppm), and fully saturated (~8.8 ppm). All oxygen concentrations were measured using a commercial optical DO probe (Hach, LDO101). Electrochemical analysis was carried out using an Autolab potentiostat, with the electrochemical cell positioned within a Faraday cage. A commercial 12.5 µm diameter

gold disc electrode as well as gold-gold and platinum-platinum IDE arrays were used for this work. CVs were performed in each concentration of oxygen sweeping from 1.2 V to – 0.8 V vs. Ag/AgCl at 50 mV/s for 3 cycles, with the data shown being the third scan. LSVs were also performed using the same parameters. The effect of pH on oxygen reduction was also investigated by performing CVs and LSVs in ADW samples between pH 5 and 9. ADW samples were adjusted with 0.1 M HCl and 0.1 M NaOH, respectively.

5.2.3 Electrochemical Oxidation of Hydrogen Peroxide on Gold and Platinum Electrodes

Varying concentrations of hydrogen peroxide solutions (between 20 and 1000 µM) were prepared by diluting a hydrogen peroxide stock (Sigma Aldrich, 30% w/w) with ADW. LSVs were performed in each sample in the voltage range of -0.2 V to 0.8 V vs. Ag/AgCl at 50 mV/s. Scans were performed in triplicate for each concentration. The effect of pH was also investigated by adjusting the pH range from 5 to 9 (adjustments using 0.1 M HCl or 0.1 M NaOH) of a 100 µM sample of hydrogen peroxide and LSVs undertaken

5.2.4 Investigation of Hydrogen Peroxide Production from Oxygen Reduction on Gold and Platinum Electrodes using Generator-Collector Analysis

ADW samples saturated with oxygen were used to determine which metal, Au or Pt, produced higher amounts of hydrogen peroxide. Both metals have the ability to sufficiently oxidise hydrogen peroxide, therefore Au-Au and Pt-Pt Generator - Collector arrays were used for this analysis. CV analysis using the same parameters described in 5.2.2 was undertaken. The only adjustment made being the biasing of the collector electrode comb at 0.6 V vs. Ag/AgCl. The effect of pH on this reaction was also

investigated, again using ADW samples between pH 5 and pH 9 adjusted as described previously.

5.2.5 Platinum Plating on the Collector Electrode

Platinum was plated on one comb of a gold IDE to give Au-Pt arrays with a view to improving the sensitivity of the hydrogen peroxide detection. As in chapter 4 a commercial platinum DNS bath was used. The collector comb was held at a cathodic current of 0.108 μA for one minute to achieve a platinum plate approximately 83 nm thick.

5.2.6 Calibration of Oxygen concentration by Detection of Hydrogen Peroxide using Gold-Platinum Interdigitated Electrode Arrays

Samples of ADW with varying concentrations of oxygen were made as previously described in section 5.2.2. LSV was performed in each concentration, using the Au-Pt mixed metal IDE, in the voltage window of 1.2 V to -0.8 V vs. Ag/AgCl. The Au generator was scanned while the Pt collector was biased at 0.3 V to oxidise the generated hydrogen peroxide. Prior to any scan, the Pt collector was biased at -0.8 V for 20 seconds as a pre-treatment step to remove any oxide that may have formed on the surface of the Pt electrode.

5.2.7 Calibration of Oxygen concentration in River Water using Gold-Platinum Interdigitated Arrays and a Homemade Portable Potentiostat

Water samples were taken from the River Lee (Cork, Ireland) and tested using the Au-Pt IDE and a bespoke portable system compromising a silicon chip based potentiostat. The system was controlled using an application developed for Android phones by Mr Aidan

Murphy. Various concentrations of oxygen in river water were made as described for ADW in section 5.2.2. CV analysis was performed for each concentration in the voltage range of 0.6 V to -0.9 V vs. Pt at 50 mV/s. The Pt collector was biased at 0.3 V for each of these scans.

5.3 Results and Discussion

5.3.1 Oxygen Reduction at a Commercial Gold Microdisc Electrode

Initial work was carried out on a commercial gold microdisc electrode with a diameter of 12.5 µm. A standard three electrode cell set-up was used with a Ag/AgCl reference electrode and a platinum mesh counter electrode. A range of oxygen concentrations in ADW at pH 8 were tested to establish how the behaviour changes in saturated and purged solutions. Figure 5-4 shows the CVs of each oxygen concentration at the gold microdisc electrode. The scans started at 1.2 V to generate a surface oxide on the gold electrode. Subsequent reduction of the gold surface ensured a clean, reproducible surface for each measurement. Two reduction events occur at the gold surface. The first event, indicated by a current plateau at approximately -0.3 V is the reduction of oxygen to hydrogen peroxide (see Equation 5.2). The second reduction event at approximately -0.8 V is the subsequent reduction of hydrogen peroxide to water (see Equation 5.3). Beyond -0.9 V, gas evolution was observed and no further information about the oxygen reduction reaction could be obtained. The variation seen in the reduction currents from low to high oxygen concentrations further confirmed that the reduction events were attributed correctly as all other components of the samples remained constant. Figure 5-5 shows the subsequent calibration plot, indicating a reasonably good linearity of 0.95 and a sensitivity to oxygen of 0.54 nA/ppm. The expected current at the microdisc was calculated using the equation:

$$i = 4nFD_0Cr \qquad \text{Equation 5.15}$$

Where F is faradays constant (96485.332 C/mol), D_0 is the diffusion coefficient of oxygen (2.01×10^{-5} cm^2/s),[39] C is the concentration of oxygen in solution (8.35 ppm = 2.61×10^{-7} mol/cm^3), r is the radius of the electrode (6.25×10^{-4} cm) and n is the number of electrons

passed (4). From this an expected current of 5.06 nA was calculated. The measured current at 8.35 ppm was determined to be 5.2 nA, which is in good agreement with the predicted value. The parameters established at the microdisc electrode were subsequently applied to the IDE electrodes.

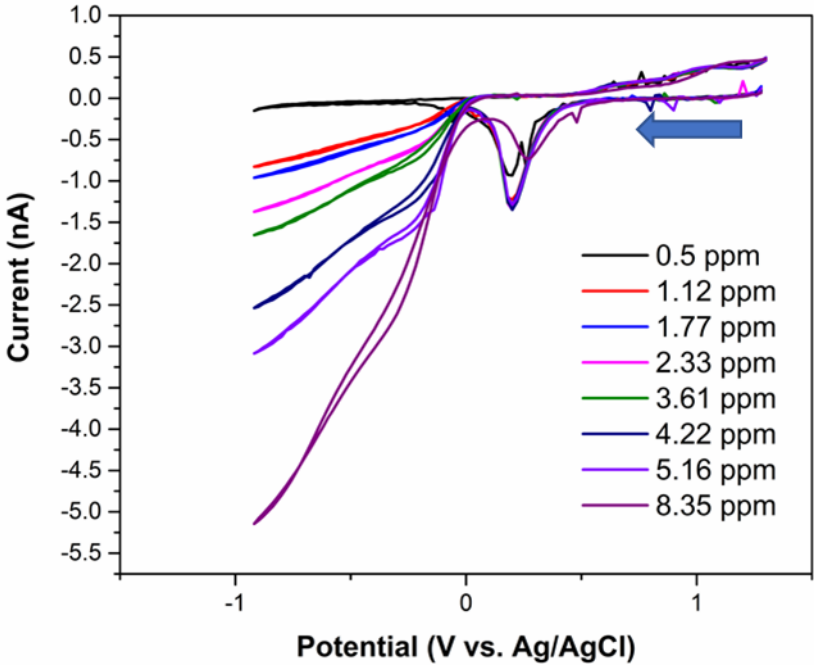

Figure 5-4 CVs of various oxygen concentrations in ADW at pH 8 on a commercial gold microdisc electrode. The electrode was swept from 1.2 V to -0.9 V at 50 mV/s. The arrow indicates the sweep direction.

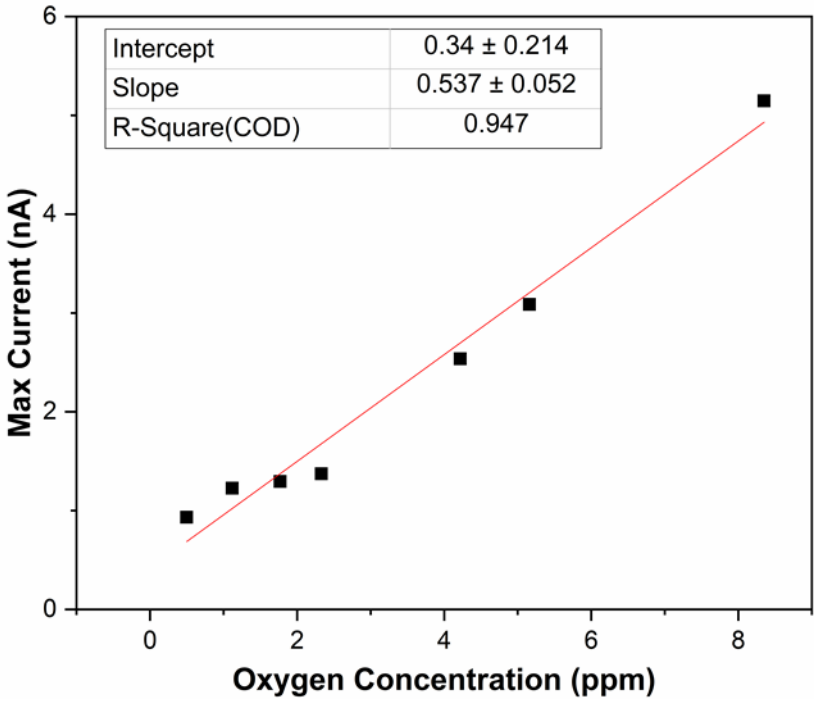

Figure 5-5 Calibration plot for current at -0.9 V for oxygen reduction in ADW at the commercial microdisc electrode.

5.3.2 Oxygen Reduction at Gold and Platinum Interdigitated Electrode Arrays – One-Step versus Two-Step Reduction Mechanisms

Oxygen reduction in ADW was subsequently investigated using one comb of both gold and platinum IDEs. In Figure 5-6 it is clear that the behaviour for the gold IDE was similar to the behaviour observed for the gold microdisc electrode. The main difference being that the second reduction at -0.9 V, attributed to the reduction of hydrogen peroxide was not a well-defined plateau. This was attributed to the earlier onset of gas evolution, as the ultra-microelectrode may be more efficient at carrying out this reaction than the larger disc electrode. The IDE device has more potential nucleation sites resulting from the corners and edges that may act as catalytic sites for gas evolution. However, this had no major impact on this work as the first reduction step, which was unaffected, and was the step of interest.

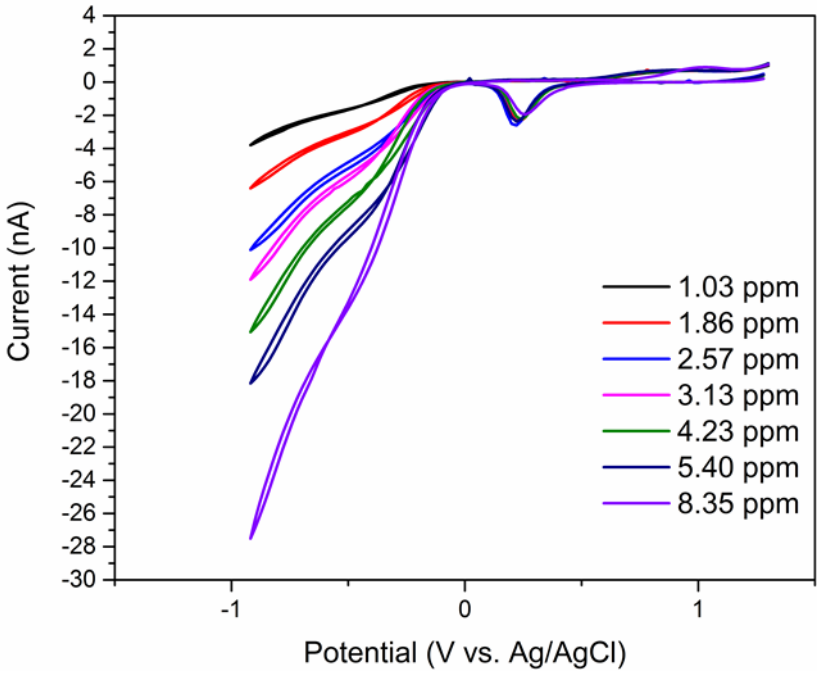

Figure 5-6 CVs of various oxygen concentrations in ADW on one comb of a 1 µm gap gold-gold IDE. The electrode was swept from 1.2 V to -0.9 V at 50 mV/s.

The subsequent calibration, shown in Figure 5-7 indicated a much greater linearity of 0.99 and an enhanced sensitivity to oxygen of 3.19 nA/ppm. The improvement in linearity was most likely a result of the experimental set-up. The 3-electrode cell set-up used for the commercial microdisc was carried out in a 10 mL beaker. Thus, a greater surface area was exposed to the atmosphere. The beaker had a surface area of 491 mm^2 exposed to the atmosphere, while the IDE cell had only a 16 mm^2 surface area exposed. This meant that oxygen could re-dissolve into the purged solutions at a faster rate in the 10 ml beaker. This may have resulted in an under estimation of the oxygen concentration, however it is difficult to know the degree to which it was underestimated, as oxygen measurements were performed in the stock solutions. As mentioned, the IDE set up required significantly less sample volume, approximately 2 mLs, and less exposure of the surface area to the atmosphere. As a result, oxygen may re-dissolve at a slower rate, so the measured values are closer to the actual oxygen concentrations. The measured currents were expected to be higher, however at the applied scan rates, diffusional overlap will occur with the 1 µm

gap spacing, and as a result the full benefits of the array were not realised.[40] To confirm the degree of overlap, the predicted currents were calculated by first estimating the current at a single microband. This was done using the microband equation:

$$i = \frac{nFlC2\pi D}{\ln\left(\frac{64Dt}{w^2}\right)} \qquad \text{Equation 5.16}$$

Where l is the length of the band (45×10^{-4} cm) and w is the width (1.2×10^{-4} cm). In this case, a concentration of 8.6 ppm oxygen was used, so the concentration value was 2.68×10^{-7} mol/cm^3. From this, a current of 5.19 nA was predicted for a single microband. In Figure 5-8, it can be seen that the measured current for oxygen reduction on the single microband was 5.46 nA, which is in agreement with the predicted value. If the IDE electrodes were each acting independently, then the predicted value would be 5.19 nA multiplied by the number of electrodes, which is twenty. Thus, the predicted value for the array is 103.8 nA. However, it was found that the measured value was 27.5 nA, which means that the electrodes are not acting independently and cannot be described using the equation given for diffusion limited currents. If instead we calculate the predicted current based on the equation for a shielded array of electrodes, which was shown in Equation 5.17:

$$i = \frac{nFC_0D_0N\left(w_e + w_g\right)l}{\left(\pi D_0 t\right)^{1/2}} \qquad \text{Equation 5.17}$$

Where w_e is the electrode width and w_g is the gap width. From this, a predicted current of 4.95 nA was calculated. Again, this does not accurately represent the measured current. From this it was established that the behaviour at the electrodes was a combination of both effects due to partial diffusional overlap. The increased sensitivity compared to the microdisc was attributed to the IDE partially behaving as multiple diffusionally

independent electrodes. However, the sensitivity would be higher still if diffusional overlap had not occurred.

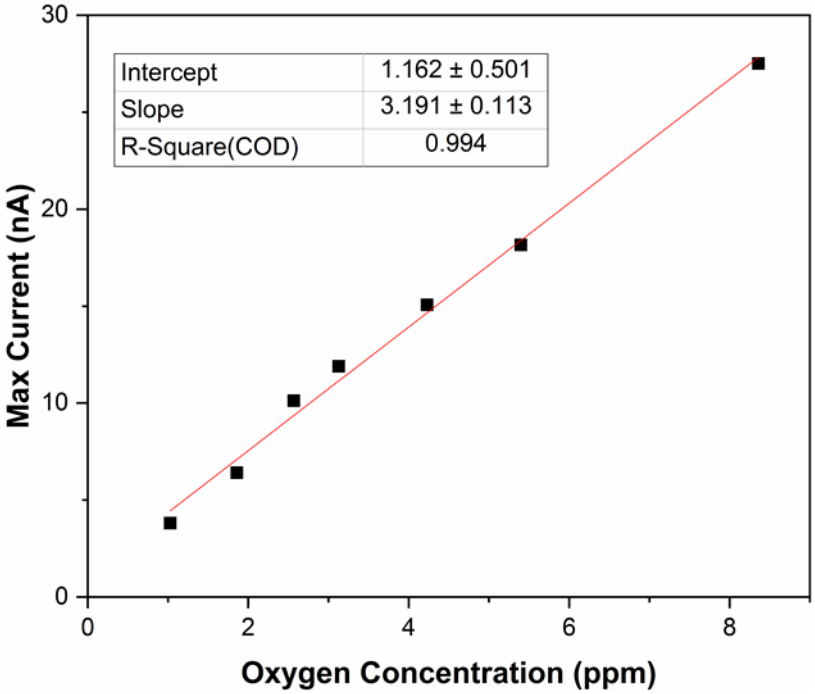

Figure 5-7 Calibration plot for current at -0.9V for oxygen reduction in ADW on the gold-gold IDE.

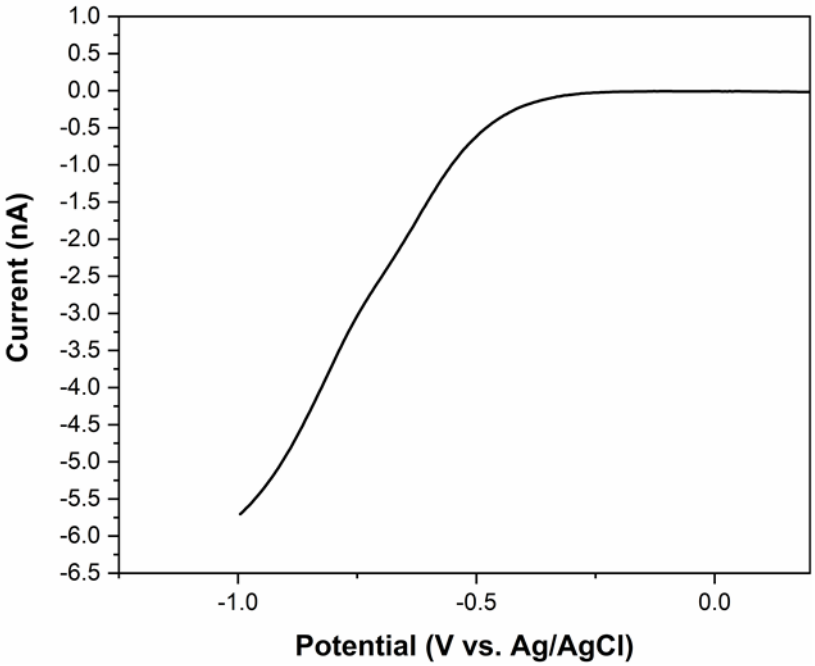

Figure 5-8 LSV of a single microband in ADW at pH 8 with 8.6 ppm oxygen. The electrode was swept from 1.2 V to -1 V at 50 mV/s.

A significantly different oxygen reduction behaviour was observed for a platinum IDE. Figure 5-9 shows the results of CVs performed in various concentrations of oxygen at the generator comb of the platinum IDE. The onset of reduction was seen at approximately -0.3 V on the forward scan. A single peak was observed with a maximum at between -0.45 V and -0.5 V, and a crossover, whereby the reverse scan crosses the forward scan, occurs on the reverse sweep. As only a single reduction event was observed, it was concluded that the platinum electrode reduces oxygen in a single step. Therefore, little or no hydrogen peroxide was produced as an intermediate species. The peak was determined to be a combination of two effects. The first being diffusional overlap, like the behaviour observed at gold. The second effect that caused this peak was reduction of the platinum oxide, which resulted in the crossover, or looping of the reverse sweep. Looping in CVs is usually explained by a complex reaction occurring due to formation of a new species, or by a change in the surface of the electrode monitoring a reaction. These scans were started at 1.2 V, where it has been shown that platinum oxides can form, much like for the gold electrode.[41] This surface oxide delays the reduction of oxygen to more cathodic potentials. When the oxide was reduced, the reverse scan showed the oxygen reduction on a bare platinum surface, hence the looping observed in the CV. To confirm this, the initial potential was changed to 0.2 V, below the oxidation potential, such that an oxide layer was not able to form. In this case, a steady state response was seen for oxygen reduction with an onset of approximately 0 V shown in Figure 5-10.

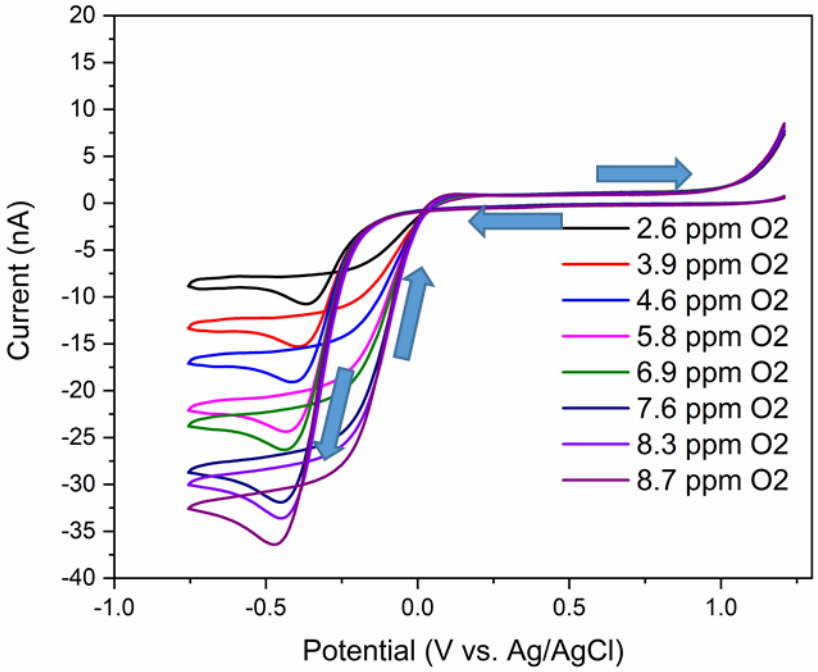

Figure 5-9 CVs of various oxygen concentrations in ADW at pH 8 on one comb of a 1 µm gap platinum-platinum IDE. The electrode was swept from 1.2 V to -0.75 V at 50 mV/s. The blue arrows show the direction of the scan.

Furthermore, the results shown in Figure 5-10 highlight other behaviours attributable to platinum electrodes. The sharp decrease in current at -0.8 V is due to gas evolution. At this potential, water splitting occurs, so hydrogen gas is being evolved at the electrode surface. Additional reduction peaks at -0.65 V and -0.75 V were observed which are a

result of adsorption of protons at the platinum surface. These protons were subsequently desorbed on the reverse sweep, shown by the oxidation peaks at -0.63 V and -0.5 V.

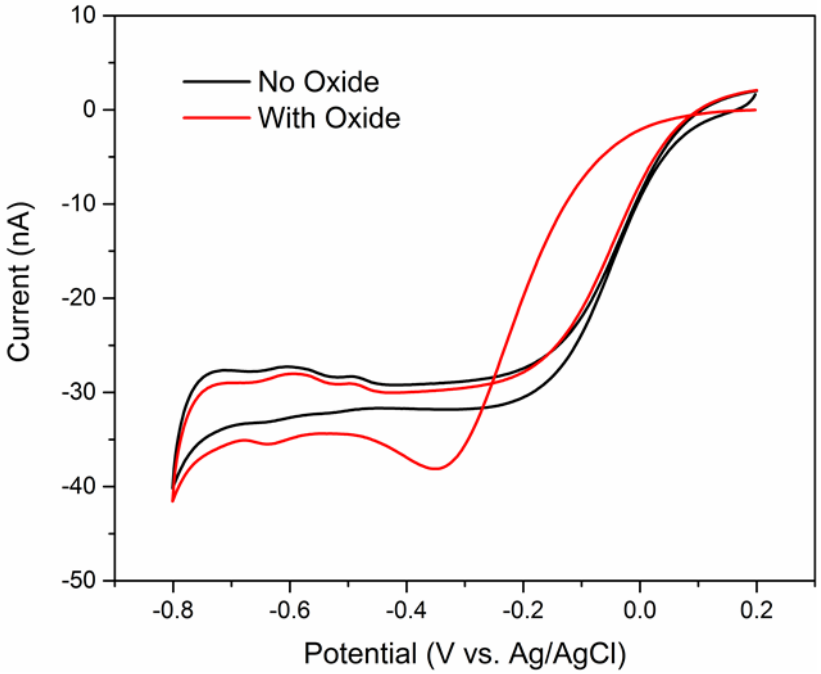

Figure 5-10 CVs in ADW at pH 8 saturated with oxygen. Red: CV started at 1.2 V to allow formation of an oxide. Black: CV started at 0.2 V so that no oxide was formed.

The resulting calibration plot, seen in Figure 5-11 showed that oxygen reduction on platinum was also linear with concentration with a R^2 of 0.99. The current values for the calibration plot were taken on the reverse sweep at -0.4 V, after the oxide had been removed. The sensitivity to oxygen was 3.81 nA/ppm, which is relatively close to the sensitivity established for a gold IDE. Both arrays have the same surface area, and ultimately reduce oxygen via a 4-electron transfer, so similar sensitivities were expected.

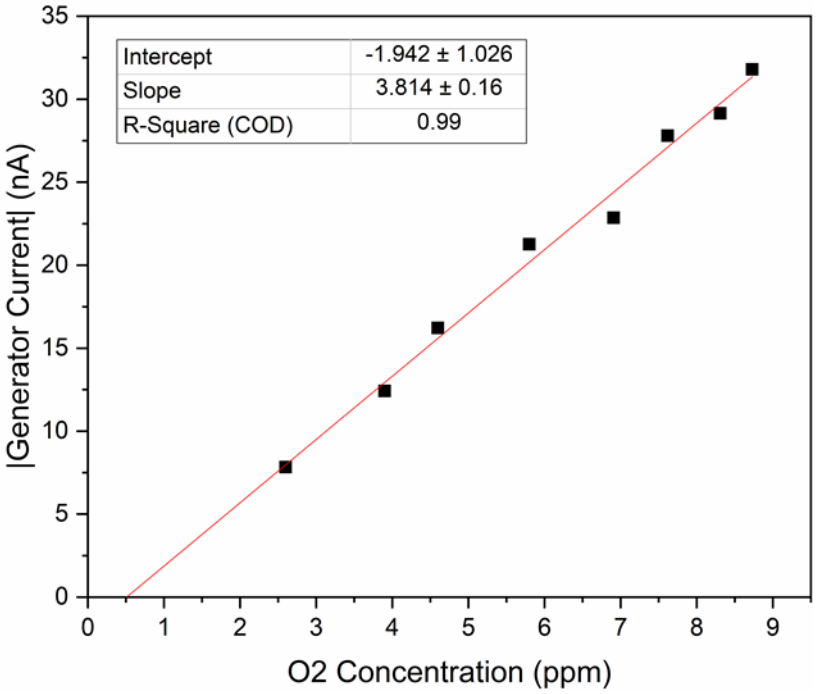

Figure 5-11 Calibration plot for the CVs of oxygen in ADW on the platinum-platinum IDE.

An additional oxidation event was observed on the reverse scan at the platinum electrode, that was not observed on gold. This is magnified in Figure 5-12 and was found to scale with concentration. This was attributed to trace amounts of hydrogen peroxide produced during the oxygen reduction. Even though gold electrodes tend to produce more peroxide, platinum shows better absorbance for oxygen species. Therefore, the produced peroxide at gold can diffuse away before subsequent oxidation, while it stays bound to the platinum surface until it can be oxidised. It was also found that platinum shows a better activity for the oxidation of hydrogen peroxide, which will be discussed in section 5.3.4.

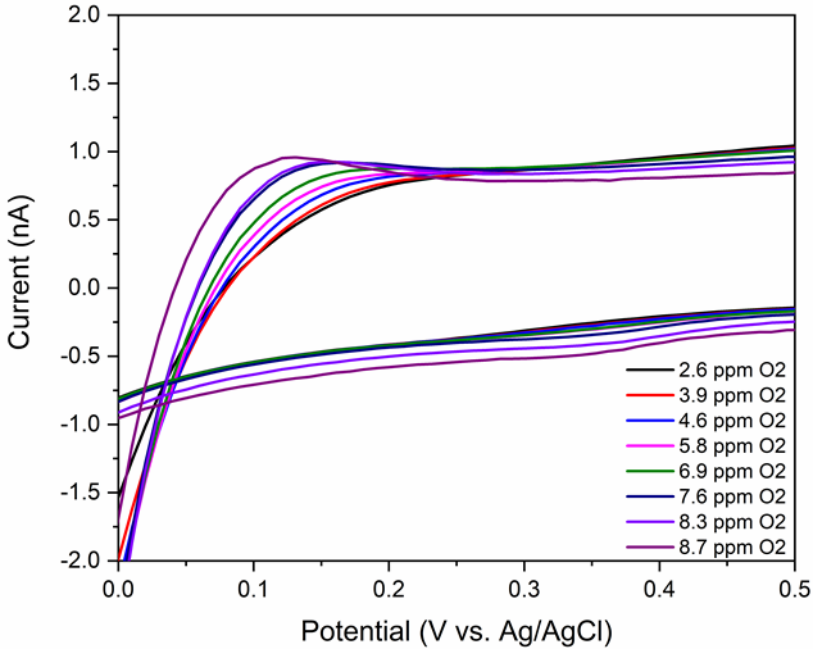

Figure 5-12 Magnification of the oxidation event observed at 0.1 V on the reverse sweep of the CVs at the platinum electrode.

Figure 5-13 shows a comparison of oxygen reduction at gold and platinum. Both electrodes were subjected to the same conditions of ADW with equivalent concentrations of dissolved oxygen. It is clear that oxygen reduction occurs at less negative potentials on platinum, however this reduction ultimately proceeds via the one step pathway. The gold electrode reduces oxygen at more cathodic potentials but does so via the two-step pathway. The current measured on the reverse sweep at the platinum electrode, therefore after the platinum oxide has been reduced, is equivalent to the current measured on gold after the second reduction step, at approximately 30 nA. Both IDEs have the same dimensions, so it was expected that the measured currents should be similar. This means that for both arrays, some degree of diffusional overlap is occurring such that the electrodes are acting as one larger electrode as opposed to an array of smaller ones.

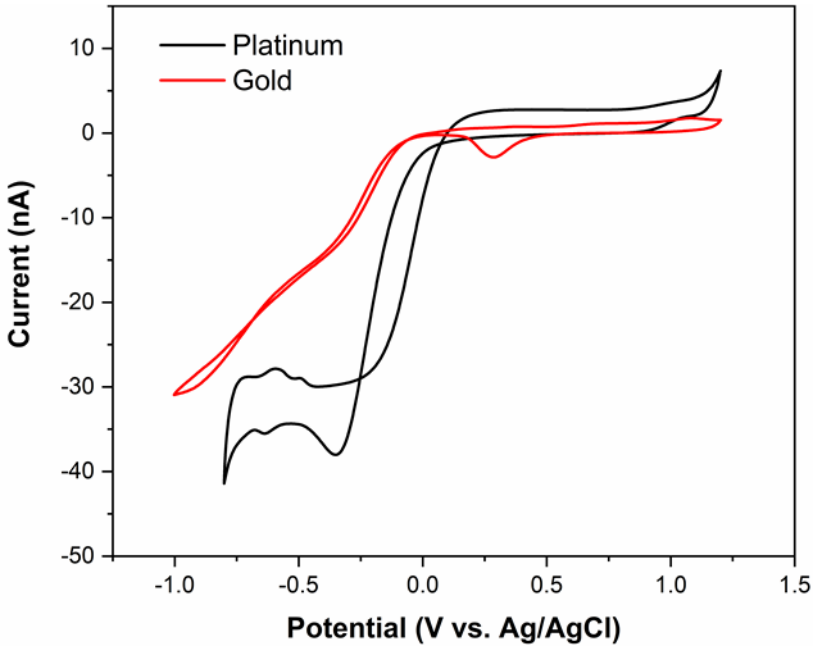

Figure 5-13 Comparison of oxygen reduction behaviour for a gold (Red) and platinum (Black) electrode in ADW at pH 8 with 8.5 ppm oxygen

5.3.3 Influence of pH on Oxygen Reduction at Gold and Platinum Electrodes

As described in Chapter 3, drinking water can have a range of pH values, consequently work was carried out to investigate how pH would affect the oxygen reduction. To this end, Figure 5-14 shows CVs for a gold IDE in ADW samples at various pH values. Typically, hydrogen peroxide production is maximised in highly alkaline conditions and at low overpotential values for most surfaces.[42, 43] This is due to the slow rate of hydrogen peroxide reduction to water as a result of the poor proton availability in basic solutions. As such, it was observed that the highest hydrogen peroxide concentration produced was at pH 9. This was determined by the increased current seen for the first reduction event, which has been attributed to hydrogen peroxide production.

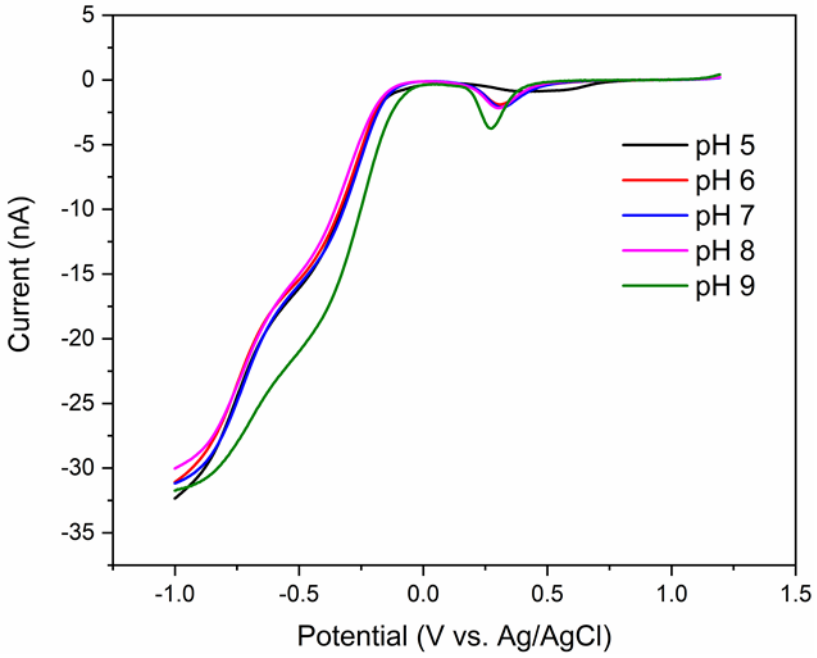

Figure 5-14 LSVs in ADW saturated with oxygen. CVs were performed on one comb of the gold-gold IDE in samples with different pH values.

The same procedure was performed on a platinum electrode. The results, shown in Figure 5-15 indicate that there was no major variation resulting from pH changes. The forward sweep, which showed the oxide reduction, was slightly different for the pH 7 sample, in that the current magnitude for the oxide reduction was lower. However, the reverse sweep, which in this case shows oxygen reduction on a clean platinum surface, showed no significant deviation. This indicated that under the range of conditions anticipated for drinking water, platinum only proceeds via the one-step reduction mechanism without peroxide formation. These tests indicated that gold was the ideal choice of material for production of hydrogen peroxide under all pH conditions. This work also indicates that an in-situ pH control method would be useful in enhancing the production of hydrogen peroxide.

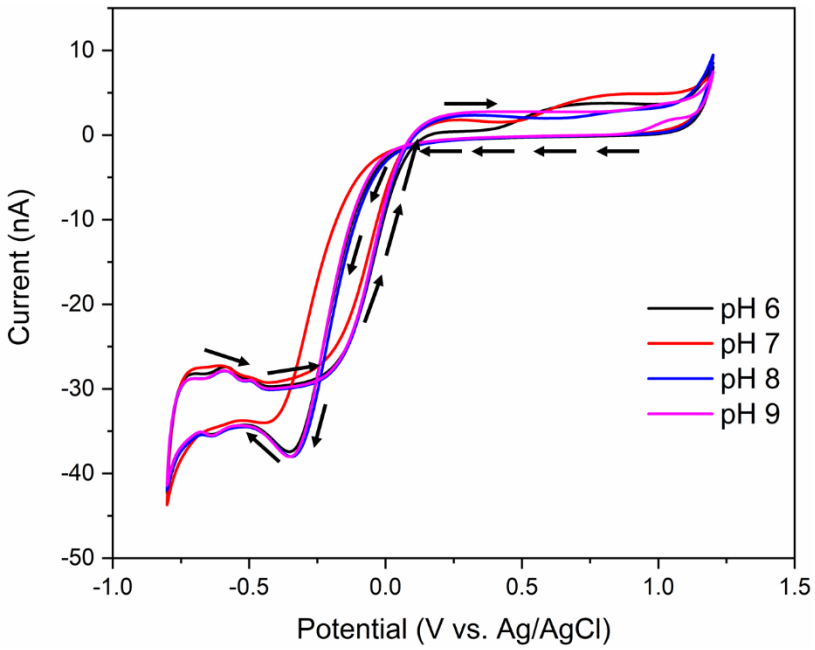

Figure 5-15 CVs in ADW saturated with oxygen. CVs were performed on one comb of the platinum-platinum IDE in samples with different pH values. The black arrows indicate the scan direction.

5.3.4 Hydrogen Peroxide Oxidation on Gold and Platinum Interdigitated Electrode Arrays

As the detection method for this sensor involves the oxidation of hydrogen peroxide, both gold and platinum were evaluated as potential detection materials by comparing the LSV response of both electrodes in 200 µM hydrogen peroxide. Hydrogen peroxide oxidation occurs via the reverse of the first step of the two-step oxygen reduction reaction, shown in Equation 5.18.

$$H_2O_2 \rightleftharpoons O_2 + 2e^- + 2H^+ \qquad \text{Equation 5.18}$$

Figure 5-16 shows the oxidation of hydrogen peroxide on one comb of both a gold IDE and a platinum IDE, respectively. The platinum electrode showed a superior oxidation, with a current taken at 0.7 V that was 1.5 times higher than the gold electrode. Interestingly, an oxidation event was observed at 0.2 V on platinum that was absent for gold. This has been attributed to dissociative binding of hydrogen peroxide to the platinum surface, before subsequently being oxidised and released as oxygen.[44, 45] The

secondary purpose of this experiment was to determine potential parameters for the fully operational device. The appropriate potential for collector electrode biasing was determined from these LSVs. The main peak was observed at 0.65 V for both materials. However, the platinum electrode could be biased at any potential from 0.2 V to 0.7 V and activity would be seen for hydrogen peroxide, which was another advantage over gold. The oxidation event on both materials displayed a peak shaped behaviour. Again, this can be explained by diffusional overlap.

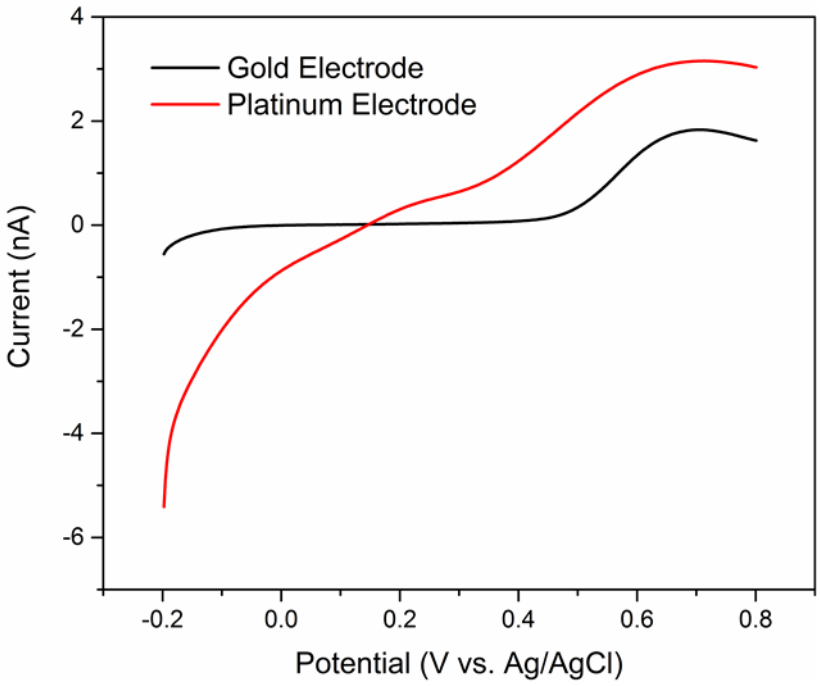

Figure 5-16 LSVs performed in 200 µM H_2O_2 solutions at pH 8. The electrodes were swept from -0.2 V to 0.8 V at 50 mV/s.

As platinum was identified as the preferred collector material, a calibration was carried out for a range of hydrogen peroxide concentrations to establish its sensitivity. The concentration range was chosen to reflect oxygen concentrations in water; which are expected to be between 2 ppm and 16 ppm depending on various factors described earlier, with 16 ppm being an extreme upper limit that requires low temperatures and high atmospheric pressures. It was observed that both the main peak at 0.65 V and the smaller peak at 0.2 V both increased with concentration, as shown by the LSVs in Figure 5-17.

The calibration plot, which is measured from the current at 0.75 V, shown in Figure 5-18 indicated that this increase was linear with a sensitivity of 0.01 nA/µM of hydrogen peroxide. Assuming that a 100% conversion occurs, this corresponds to hydrogen peroxide concentrations of approximately 60 – 500 µM .

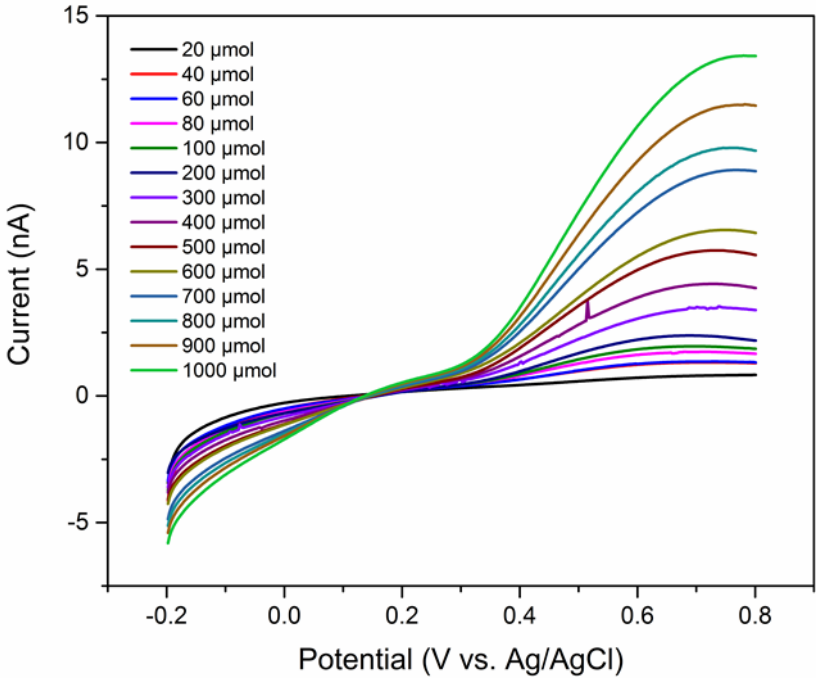

Figure 5-17 LSVs of various concentrations of H_2O_2 in ADW at pH 8 using one comb of a platinum-platinum IDE. The electrode was swept from -0.2 V to 0.8 V at 50 mV/s.

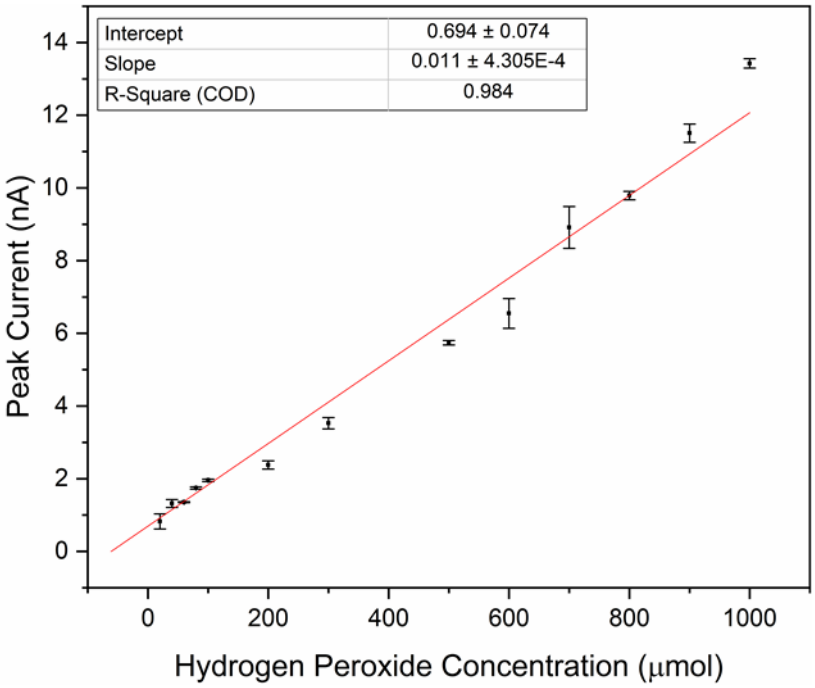

Figure 5-18 Calibration plot for H_2O_2 oxidation at 0.75 V at a the platinum IDE. Error was calculated from standard deviation of multiple scans (n=3).

5.3.5 Influence of pH on Hydrogen Peroxide Oxidation at Platinum Electrodes

As with the oxygen reduction, the pH influence on hydrogen peroxide oxidation was investigated. This was only performed using platinum, as gold has been eliminated as a potential collector material. A 500 µM of H_2O_2 sample was used to maximise any potential deviations. Figure 5-19 shows that no significant deviations were observed for each of the pH conditions tested. Each sample reached the same oxidation current, with slight deviations being attributable to experimental error. This was significant because the oxygen reduction behaviour has been shown to change with pH in Section 5.3.3. If the hydrogen peroxide oxidation was also affected by these pH deviations, then a complex calibration would need to be carried out to account for the two mechanisms. If a pH control method is employed, the only consideration is how oxygen reduction is affected, which makes the overall sensor easier to calibrate.

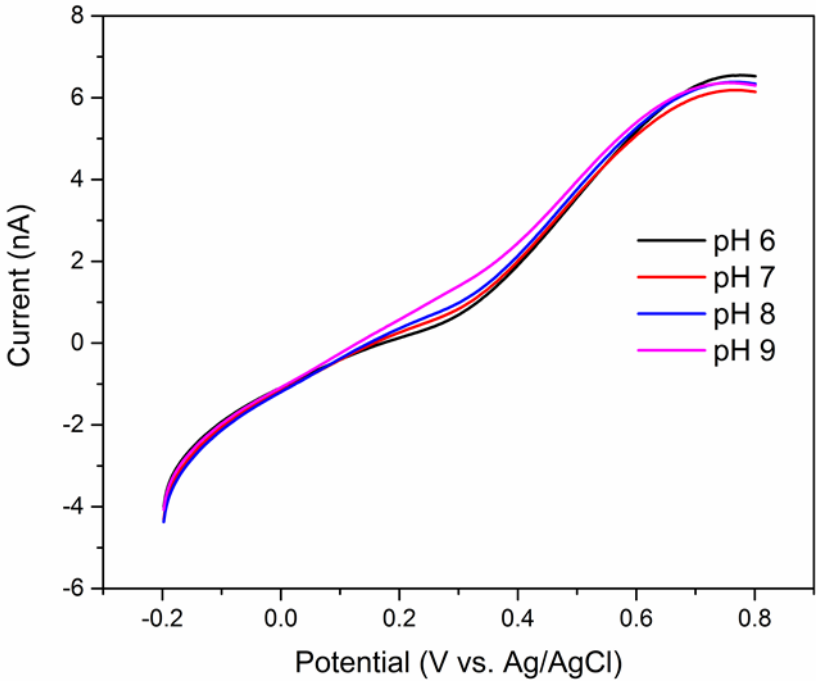

Figure 5-19 LSVs from -0.2 V to 0.8 V at 50 mV/s in 500 µM H_2O_2 at various pH values on one comb of a platinum-platinum IDE.

5.3.6 Production of Hydrogen Peroxide from Oxygen Reduction at Gold and Platinum Interdigitated Arrays

While gold had been established as the better material for the two-step reduction of oxygen, it was necessary to confirm that a detectable amount of hydrogen peroxide was being produced. This was undertaken using a gold IDE where one comb underwent CV (generator) while the other was biased at a constant potential (collector), suitable for oxidising hydrogen peroxide. The generator was swept from 1.2 V to -1 V while the collector was held at 0.6 V. Scans were performed at 50 mV/s to ensure that the produced hydrogen peroxide could diffuse to the collector before being consumed at the generator. Figure 5-20 shows the result of this test performed in ADW with an oxygen concentration of 8.6 ppm. The generator electrode measured a current of 26.86 nA, while the collector measured a current of 11.82 nA. From this, a collection efficiency of 44% was established. This value is significantly higher than current technologies where the collection of hydrogen peroxide is governed by diffusion. Improving upon this collection

efficiency makes these devices comparable to the current RRDE without the need for convective forces. While this percentage could have been increased by a smaller gap, the low collection efficiency was more likely attributed to the complex reaction mechanism. Firstly, complete conversion from oxygen in solution to hydrogen peroxide in solution is unlikely. Secondly, it is possible that the subsequent reaction consuming the hydrogen peroxide may result in lower amounts of the species reaching the detector. This is also why the collector scan shows a peak rather than a steady-state response. Consumption of hydrogen peroxide by the generator electrode results in the concentration at the collector reaching a maximum and subsequently decreasing. Similarly, the reactions of the two individual species needed to be considered. The collection efficiency can be quite high when testing ferrocene, as the analyte does not undergo a chemical change. In this case, the oxygen is chemically changing therefore a simple calculation for collection efficiency does not apply.

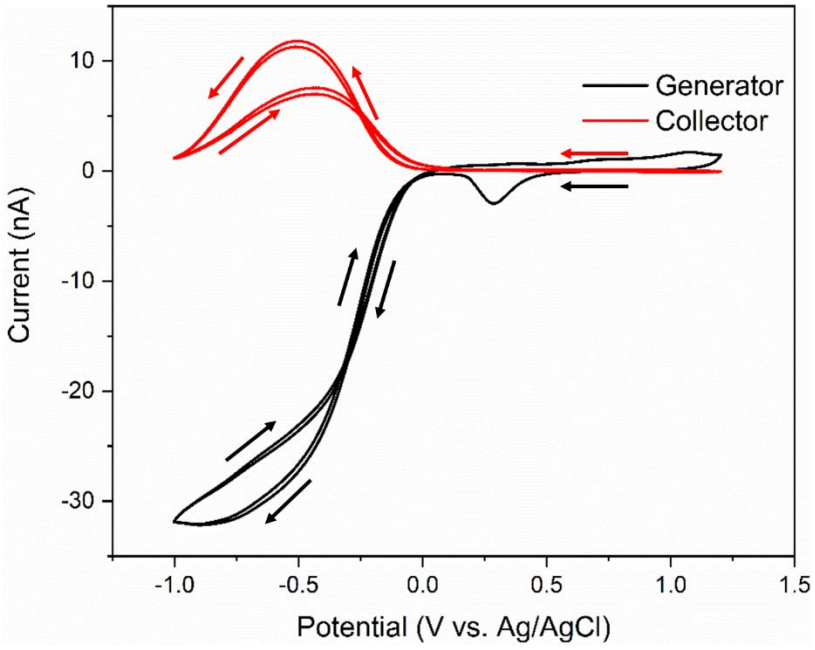

Figure 5-20 CVs performed in ADW at pH 8 saturated with oxygen on a gold-gold IDE. The generator electrode was swept from 1.2 V to -1 V at 50 mV/s while the collector electrode was biased at 0.6 V. The arrows indicate the scan direction for the generator and collector scans.

Comparison of the CVs performed in single mode and generator-collector (GC) mode showed that the oxygen/hydrogen peroxide species underwent significant redox cycling. In Figure 5-21, it can be seen that the current associated with the reduction of oxygen to hydrogen peroxide more than doubled when the collector was biased. In single mode, the current associated with reduction of oxygen to hydrogen peroxide was 15 nA. The predicted current for this reaction was 51.9 nA, based on equation 5.16. The measured current in generator-collector mode was found to be 26.86 nA. This increase is the result of two beneficial factors. The diffusion layer established at the collector electrode due to the oxidation of hydrogen peroxide prevents diffusional overlap, thus each microelectrode within the IDE acts independently. The second factor that caused a current increase was the redox cycling effect. The oxidation of hydrogen peroxide at the collector resulted in the production of oxygen. This then diffused back to the generator where it was again reduced to hydrogen peroxide. This process resulted in the same molecule being detected numerous times, i.e., redox cycling thus a current increase was observed. Although there was a current increase, it was still not as high as predicted (51.9 nA). The cycled hydrogen peroxide was consumed by the subsequent reaction to produce water. The produced water could not be oxidised back to hydrogen peroxide at the collector therefore no redox cycling was observed. The current for the second reduction step did not increase when the collector was biased because no competing reaction was occurring at the collector. A potential of 0.6 V has no effect on the produced water, therefore no reaction happened at the collector. The diffusion layers can subsequently overlap again, and the IDE behaves like a larger microelectrode. Overall a simple explanation is given for the redox cycling behaviour of the oxygen reduction reaction. In reality, surface adsorption of oxygen species, low collection efficiency of the reaction and the general

complexity of oxygen reduction make it difficult to accurately describe the processes occurring between the generator and collector electrodes.

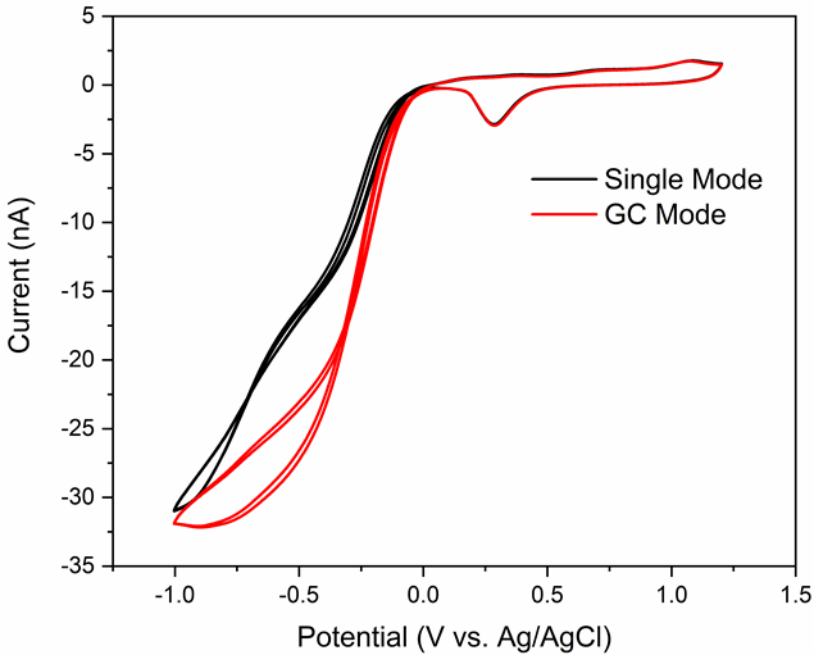

Figure 5-21 Comparison between CVs of gold electrodes in ADW. Black: No bias at the collector and no redox cycling observed. Red: Collector biased at 0.6 V resulting in redox cycling.

The same test was performed on a platinum IDE to further confirm that hydrogen peroxide is not produced in great quantities. Figure 5-22 shows that the collector response for platinum under the same conditions is extremely small. The reverse sweep of the generator electrode measured 29 nA, while the collector sweep measured approximately 1.2 nA. Again, the collector efficiency cannot give the complete picture but for platinum it is only 4%, significantly less than the gold electrode. Interestingly, the small amount of hydrogen peroxide produced is only measured on the forward sweep. Gold displayed hydrogen peroxide production on the reverse sweep, even though it was lower the forward sweep. Platinum however showed no hydrogen peroxide production at all. This indicates that the presence of a surface platinum oxide in some way facilitates the production of

hydrogen peroxide. The amount produced however was still too low for platinum to be considered as a generator material for the sensor.

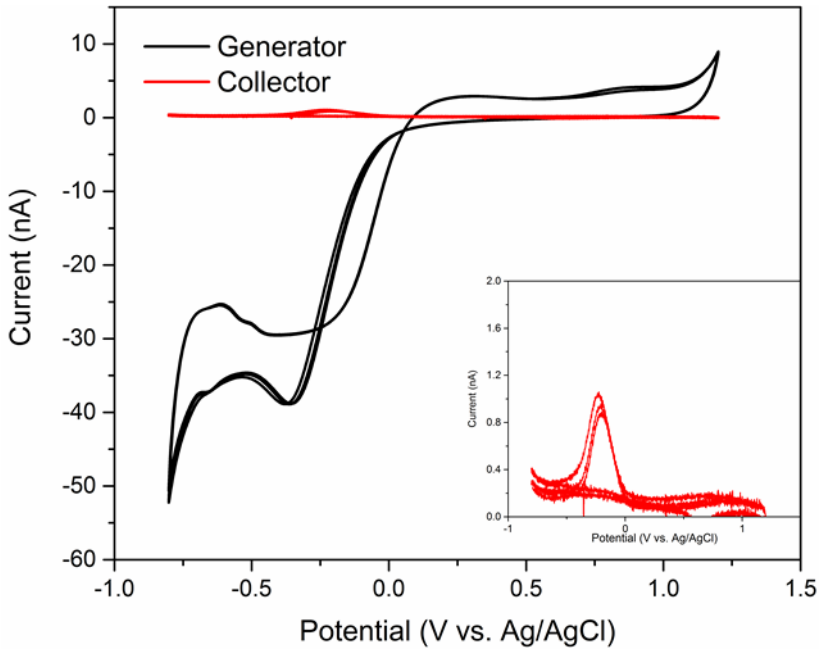

Figure 5-22 CVs performed in ADW saturated with oxygen on a platinum-platinum IDA. The generator electrode was swept from 1.2 V to -0.8 V at 50 mV/s while the collector electrode was biased at 0.6 V.

A comparison of platinum scans in single mode and generator collector mode is shown in Figure 5-23. Very little change was observed between the two scans, as redox cycling does not occur. The minute increase in current seen in generator collector mode stems from the collector bias preventing diffusional overlap.

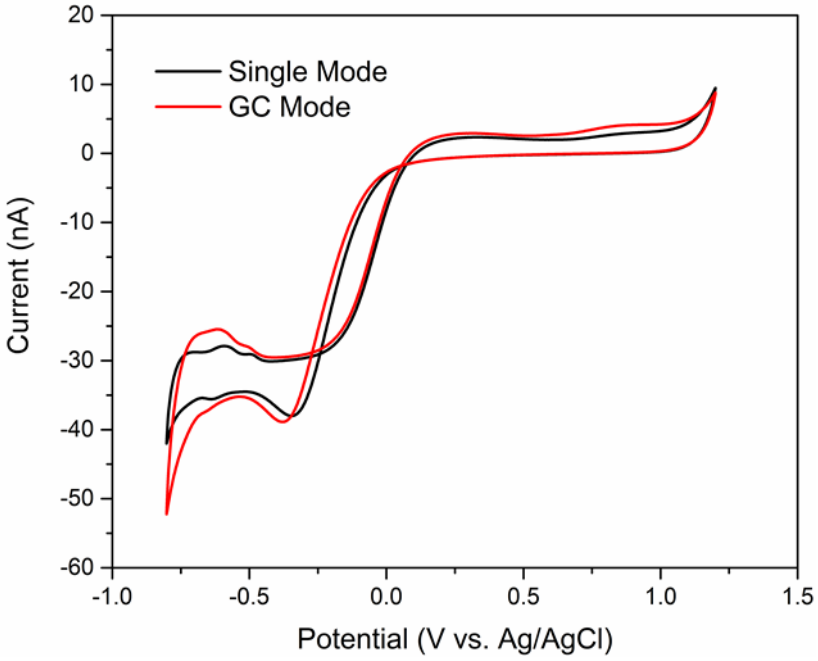

Figure 5-23 Comparison between CVs of platinum electrodes in ADW. Black: No bias at the collector. Red: Collector biased at 0.6 V. Redox cycling was not observed in either case.

5.3.7 Influence of pH on Hydrogen Peroxide Production at Gold Interdigitated Electrode Arrays

It was previously shown that pH has an impact on the oxygen reduction. Further tests were performed at the gold IDE to determine how pH would affect the production and subsequent detection of hydrogen peroxide. This was carried out following the same method used in 5.3.6 in ADW with different pH values. The results, shown in Figure 5-24 showed interesting behaviour. The LSV performed at pH 5 did not differ significantly from the scan performed with no collector bias. As the solutions became more alkaline, the current associated with hydrogen peroxide production became more significant. It was evident that more alkaline pH values facilitated redox cycling better than acidic pH values. This could result from the increased concentration of protons in the acidic solutions. The additional protons facilitate the subsequent reduction to water. As such, less hydrogen peroxide was available to be detected at the collector as it was undergoing

further reduction too quickly. The current associated with the further reduction to water was found to be relatively unaffected by pH conditions, indicated by the minimal deviations observed at each LSV.

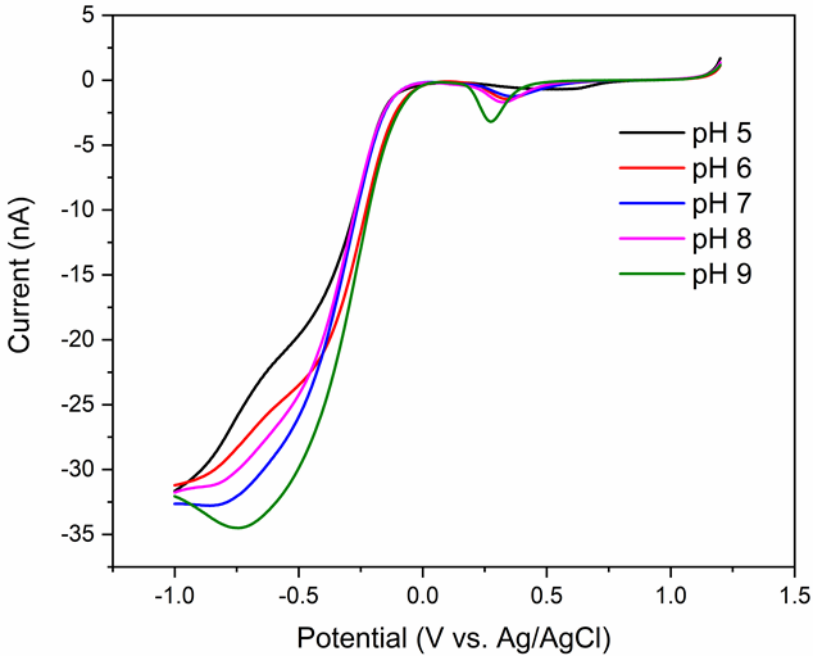

Figure 5-24 Comparison of LSVs at the generator electrode of a gold IDE at various pH values. The generator electrode was swept from 1.2 V to -1 V at 50 mV/s, while the collector electrode was biased at 0.6 V.

The resulting behaviour observed at the collector electrode further confirmed this theory. The greatest current for hydrogen peroxide oxidation was seen in the pH 9 solution seen in Figure 5-25, even though each solution had the same concentration of oxygen. Previous work shown in Figure 5-14 indicated that while the production of hydrogen peroxide was greatest at pH 9, the other pH values should not deviate significantly. The deviations observed in Figure 5-25 were attributed to the lack of hydrogen peroxide reaching the collector, rather than a lower production at each pH value. The lower concentration of protons at pH 9 means that the subsequent reduction of H_2O_2 to water proceeded at a slower rate. As such, a greater amount of hydrogen peroxide had time to diffuse to the

collector. This also explains why the reduction peaks at the generator electrode became so significant at pH 9 (Figure 5-24), as significantly more redox cycling began to occur.

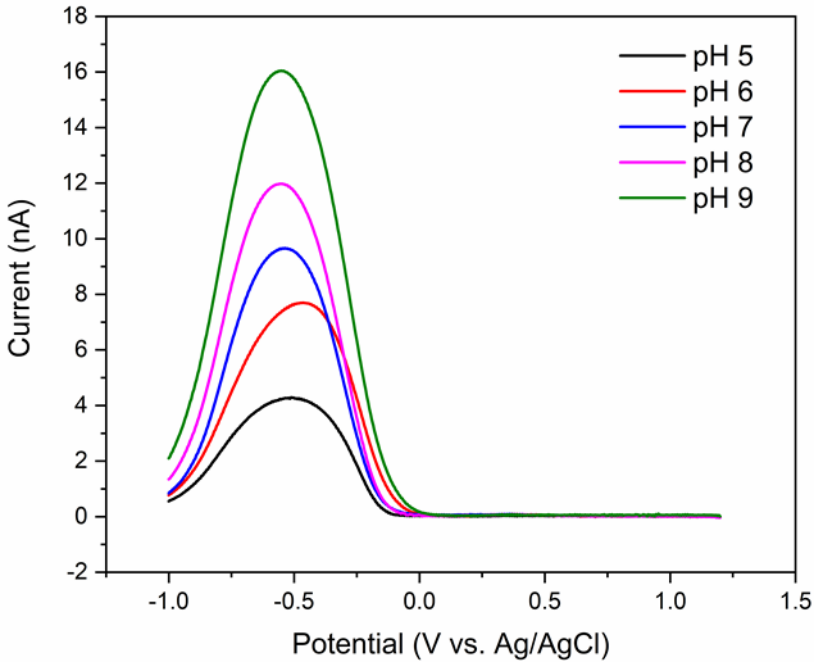

Figure 5-25 Comparison of LSVs at the collector electrode of a gold IDE at various pH values. The generator electrode was swept from 1.2 V to -1 V at 50 mV/s, while the collector electrode was biased at 0.6 V.

5.3.8 Platinum Plating on One Gold Comb of an Interdigitated Electrode Array

It was established that a gold generator and a platinum collector would provide the optimum sensor performance. Therefore, platinum was plated onto one comb of a gold IDE to improve the collector performance, and thus give the optimal sensing conditions. This was done using a commercial platinum plating bath as described in the experimental section. The datasheet optimum parameters for plating were a current bias of 1 A/dm^2 of electrode surface to give a deposition rate of 5 μm/hr. As the surface area of one comb of electrodes was 1.08 x 10^{-7} dm^2, the applied current was set at 0.108 μA. It was found that the optimum deposition thickness was 100 nm, as this was the thickness at which complete coverage of the electrode was observed, therefore deposition was carried out for 60 seconds. Typical deposition data is shown in Figure 5-26.

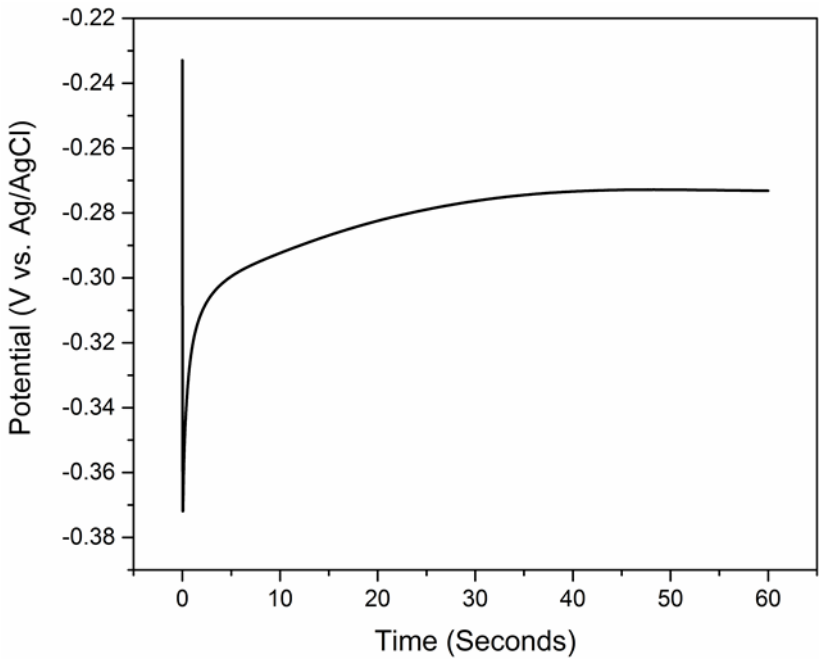

Figure 5-26 Chronopotentiometry in a platinum DNS bath on one comb of a gold IDE. The electrode was biased at 0.108 μA for 60 seconds.

Following the plating procedure, an array of characterisation techniques was applied to determine how well the platinum had deposited on the surface. The simplest method of characterisation was to assess the array optically, as shown in Figure 5-27. Platinum was clearly seen on one comb, indicated by the grey colouration of one comb. CV was then performed in single mode at the plated comb. Figure 5-28 the comparison of CVs of 1 mM FCA at a gold comb before platinum plating and subsequently after the comb had been plated with platinum. The peak shaped behaviour is again a result of diffusional overlap, which resulted in time dependent diffusion-limited mass transfer behaviour. The peak current increased by approximately 1 nA as a result of the platinum plating increasing the surface area. A significant behaviour change was seen on the platinum coated electrodes, where a reduction current was observed between 0 V and 0.1 V. This was determined to be the onset of oxygen reduction. Again, this further indicated that platinum had deposited onto the electrode comb, as platinum reduces oxygen at more anodic potentials than gold.

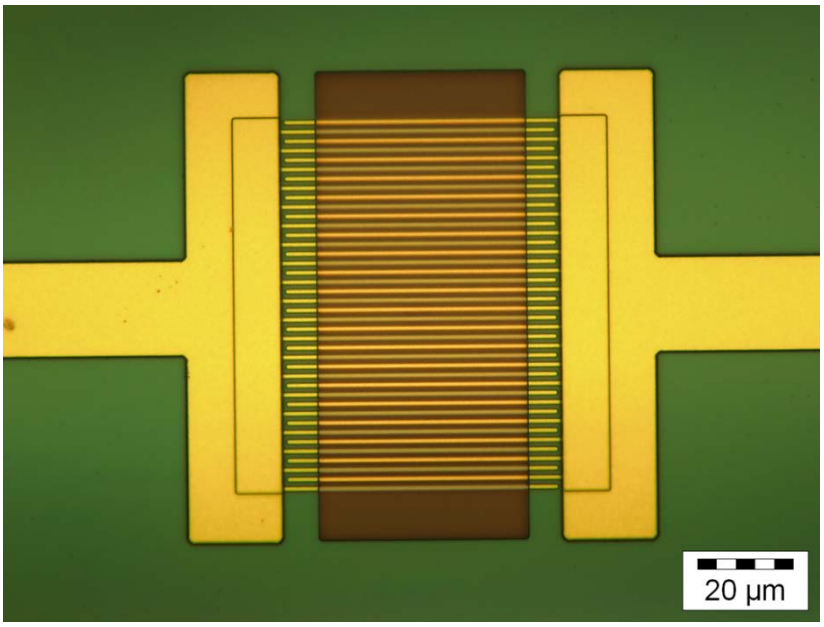

Figure 5-27 Optical image of platinum plated onto one comb of a gold IDE.

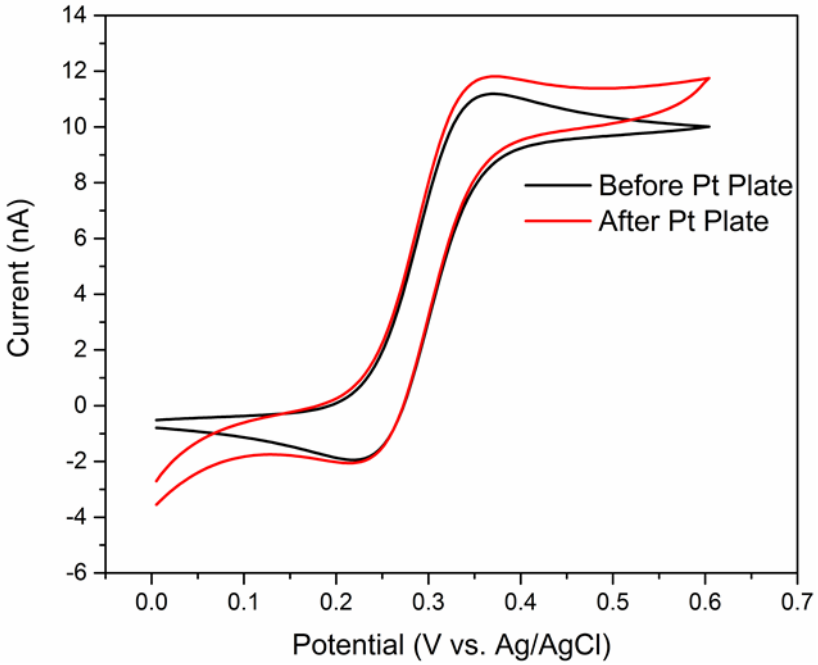

Figure 5-28 Comparison of electrode comb in 1 mM FCA before platinum plating (black) and after platinum plating (red). CVs were performed from 0 V to 0.6 V at 50 mV/s.

The performance of the gold-platinum IDE was further tested by performing CVs in GC mode, wherein the platinum comb was kept as the collector electrode to determine if the platinum plating degraded the overall IDE performance. Figure 5-29 shows a typical CV performed in FCA in GC mode for a gold-gold IDE and a gold-platinum IDE. In this case, the collector was biased at 0 V to reduce the oxidised species produced at the generator. A collection efficiency of 91.1% was calculated from the limiting current of the generator and collector scans when both electrodes were gold, which was typical for the 1 µm gap IDEs. The same procedure was performed on the IDE where one comb had been plated with platinum. No significant changes where observed for this CV, as the gold electrode behaved as normal. This also indicated that the platinum plating did not cause shorting between the generator and collector combs of electrodes. The current at the generator electrode remained the same, which is expected as the surface area of the gold did not change. The current measured at the collector however, increased by 3 nA compared to the gold collector. As the collector electrode could only measure species produced from

the generator, this increase was attributed to an enhanced collection efficiency. The collection efficiency of the gold-platinum IDE was calculated as 95.7%, an increase of 4.6% over the gold-gold array. The reason for the increase in collection efficiency resulted from increasing the width of the electrode, which subsequently decreased the gap between the generator and the collector electrodes. As previously discussed, increased electrode width and decreased gap size and the main methods of enhancing the efficiency of diffusion-only generator collector devices.

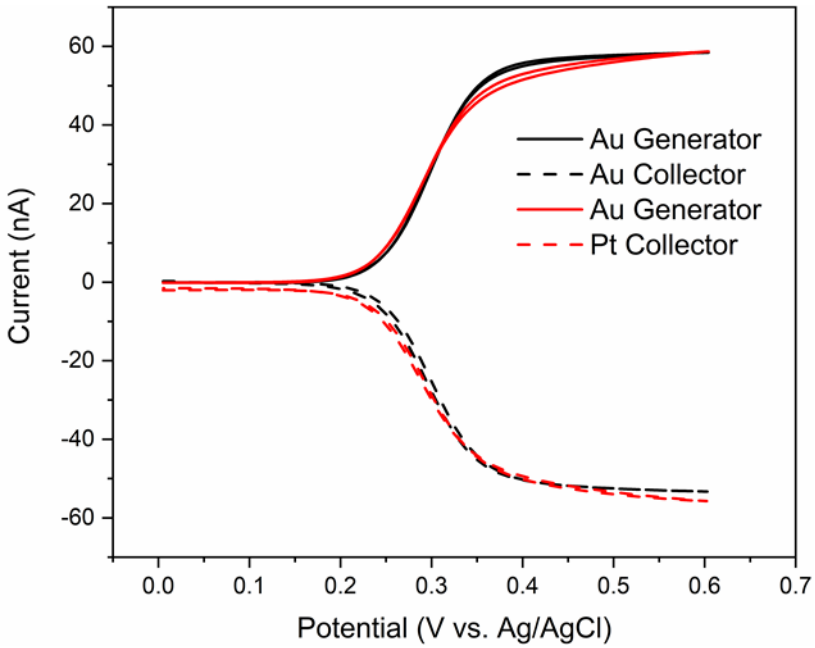

Figure 5-29 CV on a gold-gold (Black) and a gold-platinum (Red) IDE in generator-collector mode. The generator was swept from 0 V to 0.6 V at 50 mV/s while the collector was biased at 0 V.

Further non-electrochemical characterisation was carried out using SEM and energy dispersive x-ray (EDX) spectroscopy to characterise the efficacy of the deposition process. Both techniques were performed on a gold-gold IDE and a gold-platinum IDE to compare the plated with the bare electrodes. Figure 5-30 and Figure 5-31 show the SEM and EDX, respectively, of a gold-gold IDE. From SEM analysis it was determined that both the generator and collector combs were approximately the same width, and the gap was slightly over 1.24 µm. The electrodes shown in the SEM image are electrically

independent of each other, such that plating on one of these electrodes should not impact the other one. EDX was performed on both combs of electrodes and spectra were obtained for each. The EDX spectra showed that gold was the dominant species present, indicated by the gold coloured arrows. Other elements were present, summarised in Table 5-1, but no platinum was found to be present prior to the plating procedure.

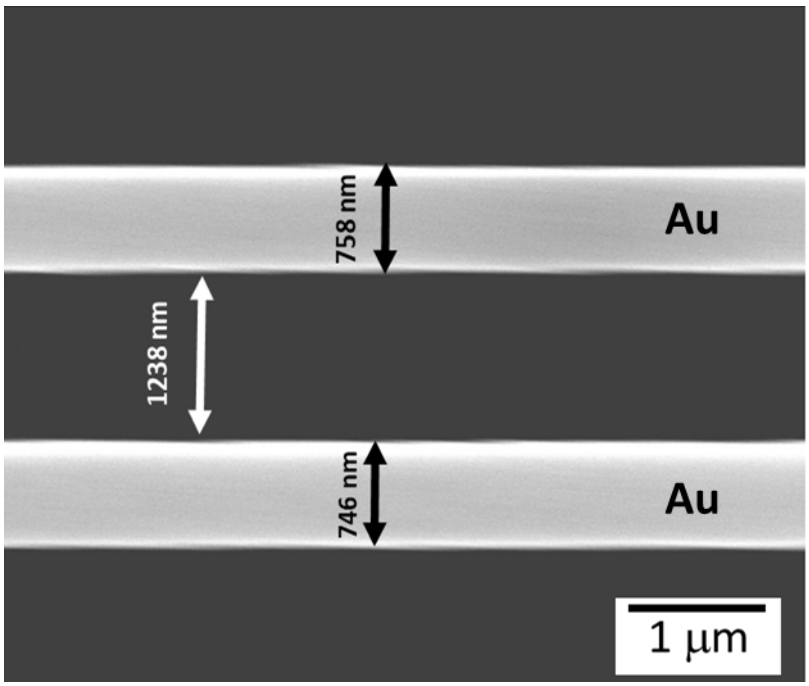

Figure 5-30 SEM image of the gold IDE.

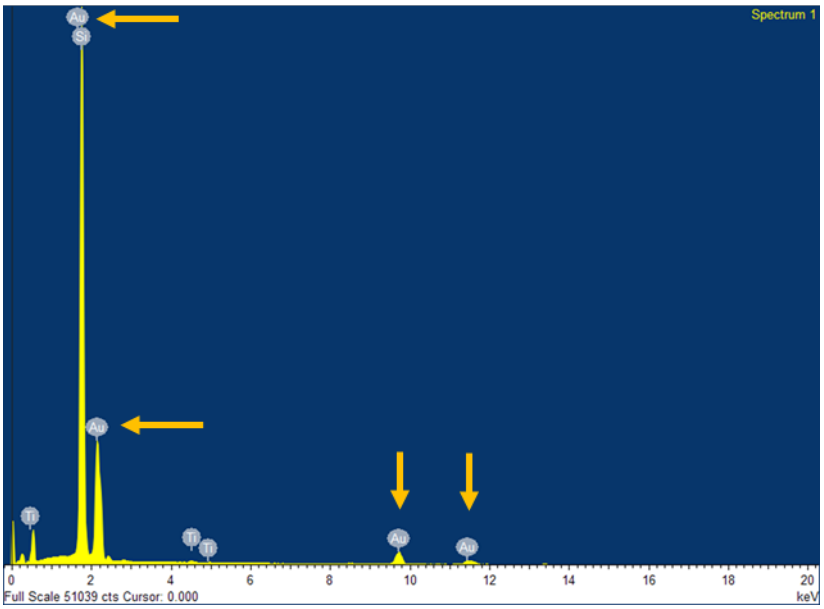

Figure 5-31 EDX spectrum taken at the gold IDE. The orange arrows indicate where a gold peak was observed.

The SEM image in Figure 5-32 that was obtained from the platinum plated electrode indicates that approximately 100 nm of platinum was deposited on the collector comb of electrodes. The platinum comb has a width now of 874 nm, and subsequently the gap has decreased to 1.17 µm. The EDX spectrum for a plated electrode shown in Figure 5-33 highlights that while gold was still the dominant species, platinum was also present on the surface, indicated by the silver coloured arrows. Gold was found to be dominant in the EDX spectrum since only a thin layer of platinum was deposited. Thus, the X-rays can penetrate through the platinum layer and detect gold. The penetration was so deep in fact, that titanium, which was underneath the gold, was also detected in trace amounts. An EDX was also performed on the unplated gold comb of electrodes. This was done as the width of the gold electrodes seemed larger than the non-plated IDE (777 nm vs. 758 nm). The EDX showed that no platinum was present on the gold electrode, and the larger width observed in SEM may have been due to variability in the fabrication process.

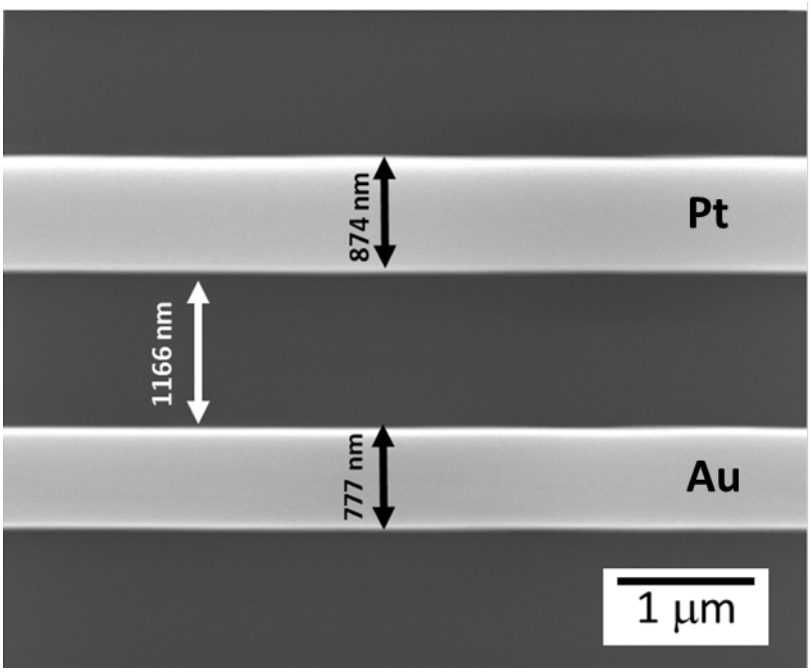

Figure 5-32 SEM image of a gold IDE after one comb was plated with platinum.

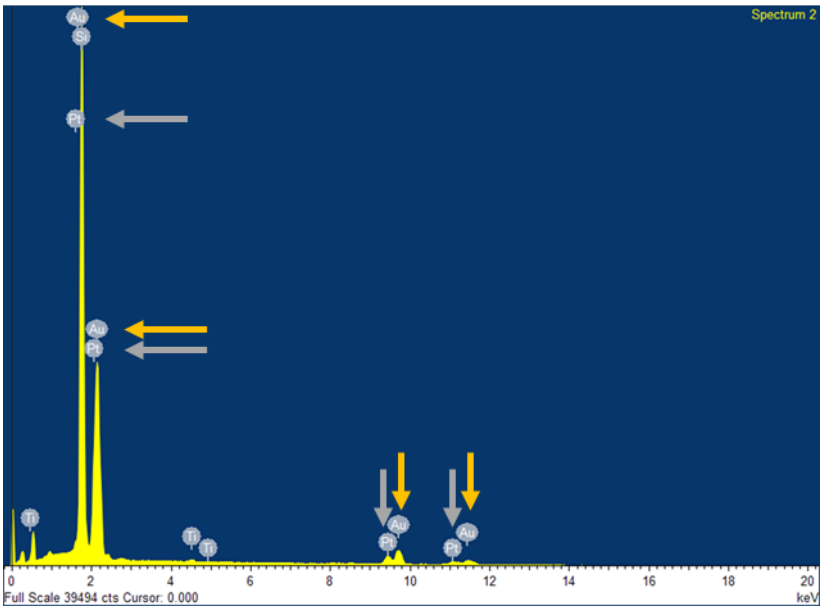

Figure 5-33 EDX spectrum taken at the gold IDE after platinum plating. The orange arrows indicate where a gold peak was observed, and the grey arrows indicate where a platinum peak was observed.

Electrode	*Si*	*Ti*	*Au*	*Pt*	*Total*
	(%)				
Au-Au	43.69	0.49	55.82	0	100
Au-Pt	32.03	0.36	43.91	23.7	100

Table 5-1 Summary of results from EDX analysis.

5.3.9 Oxygen Quantification by Hydrogen Peroxide Oxidation at a Gold-Platinum Interdigitated Electrode Array in ADW

After the platinum deposition had been optimised and the Au-Pt arrays were found to be functional, the sensing approach was then tested and optimised. The initial parameters were determined based on the previous work with gold and platinum as separate electrodes. Therefore, the gold electrode was scanned from 1.2 V to -0.9 V, while the platinum electrode was biased at 0.6 V. This potential bias was determined from the work discussed in section 5.3.4. The potential chosen was where the maximum hydrogen peroxide oxidation current was measured. However, initial work using this approach found that the collector current measured was smaller than expected. Measured currents were found to be lower than the equivalent tests performed using gold-gold IDEs, even though platinum should have given superior hydrogen peroxide oxidation. To understand what was occurring at the platinum electrode, the generator and collector electrodes were switched. As such, the gold comb was biased at a constant potential and the platinum comb was scanned using CV. The platinum was swept under the usual parameters, while the gold electrode was biased at -0.5 V, the potential at which the maximum hydrogen peroxide production was observed. These parameters were chosen in this way to create an excess of hydrogen peroxide at the gold electrode. The platinum electrode subsequently oxidised the produced hydrogen peroxide and the potential where the maximum oxidation occurred was then monitored. The result of this is shown in Figure 5-34, which shows the comparison between the biased, and unbiased gold comb. In the

scan where the gold was unbiased, no activity was seen on platinum between 0.1 and 1.2 V. It is important to note that while no major surface oxidation peak was seen for platinum, the oxide reduction was still observed on the reverse sweep. When the gold comb was biased, two major differences were observed for the platinum CV. Firstly, the intensity of the oxygen reduction reaction decreases dramatically. This was due to the gold comb having consumed a significant amount of oxygen while producing hydrogen peroxide. As the gold comb was constantly biased, therefore constantly consuming oxygen, diffusion of oxygen to the platinum electrode was minimised. Local concentration of dissolved oxygen is therefore lower so less can react at the platinum surface. The second major difference that was observed was the oxidation reaction between 0 V and 0.5 V. This was attributed to the oxidation of the produced hydrogen peroxide. Interestingly, the maximum intensity was observed at 0.3 V rather than the expected 0.6 V based on previous work. While it is said that hydrogen peroxide was produced as an intermediate, this may not be hydrogen peroxide in the conventional sense. It is more likely an activated peroxy species (such as HO_2^-) was produced, which reacts at less anodic potentials. As such, the parameters were adjusted to account for this variation.

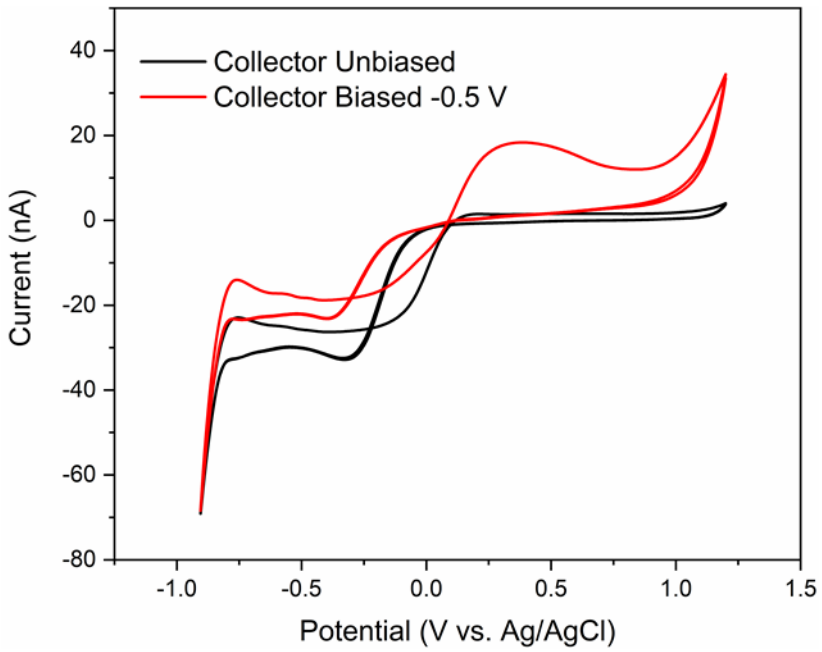

Figure 5-34 CV on a gold-platinum mixed metal IDE in ADW saturated with oxygen. The platinum electrode was used as the generator and swept from -0.9 V to 1.2 V at 50 mV/s. Black: Collector electrode unbiased. Red: Collector electrode biased at -0.5 V.

Following on from the establishment of the appropriate parameters, calibrations were carried out using the gold-platinum IDE. The gold comb was swept using LSV from 1.2 V to -0.8 V and the platinum comb was biased at 0.3 V. Figure 5-35 and Figure 5-36 show the LSVs and the subsequent calibration for oxygen reduction at the gold generator electrodes. The shape of the LSVs in Figure 5-35 were significantly different than previous oxygen reduction work. The plateaus associated with redox cycling of oxygen/hydrogen peroxide were mostly lower than equivalent concentrations in single mode at gold, with the exception of the currents for the 0 – 3 ppm range. The sensitivity to oxygen, which was found to be 2.37 nA/ppm was lower than the measured sensitivity of 3.19 nA/ppm for the single mode calibration.

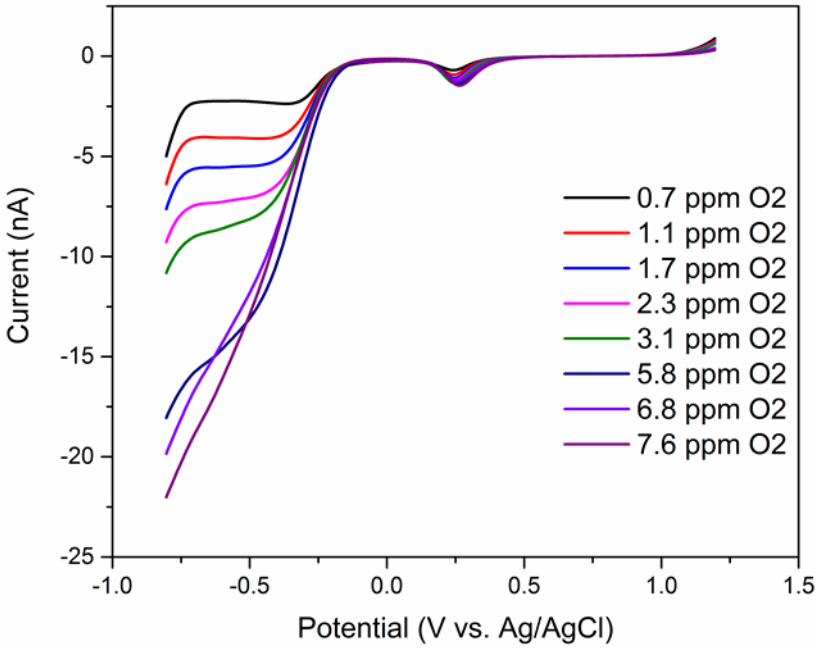

Figure 5-35 Generator electrode LSVs performed in various oxygen concentrations on the gold comb of the gold-platinum IDE. The electrode was swept from 1.2 V to -0.8 V at 50 mV/s while the collector was held at 0.3 V.

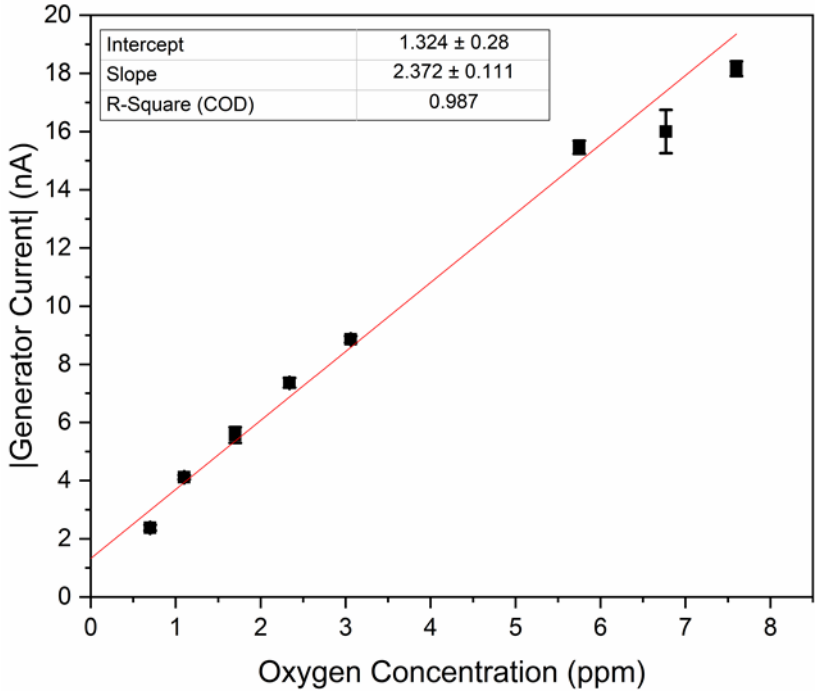

Figure 5-36 Calibration plot for the generator scans in various oxygen concentrations. Current values were taken at -0.7 V. Error was calculated from standard deviation of multiple scans (n=3).

Figure 5-37 and Figure 5-38 show the equivalent LSVs and calibration plot for hydrogen peroxide oxidation at the platinum collector electrodes. Again, a significant deviation from expected behaviour was observed. The peak currents were lower than expected even with the adjusted parameters. This could be explained by less hydrogen peroxide production at the generator or poor oxidation kinetics at the collector. The generator electrodes were unmodified and as such should have behaved similar to those in previous experiments. Therefore, it could be concluded that the poor performance of the overall sensor was a product of the collector comb of electrodes. It was previously noted that hydrogen peroxide oxidation on platinum is preceded by an adsorption step. When LSV was used, each scan started negative of this reaction, thus any bound hydrogen peroxide was removed from the surface. In this work, the platinum electrode was constantly biased at the same potential, therefore any bound hydrogen peroxide could not be removed.

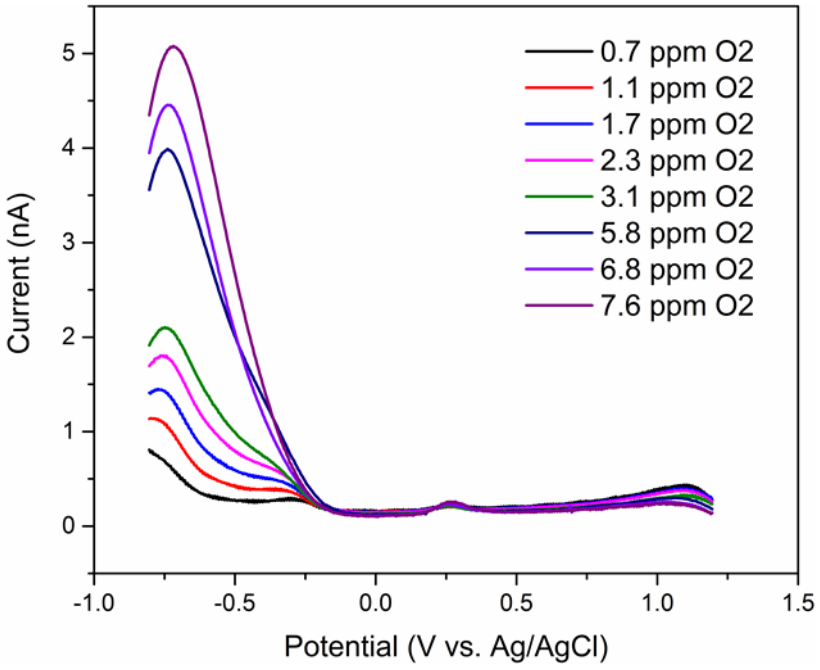

Figure 5-37 Platinum collector electrode response to the LSV performed at the generator electrode.

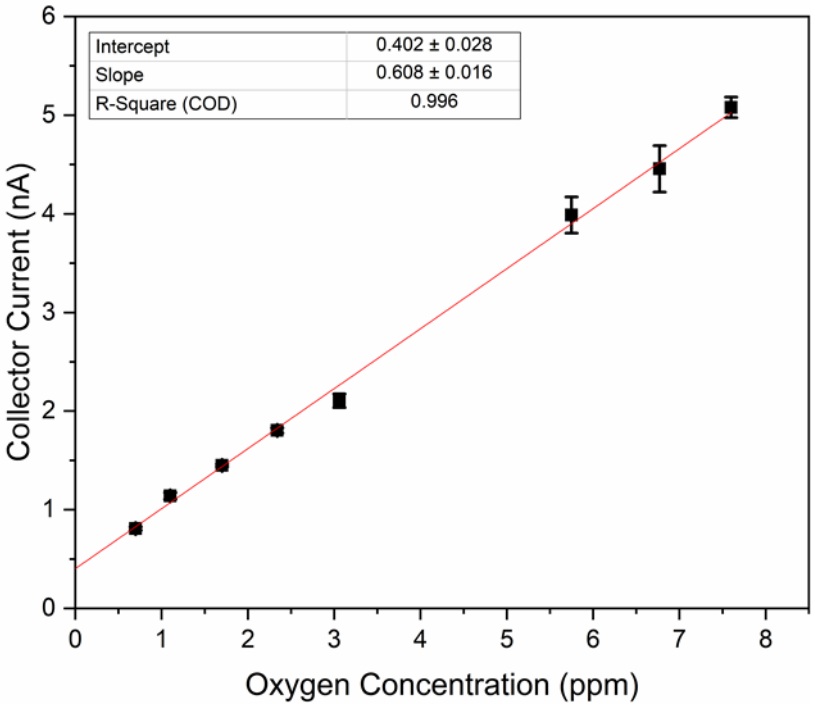

Figure 5-38 Calibration plot for the collector response in various oxygen concentrations. Current values were measured at -0.7 V. Error was calculated from standard deviation of multiple scans (n=3).

To rectify the issues that were a result of possible surface adsorption, a pre-treatment step was employed before any analysis was undertaken. This pre-treatment step involved biasing the platinum comb at -0.5 V for ten seconds prior to oxygen measurement. This was done to remove the bound hydrogen peroxide, but also had the benefit of reducing any surface oxide that may have formed during previous scans. Figure 5-39 and Figure 5-40 show the LSVs and equivalent calibration of the generator electrode in a range of oxygen concentrations following the implementation of a pre-treatment step. From the LSVs it was clear that pre-treating the collector comb had a significant impact on the generator comb. Measured currents are higher than those where no pre-treatment step was performed as a result of the increased efficiency of redox cycling. The calibration plot also indicated a sensitivity to oxygen of 3.72 nA/ppm, which was higher than both the untreated scans, and the initial work done in non-GC mode.

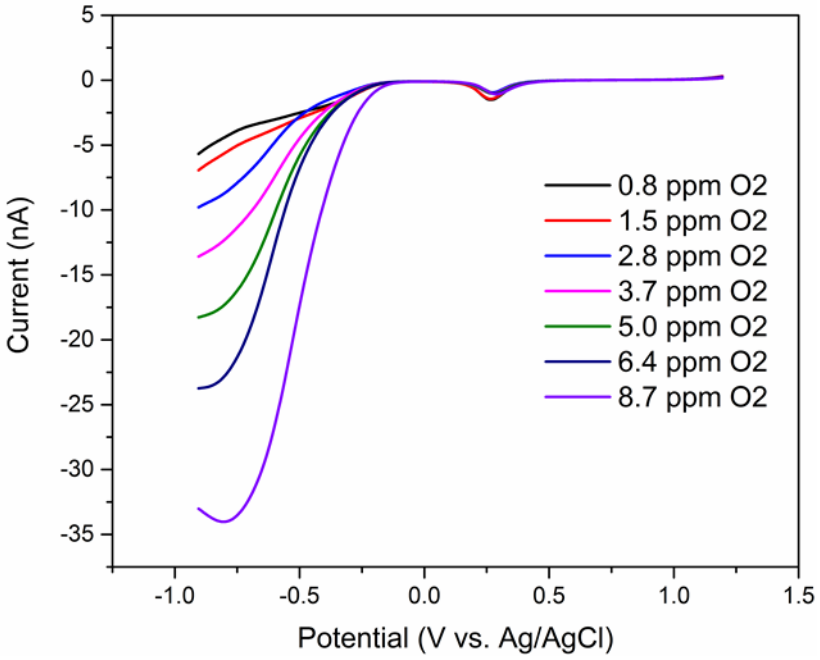

Figure 5-39 Generator electrode LSVs performed in various oxygen concentrations on the gold comb of the gold-platinum IDE after treating the platinum comb. The generator electrode was swept from 1.2 V to -0.8 V at 50 mV/s while the collector was held at 0.3 V.

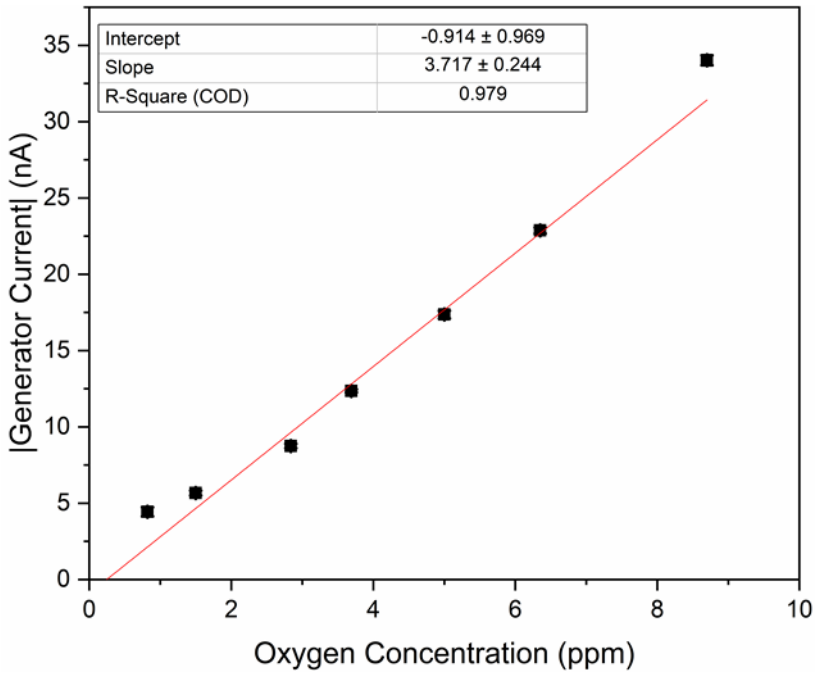

Figure 5-40 Calibration plot for the generator scans in various oxygen concentrations after treating the platinum comb of electrodes. Error bars contained within the data points (n=3).

The equivalent collector scans and calibration are shown in Figure 5-41 and Figure 5-42.

A major improvement was seen in each of the oxygen concentrations, where the signal

intensity increased for each concentration. The sensitivity of the collector electrodes to hydrogen peroxide was found to be 1.82 nA/ppm, which is three times higher than the equivalent sensitivity on the untreated electrode (0.61 nA/ppm). The linearity, however, was found to be lower than the untreated platinum electrode (0.99 vs. 0.96). This was possible due to inadequate pre-treatment. The 10 second bias of -0.5 V may not have been sufficient to remove all the adsorbed species; thus, the electrode surface condition may not have been consistent for each concentration, resulting in slight variability. The untreated electrodes, while lower in intensity, had a constant surface condition and therefore linearity was maintained as the electrode remained unchanged. The pre-treatment step was found to be important to improve the signal but may need to be refined to minimise variability.

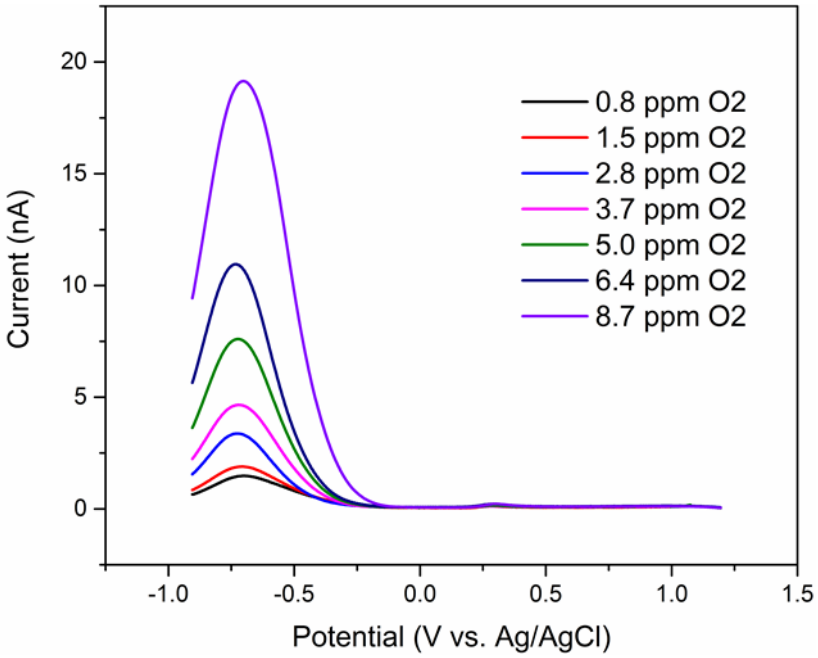

Figure 5-41 Platinum collector electrode response to the LSV performed at the generator electrode after being treated.

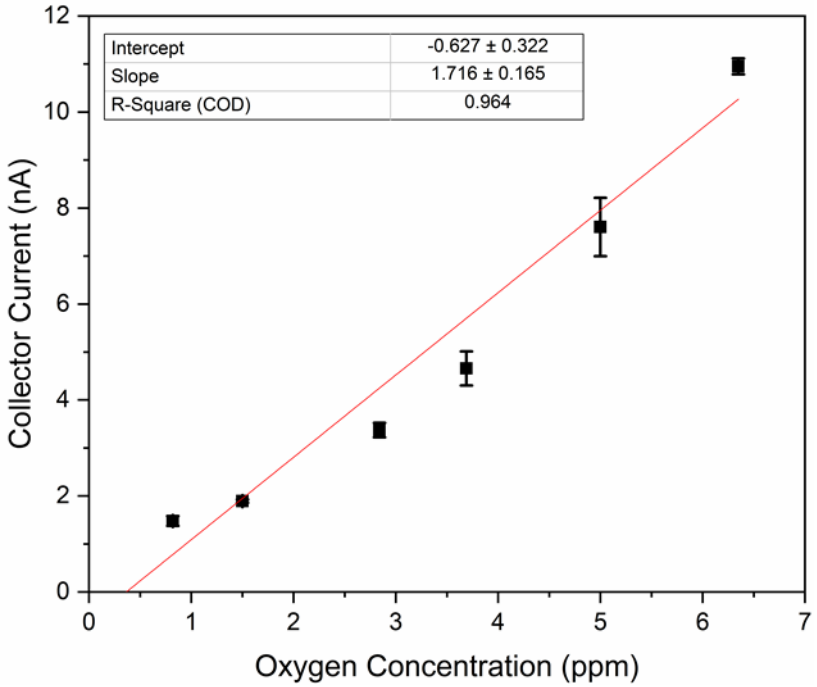

Figure 5-42 Calibration plot for the collector response in various oxygen concentrations after being treated. Error was calculated from standard deviation of multiple scans (n=3).

A comparison of the collector data for a gold-gold IDE, a gold-platinum IDE that has not been pre-treated and a gold-platinum array that has been pre-treated is shown in Figure 5-43. Each of these scans had been performed in ADW with equivalent concentrations of dissolved oxygen. It is evident that the pre-treatment step is crucial to ensure enhanced detection of hydrogen peroxide at the collector electrode.

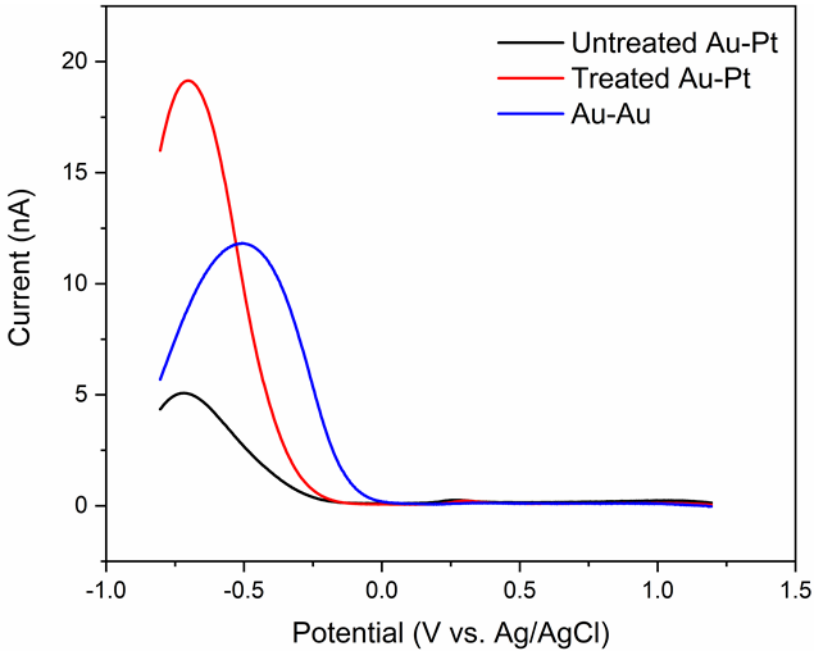

Figure 5-43 Comparison of the collector currents for each different IDE set-up and pre-treatment steps. Each scan was performed in ADW at pH 8 with oxygen concentrations of approximately 8 ppm.

This method was subsequently tested in the presence of FCA as an interferent, to determine how the hydrogen peroxide peak would be affected. An ADW sample with a low concentration of oxygen was spiked with FCA and tested with the gold-platinum IDE. While FCA is not a common interferent in water, it is a redox species that should interfere with both the generator and collector scans. The low oxygen concentration was chosen to maximise any interference issues. In Figure 5-44 the effect that a low concentration of iron had on oxygen reduction can be seen. The presence of iron shifted the onset of oxygen reduction to more cathodic potentials. Taking a measurement at a set potential in this case would result in underestimation of the oxygen concentration, which was the same in both cases. Figure 5-45 shows the response of the platinum collector to oxygen reduction at the generator in the presence of iron as FCA. It was clear that the peak current increases in the presence of iron, as it can oxidise at 0.3 V. However, the increase in current was also seen at the start of the scan between – 0.2 V and 0.2 V. In

this region, no hydrogen peroxide was being produced, therefore the only activity is from iron. When hydrogen peroxide was produced, the resulting peak is a combination of iron and hydrogen peroxide oxidation. The iron component could easily be subtracted as its oxidation current is constant. Using this approach, oxidative interferents can easily be removed from the oxygen analysis. As such, the measurement of oxygen concentration using the developed method was unaffected by the presence of an interferent.

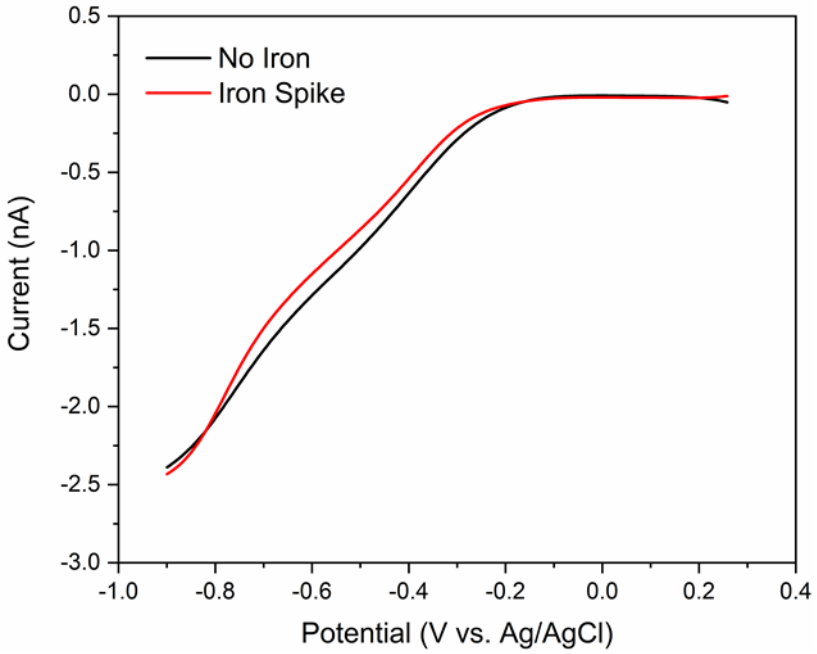

Figure 5-44 Oxygen reduction at a gold generator being swept in ADW with 1 ppm oxygen. The ADW sample was spiked with a low concentration of iron to monitor the effect on oxygen reduction.

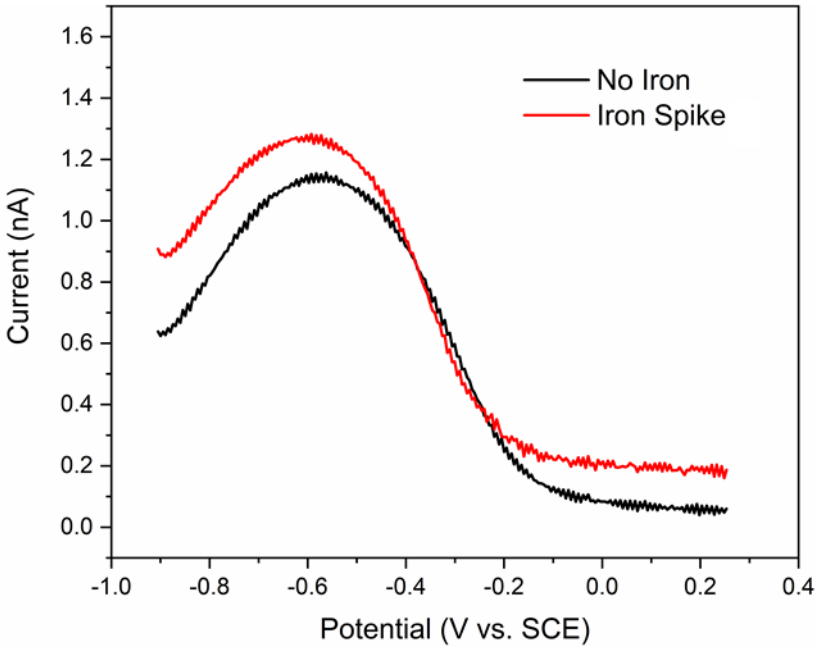

Figure 5-45 Platinum collector response to a gold generator being swept in ADW with 1 ppm oxygen. The ADW sample was spiked with a low concentration of iron to monitor the effect on the collector current.

5.3.10 Oxygen Quantification in River Water using a Gold-Platinum Interdigitated Array and a miniaturised custom built Portable Potentiostat

With the sensor system characterised, preliminary work was carried out using a portable potentiostat device for real river water samples. To facilitate the portability, the on-chip platinum reference was used instead of an external Ag/AgCl reference. The parameters were adjusted to account for this; therefore, the collector electrode was biased at 0.2 V and the pre-treatment was done using a potential of -0.9 V. Due to the limitations of the electronics, the lower potential value could not be negative of -0.9 V at this collector potential. Figure 5-46 and Figure 5-47 show the LSVs and subsequent calibration of the platinum collector electrode in river water. From the collector LSVs, it was clear the peroxide production at the generator had a maximum beyond the range of the portable potentiostat. However, from the calibration it was shown that the response observed was still linear with concentration of oxygen and showed an R^2 value of 0.98. The measured

currents were lower than the equivalent scans in ADW, which is most likely due to the pseudo reference electrode. It was shown previously that the hydrogen peroxide oxidation at the collector can have lower intensity at certain potential values. As platinum is only a pseudo reference electrode, the optimum oxidation potential may shift depending on the matrix conditions. In this case, 0.2 V was applied which was adequate for ADW but may have been less efficient in river water. It was also possible that due to the complexity of river water, hydrogen peroxide production may be less efficient, and thus less was measured at the collector. To improve this sensor, and to eliminate matrix effects as a cause for concern, a stable on-chip reference electrode will need to be incorporate in the test apparatus.

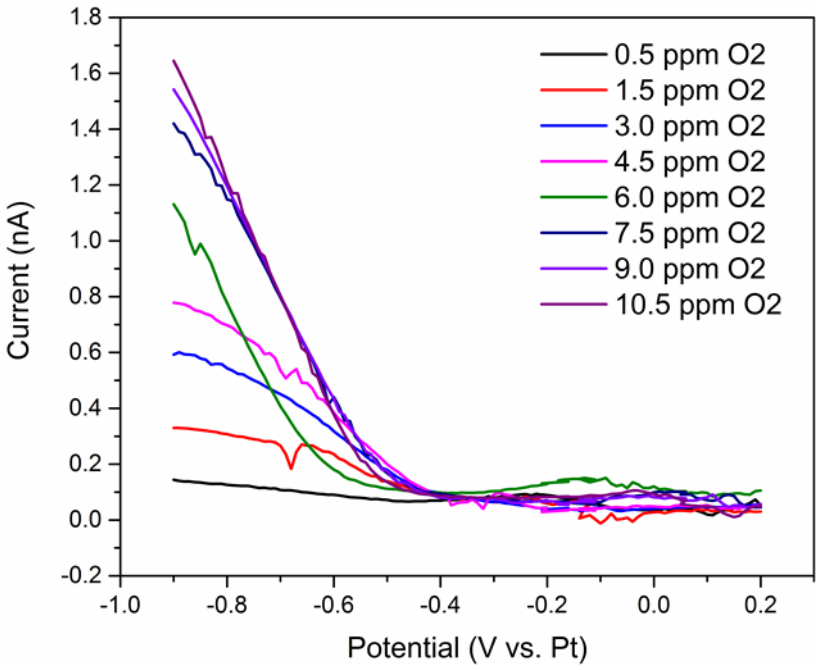

Figure 5-46 Platinum collector response to LSVs performed at the gold generator electrode in various concentrations of oxygen in river water. The generator was swept from 0.6 V to -0.9 V at 50 mV/s while the collector was biased at 0.2 V.

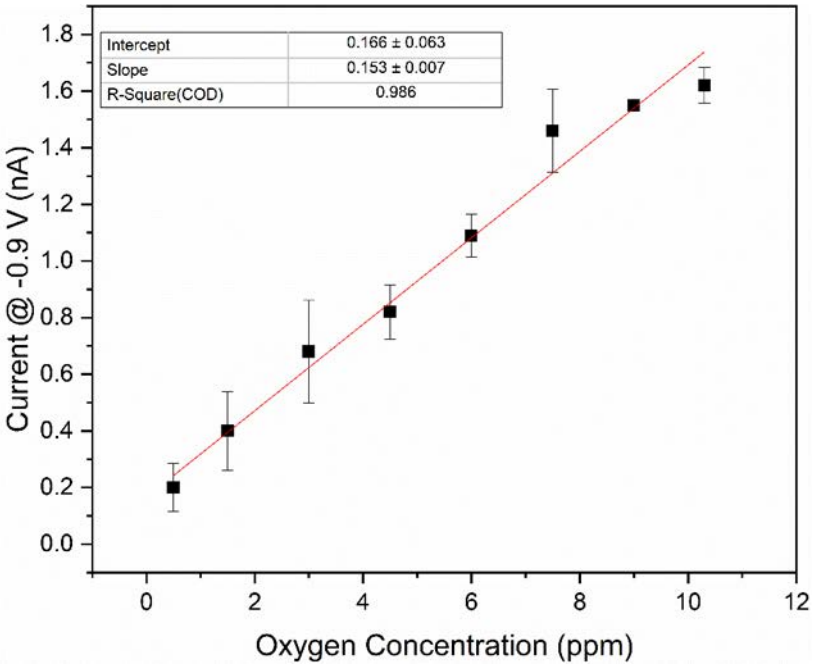

Figure 5-47 Calibration plot for the platinum collector response to oxygen in river water. Error was calculated from standard deviation of multiple scans (n=3).

5.4 Conclusions and Future Work

In this chapter, work based on the development of a dissolved oxygen sensor using IDEs has been shown. The IDEs used have been discussed in Chapters 3 and 4, with the exception being that the devices used for this work had a 1 μm gap. A voltammetric technique was developed that enabled the quantification of oxygen in water, by detecting the intermediate hydrogen peroxide species produced during the reduction reaction.

The choice of IDE dimensions was crucial to ensure a high collection efficiency of the produced hydrogen peroxide. As such the smallest inter-electrode gap was chosen as the base sensor device. Initial work was carried out to determine which electrode material was suitable for producing hydrogen peroxide, and subsequently which material better facilitated the detection of hydrogen peroxide. Gold electrodes were found to have a significantly higher production of hydrogen peroxide illustrated by the presence of two reduction waves in a typical CV experiment. This was further confirmed by employing generator-collector techniques were the collector electrode was biased to oxidise hydrogen peroxide. Gold measured a current of 12 nA which, in comparison to the 1 nA measured at platinum, indicated a superior hydrogen peroxide production. Platinum was subsequently identified as the appropriate material for detection of hydrogen peroxide, showing currents twice as large as gold for equivalent concentrations, and an onset of oxidation at less anodic potentials. Hydrogen peroxide detection on platinum was calibrated to concentrations as low as 20 μM without loss of sensitivity.

The pH dependence of both production of hydrogen peroxide, and detection of hydrogen peroxide was investigated to determine if pH was a potential interferent. It was found that the detection of hydrogen peroxide was unaffected by pH, however the production of

hydrogen peroxide was enhanced at alkaline pH values. Coupling the pH control methods developed in chapter 3 and 4 with this sensing technique could further enhance the detection of dissolved oxygen.

It was determined that the ideal sensor for detection of dissolved oxygen should contain a gold generator electrode to produce hydrogen peroxide, and a platinum collector electrode to subsequently detect the hydrogen peroxide. To facilitate this, platinum was plated onto one comb of a gold interdigitated array. This was done using a modified version of the plating technique used in chapter 4. This allowed for the deposition of a thin layer of platinum creating a dual metal IDE. This had the additional benefit of decreasing the inter-electrode gap, thereby increasing the collection efficiency.

The dual metal IDE was then used to calibrate dissolved oxygen in water using LSV. A pre-treatment step was developed that improved the sensitivity of platinum to hydrogen peroxide by ensuring a clean, reproducible surface for each test. The developed sensor accurately detected oxygen concentrations between 0.8 and 8.7 ppm. The resulting collector signal was double the equivalent scan done using a gold-gold IDE and 20 times higher than a platinum-platinum IDE. The detection of oxygen was also tested in the presence of FCA as an interferent. It was found that the magnitude of hydrogen peroxide oxidation was unaffected by the presence of FCA, indicating a potential for interferent free oxygen detection without the requirement of oxygen permeable membranes. Further work will be done using an array of interferents to determine the viability of the sensor in real water systems.

Finally, this the developed sensor was tested using a developed portable potentiostat device. For this work, the on-chip pseudo reference electrode was utilised. As such, this system was fully portable and did not require any additional electrodes or devices. The portable potentiostat was controlled using a developed app on a standard smart phone device. Calibration of oxygen was possible using the portable potentiostat system, indicating the potential for a fully portable oxygen electrochemical sensor.

5.5 References

1. P. C. Wilson, *University of Florida IFAS*, 2010, **SL313**.
2. R. Francis-Floyd, A. Riggs and E. Philips, *Florida Lakewatch Information Circular*, 2004, **IC109**.
3. B. Oram, Dissolved Oxygen in Water, https://water-research.net/index.php/dissovled-oxygen-in-water, (accessed 18/02/2020).
4. R. Francis-Floyd, A. Riggs and E. Philips, *Florida Lakewatch Information Circular*, 2004, **IC107**.
5. B. Patella, R. R. Russo, A. O'Riordan, G. Aiello, C. Sunseri and R. Inguanta, *Talanta*, 2021, **221**, 121643.
6. M. Gallant, Nitrates and Their Effect on Water Quality – A Quick Study, http://www.wheatleyriver.ca/media/nitrates-and-their-effect-on-water-quality-a-quick-study/, (accessed 18/02/2020).
7. M. F. Chislock, E. Doster, R. A. Zitomer and A. Wilson, *Nature Education Knowledge*, 2013, **4**, 10.
8. I. Helm, L. Jalukse and I. Leito, *Analytica Chimica Acta*, 2012, **741**, 21-31.
9. Z. Zhang, Z. Chen, F. Cheng, Y. Zhang and L. Chen, *Analyst*, 2016, **141**, 2955-2961.
10. Q. Wang, J. M. Zhang and S. Li, *Instrumentation Science and Technology*, 2019, **47**, 19-50.
11. Y. Lee and J.-Y. Park, *Journal of the Korean Physical Society*, 2011, **58**, 1505.
12. I. Helm, G. Karina, L. Jalukse, T. Pagano and I. Leito, *Environmental Monitoring and Assessment*, 2018, **190**, 313.
13. D. L. Short and G. S. G. Shell, *Journal of Physics E: Scientific Instruments*, 1984, **17**, 1085-1092.
14. J. Park, J. Chang, M. Choi, J. J. Pak, D. Lee and Y. K. Pak, 2007.

15. Y. Wei, Y. Jiao, D. An, D. Li, W. Li and Q. Wei, *Sensors*, 2019, **19**, 3995.

16. L. S. S. Santos, R. Landers and Y. Gushikem, *Talanta*, 2011, **85**, 1213-1216.

17. S. M. Silva, L. F. Aguiar, R. M. S. Carvalho, A. A. Tanaka, F. S. Damos and R. C. S. Luz, *Microchimica Acta*, 2016, **183**, 1251-1259.

18. P. Quaino, N. B. Luque, R. Nazmutdinov, E. Santos and W. Schmickler, *Angewandte Chemie International Edition*, 2012, **51**, 12997-13000.

19. Y. L. Zheng, D. Mei, Y.-X. Chen and S. Ye, *Electrochemistry Communications*, 2014, **39**, 19-21.

20. Y. Zheng, W. Chen, X.-Q. Zuo, J. Cai and Y.-X. Chen, *Electrochemistry Communications*, 2016, **73**, 38-41.

21. A. Sarapuu, K. Tammeveski, T. T. Tenno, V. Sammelselg, K. Kontturi and D. J. Schiffrin, *Electrochemistry Communications*, 2001, **3**, 446-450.

22. K. Tammeveski, T. Tenno, J. Claret and C. Ferrater, *Electrochimica Acta*, 1997, **42**, 893-897.

23. C. M. Sánchez-Sánchez and A. J. Bard, *Anal. Chem.*, 2009, **81**, 8094-8100.

24. A. Ignaczak, E. Santos and W. Schmickler, *Current Opinion in Electrochemistry*, 2019, **14**, 180-185.

25. S. Tanimoto and A. Ichimura, *J. Chem. Educ.*, 2013, **90**, 778-781.

26. Z. Tang, W. Wu and K. Wang, *Catalysts*, 2018, **8**, 65.

27. B. Jayasankar and K. Karan, *Electrochimica Acta*, 2018, **273**, 367-378.

28. V. Andoralov, M. Tarasevich and O. Tripachev, *Russian Journal of Electrochemistry*, 2011, **47**, 1327-1336.

29. V. Viswanathan, H. A. Hansen, J. Rossmeisl and J. K. Nørskov, *Acs Catalysis*, 2012, **2**, 1654-1660.

30. A. Prieto, J. Hernández, E. Herrero and J. M. Feliu, *Journal of Solid State Electrochemistry*, 2003, **7**, 599-606.

31. I. Srejić, M. Smiljanić, Z. Rakočević and S. Štrbac, *Int. J. Electrochem. Sci*, 2016, **11**, 10436-10448.

32. A. Damjanovic, M. A. Genshaw and J. O. Bockris, *Journal of the Electrochemical Society*, 1967, **114**, 466-472.

33. A. Sarapuu, M. Nurmik, H. Mändar, A. Rosental, T. Laaksonen, K. Kontturi, D. J. Schiffrin and K. Tammeveski, *Journal of Electroanalytical Chemistry*, 2008, **612**, 78-86.

34. R. Zeis, T. Lei, K. Sieradzki, J. Snyder and J. Erlebacher, *Journal of Catalysis*, 2008, **253**, 132-138.

35. U. A. Paulus, T. J. Schmidt, H. A. Gasteiger and R. J. Behm, *Journal of Electroanalytical Chemistry*, 2001, **495**, 134-145.

36. A. Bonakdarpour, M. Lefevre, R. Yang, F. Jaouen, T. Dahn, J. P. Dodelet and J. R. Dahn, *Electrochemical and Solid-State Letters*, 2008, **11**, B105-B108.

37. V. Stamenković, T. J. Schmidt, P. N. Ross and N. M. Marković, *Journal of Physical Chemistry B*, 2002, **106**, 11970-11979.

38. T. A. Postlethwaite, J. E. Hutchison, R. Murray, B. Fosset and C. Amatore, *Anal. Chem.*, 1996, **68**, 2951-2958.

39. W. Xing, M. Yin, Q. Lv, Y. Hu, C. Liu and J. Zhang, in *Rotating Electrode Methods and Oxygen Reduction Electrocatalysts*, eds. W. Xing, G. Yin and J. Zhang, Elsevier, Amsterdam, 2014, DOI: https://doi.org/10.1016/B978-0-444-63278-4.00001-X, pp. 1-31.

40. A. Wahl, K. Dawson, J. MacHale, S. Barry, A. J. Quinn and A. O'Riordan, *Faraday Discussions*, 2013, **164**, 377-390.

41. K. A. Striebel, F. R. McLarnon and E. J. Cairns, *Journal of the Electrochemical Society*, 1990, **137**, 3351-3359.

42. J. Kim and A. A. Gewirth, *The Journal of Physical Chemistry B*, 2006, **110**, 2565-2571.

43. Z. Qiang, J.-H. Chang and C.-P. Huang, *Water Research*, 2002, **36**, 85-94.

44. I. Katsounaros, W. B. Schneider, J. C. Meier, U. Benedikt, P. U. Biedermann, A. A. Auer and K. J. J. Mayrhofer, *Physical Chemistry Chemical Physics*, 2012, **14**, 7384-7391.

45. S. B. Hall, E. A. Khudaish and A. L. Hart, *Electrochimica Acta*, 1998, **43**, 579-588.

Chapter 6 Summary and Future Work

6.1 Summary

The focus of this PhD work was to develop electrochemical sensors using an interdigitated electrode (IDE) platform, for point of use water analysis applications. The proposed devices were economical, reproducible, and capable of use both in the lab and on-site analysis in the field. As discussed in chapter 1, IDEs can be used to boost the sensitivity of a sensor due to redox cycling or generator collector approaches. Advances in fabrication methods have facilitated the development of ultra-micro and nano scale IDE devices. Similarly, these devices have been shown to improve the detection of a variety of chemical and biological species, as well as providing an interference free method of analysis.

In chapter 2, fabrication and characterisation of a nanoscale IDE array was shown. Initial experiments in generator-collector mode showed a 7-fold increase in current output compared to experiments in single mode for an array with a 500 nm gap. This increase was attributed to each electrode acting independently, and redox cycling of the active molecular species between the two combs of electrodes. Simulations were undertaken to further describe the processes occurring at the electrode surface. The fully characterised devices were then used in the detection of iron in tap water samples. The redox cycling effect was used to increase the signal generated for iron, which resulted in extremely low detection limits (0.6 µg/L).

In chapter 3, an in-situ pH control method was developed for use with micron sized IDE arrays. Characterisation of IDE arrays with varying gap sizes was performed, with 2 µm gaps ultimately being selected for use in further chlorine analysis. Initial simulations were performed to determine if a pH gradient could be created, followed by initial tests in water

samples. The gold oxide reduction peak was used as a means of reading local pH, at a sensor, by first calibrating the response in various pH buffers. The developed method was applied to the detection of free chlorine in water samples. Solutions of pH 3 were found to convert free chlorine to hypochlorous acid, which was more easily detected electrochemically. Local in-situ pH control was used to measure chlorine as low as 0.35 ppm in solution, and was subsequently used to measure the concentration of free chlorine in a tap water sample by standard addition approach.

Chapter 4 focused primarily on the detection of monochloramine (MCA), using the previously developed in-situ pH control method. pH control enabled oxygen to be removed as an interferant by converting MCA to dichloroamine (DCA), which is detected outside of the oxygen reduction window. In this chapter, refinement of the pH control method was performed along with testing the method in harsher conditions, to determine viability of the sensor in real-world applications. Platinum was identified as a superior protonator material and facilitated in-situ pH control in highly alkaline solutions and at lower potential biases. The developed MCA sensor had a limit of detection of 0.1 ppm with minimal drift (<5%) over multiple scans. The detection of MCA was found to be unaffected by oxygen, fulfilling the desired goal.

Chapter 5, the final experimental chapter of this thesis, focused on the development of a membrane free dissolved oxygen sensor utilising the benefits of an IDE device. For this work, a 1 µm gap IDE array was used as the sensing platform. The sensing mechanism involved the oxidation of hydrogen peroxide produced as an intermediate in the oxygen reduction reaction. Both gold and platinum metals were investigated, and it was found that gold was the ideal hydrogen peroxide production material, while platinum was the

ideal hydrogen peroxide oxidation material. The mixed metal device was used to measure various concentrations of oxygen in water samples. Redox cycling was found to enhance the signal attributed to oxygen reduction, further increasing the sensitivity of the detection method. Finally, a portable potentiostat device was developed (in collaboration with Mr Aidan Murphy and Dr. Ivan O'Connell, MCCI) which was capable of detecting oxygen in water using the mixed metal IDE sensor, thereby facilitating point of use oxygen measurements.

In conclusion, this thesis has shown the advantages of using IDE as a sensing platform for analysis of key analytes in water samples. These devices have a lower sensor footprint, as electrodes can be spaced together without concern of diffusion layer overlap and can be fabricated on a wafer scale, meaning a fast throughput of multiple devices. Redox cycling has been shown to improve the sensitivity, while in-situ pH control method facilitates reagent free and interferent free analysis. These devices are simple to use and are easily portable to suit point of care applications.

6.2 Future Work

The work undertaking in this PhD project involved the development of various proof of concept sensors for the detection of various components of water. To determine viability as a commercial sensor, further tests need to be done such as lifetime tests and a complete interferent study. These sensors have been shown to be highly sensitive, but this can be further improved by using nanoscale IDE like those used for the detection of Iron in chapter 2. As the methods for pH control and dissolved oxygen detection are refined, the sensing platform can be moved to nanowires to further improve the detection limits.

In each case, the sensor platform will be moved to a newly developed HDMI based chip, as shown in Figure 6-1. This has been developed with all contact pads on one side of the device to simplify integration with potentiostat electronics, which is highlighted in Figure 6-2. This also removes the requirement for a chip holder, as the electrodes can be inserted directly into the desired solution. These chips also feature an on-chip platinum pseudo reference electrode which will be utilised in future experiments to further simplify the sensing mechanism. Platinum as a reference electrode, has been seen to be unstable, so this may need further refinement to increase its stability, which will eliminate any variability in the sensor performance.

Regarding the pH control method, further protonator materials will be investigated. Platinum was identified as being superior to gold at electrochemical water splitting, however there are many other materials that outperform platinum. Identifying the ideal protonator material will decrease the overall power demand of the sensor, meaning a longer performance using a portable potentiostat device. Furthermore, the method used to produce protons for pH adjustment will be refined. Currently it is done by constant bias at the protonator electrode. However, it may prove more efficient to pulse the protonator to a high potential to produce an excess of protons that gradually diffuse to the sensing electrode.

The dissolved oxygen detection method can be further improved by decreasing the gap between the two electrode combs. This can be done by using the 500 nm gap IDE as described in chapter 2, but this gap can be further decreased to improve collection efficiency. Moving the sensing technique to the nanoscale means that the platinum plating technique may need to be further refined. As the gap between the electrode combs gets

smaller, there is an increased likelihood that plating of materials will result in short-circuiting of the device. Furthermore, combination of the pH control method with the dissolved oxygen detection may prove beneficial. It was shown that the reduction of dissolved oxygen, and subsequent oxidation of hydrogen peroxide increased at basic pH conditions. Controlling the pH to suit this, will result in a further increase of sensitivity. This would require the development of a five electrode cell, now with three working electrodes, which in itself would permit a variety of other interesting electrochemical applications.

Figure 6-1 HDMI chip platform for IDE arrays

.

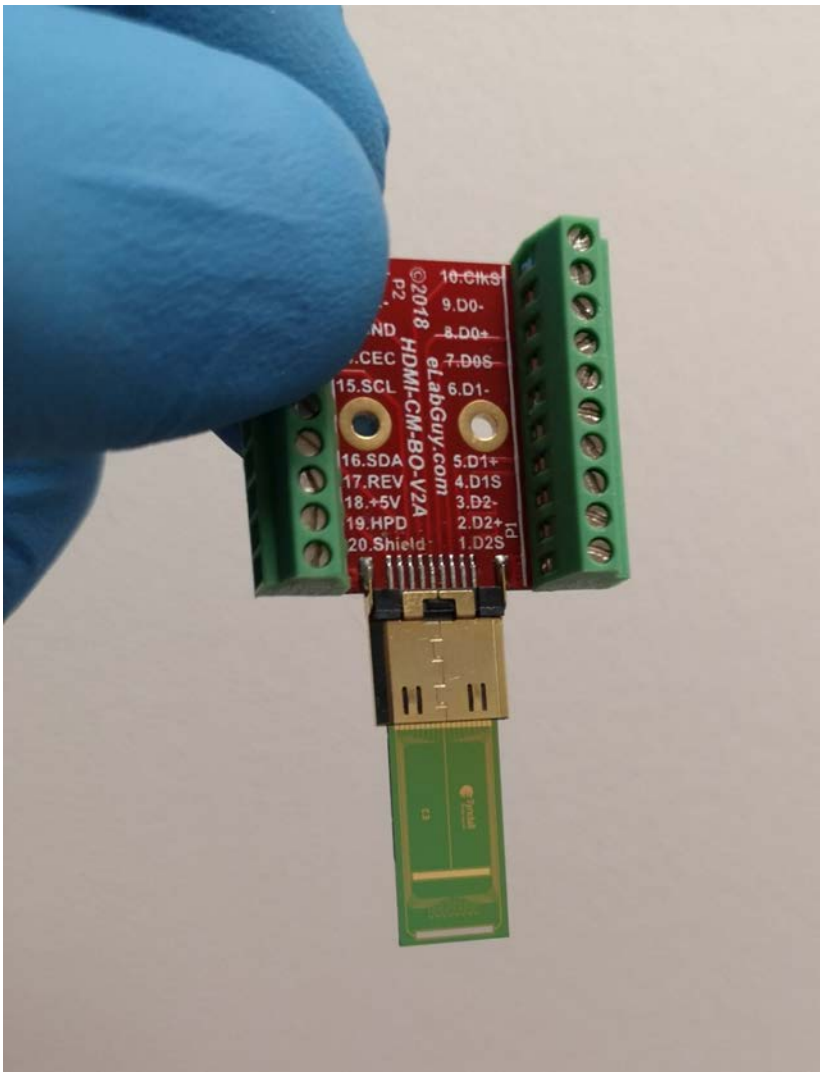

Figure 6-2 HDMI chip inserted into a HDMI reader for integration with the potentiostat electronics

Appendices

A.1 Experimental Set-up for IDEs

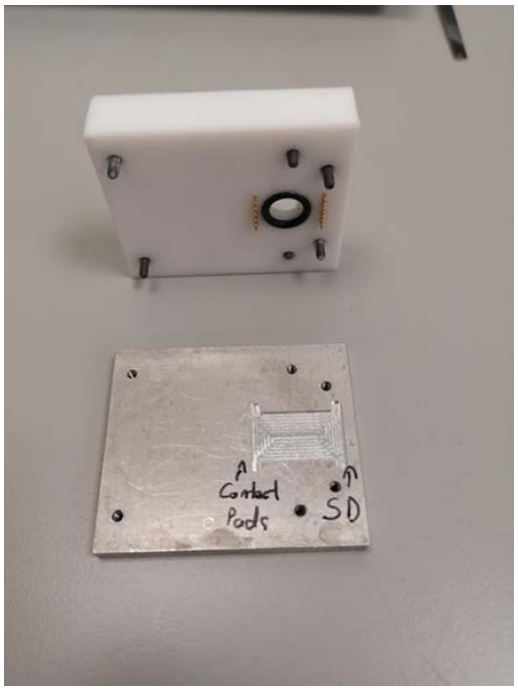

Figure A.1 - 1 Image of the chip holder when disassembled. The chip sits in the aluminium base and the pins enable electrical contact between the potentiostat and the working electrodes. The black o-ring prevents leakage of the sample solutions.

Figure A.1 - 2 Image of the assembled chip holder. The sample can be inserted into the well up to a maximum volume of 9 mLs. The shows the completed set-up, excluding connections to the potentiostat, when using the on-chip pseudo reference electrode.

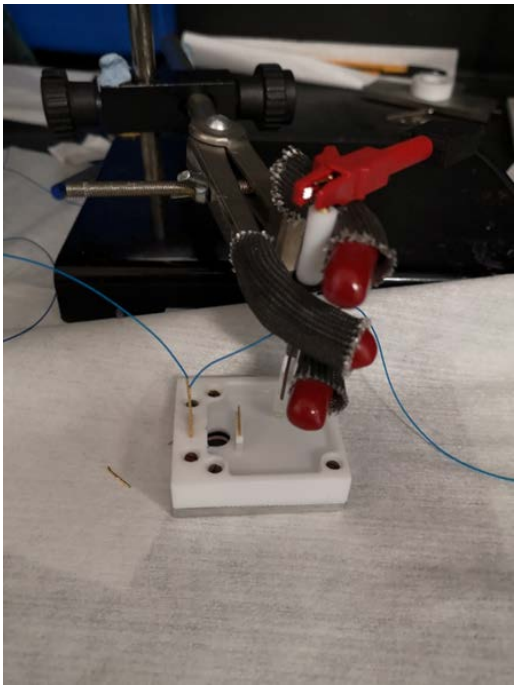

Figure A.1 - 3 Image of the assembled device when an external reference electrode is required. The sample well is filled to an adequate volume to allow for contact with the reference electrode, which is held in place using a retort stand.

A.2 Microdisc Arrays for Initial MCA Measurements

Microdisc arrays were used for initial characterisation of MCA samples. These were devices that had been fabricated as part of previous work and as such had been extensively characterised. The fabrication processes to make these devices were comparable to those used for the IDEs, therefore it was simpler to make comparisons between these devices than to commercial electrodes. A schematic of the device and the experimental set-up is shown in Figure A.2-1. The microdisc arrays consisted of 56 disc electrodes with diameters of 20 µm separated by 500 µm to ensure diffusional independence, shown in Figure A.2-2.

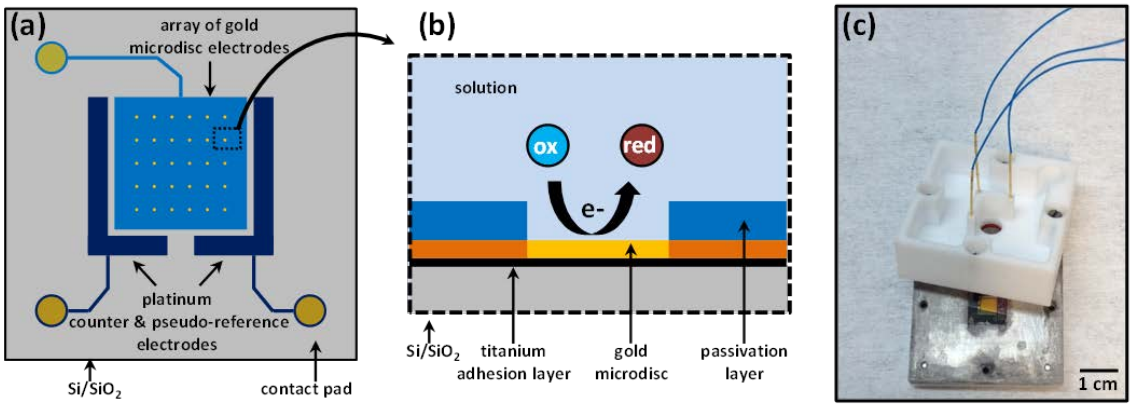

Figure A.2-1 (a) Schematic representation of the microdisc array device. (b) Schematic representation of a single microdisc in contact with sample solution. (c) Image of the microdisc array in the required sample holder.

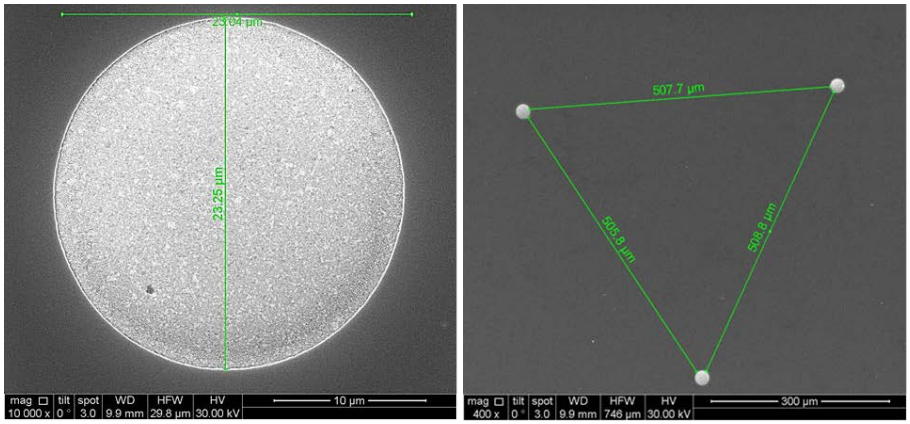

Figure A.2-2 SEM images of one microdisc (left) and three microdiscs showing the spacing between each (right).

A.3 Colorimetric Measurements

Commercial colorimetric test kits were used to determine free-chlorine and MCA concentrations. The procedure for testing both species was the same and differed only by choice of reagent. The reagent N,N-diethyl-p-phenylenediamine (DPD) was used for measuring free-chlorine, while Monochlor F was used to measure MCA. Sample vials were rinsed with DI water and the sample solution prior to analysis. The vial was then filled to 10 mLs with the sample and used to get a background reading in the colorimeter. The desired reagent was then added to the sample and allowed to react for 5 minutes. A colour change was observed, from colourless to either purple (free-chlorine and DPD) or green (MCA and monochlor F). The sample vials were then placed in the colorimeter and a measurement was performed where a reading in parts per million (ppm) was obtained. The calibrations plots in both chapters 3 and 4 are based on the concentrations as measured by the colorimetric tests.

A.4 Publications

1. Murphy, A.; **Seymour, I**.; O'Riordan, A.; O'Connell, I. “Portable Data Acquisition System for Nano and Ultra-Micro Scale Electrochemical Sensors” **2020** *ChemRxiv. Preprint* 10.26434/chemrxiv.12320291 – Submitted to IEEE Sensors, in review.
2. **Seymour, I.;** O'Sullivan, B.; Lovera, P.; Rohan, J.; O'Riordan, A. “Electrochemical Detection of Free-Chlorine in Water Samples Facilitated by In-Situ pH Control Using Interdigitated Microelectrodes” **2020** *ChemRxiv. Preprint*. https://doi.org/10.26434/chemrxiv.11898126.v1 - Submitted to Sensors and Actuators B, awaiting final decision.
3. O’Riordan, A.; **Seymour, I**.; O’Sullivan, B.; Wahl, A.J.C.; Lovera, P. and Rohan, J.F. “Nanoelectrochemical Sensor Systems: Molecular Diffusion Simulations, Sensor Design, Fabrication and Characterization” 2019 *In Proceedings of the Sixth Annual ACM International Conference on Nanoscale Computing and Communication (NANOCOM ’19)* 10.1145/3345312.3345500 – Conference Paper
4. **Seymour, I.;** O’Sullivan, B.; Lovera, P.; Rohan J. F.; and O’Riordan, A. "Removal of Dissolved Oxygen Interference in the Amperometric Detection of Monochloramine Using a pH Control Method," *2019 IEEE SENSORS*, Montreal, QC, Canada, **2019**, pp. 1-4, 10.1109/SENSORS43011.2019.8956674 – Conference Paper
5. **Seymour, I**.; Lovera, P.; Wahl, A.; Rohan, J. F. and O'Riordan, A. “Redox Cycling at Interdigitated Nanowire Electrode Arrays: Enhanced Electrochemical Sensing”, ***2018*** *IEEE 18th International Conference on Nanotechnology (IEEE-*

NANO), Cork, Ireland, 23-26 July, pp. 1-4. doi: 10.1109/NANO.2018.8626262 – Conference Paper

6. Murphy, A.; **Seymour, I**.; O'Riordan, A. and O'Connell, I. "Generator Collector Voltammetry Data Acquisition for Nanowire Interdigitated Sensors," **2018** *IEEE 18th International Conference on Nanotechnology (IEEE-NANO)*, Cork, Ireland, pp. 1-3, doi: 10.1109/NANO.2018.8626360. – Conference Paper
7. Wahl, A.; **Seymour, I**.; Moore, M.; Lovera, P.; O'Riordan, A.; Rohan, J.F. "Diffusion profile simulations and enhanced iron sensing in generator-collector mode at interdigitated nanowire electrode arrays." **2018** *Electrochimica Acta*. 277. 10.1016/j.electacta.2018.04.181.

A.5 Publications in Preparation

1. **Seymour, I**.; O'Sullivan, B.; Lovera, P.; Wahl, A.J.C.; O'Riordan, A.; Rohan, J. F. "Removal of Oxygen Interference in the Electrochemical Detection of Monochloramine using in-situ pH Control at Interdigitated Microelectrodes" – In Preparation
2. **Seymour, I**.; Murphy, A.; Rohan, J. F.; O'Riordan, A. "Quantification of Dissolved Oxygen using Generator-Collector Mode at an Interdigitated Microelectrode Array" – In Preparation

A.6 Conferences Attended

1. Electrochemistry in Graduate Research, ISE Student Symposium, Dublin, Ireland 2019 "Removal of Dissolved Oxygen Interference in the Amperometric Detection of Monochloramine Using a pH Control Method" – Oral Presentation
2. IEEE Sensors, Montreal, Canada, 2019 "Removal of Dissolved Oxygen Interference in the Amperometric Detection of Monochloramine Using a pH Control Method" – Oral Presentation
3. Analytical Research Forum, RSC, London, United Kingdom, 2019 "Electrochemical pH Control for Enhanced Sensing Applications" – Poster Presentation
4. Electrochemistry in Graduate Research, ISE Student Symposium, Limerick, Ireland 2018 "Interdigitated Nanowire Electrode Arrays for Enhanced Electrochemical Sensing" – Poster Presentation
5. IEEE Nano, Cork, Ireland, 2018 "Interdigitated Nanowire Electrode Arrays for Enhanced Electrochemical Sensing" – Oral Presentation
6. First Symposium on Electrochemistry in Graduate Research, ISE Student Symposium, Cork, Ireland 2017 "Interdigitated Nanowire Electrode Arrays for Enhanced Electrochemical Sensing" – Oral Presentation and Chair